UNIVERSITY OF SOUTHAMPTON

FACULTY OF ENGINEERING, SCIENCE AND MATHEMATICS

School of Physics and Astronomy

Modifying the magnetic properties of Laves phase intermetallic multilayers and films by nano-patterning and ion implantation

by

Andrew Roger Buckingham

Thesis for the degree of Doctor of Philosophy

March 2010

ABSTRACT

Since the pioneering work of Kneller & Hawig and Skomski & Coey some 20 years ago, the topic of exchange springs has received considerable attention. Exchange springs, systems where thin hard and soft magnetic layers are alternately arranged in multilayer stacks, provide great potential in improving the performance of a wide range of devices, from permanent hard magnets and microelectromechanical sensors and actuators, to magnetoresistive random access memory and permanent magnetic data storage. Artificial structuring on the nano-scale will be beneficial in improving the functionality of exchange spring systems in all of these areas. In this work, two distinctly different routes to nano-structuring in epitaxially grown rare earth – iron ($REFe_2$) films and exchange spring materials are described. Namely i) electron beam lithography and Ar^+ ion milling to define three-dimensional nano-scale structures, and ii) ion implantation to directly alter the crystalline structure of the material at the atomic-scale. Nano-scale elements defined in $REFe_2$ exchange spring materials are presented, providing not only the first demonstration of nano-structuring in these materials, but also the successful implementation of electron beam lithography and Ar^+ ion milling on these novel systems. Nano-scale patterning confirms the suitability of the $REFe_2$ exchange spring materials as excellent candidates for magnetic data storage media, since they remain relatively unaffected by nano-structuring, retaining their thermal stability and comparatively small coercivity. Ar^+ ion implantation is shown to be effective at artificial structuring on the atomic-scale. In addition, energetic Ar^+ ions have been successfully used to accurately control the easy and hard axes of magnetization within epitaxial YFe_2 and $DyFe_2$ films and a $DyFe_2$ / YFe_2 exchange spring multilayer. At a fluence of ~ 10^{17} Ar^+ ions cm^{-2}, the magnetoelastic anisotropy (dominant at room temperature in the epitaxially grown films) is reduced to such an extent that the intrinsic magnetocrystalline anisotropy begins to dominate. Thus Ar^+ ion implantation serves to alter the easy and hard axes of magnetization, rotating them through 90°. Such behaviour is clearly evident in hysteresis loops obtained by both the magneto optical Kerr effect and vibrating sample magnetometry, and is further confirmed by micromagnetic modelling. The reduction in magnetoelastic anisotropy is attributed to energetic Ar^+ ions causing RE atoms to relax to their unstrained lattice positions, thereby relieving the strain responsible for the magnetoelastic anisotropy. This interpretation is confirmed by X-ray diffraction measurements.

Contents

DECLARATION OF AUTHORSHIP

I, **Andrew Roger Buckingham**,

declare that the thesis entitled

Modifying the magnetic properties of Laves phase intermetallic multilayers and films by nano-patterning and ion implantation

and the work presented in the thesis are both my own, and have been generated by me as the result of my own original research. I confirm that:

- this work was done wholly or mainly while in candidature for a research degree at this University;
- where any part of this thesis has previously been submitted for a degree or any other qualification at this University or any other institution, this has been clearly stated;
- where I have consulted the published work of others, this is always clearly attributed;
- where I have quoted from the work of others, the source is always given. With the exception of such quotations, this thesis is entirely my own work;
- I have acknowledged all main sources of help;
- where the thesis is based on work done by myself jointly with others, I have made clear exactly what was done by others and what I have contributed myself;
- parts of this work have been published as:
    1. Engineering coercivity in epitaxial Laves phase rare earth - transition metal multilayers, A. R. Buckingham, K. Wang, D. Wang, G. J. Bowden, R. C. Ward & P. A. de Groot, *Proc. 53rd Ann. Conf. Mag. Mag. Mater.*, EG-11, p. 316, 2008.
    2. Room temperature magneto optic exchange springs in $DyFe_2$ / YFe_2 super-lattices, D. Wang, C. G. Morrison, A. R. Buckingham, G. J. Bowden, R. C. C. Ward & P. A. J. de Groot, *J. Mag. Mag. Mater.*, vol. **321**, pp. 586 – 589, 2009.
    3. Nano- and micro-scale patterned arrays in Laves phase intermetallic films and multilayers, A. R. Buckingham, D. Wang, G. J. Bowden, R. C. C. Ward & P. A. J. de Groot, *Proc. 20th Int. Colloq. Mag. Films Surf.*, P-Th06, pp. 496 - 497, 2009.
    4. Some comments on the magnetic moments used in $REFe_2$ exchange spring micro-magnetic simulations, G. J. Bowden, A. R. Buckingham, G. B. G. Stenning & P. A. J. de Groot, submitted to *J. Phys.: Condens. Matt.*, 2010.

Signed:

Date: 8th June 2010

Acknowledgements

First, I would like to express my gratitude to Prof. Peter de Groot for his continuing supervision and support of my research. Peter has always been there to answer questions from both theoretical and experimental standpoints, ensuring that there is never a dull moment in the office or the laboratory! I would also like to thank Peter for coordinating and leading the research group in magnetism and superconductivity at the University of Southampton, arranging financial support from the Engineering and Physical Sciences Research Council, for giving me the opportunity to represent our group at a number of international conferences and for providing me with such a welcoming group of colleagues. Next I wish to thank two visiting academics; Profs. Graham Bowden and Alan Fox. Graham has been "visiting" for over a decade and in this time has made our group his home in retirement! He has brought with him over 50 years experience in both practical and theoretical aspects of magnetism which has been invaluable in my research. Alan spent two years visiting Southampton, in which time he put considerable effort into passing some of his extensive knowledge of electron microscopy onto me. Without Alan's input I am sure much of the nano-fabrication discussed in this work would have taken longer to reach fruition. I would also like to express my gratitude to Dr Roger Ward at the University of Oxford for the growth and X-ray diffraction analysis of the samples used in this work. I should also express my thanks to my postgraduate colleagues, many of whom have now graduated. Thanks to Dr Kevin Martin for giving me useful practical demonstrations of vibrating sample magnetometry experiments. Especial thanks goes to Dr Chris Morrison, in part for his practical expertise but primarily for his enlightening conversations! Dr Daowei Wang's assistance in theoretical modelling was crucial to the success of my work, so special thanks go to him for spending many an hour working on `OOMMF` micromagnetic simulations with me! I would also like to thank Gavin Stenning for practical assistance at the end of my research – hopefully some of *my* knowledge of magnetism and nano-fabrication has now been passed-on! Also worthy of thanks is Zondy Webber; a great technician! Finally I would like to thank my parents, Andrew and Pam, for their continuing support in whatever I choose to do. Specifically, I would like to thank my father for his practical expertise and computational design assistance, and my mother for her proof-reading of my work – hopefully this thesis will read well!

Chapter 1

Introduction

The properties of nano-structured elements in thin magnetic materials have been the subject of intense investigation for more than 60 years [1, 2, 3, 4]. Until the 1960s and 1970s, much of this pioneering work went unnoticed since the processes required to grow high quality thin metallic films simply did not exist. Breakthroughs in thin film deposition techniques began some 40 years ago. Specifically, the work on molecular beam epitaxy (MBE) by Arthur and Cho [5] led to the experimental realization of nano-scale magnetism in thin films. The use of such deposition techniques made the possibility of manipulating atomic planes of ferromagnetic materials a reality. Comparatively recently, true three-dimensional control of ferromagnetic materials has been made possible with rapid developments in lithographic techniques [6, 7]. Artificially defined nano-elements provide an exciting opportunity to study fundamental magnetic behaviour, since physical properties, such as domain wall widths and magnetic exchange lengths, occur at similar dimensions. For example, the mechanism of magnetization reversal may change drastically between an un-patterned thin magnetic film and one which is patterned at the nano-scale, whilst ordering between these elements may also affect magnetic properties [8, 9]. From a technological standpoint, nano-structured magnetic materials are of great importance. They exhibit the potential to revolutionise magnetic data storage [10, 11, 12] by overcoming fundamental hurdles such as the well-known superparamagnetic limit [13], as well as proving to be excellent candidates for new memory devices such as magnetic random access memory (MRAM) [14, 15, 16, 17].

Lithographic techniques for the fabrication of three-dimensional nano-structures can be grouped into two key categories; “lift-off” and “etch-back”. Lithography is at the heart of lift-off processes, whereby the desired patterned elements are defined from the outset on the bare substrate, using either photolithography, electron beam lithography, or a combination of both. These patterns form a template through which the magnetic materials are grown, and thus the materials are structured on the nano-scale inherently. Lift-off lends itself to the rapid fabrication of prototype designs, often

in polycrystalline or amorphous magnetic materials. As such, it is unsuitable for applications which require nano-scale magnetic materials with well-defined crystalline properties, although structures as small as tens of nm may readily be defined. In the etch-back process, a high quality (often epitaxial) continuous magnetic film provides the landscape onto which the patterned elements are defined. A mask is defined lithographically, serving as a template through which material is removed, usually via ion milling or reactive ion etching. Scaling properties of the etch-back processes are generally good, although such subtractive processing does eventually reach limits on the scale of tens of nm. Use of the etch-back processes on high quality films permits the rapid, large-scale fabrication of nano-structured magnetic devices with well-defined crystalline properties, ideal for use in magnetic data storage, MRAM and even microelectromechanical systems (MEMS) [18, 19].

Nano-structured magnetic materials for applications in data storage and MEMS require well-defined properties. These include a high saturation magnetization (M_S) and a high thermal stability, yet the materials must have a coercivity (H_C) that is not so large that it cannot be switched by a small applied magnetic field. Rare earth – Transition metal (RE-TM) intermetallic compounds, first developed in the 1960s to overcome limits reached in the development of Alnico and ferrite materials, offer such properties [20]. The RE elements are characterized by a relatively large H_C, a small M_S and Curie temperatures (T_C) below room temperature. But by combining the REs with TMs, for example in the form of $SmCo_5$ or Sm_2Co_{17}, materials with not only a relatively large H_C, but with a high M_S and a T_C well above room temperature are obtained [21, 22]. Magnets with large H_C and M_S are often referred to as high energy product magnets. The well known $Nd_2Fe_{14}B$ magnets, also a member of this high energy product RETM family, were developed in the 1980s to reduce production costs of permanent magnets since Fe is far more abundant and cheaper than Co. Further development took place in the 1990s when Skomski & Coey [23, 24, 25] and Kneller & Hawig [26] proposed that nano-structured, layered hard and soft magnetic materials could lead to composite systems with an even greater energy product. These composite multilayer systems are referred to as exchange spring magnets. The hard magnetic layer, typically a RE-TM, gives a large H_C, whilst the soft layer, typically Fe, is responsible for an increased M_S. Such composite multilayer systems provide a room temperature ferromagnet that is both hard and exhibits a large saturation magnetization with minimal RE content, thus serving to significantly reduce the production costs. This work focuses on the use of

$DyFe_2$ and YFe_2, both as isolated RETM systems and in an antiferromagnetically coupled exchange spring system, to provide an ideal model structure with well defined magnetic properties.

In magnetic data storage it is crucial for media to exhibit good thermal stability in order to avoid superparamagnetic effects. This criterion is met by some hard magnetic materials, but may be coupled to a coercivity that is so large it cannot be reached by magnetic write heads. In exchange spring media, the "effective thickness" of the media are reduced due to the exchange coupling, whilst the physical thickness clearly remains constant. This reduces the coercivity of the media to a value more approachable by magnetic write heads whilst retaining excellent thermal stability due to the relatively large media thickness. Antiferromagnetically coupled exchange spring systems have been grown by MBE [27, 28], thus allowing the thickness of the material to be accurately controlled. This has been exploited by Sawicki *et al.* [29, 30] who accurately tailored the magnetic properties of these media by independently varying the thicknesses and ratios of the hard and soft layers. These epitaxial $REFe_2$ media thus provide an excellent starting point for the investigation of fundamental nano-structured magnetic properties in exchange-spring systems.

This thesis describes work regarding three-dimensional structuring of antiferromagnetically coupled $REFe_2$ exchange spring media at the nano-scale. It builds upon the aforementioned work of Sawicki *et al.* and that of Beaujour *et al.* [31, 32] and Gordeev *et al.* [33], whereby the magnetic properties of the media were successfully tailored in two-dimensions. It also significantly extends the fundamental investigations of Wang *et al.* [34] where basic three-dimensional control of $REFe_2$ media at the micron-scale was demonstrated. Not only have standard lithographic and ion milling processes been used, but a new technique of ion implantation has been exploited where the properties of the $REFe_2$ media may be modified both directly and controllably. This novel process represents a key development in the understanding of the complex nature of the magnetic anisotropies in these media. In particular, it allows direct identification of the dominant magnetic anisotropy.

To provide a firm basis for the interpretation of the results, a review of the subject of magnetism as a whole is presented in Chapter 2. This begins at a relatively basic level within a classical framework, but is quickly extended to include a quantum mechanical treatment where more complex theories are introduced. These include details of ferromagnetism in transition metals and lanthanides, magnetic anisotropies,

and exchange interactions. Details are also presented regarding various strains present in the Laves phase materials since these will form the basis to understanding the effects of ion implantation. Following this, a summary of various magnetic characteristics including coercivity, reversal mechanisms and magnetic domains is given. This is followed by a short description of the micromagnetic modelling software used to simulate such characteristics, in order to gain a better understanding of the experimental results presented. Finally, a brief review of magnetic data storage is presented. Whilst this is by no means the only application of nano-scale patterned magnetic media, it is a very interesting and technically relevant topic as the superparamagnetic limit draws ever closer.

Understandably, artificial three-dimensional structuring of any material, not least $REFe_2$ magnetic films, is a significant challenge, requiring the development and implementation of several fabrication processes. This forms the focus of Chapter 3. First, a brief overview of vacuum deposition techniques is given, followed by an extensive description of electron microscopy. Considerable time was spent improving existing in-house electron beam lithography processes and resist technologies in order to achieve the desired nano-scale resolution. Following this, various etching processes to facilitate the etch-back approach to nano-scale patterning are described, including the design and implementation of an Ar^+ ion source. Finally, experimental techniques for sample characterization are described, including X-ray diffraction, the new process of He^+ ion microscopy, scanning probe microscopy, the magneto optical Kerr effect (MOKE) and the vibrating sample magnetometer (VSM).

In Chapter 4, the first demonstration of nano-scale patterned elements defined in $REFe_2$ films and exchange spring multilayer systems is presented and discussed. This brings together all of the fabrication techniques described in Chapter 3. A brief review of previous work to define patterned structures in $REFe_2$ media is presented, with the aim of highlighting the need for developments in lithography and pattern transfer processes. This will highlight the benefits of the newly derived process, for which a step-by step demonstration is then provided. To conclude this chapter, details regarding re-deposition of material and ion implantation are given.

In Chapter 5 it is argued that ion implantation can be used to great advantage. It will be shown that Ar^+ ion implantation provides a tool whereby accurate modification to magnetic anisotropy energies can be realised. The chapter begins with a section detailing the interactions of energetic ions incident on a solid target. This section also

includes a description of SRIM, a Monte Carlo based software package used to model these interactions [35]. The effects of Ar^+ ion implantation are considered in three separate materials: YFe_2 and $DyFe_2$ films, and a $DyFe_2$ / YFe_2 antiferromagnetically coupled exchange spring multilayer. For each material, a brief overview of the experimental procedure is given, describing the key facts concerning the implantation of Ar^+ ions into that material. The magnetic properties of the samples are characterized before and after Ar^+ ion implantation by MOKE and VSM. These data are then compared to micromagnetic simulations conducted using the OOMMF software package. The structure of the samples were analysed by X-ray diffraction and atomic force microscopy. The $DyFe_2$ sample was also studied using the new experimental procedure of He^+ ion microscopy, a process which reveals unique and detailed information regarding the texture of both as-grown and Ar^+ ion implanted samples. All the data are then brought together in the concluding sections to describe the observed effects. It is shown that energetic Ar^+ ions can be used to drastically modify the magnetic behaviour of these materials by altering the dominant magnetic anisotropy.

The magnetic properties of nano-scaled elements in a $DyFe_2$ / YFe_2 exchange spring system are presented and discussed in Chapter 6. An extended description of MFM is given in order to provide a measure of quantification concerning the magnetic properties of different samples. MFM was then used to characterize nano-scale elements patterned in a bi-layer $REFe_2$ exchange spring system, identifying critical domain sizes and demonstrating the lack of interaction between neighbouring patterned elements. MFM is subsequently used to visualise the stray magnetic field from a multilayer $REFe_2$ exchange spring sample. The sample possesses arrays of lines and squares on both the micro- and nano-scales, and is subject to an applied magnetic field in various directions. The associated effects are visualised and explained. Finally, quantitative measurements using MOKE are made. From these, the effects due to induced shape anisotropies are compared with intrinsic magnetic anisotropies.

Finally, in Chapter 7 the conclusions are briefly summarised and details of possible future work are outlined. The key findings are reiterated in order to draw parallels between the demonstrated results and the aims of this work. In particular, it will be argued that this work forms the first demonstration of three-dimensional nano-scale modification to $REFe_2$ media, using both lithographic techniques and energetic ion implantation.

References

[1] C. Kittel, *Rev. Mod. Phys.*, vol. **21**, no. 4, pp. 541 – 583, 1949.

[2] W. F. Brown, *Phys. Rev.*, vol. **105**, no. 5, pp. 1479 – 1482, 1957.

[3] A. Aharoni, *Rev. Mod. Phys.*, vol. **34**, no. 2, pp. 227 – 238, 1962.

[4] W. F. Brown, *J. Appl. Phys.*, vol. **39**, no. 2, pp. 993 – 994, 1968.

[5] A. Y. Cho & J. R. Arthur, *Phys. Rev. Lett.*, vol. **22**, no. 22, pp. 1180 – 1181, 1969.

[6] M. Khoury & D. K. Ferry, *J. Vac. Sci. Technol. B*, vol. **14**, no. 1, pp. 75 – 79, 1996.

[7] C. Vieu, F. Carcenac, A. Pépin, Y. Chen, M. Mejias, A. Lebib, L. Manin-Ferlazzo, L. Couraud & H. Launois, *Appl. Sur. Sci.*, vol. **164**, pp. 111 – 117, 2000.

[8] R. Sbiaa & S. N. Piramanayagam, *Rec. Pat. Nanotech.*, vol. **1**, pp. 29 – 40, 2007.

[9] E. Paz, F. Cebollada, F. J. Palomares, F. García-Sánches & J. M. González, *Nanotech.*, vol. **21**, p. 255301, 2010.

[10] A. Moser, K. Takano, D. T. Margulies, M. Albrecht, Y. Sonobe, Y. Ikeda, S. Sun & E. E. Fullerton, *J. Phys. D: Appl. Phys.*, vol. **35**, pp. R157 – R167, 2002.

[11] S. N. Piramanayagam, *J. Appl Phys.*, vol. **102**, p. 011301, 2007.

[12] H. J. Richter, *J. Phys. D: Appl. Phys.*, vol. **40**, pp. R149 – R177, 2007.

[13] E. P. Wohlfarth, *J. Mag. Mag. Mater.*, vol. **39**, no. 1 – 2, pp. 39 – 44, 1983.

[14] J-. G. Zhu, Y. Zheng & G. A. Prinz, *J. Appl. Phys.*, vol. **87**, no. 9, pp. 6668 – 6673, 2000.

[15] S. Tehrani, J. M. Slaughter, M. Deherrera, B. N. Engel, N. D. Rizzo, J. Salter, M. Durlam, R. W. Dave, J. Janesky, B. Butcher, K. Smith & G. Grynkewich, *Proc. IEEE*, vol. **91**, no. 5, pp. 703 – 714, 2003.

[16] J-. G. Zhu, *Proc. IEEE*, vol. **96**, no. 11, pp. 1786 – 1798, 2008.

[17] J. M. Slaughter, *Annu. Rev. Mater. Res.*, vol. **39**, pp. 277 – 296, 2009.

[18] R. Bogue, *Assem. Autom.*, vol. **29**, no. 4, pp. 313 – 320, 2009.

[19] D. P. Arnold & N. Wang, *J. Microelectromech. Sys.*, vol. **18**, no. 6, pp. 1255 – 1266, 2009.

[20] J. J. Becker, *IEEE Trans. Mag.*, vol. **Mag4**, no. 3, pp. 239 – 249, 1968.

[21] C. W. Searle, *J. Appl. Phys.*, vol. **57**, no. 2, pp. 481 – 483, 1984.

[22] H. Kronmüller & D. Goll, Scripta Mat., vol. 48, pp. 833 – 838, 2003.

[23] R. Skomski & J. M. D. Coey, *Phys. Rev. B*, vol. **48**, no. 21, pp. 15812 – 15816, 1993.

[24] J. M. D. Coey, *Sol. Stat. Com.*, vol. **102**, no. 2 – 3, pp. 101 – 105, 1997.

[25] R. Skomski, *J. Appl. Phys.*, vol. **76**, no. 10, pp. 7059 – 7064, 1994.

[26] E. F. Kneller & R. Hawig, *IEEE Trans. Mag.*, vol. **27**, no. 4, pp. 3588 – 3600, 1991.

[27] M. J. Bentall, R. A. Cowley, W. J. L. Buyers, Z. Tun, W. Lohstroh, R. C. C. Ward & M. R. Wells, *J. Phys.: Condens. Matt.*, vol. **15**, pp. 4301 – 4330, 2003.

[28] M. J. Bentall, R. C. C. Ward, E. J. Grier & M. R. Wells, *J. Phys.: Condens. Matt.*, vol. **15**, pp. 6493 – 6512, 2003.

[29] M. Sawicki, G. J. Bowden, P. A. J. de Groot, B. D. Rainford, R. C. C. Ward & M. R. Wells, *J. Appl. Phys.*, vol. **87**, no. 9, pp. 6839 – 6841, 2000.

[30] M. Sawicki, G. J. Bowden, P. A. J. de Groot, B. D. Rainford, J-. M. L. Beaujour, R. C. C. Ward & M. R. Wells, *App. Phys. Lett.*, vol. **77**, no. 4, pp. 573 – 575, 2000.

[31] J-. M. L. Beaujour, *Ph. D. Thesis*, University of Southampton, UK, 2003.

[32] J-. M. L. Beaujour, S. N. Gordeev, G. J. Bowden, P. A. J. de Groot, B. D. Rainford, R. C. C. Ward & M. R. Wells, *Appl. Phys. Lett.*, vol. **78**, no. 7, pp. 964 – 966, 2001.

[33] S. N. Gordeev, J-. M. L. Beaujour, G. J. Bowden, P. A. J. de Groot, B. D. Rainford, R. C. C. Ward & M. R. Wells, *J. Appl. Phys.*, vol. **89**, no. 11, pp. 6828 – 6830, 2001.

[34] K. Wang, K. N. Martin, C. G. Morrison, R. C. C. Ward, G. J. Bowden & P. A. J. de Groot, *Appl. Phys. A*, vol **86**, pp. 325 – 328, 2007.

[35] J. F. Ziegler, M. D. Ziegler & J. P. Biersack, `SRIM-2008.04`, PC software available at http://www.srim.org

Chapter 2

Nano-magnetism in $REFe_2$ Laves Phase Compounds

Chapter 2 begins by refreshing the reader on the basic ideas of magnetism in sections 2.1 and 2.2. Magnetism in general is briefly introduced in a classical context before being given a quantum mechanical framework. The results chapters' of the thesis will describe the effects that both patterning and ion implantation has on the magnetic materials studied throughout this work. The descriptions of magnetic anisotropy in section 2.3 are crucial to the interpretation of these results. Details of exchange interactions are presented in section 2.4 to provide a framework to describe the interactions when different ferromagnetic elements are combined, such as iron with rare earth elements in the case of YFe_2 or $DyFe_2$. These ideas are then taken further in section 2.5 where YFe_2 and $DyFe_2$ are placed together to form an "exchange spring" system, a novel material studied in this work. In section 2.6 details and models of the magnetic reversal mechanisms in some magnetic materials are described. The models will be useful when discussing the physics associated with changes induced by the aforementioned patterning and ion implantation processes. Following this, a review of magnetic data storage is presented in section 2.7. As will be seen, the present materials are excellent candidates for providing underpinning research into improving the performance of magnetic data storage devices. Finally in section 2.8, attention is given to the effects of implanting energetic ions into various magnetic media. It will be shown how implanted ions may disrupt the crystalline structures of various media, leading to drastic changes in magnetic properties. It will become clear that this offers an attractive route towards the fabrication of patterned magnetic media for use in data storage devices.

2.1 Spontaneous Magnetization

Section 2.1 provides an introduction to the concept of magnetism as a whole, providing refreshers on the basic ideas of classical magnetism and quantum mechanics. The

"electron shell" model is introduced as a useful way to picture the arrangement of electrons within the classical atom. Further to this, spatial and spin wavefunctions are introduced in conjunction with bonding and antibonding orbitals. This provides a more complete quantum mechanical picture of ferromagnetism in isolated atoms.

2.1.1 Classical magnetism

Within the classical Bohr model of the atom [1], the electron orbits the nucleus and therefore has an intrinsic orbital angular momentum **L**. This theory can be extended to describe classical diamagnetism by assuming that each electron orbiting a nucleus (subtending an area $A = \pi {R_0}^2$ (with R_0 the Bohr radius)) induces a current I under the application of a magnetic field **B**. This induces an orbital angular magnetic moment $\mu_L = IA$ [2]. The electron has an angular frequency $\omega = 2\pi f = \frac{v}{R_0}$, which, whilst remembering that $I = \frac{Q}{t} = Qf$, gives

$$\mu_L = ef\pi {R_0}^2 = \frac{evR_0}{2} \tag{2.1}$$

with f and v the linear frequency and velocity respectively, Q (= e) the charge of an electron, and t the time. The ratio of angular momentum to the orbital angular magnetic moment is given by

$$\gamma_L = \frac{\mu_L}{\mathbf{L}} \tag{2.2}$$

with γ_L a constant of proportionality called the gyromagnetic ratio. Taking $\mathbf{L} = \mathbf{r} \times \mathbf{p} = R_0 mv$ (with **p** the linear momentum and m the mass of the electron) and combining equations (2.1) and (2.2) gives

$$\gamma_L = \frac{e}{2m} = -8.78 \times 10^{10}\ \text{Askg}^{-1} \tag{2.3}$$

The magnitude of μ_L for a H atom can be calculated by combining equations (2.2) and (2.3) with the kinetic energy E_K of the 1s electron (calculated from $E_K = \frac{mv^2}{2} =$ 13.6 eV) to give

$$\mu_L = R_0 e\sqrt{\frac{E_K}{2m}} \approx 9.26 \times 10^{-24}\text{Am}^2 \tag{2.4}$$

The orbital angular momentum is also subject to a torque which causes it to precess around the nucleus. The frequency of precession is called the Larmor frequency, and it is always in the direction of **B**. The precession in turn gives rise to a (field induced)

change in orbital angular momentum $d\mathbf{L}$, which causes a change in the orbital angular magnetic moment $d\mu_L$. It is this precession of the orbital angular momentum which is responsible for creating the diamagnetic response, a phenomenon that is atomic in nature and thus present in all materials.

The classical model of magnetism was first seen to fail when attempting to explain the splitting of spectral lines under the application of a magnetic field, when observed in classical spectroscopy experiments by Zeeman [3]. Lorentz was able to explain this in part by using the theory of precession of **L** to give rise to two possible changes in frequency $\Delta\nu$ and hence emission at ν and $\nu \pm \Delta\nu$. The splittings that could not be explained were termed as the anomalous Zeeman effect.

2.1.2 Quantum mechanics in magnetism

To explain the anomalous Zeeman effect the transition between classical and quantum mechanics has to be made. At the atomic scale, where quantum mechanics dominates, Heisenberg's uncertainty principle states that both position (**r**) and momentum (**p**) cannot be known simultaneously, and that the electronic charge is not at a well known **r**, but rather distributed as a "cloud" in space. Further to this, **r, p** and energy take on a range of discrete values in quantum mechanics rather than being continuous variables. The classical term $\mathbf{L} = \mathbf{r} \times \mathbf{p}$ is replaced with the quantum mechanical term given by Schrödinger's equation, giving an expectation value $\langle \mathbf{L} \rangle = \hbar\sqrt{l(l+1)}$. Here, $\hbar$ is Plank's constant divided by 2π and l is the orbital angular momentum quantum number. Thus **L** can only take discrete values. The expectation value for a component of **L** in a particular direction **r** is given by $\langle \mathbf{L_r} \rangle = \hbar m_l$, with m_l the orbital magnetic moment quantum number, taking integer values $-l \leq m_l \leq l$. Hence $\mathbf{L_r}$ can also only take discrete values. Thus μ_l is now given by

$$|\mu_l| = \gamma_L \hbar\sqrt{l(l+1)}$$
$$\mu_{l_r} = \gamma_L \hbar m_l \tag{2.5}$$

where μ_{l_r} defines the component along the direction **r** (*c.f.* equation (2.4)).

To explain the anomalous Zeeman effect, a further quantum number to describe an additional degree of freedom to the electron's motion is required. This is the electron's intrinsic angular momentum, referred to as "spin", introduced by Uhlenbeck & Goudsmit in 1925 [4]. Spin is analogous to orbital angular momentum and thus the spin magnetic moment, μ_s, is given by

$$|\mu_s| = \gamma_S \hbar \sqrt{s(s+1)}$$
$$\mu_{s_r} = \gamma_S \hbar m_s \tag{2.6}$$

Here, s is the spin quantum number and m_s is the spin magnetic moment quantum number, with $-s \leq m_s \leq s$. The spin gyromagnetic ratio, γ_S, is exactly twice that of γ_L, thus

$$\gamma_S = \frac{e}{m} = 1.76 \times 10^{11} \text{Askg}^{-1}. \tag{2.7}$$

Returning to the case of the H atom, the electron has a spin s = ½ hence m_s = ± ½, which gives, from equations (2.6) and (2.7)

$$\mu_{s_r} = \pm \frac{\gamma_S \hbar}{2} = \frac{e\hbar}{2m} = \mu_B \approx 9.26 \times 10^{-24} \text{Am}^2 \tag{2.8}$$

with μ_B the Bohr magneton. This is exactly the same as in equation (2.4).

Contributions from both the orbital angular momentum **L** and the spin angular momentum **S** of the electron make up the magnetism of an atom. **L** and **S** are not independent, rather their vector sum, given by the total angular momentum $\mathbf{J} = \mathbf{L} + \mathbf{S}$, is a constant of motion. Similarly to equations (2.5) and (2.6), **J** has the expectation values

$$\langle \mathbf{J} \rangle = \hbar \sqrt{j(j+1)} \text{ and}$$
$$\langle \mathbf{J_r} \rangle = \hbar m_J \tag{2.9}$$

with j the spin-orbit quantum number and m_J the spin-orbit magnetic moment quantum number. Since the magnitudes of **L** and **S** and the associated magnetic moments μ_L and μ_S are generally different, μ_J is not necessarily along **J**, rather a component of μ_J is measured along **J**, given by

$$\mu_J{}' = g \mu_B m_J \tag{2.10}$$

with g the Landé g-factor [5], given by

$$g = 1 + \frac{j(j+1) + s(s+1) - l(l+1)}{2j(j+1)} \tag{2.11}$$

The additional concept of spin explains the anomalous Zeeman effect since the extra degree of freedom in the electron's motion leads to further possible splitting of energy levels. m_J can take on a larger range of values than m_l could alone, since it has components from both m_l and m_s.

2.1.3 Electron shells and Hund's rules

From the standpoint of the periodic table, electrons can be seen to occupy discrete "shells" around a nucleus[i]. These shells are given a name relating to both their principle and orbital angular momentum quantum numbers n and l respectively. In a purely atomic model the shells are filled in order of increasing energy, as illustrated in Figure 2.1.

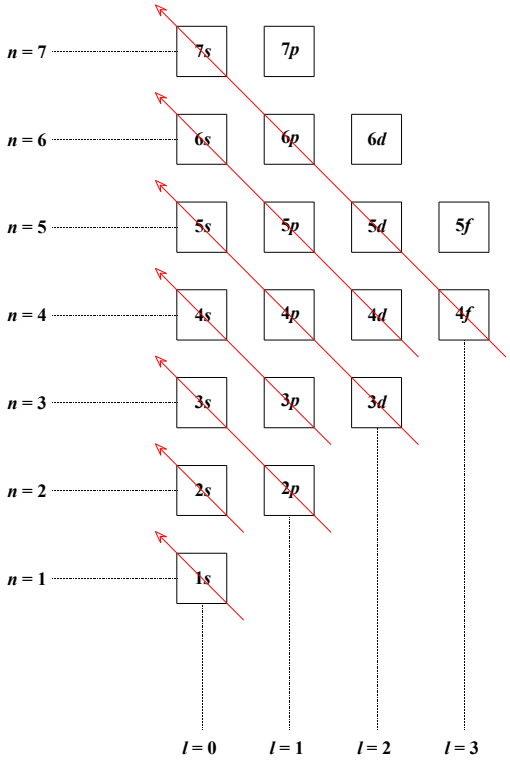

Figure 2.1: Schematic representation of the order in which shells are filled in the periodic table, from bottom right to top left. The standard convention of $l = 0 = s$, $l = 1 = p$, $l = 2 = d$ *etc.* has been used.

The electrons occupy these shells in an order given by Hund's three rules:

1. Rule one requires the maximization of the spin angular momentum $\mathbf{S} = \sum s$. According to the Pauli exclusion principle, the same set of quantum numbers cannot be shared by electrons within the same spatial orbital (*i.e.* those with the same orbital angular momentum quantum number). Thus, any pair of electrons within the same spatial orbital must have opposite spins. This forces them into different states thereby reducing their Coulomb repulsion.

[i] Whilst it is clear that this is a classical rather than a quantum mechanical stance it still forms a reliable and intuitive model to describe the location of electrons relative to the nucleus.

2. Rule two requires the maximization of the orbital angular momentum $\mathbf{L} = \sum l$. This also serves to reduce the Coulomb repulsion since (in a classical sense) the electrons are all orbiting in the same direction and therefore experience less repulsion from each other than they would if orbiting in opposite directions.
3. The third rule concerns the total angular momentum **J**. When the shell is less than half filled with electrons, $J = |L - S|$; when it is more than half full, $J = |L + S|$ and when it is exactly half full the first rule gives $L = 0$ so $J = S$.

It is clear that Hund's rules account for both Coulomb repulsion and spin-orbit interaction.

In many elements the electrons' spins are paired off, giving rise to no atomic magnetic moment. These are diamagnetic elements. However, when a shell is partially filled the atom exhibits a net magnetic moment. Using a quantum mechanical model for the electrons motion around the nucleus, the magnetic moment μ_B can only take a discrete set of values which are averaged over the probability of their occupation. Full treatment of this problem results in a Brillouin Function, from which the total magnetization M is given by

$$M = N_v g \mu_B J B_j(x) \tag{2.12}$$

with N_v the number of moments per unit volume, g the Landé g-factor, μ_B the Bohr magneton, and $J = m_j$ in the case of ferromagnetic materials and $J = \sqrt{j(j+1)}$ for paramagnetic materials. The variance in J is because in paramagnetic materials it is the effect of the total magnetic moment that governs the magnetic behaviour of a material, whilst in ferromagnetic materials it is the maximum value of the magnetic moment that can be aligned along a specific direction which is of importance.

2.1.4 Quantum mechanics in ferromagnetism

Hund's rules govern the formation of atomic magnetic moments. This is an *intraatomic* exchange interaction. There are also interactions between the individual atoms within a solid – *interatomic* exchange – which dictates how strongly atomic moments couple to each other. For illustrative purposes, consideration is given to two H atoms covalently bonded to form a molecule. Between the two electrons and between the two protons there are repulsive Coulomb forces, whilst the forces felt between the electrons and protons are attractive. There is also a further "exchange force" arising from the Pauli exclusion principle. Since electrons are fermions they are described by a wavefunction

$\mathbf{\Psi} = \varphi(r)\chi(s)$ which is antisymmetric on the interchange of space $\varphi(r)$ and spin $\chi(s)$ contributions, that is

$$\mathbf{\Psi}(r_1, r_2, r_3, \dots, s_1, s_2, s_3, \dots) = -\mathbf{\Psi}(r_1, r_3, r_2, \dots, s_1, s_3, s_2, \dots) \tag{2.13}$$

Therefore an exchange operator, $\mathbf{P}$, acting on this wavefunction gives $\mathbf{P\Psi} = -\mathbf{\Psi}$. Interacting indistinguishable fermions therefore experience an additional repulsive force relative to equivalent distinguishable particles and are thus found further apart. The spatial (ψ) and spin (χ) parts of $\mathbf{\Psi}$ can be written as

$$\begin{aligned} \psi^{\pm} &= \varphi_1(1)\varphi_2(2) \pm \varphi_1(2)\varphi_2(1) \\ \chi_{T,S} &= \chi_+(1)\chi_-(2) \pm \chi_+(2)\chi_-(1) \end{aligned} \tag{2.14}$$

where $\varphi_1(1)$ describes electron 1 in state 1 and $\chi_+(1)$ describes electron 1 in a spin up state. The antisymmetric (–) form describes the spin singlet state χ_S ($S = 0 \Rightarrow 2S + 1 = 1$), and the symmetric (+) form describes the spin triplet state χ_T ($S = 1 \Rightarrow 2S + 1 = 3$). The total wavefunction for the singlet or triplet state of a system of fermions is given by

$$\begin{aligned} \mathbf{\Psi_S} &= \sqrt{\frac{1}{2}}[\varphi_1(1)\varphi_2(2) + \varphi_1(2)\varphi_2(1)]\chi_S \\ \mathbf{\Psi_T} &= \sqrt{\frac{1}{2}}[\varphi_1(1)\varphi_2(2) - \varphi_1(2)\varphi_2(1)]\chi_T \end{aligned} \tag{2.15}$$

since clearly if the spatial part of $\mathbf{\Psi}$ is symmetric the spin part must be antisymmetric and *vice versa* in order to leave $\mathbf{\Psi}$ antisymmetric.

The Coulomb repulsion between the two electrons in states i and j gives rise to an energy integral C_{ij}, whilst the exchange force described above gives rise to an energy integral J_{ij}, given in O'Handley [2] as

$$\begin{aligned} C_{ij} &= \int \varphi_i{}^*(1)\varphi_j{}^*(2)\left(\frac{e^2}{4\pi\varepsilon_0 r_{12}}\right)\varphi_i(1)\varphi_j(2)dv \\ J_{ij} &= \int \varphi_i{}^*(1)\varphi_j{}^*(2)\left(\frac{e^2}{4\pi\varepsilon_0 r_{12}}\right)\varphi_i(2)\varphi_j(1)dv \end{aligned} \tag{2.16}$$

with r_{12} denoting the separation between the two electrons, e the charge on an electron and ε_0 the permittivity of free space. The energy of the singlet and triplet states are thus given by

$$\begin{aligned} E_S &= E_0 + C_{ij} + J_{ij} \\ E_T &= E_0 + C_{ij} - J_{ij} \end{aligned} \tag{2.17}$$

with E_0 the ground state energy of the electron. In many cases, J_{ij} is negative and thus $E_S < E_T$. However, as will be shown, this is intimately related to bonding orbitals and,

in some instances, J_{ij} is positive, hence $E_T < E_S$ which explains the possibility for ferromagnetism.

2.1.5 Bonding and Antibonding Orbitals

Information from the wavefunction $\mathbf{\Psi}$ can be used to describe bonding and antibonding orbitals. In the simplest case of a bonding orbital, which corresponds to a symmetric spatial part of the wavefunction (ψ^+), electrons will occupy (to some extent) the same region in space and therefore the spin part of the wavefunction must be antisymmetric (χ_S). In the case of the antibonding orbital these wavefunctions are exchanged to ψ^- and χ_T. This obeys the Pauli exclusion principle, *i.e.* when two electrons are confined to the same region in space their spins must align antiparallel ("paired off"). Clearly the bonding state (with paired off spins) does not support a magnetic moment, whereas the antibonding state does.

The Heisenberg Hamiltonian H_H was introduced in 1923 by Dirac to describe the spin-dependent energy due to the Pauli exclusion principle [6]. It describes the alignment between neighbouring magnetic moments, and is given by

$$H_H = -2\sum_{i<j} J_{ij}\mathbf{S_i}\cdot\mathbf{S_j} \tag{2.18}$$

Due to the small spatial extent of atomic wavefunctions, equation (2.18) can be simplified to include only nearest neighbour (*nn*) interactions in order to determine the exchange energy,

$$E_E = -2J\sum_{i<j}^{nn}\mathbf{S_i}\cdot\mathbf{S_j} \tag{2.19}$$

between atoms i and j. Clearly if $J > 0$, to minimize E_E there will be a parallel alignment of spins (antibonding orbitals) forming a ferromagnet. Similarly if $J < 0$, minimization of E_E will favour an antiparallel alignment of spins (bonding orbitals), forming an antiferromagnet or a ferrimagnet (depending on the relative strengths of magnetization within the bonding orbitals (see Figure 2.2)). It is important to note that this model is only suited to describing magnetic insulators, *i.e.* those materials where the electrons are localized. Magnetic properties of localized electrons can be used to describe systems such as magnetic oxides using the principle of superexchange. Attention will now be given to the more relevant topic of ferromagnetism in systems such as metals, where electrons are *not* localized.

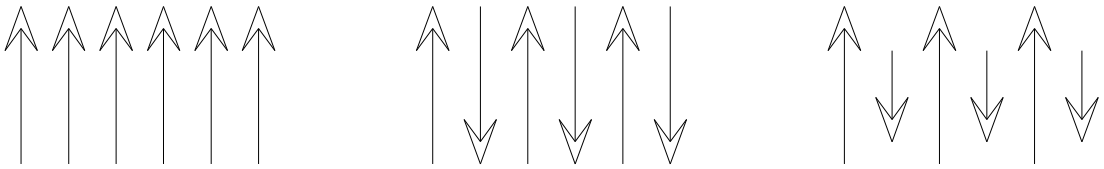

Figure 2.2: Illustration of the electron spin (direction of the arrows) and strength of magnetization (magnitude of arrows) in the three main types of ferromagnetic structures.

2.2 Ferromagnetism

Section 2.2 aims to cover the fundamental aspects of ferromagnetism in metals. After the basics of ferromagnetism are covered with respect to 3*d* transition metal elements, the Lanthanide group of metals is introduced.

2.2.1 Ferromagnetism in transition metals

In section 2.1.3 the incompletely filled shells were described as being responsible for paramagnetic and ferromagnetic materials. Within the periodic table, there are five groups of magnetic materials in which an electron shell is incompletely filled.

1. The transition metal group (incomplete 3*d* shell)
2. The palladium group (incomplete 4*d* shell)
3. The lanthanide group (incomplete 4*f* shell)
4. The platinum group (incomplete 5*d* shell)
5. The actinide group (incomplete 5*f* shell)

The work described here focuses on elements from groups 1 and 3, therefore the other groups will be discussed no further. Consideration is first turned to group 1 before attention is given to group 3 in section 2.2.2.

Elemental Fe in its ionic form (Fe^{2+} ($[Ar]3d^6$)[ii]) has 24 electrons in total which are distributed into the different shells according to Figure 2.1; that is they completely fill the 1*s*, 2*s*, 2*p*, 3*s* and 3*p* shells (2 + 2 + 6 + 2 + 6 = 18 electrons) and partly fill the 3*d* shell. The 6 electrons partly filling the 3*d* shell are valence electrons. Obeying Hund's rules (section 2.1.3), the remaining 6 electrons first fill the 10 possible *d*-shell

[ii] Standard "noble gas notation" is used to emphasise the electron structure within the atom. In this notation, the inner electron structure is given by the preceding noble gas ([He]…[Rn]) followed by the outer structure of the electrons.

eigenstates with spin up (accounting for 5 of the 6 electrons), leaving one electron to fill an eigenstate with spin down. This has the net effect of leaving 4 unpaired spins, as shown in Figure 2.3. The remaining spaces for electrons can be considered as "spin holes" which can be filled when other elements are introduced, as will be seen with exchange interactions in sections 2.4.2 and 2.4.3.

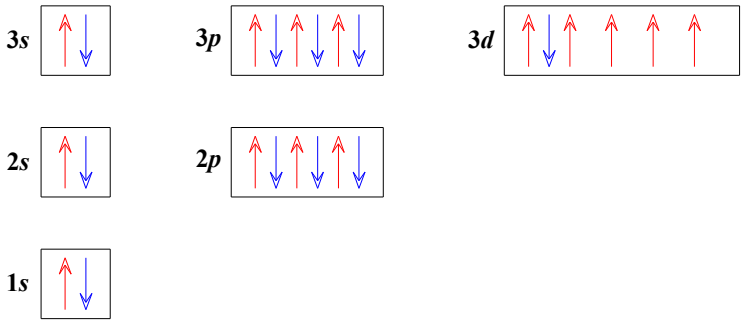

Figure 2.3: Schematic representation of the order in which shells are filled for Fe^{2+}. The red arrows represent spin up electrons, the blue spin down electrons. There are 4 unpaired electrons in the 3*d* shell.

Within a solid such as Fe^{2+} there are in fact many available energy levels which form continuous energy bands rather than discrete energy levels. This occurs when atoms are brought together to form solids, the result of which is broadening of the energy levels, *i.e.* splitting into different levels corresponding to bonding and antibonding orbitals. In Fe ($[Ar]3d^6 4s^2$), the bands for the outer *s* and *d* shells split as follows: the 4*s* states in general have lower energy than the 3*d* states, but the 4*s* states also extend over a larger distance in space, that is, they are less localized. Therefore electrons in the 4*s* shells are responsible for bonding whereas those in the localized 3*d* states are responsible for the magnetic properties of the material. When the energy levels available form continuous bands, the number of available electron states are referred to as the density of states, $D(E)$. A schematic representation of $D(E)$ is given in Figure 2.4 where the lower energy associated with the 4*s* shell compared to the 3*d* shell can be seen. There is also a clear shift in $D(E)$ for the spin up and spin down states. The latter may be considered as a footprint left by Hund's rules. In Figure 2.3, the Coulomb repulsion is minimized in the 3*d* band by the majority of electrons occupying different degenerate states, thereby minimizing the overlap of their spatial wavefunctions. However in the case of metals where the energy levels are not degenerate, there is an increase in energy associated with filling a particular band first (in Figure 2.4 this is the spin up band). This energy cost is larger when the available states within a band are spaced over a large range of energies, *i.e.* $D(E)$ is small as in the

case of the *s*-band in Figure 2.4. Shifting the spin up and spin down bands relative to each other to favour parallel spins gives a lower energy level thereby reducing J_{ij}. However, at the same time there is a kinetic energy cost proportional to $^{1}/_{D(E)}$ which favours paired spins. The competition between exchange energy and kinetic energy at the Fermi energy level (E_F),

$$J(E_F)D(E_F) > 1 \tag{2.20}$$

is the Stoner criterion for the occurrence of ferromagnetism [7]. Upon inspection of Figure 2.4 it is clear that the spin imbalance of the *d* band can give rise to a spontaneous magnetic moment.

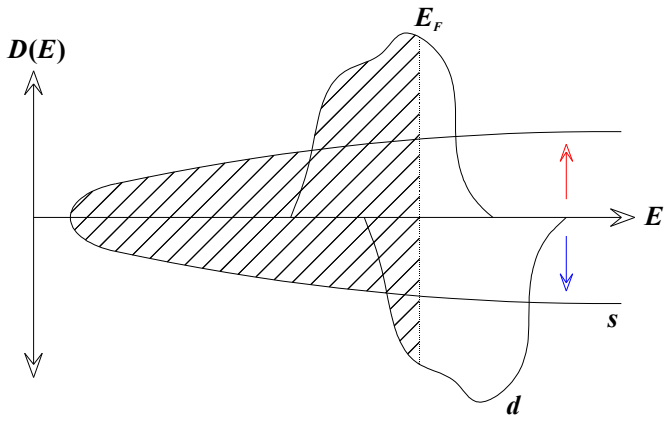

Figure 2.4: Schematic representation of density of states $D(E)$ as a function of energy (E) showing splitting of a *d* band into spin up and spin down states (indicated by the arrows).

Recall from section 2.1.5 that bonding orbitals were said to favour antiparallel spins, whilst antibonding orbitals favoured parallel spins. The E_F lies in the bonding part of the *d* band for the first half of the transition metal series (V, Cr & Mn) and therefore favours antiferromagnetism. In the second half of the series (Fe, Co & Ni), E_F lies in the antibonding part of the band thus favouring ferromagnetism. The dependence of the strength of J_{ij} with respect to the ratio between the atomic and 3*d* shell radii is given by a graph often referred to as a "Bethe – Slater curve" (Figure 2.5). Clearly antiferromagnetism (negative J_{ij}) is favoured when $^{R_a}/_{R_{3d}}$ is small (*i.e.* bonding orbitals), and ferromagnetism (positive J_{ij}) is favoured when $^{R_a}/_{R_{3d}}$ is large (*i.e.* antibonding orbitals). As $^{R_a}/_{R_{3d}}$ increases further, the exchange interaction disappears due to negligible electrostatic interactions.

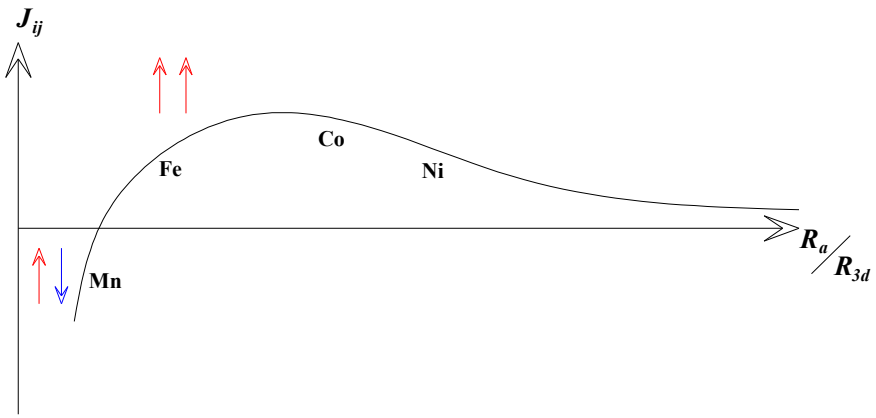

Figure 2.5: Schematic representation of a "Bethe – Slater curve" showing the relationship of the exchange interaction J_{ij} to the ratio of atom radius to 3*d* shell radius, $^{R_a}/_{R_{3d}}$. The arrows indicate electron spins. Some 3*d* transition metal elements are shown for comparison.

Due to the broadening of the bands encountered in metallic solids, Hund's rules can only give a rough indication as to which shells are filled and in which order. Fe and Ni have 8 and 10 valence electrons respectively; following Hund's rules and Figure 2.1 would suggest that the $4s^2$ shell is completely filled and the $3d^{10}$ shell has an occupancy of 6 or 8 electrons respectively. Due to the broadening of the energy levels, the 4*s* and 3*d* shells (bands) overlap (Figure 2.4), and experimental measurements show that for Fe (Ni), 0.95 (0.6) electrons occupy the 4*s* shell and 7.05 (9.4) occupy the 3*d* shell. Coupled with knowledge of the magnetic moment for Fe and Ni, this can be used to show that both spin up and spin down 3d bands in Fe are partially full, whereas in Ni the spin up band is full and the spin down band partially full (*c.f.* Figure 2.4). Accordingly, Fe is said to be a weak ferromagnet and Ni a strong ferromagnet.

2.2.2 Ferromagnetism in lanthanides

The lanthanide group describes the elements from La to Lu with atomic densities (*Z*) from 57 to 71. These are often referred to as "rare earth" (RE) elements, with the name originating from the uncommon oxide minerals from which they were extracted. Both Sc and Y (Z = 21 & 39 respectively) are often included in the RE terminology since both have very similar chemical characteristics.

The electron configuration in the lanthanide group is depicted as [Xe]$5d^1 6s^2$ for La, through to [Xe]$4f^{14} 5d^1 6s^2$ for Lu. Note that when studying RE *metals*, they all have the same outer electronic structure with $5d^1$ and $6s^2$ conduction electrons due to the splitting of energy levels into bands. The conduction electron shells are filled before the

4*f* shell, analogous to the case of transition metals whereby the 4*s* shell is filled before the 3*d* shell. In the lanthanides, the $5d^1$ and $6s^2$ electrons are responsible for bonding (*c.f.* the 4*s* electrons in the transition metals) whilst the partly filled, localized 4*f* states are responsible for the element's magnetic properties (*c.f.* 3*d* electrons in the transition metals). Note that the 4*f* state is more tightly bound than the 3*d* state, thus the 4*f* bands extend to large $D(E)$ but cover small E (see Figure 2.4).

The RE series can be split into two groups, determined by the filling of the 4*f* shell. Light REs (*e.g.* Ce) are determined by a 4*f* shell which is less than half full, such that the spin angular momentum (S) and orbital angular momentum (L) are antiparallel, leading to a total angular momentum $J = |L - S|$. Heavy REs (*e.g.* Dy) have a 4*f* shell more than half full with S and L parallel, giving $J = |L + S|$. For all REs except Gd, $L \geq S$, meaning that the direction of J is determined primarily by L (this is described further in section 2.4). It should be noted that in REs, the ferromagnetic ordering occurs below room temperature.

2.3 Magnetic Properties of Crystalline Solids

Before attention is given to the properties associated with combining the aforementioned transition metal and lanthanide groups into RE-TM compounds, it is important to consider the effects of the crystalline lattice on magnetic properties. When a property of a material is different in one direction to another, that property is said to be anisotropic. Before continuing with the topic of anisotropy, it is worthwhile noting the basic form of the energy associated with a thin-film sample such as those studied within this work. The total energy (E) may be expressed as

$$E = E_{EX} + E_A + E_Z \tag{2.21}$$

Here, E_{EX} is the magnetic exchange energy (from section 2.1.5), E_A is the *total* anisotropy energy and E_Z is the Zeeman energy. E_Z is the potential energy of a magnetic moment within an applied magnetic field, given by

$$E_Z = -\mathbf{M} \cdot \mathbf{B} \tag{2.22}$$

with **M** the magnetization of the sample and **B** the applied field.

Within this section attention is given to the term E_A which will be seen to originate from several different magnetic anisotropies; specifically shape ("magnetostatics"), magnetocrystalline and magnetoelastic effects. It is worth noting

that the presence of these anisotropies, and modifications thereof, will be discussed in depth throughout Chapter 5 and Chapter 6. Further details on magnetoelastic anisotropies will also be presented in section 3.2 when discussing material deposition.

2.3.1 Shape anisotropy

Magnetostatic energy, E_{MS}, arises from classical interactions between the volume of the sample being magnetized and the associated formation of surface magnetic charges. Accordingly, magnetostatic effects due to the non-uniform nature of a sample may be considered as shape anisotropy. A classic example of magnetostatics is given in Figure 2.6. The two magnetic samples shown as a) and b) have different shapes but equal volume and are constructed from the same ferromagnetic material. It is found experimentally that at a distance illustrated by the dashed line, $H_2 > H_1$, where H_n represents the stray magnetic field from the sample. Assuming the samples are magnetized to saturation along the *z*-axis, the total magnetic flux emanating from the *x*-*y* plane of sample a) and b) is equal. However, the magnetic flux from sample b) is concentrated to a smaller region thus the measured field is greater. A further example of magnetostatics may be given with respect to magnetizing samples a) and b) along three orthogonal axes, *x*, *y* and *z*. Assuming no other anisotropies exist, a hysteresis loop for sample a) will look identical whether the applied magnetic field **B** is along the *x*, *y* or *z*-directions ($\mathbf{B}_x$, $\mathbf{B}_y$ & $\mathbf{B}_z$ respectively). However, for sample b), two distinctly different hysteresis loops will be obtained; one for $\mathbf{B}_z$ and one for $\mathbf{B}_x$ and $\mathbf{B}_y$ as illustrated to the right of Figure 2.6. From these hysteresis loops it is clear that the applied magnetic field (B_S) required to reach saturation of the sample magnetization (M_S) is greater for $\mathbf{B}_x$ and $\mathbf{B}_y$ than $\mathbf{B}_z$, *i.e.* $\mathbf{B}_{S_{x,y}} > \mathbf{B}_{S_z}$. Because there is a much larger surface area perpendicular to the applied magnetic field when sample b) is magnetized along a short axes, there exists a much greater region from which the magnetic flux may escape. The magnetic flux may be considered to create surface "charges" on the material. Since magnetic "charges" (monopoles) may not exist [8], there exists a dipolar field between these surface charges known as a demagnetizing field. The demagnetizing field is often through the sample, thus opposes the applied magnetic field which set up the demagnetizing field in the first place. Accordingly, the magnetization characteristics of the sample are determined by the samples shape. Clearly it is harder to magnetize sample b) along one of its short dimensions compared to its long dimension since it experiences a grater demagnetizing field.

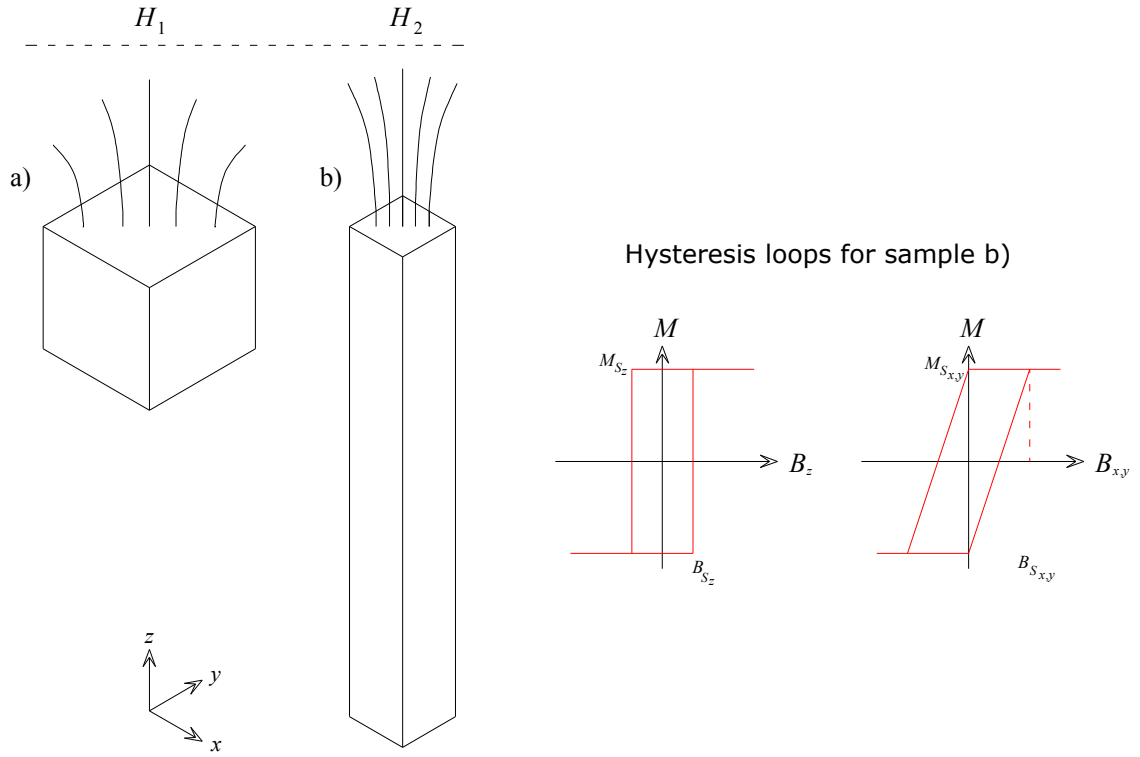

Figure 2.6: Samples a) and b) are composed of identical ferromagnetic material and have equal volume but different shape. The field H_2 emanating from sample b) is greater than H_1 from sample a) at the fixed distance indicated. The hysteresis loops show the required extra magnetic field $\mathbf{B}_S$ required to magnetize sample b) along either the x- or y-direction compared to the z-direction due to magnetostatics.

The demagnetizing field, $\mathbf{H}_d$ is given by

$$\mathbf{H}_d = -\mathbf{N}\mathbf{M} \tag{2.23}$$

for a uniformly magnetized sample. **M** is the sample magnetization and the constant of proportionality, **N**, is the demagnetizing factor[iii]. **N** is a tensor function of the shape and describes the flux density normal to a surface. In the case of an ellipsoid, $N_{ij} = 0$ for $i \neq j$ and $N_{xx} + N_{yy} + N_{zz} = 1$. Therefore $\mathbf{H}_d$ is given as

$$\mathbf{H}_d = -\left(N_{xx}M_x\,,\, N_{yy}M_y\,,\, N_{zz}M_z\right) \tag{2.24}$$

and using the fact that the magnetostatic energy is a magnetic moment by moment assembly *i.e.* $E_{MS} = \int_{M=0}^{M=M_S} MdM = \frac{{M_S}^2}{2}$, the energy associated with the demagnetizing field is given by

[iii] The only sample for which an exact analytical solution for **N** exists is an ellipsoid.

$$E_{MS} = -\frac{1}{2}\mu_0 \mathbf{M}_s \cdot \mathbf{H}_d = \frac{1}{2}\mu_0 \left(N_{xx} {M_{s,x}}^2 + N_{yy} {M_{s,y}}^2 + N_{zz} {M_{s,z}}^2\right) \quad (2.25)$$

with $\mathbf{M}_s$ the saturation magnetization.

Equation (2.25) clearly shows that E_{MS} is lowest for states with magnetization along the direction with lowest N_{ii}. The difference in demagnetizing fields in two orthogonal directions within a sample (for example width (w) and height (h)) gives the shape anisotropy field

$$H_s = M(N_w - N_h) = M\Delta N \quad (2.26)$$

Combining equations (2.25) and (2.26) leads to the definition of shape anisotropy K_s, *i.e.* the difference in magnetostatic energy between two directions

$$K_s = \frac{1}{2}\mu_0 {M_s}^2 \Delta N \quad (2.27)$$

It is useful to express the magnetostatic energy in terms of direction cosines (α_i) (in this instance this is the direction of the magnetization vector **M** with respect to the crystallographic axes) since it is rare that they are orthogonal. E_{MS} is then given as [9]

$$E_{MS} = \frac{1}{2}\mu_0 {M_S}^2 \Delta N \left({\alpha_x}^2 + {\alpha_y}^2\right) = K_s \left({\alpha_x}^2 + {\alpha_y}^2\right) \quad (2.28)$$

Note that for a uniaxial system the direction cosines may be replaced by a simple periodic potential, represented by an angle θ made between **M** and the axes of the system, leading to the more familiar form of equation (2.28); $E_{MS} = K_s \sin^2 \theta$.

Within a polycrystalline magnetic sample, the shape anisotropy gives the preference for the magnetization to lie in a particular direction. There exists the possibility to induce shape anisotropy effects into a single-crystal material via artificial structuring. This process forms the basis for some of the work conducted for this thesis and is described in Chapter 6.

2.3.2 Spin-orbit interaction and crystal fields

For elemental atoms or ions incorporated within the crystal lattice of a solid, the total Hamiltonian $\mathcal{H}$ describing that atom or ion is given by

$$\mathcal{H} = \mathcal{H}_C + \mathcal{H}_{SO} + \mathcal{H}_{CF} \quad (2.29)$$

with $\mathcal{H}$ denoting a Hamiltonian, and the subscripts *C*, *SO* and *CF* relating to the Coulomb, spin-orbit and crystal field interactions respectively. $\mathcal{H}_C$ describes the electrostatic interactions responsible for coupling moments in a multi electron atom.

$\mathcal{H}_{SO}$ gives the interaction between the orbital and spin angular moments of an atom; $\mathcal{H}_{SO} = \lambda \mathbf{L} \cdot \mathbf{S}$, with λ a coupling constant. $\mathcal{H}_{CF}$ details the coupling between **L** and the "crystal field"; within the crystalline lattice of a solid, the electron spatial distribution functions can align and remain fixed along a specific axis of symmetry. In the case of transition metals, where the 3*d* electrons form the bulk of the outer electrons, it is clear that these electrons will experience a significant reduction in **L** due to the crystal field. When $\mathbf{L} = 0$ it is said to be *quenched*, *i.e.* μ_L is locked in a fixed direction by the crystal field. In RE elements, the spin-orbit interaction is greater and the 4*f* electrons are shielded from the outside of the atom by the outer 5*s* and 5*p* electrons and **L** is not quenched.

In summary this gives $\mathcal{H}_{CF} \gg \mathcal{H}_{SO}$ for transition metals and $\mathcal{H}_{CF} \ll \mathcal{H}_{SO}$ for REs. In the ferromagnetic transition metals the orbital angular momentum is averaged out ($\mathbf{L} = 0$) due to crystal field interactions resulting in $\mathbf{J} = \mathbf{S}$, hence the magnetism of the material is due primarily to the electrons' spin. This is illustrated in Figure 2.8. In these transition metals the response of the magnetization to an applied magnetic field is only weakly anisotropic. In ferromagnetic REs both the orbital and spin angular momenta are responsible for the magnetic properties, resulting in a strongly anisotropic behaviour of the magnetization to an applied field.

2.3.3 Magnetocrystalline anisotropy

The magnetocrystalline anisotropy causes the magnetization to experience preferential directions within the crystalline ferromagnetic material. These directions are referred to as *easy axes* of magnetization. Correspondingly there are accompanying directions along which it is difficult for the magnetization to lie, known as *hard axes* of magnetization. The magnetocrystalline anisotropy energy is a measure of the difference in energy required to magnetize the material in these directions. The spin-orbit interaction is primarily responsible for magnetocrystalline anisotropy since the spin of the electron is directly coupled to the orientation of the electron orbital, thereby any symmetry of the crystalline lattice is felt by the electron's spin, causing the spins to preferentially align along a particular crystallographic axis. Since the spin-orbit coupling in REs is far greater than in transition metals, the magnetocrystalline anisotropy energy is generally much larger in REs than transition metals.

The magnetocrystalline anisotropy energy within RE materials has been described by the Callen-Callen model [10] and is given, for cubic anisotropy, as a function of the magnetization vector **M** and temperature T as

$$E_{MC}(\mathbf{M},T) = K_1(T)\left(\alpha_x{}^2\alpha_y{}^2 + \alpha_x{}^2\alpha_z{}^2 + \alpha_y{}^2\alpha_z{}^2\right) + K_2(T)\left(\alpha_x{}^2\alpha_y{}^2\alpha_z{}^2\right) \tag{2.30}$$

with α_i the directional cosines of the magnetization vector with respect to the crystallographic axes [2] and K_1 and K_2 first and second order temperature dependent phenomenological (cubic) anisotropy constants, respectively. The only easy directions of magnetization permitted in this model are the major cubic symmetry axes of [001], [101] and [111] which are obtained when equation (2.30) is minimized. However, work by Atzmony and Dariel [11] showed that for various Laves phase materials of RE and Fe such as $CeFe_2$, $SmFe_2$ and $HoFe_2$ (very similar to those studied within this work) that there can be an easy axis of magnetization along a direction other than the major cubic symmetry axes. To explain this a third cubic anisotropy constant K_3 was introduced to the model to give

$$E_{MC}(\mathbf{M},T) = K_1(T)\left(\alpha_x{}^2\alpha_y{}^2 + \alpha_x{}^2\alpha_z{}^2 + \alpha_y{}^2\alpha_z{}^2\right) + K_2(T)\left(\alpha_x{}^2\alpha_y{}^2\alpha_z{}^2\right) + K_3(T)\left(\alpha_x{}^4\alpha_y{}^4 + \alpha_x{}^4\alpha_z{}^4 + \alpha_y{}^4\alpha_y{}^4\right) \tag{2.31}$$

Atzmony and Dariel also found that there should be a change of sign of K_1 (K_2) for $HoFe_2$ ($DyFe_2$) as the temperature was increased; something which cannot be explained by the Callen-Callen model and was only fully described by Martin *et al.* in 2006 [12]. Within this work it was also discovered that higher order K_i terms can dominate over lower order terms as temperatures are varied.

Within the micromagnetic simulations used in this work to describe the experimental results, values for K_i are calculated using the data tables for multipolar coefficients $\tilde{A}_j$ provided in Zimmermann [13]. Tables for $\tilde{A}_j$ are calculated for a wide range of temperatures (0 – 350 K), introducing the required temperature dependence into the micromagnetic simulations. $\widetilde{K}_j$ (a per unit volume multipolar coefficient) is calculated from the supplied values for $\tilde{A}_j$ using

$$\widetilde{K}_j = \frac{8k_B\tilde{A}_j}{V_{cell}} \tag{2.32}$$

where k_B is Boltzmann's constant and V_{cell} is the volume of a unit cell which can be calculated from data in section 3.2 and Mougin *et al.* [14]. The appearance of 8 is due

to there being 8 formula units (f.u.) per Laves phase unit cell (as shown in section 2.4.1). Finally, the cubic anisotropy constants are given by [12, 13]:

$$K_1 = -\frac{15}{2\sqrt{\pi}}\widetilde{K}_4 - \frac{21}{4}\sqrt{\frac{13}{\pi}}\widetilde{K}_6 - 9\sqrt{\frac{17}{\pi}}\widetilde{K}_8$$
$$K_1 = \frac{231}{4}\sqrt{\frac{13}{\pi}}\widetilde{K}_6 + 39\sqrt{\frac{17}{\pi}}\widetilde{K}_8 \qquad (2.33)$$
$$K_1 = \frac{65}{2}\sqrt{\frac{17}{\pi}}\widetilde{K}_8$$

which can then be used to model the magnetocrystalline anisotropy energy associated with the $REFe_2$ cubic Laves phase intermetallics studied within this work. Detailed examples of micromagnetic simulations of the present $REFe_2$ exchange spring systems based upon these data may be found in Zimmermann *et al.* [15, 16].

2.3.4 Magnetoelastic anisotropy

Within a magnetic material the volume may change as a magnetic field is applied due to the creation of local magnetic moments and the associated creation of magnetic domains. This is a process known as magnetostriction and was first discovered as early as 1842 by Joule [17]. This point can be extended further to include crystalline anisotropy, whereby the volume change of a material can be different along different crystalline directions, *i.e.* an anisotropic strain. There must, therefore, be a coupling between the magnetization direction and the mechanical strains within the material. This is created by the coupling of the directional cosines α_i of the magnetization vector with the components of a strain tensor ε_{ij} ($i,j = x,y,z$). The strain tensor can be understood as compressive- or tensile-strain with ε_{ii} (*e.g.* pushing or pulling in the *x*-*y* plane perpendicular to the *z*-axis), or as a shear-strain with ε_{ij} (*e.g.* twisting within the *x*-*y* plane).

Including terms from sections 2.3.1 and 2.3.3, the *total* magnetic anisotropy energy, E_A, can be expressed as

$$E_A = E_{MS} + E_{MC}(\alpha_i) + E_E(\varepsilon_{ij}) + E_{ME}(\alpha_i\varepsilon_{ij}) + \cdots \qquad (2.34)$$

i.e. as a sum of the magnetostatic energy E_{MS}, the magnetocrystalline energy E_{MC}, the pure elastic energy E_E (independent of α_i), and the magnetoelastic energy E_{ME}. For a cubic crystalline lattice, Lee [18] shows that E_E and E_{ME} may be expanded as

$$E_E = \frac{1}{2}C_{11}\left(\varepsilon_{xx}{}^2 + \varepsilon_{yy}{}^2 + \varepsilon_{zz}{}^2\right) + C_{12}\left(\varepsilon_{xx}\varepsilon_{yy} + \varepsilon_{yy}\varepsilon_{zz} + \varepsilon_{xx}\varepsilon_{zz}\right) + \frac{1}{2}C_{44}\left(\varepsilon_{xy}{}^2 + \varepsilon_{yz}{}^2 + \varepsilon_{xz}{}^2\right)$$
$$E_{ME} = b_1\left(\alpha_x{}^2\varepsilon_{xx} + \alpha_y{}^2\varepsilon_{yy} + \alpha_z{}^2\varepsilon_{zz}\right) + b_2\left(\alpha_x\alpha_y\varepsilon_{xy} + \alpha_x\alpha_z\varepsilon_{xz} + \alpha_y\alpha_z\varepsilon_{yz}\right) \quad (2.35)$$

with C_{11}, C_{12} and C_{44} cubic elastic stiffness constants, and b_1 and b_2 the magnetoelastic coefficients. E_E may be eliminated from further discussion since it is independent of the direction cosines, whilst Mougin *et al.* [19] have demonstrated that b_2 is two orders of magnitude larger than b_1 thus the latter also need not be considered further. Within the scope of the thin films studied in this work, the term of most relevance is ε_{xy}, since the strain terms ε_{xz} and ε_{yz} are equal to zero as a result of homogenous strains in the film plane (determined experimentally in Mougin *et al.* [20]). It has been shown in Bowden *et al.* [21] that the main contributions to E_{ME} at room temperature are given by first and second order approximations relating to the multipolar coefficients $\widetilde{K}_2{}'$ and $\widetilde{K}_{242}{}''$ respectively, in much the same vein as those described for the magnetocrystalline anisotropy energy. E_{ME} is thus given as [13, 21]

$$E_{ME} = \sqrt{\frac{15}{2\pi}}\left(\widetilde{K}_2{}' + \widetilde{K}_{242}{}''\right)\alpha_x\alpha_y \quad (2.36)$$

with complete values for the multipolar coefficients given in [13], and converted to the appropriate form for use in equation (2.36) using equations in [21] and equation (2.32).

2.3.5 Concluding remarks on magnetic anisotropy

Referring back to equation (2.21), each of the individual energy terms has been accounted for. E_{EX} and E_Z are characteristics of the material's fundamental properties, whilst the three key terms corresponding to E_A (equation (2.34)) are dependent on the thin film's crystalline properties.

1. E_{MS} favours an in-plane alignment of the magnetization vector **M**.
2. E_{MC} shows that in a *bulk* material the easy and hard axes of magnetization are related to the sign and value of the anisotropy coefficients K_{ci}. Mougin *et al.* [20] show, for example, that in *bulk* $DyFe_2$ the easy axis of magnetization is along a $\langle 001 \rangle$ direction at room temperature.
3. E_{ME} can be approximated to include only the $b_2\alpha_x\alpha_y\varepsilon_{xy}$ terms, which, using the derived negative values for b_2 and ε_{xy} for the case of *strained thin films* [19],

results in a minima for E_{ME} when the magnetization of the *thin film* sample points along $[\bar{1}10]$ or $[1\bar{1}0]$.

Equation (2.34) can be re-written in a more expanded form to include explicitly the three terms above as

$$E_A(\mathbf{M},T) = K_S\left(\alpha_x{}^2 + \alpha_y{}^2\right) + \{K_1\left(\alpha_x{}^2\alpha_y{}^2 + \alpha_x{}^2\alpha_z{}^2 + \alpha_y{}^2\alpha_z{}^2\right) + K_2\left(\alpha_x{}^2\alpha_y{}^2\alpha_z{}^2\right) + K_3\left(\alpha_x{}^4\alpha_y{}^4 + \alpha_x{}^4\alpha_z{}^4 + \alpha_y{}^4\alpha_y{}^4\right)\} + b_2\alpha_x\alpha_y\varepsilon_{xy} \quad (2.37)$$

The equilibrium direction of **M** is determined by minimizing E_A. Inspection of equation (2.37) and ref. [20] shows that the strain term ε_{xy} plays an important role in determining **M**, and as such, consideration is given to its appearance during the growth of the thin film samples within section 3.2. In addition to this, direct modifications to this term through Ar^+ ion implantation, which causes changes to the internal crystalline structure of the material, will form the basis of Chapter 5.

The appearance of a large E_{ME} term can influence the direction of easy magnetization in a thin film sample. In Mougin *et al.* [20] it was shown that the ratio of $\left|\frac{b_2\varepsilon_{xy}}{K_1}\right|$ is strongly temperature dependent. At low temperatures (4.2 K), $K_1 > b_2\varepsilon_{xy}$ and the easy axis of magnetization of the thin films and bulk samples are the same. At higher temperatures (300 K) $K_1 \lesssim b_2\varepsilon_{xy}$ and the easy axis of magnetization is not the same as that in the bulk compound. Therefore there is a clear dependence of easy axis of magnetization with temperature. In the case of a *thin film* sample of epitaxially grown $DyFe_2$, the easy axis at low temperatures is $[001]$ (the same as the *bulk* sample). As the temperature increases, this rotates towards the $[1\bar{1}0]$ direction.

Continuing with the example of $DyFe_2$, vector magnetometry measurements taken by Zhukov *et al.* [22] show that the easy axis makes an angle of about 15° out of the plane of the sample, above the $[1\bar{1}0]$ axis. The consequences of this will be studied when discussing the effects of ion implantation and patterning of such samples. It is worthwhile noting that in the case of YFe_2 thin films, the direction of easy magnetization does not vary much with temperature [20]. This is because the contribution to the total energy from E_{ME} is very small. Nevertheless, the reader will encounter some interesting results obtained by the direct modification of this small E_{ME}, which give rise to some surprising physics, potentially very useful in technological applications. Again, this will be covered in Chapter 5.

2.4 Laves Phase Materials and Exchange Interactions

Within this section attention is given to the effects observed and measured when transition metals are combined with lanthanide group materials to form intermetallic compounds. First the intermetallic compounds are briefly described, before attention is given to the various interactions between the magnetic moments within these compounds which give rise to the observed long and short-range magnetic ordering. This includes the iron – iron and the rare earth – iron exchange interactions.

2.4.1 The Laves phase materials

RE metals have moderate elastic constants [14, 20, 23] and exhibit a large orbital component to their magnetic moments (section 2.2.2). The result of this is that RE metals exhibit the largest known magnetostriction as well as having a large magnetic moment per atom. They also provide a large magnetocrystalline anisotropy. However, as mentioned in section 2.2.2, these materials are only ferromagnetic below room temperature, exhibiting paramagnetic properties above this, rendering useful physical applications impossible at room temperature.

To overcome this problem, the RE metals have been combined with transition metal elements. This work uses materials based on the combination of REs with Fe, forming what is known as a Laves phase intermetallic compound (see Figure 2.7). The strong anisotropic behaviour is governed by the RE elements [24], whilst the Curie temperature is substantially increased by the Fe to temperatures of ~ 1000 °C [2]. The magnetic and electric properties of these Laves phase $REFe_2$ intermetallic compounds have been extensively studied for more than 40 years within many groups, for example see original work by Buschow [25], Bowden [24] and Cohen [26].

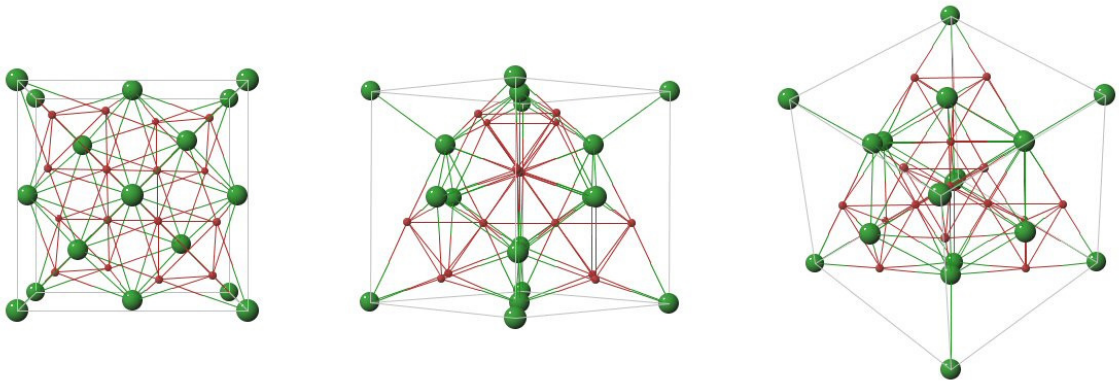

Figure 2.7: Schematic representations of the cubic Laves phase of the $REFe_2$ structures [27]. The three images show one, two and three planes of the material respectively. The green spheres denote RE (in this work, RE = Y, Dy, although Y is not a true RE), and the red spheres denote Fe.

The Laves phase structure shown in Figure 2.7 is the C-15 $MgCu_2$ type, space group Fd3m. The RE ions, of which there are 8 per unit cell, have a local cubic symmetry (green spheres), whilst the Fe ions (16 per unit cell) have a tetragonal symmetry (red spheres). Within a single laves phase unit cell there are 8 formula units (f.u), *e.g.* 8 × a single $DyFe_2$. For the materials studied in this work (YFe_2 and $DyFe_2$), the bulk compounds have lattice parameters of $a_{YFe_2} = 0.7362$ nm and $a_{DyFe_2} = 0.7324$ nm. It is worthwhile noting that most Laves phase $REFe_2$ compounds have very similar lattice parameters, ranging from 0.724 nm for $LuFe_2$ through to 0.7415 nm for $SmFe_2$ [14]. Thus any mis-match between the Laves phase and substrate during thin film growth is likely to be very similar whatever the RE, resulting in similar strains and growth properties throughout the series.

It will be shown in sections 2.4.2 and 2.4.3 that the interaction between the spins of the electrons in the Fe and those in the RE (*i.e.* the 3*d* and 4*f* electrons, respectively) will be crucial in order to determine the magnetic properties of these materials. Within the $REFe_2$ elements studied within this work, there are strong ferromagnetic Fe-Fe exchange interactions and antiferromagnetic RE-Fe exchange interactions. In addition to these there is also a ferromagnetic RE-RE exchange but this is far weaker than the aforementioned two so will not be considered further.

2.4.2 Iron – iron exchange

The Fe-Fe exchange interaction is strong and extends over a large distance. In samples of elemental Fe it persists up to temperatures of 1000 K whilst in $REFe_2$ intermetallics it can be as high as 600 K. It has already been shown that the 3*d* electrons, responsible

for the magnetism of transition metals, have localized wavefunctions. The spatial extent of these wavefunctions are shown to be smallest for the ferromagnetic transition metals [28] and extend to, at most, approximately half an interatomic distance for Fe [2]. A model whereby the localized 3*d* electrons cause the polarization of the conduction (*s*) electrons was proposed by Zener in 1951 [29]. Due to the extended wavefunctions of the *s* electrons (extending further than a single interatomic distance) these can cause alignment of localized 3*d* electrons on neighbouring atoms within the material. Therefore there is a direct exchange between 3*d* and *s* electrons and an indirect exchange between the localized 3*d* electrons on each atom. The indirect exchange theory was extended further by Ruderman and Kittel [30] and Kasuya and Yosida [31, 32] independently (hence the common abbreviation to RKKY) throughout the mid to late 1950s. The RKKY model introduces an oscillatory spatial polarization of the conduction electrons which originates from variations in electron charge distribution about an impurity in a metal ("Friedel oscillations"). Therefore the RKKY model can introduce either antiferromagnetism or ferromagnetism as the strength of the exchange interaction oscillates from positive to negative with increasing atomic separation. Stearns however showed that the conduction electrons are spin polarized in the *opposite* direction to the central atom out to a distance beyond the next nearest neighbours [33]. Whilst this confirms the long range interactions of *s* electrons, it does mean that conduction electrons cannot account for the observed ferromagnetism in Fe since the polarization required both by Zener and RKKY models cannot be achieved, leading to antiferromagnetism. Stearns later proposed a model [34] to explain the Fe-Fe exchange whereby it was suggested that the localized 3*d* electrons were coupled through a small number of free (itinerant) *d* electrons (5 – 8 %) produced from the mixing of the *s* and *d* bands. This gives rise to longer range interactions such that nearest neighbours reside within the first crossover of the RKKY function, thereby experiencing a positive exchange interaction and therefore ferromagnetic ordering. This is a model which is currently still in use, but it is clear that there is still some confusion and active research is ongoing regarding the method behind the Fe-Fe exchange interaction.

2.4.3 Rare earth – iron exchange

The 4*f* electrons which are responsible for the ferromagnetism in RE elements are even more localized than the 3*d* electrons (responsible for ferromagnetism in transition metals). The 4*f* spatial wavefunctions extend to only ~ 10% of an interatomic spacing

[35] and therefore the long range magnetic ordering in REs cannot be due to direct Heisenberg exchange. The long range ordering can be explained by the RKKY model whereby the localized 4*f* electrons can polarize the 6*s* conduction electrons, however this model runs into difficulties when explaining the constant antiferromagnetic coupling observed between heavy RE and Fe elements at different interatomic spacings. This should oscillate between ferromagnetic and antiferromagnetic due to the form of the RKKY interaction. A model by Campbell [36] proposes the creation of a magnetic moment on the 5*d* electrons through exchange with the localized 4*f* electrons, and then direct spin conserving electron exchange from the 5*d* electrons in the RE to the 3*d* spin-holes in the Fe. As already stated in section 2.2.2, the spin and orbital angular moments are antiparallel (parallel) in light (heavy) REs. Since the RE and the Fe are at different ends of the transition metal series, the *d* electrons couple antiferromagnetically, meaning that the coupling between the light REs and Fe is ferromagnetic whilst it is antiferromagnetic between heavy REs and Fe since it is known that $|\mathbf{L}| \geq |\mathbf{S}|$ in almost all REs. For clarity this is illustrated in Figure 2.8.

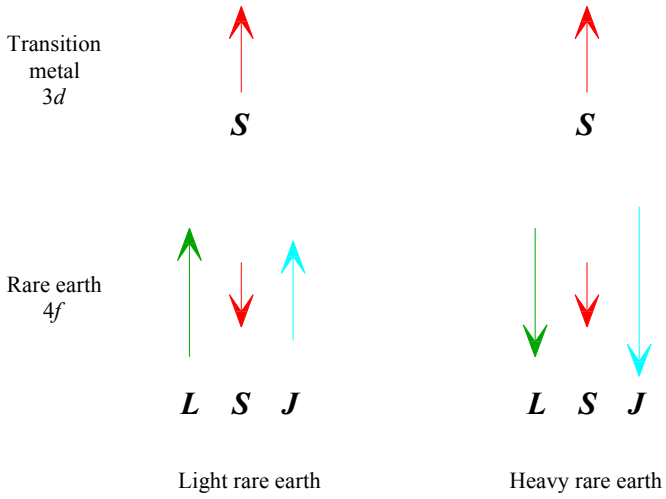

Figure 2.8: Schematic representation of the coupling between RE and TM ferromagnetic elements. Note that the spin-spin coupling is always antiferromagnetic whilst the overall coupling between ***S*** and ***J*** can be feromagnetic for light REs and antiferromagnetic for heavy REs.

2.5 Exchange Springs in $REFe_2$ Multilayers

Section 2.5 is dedicated to the subject of combining hard and soft magnetic layers to form novel, composite systems with a wealth of interesting and, more importantly, useful technological properties. The combination of such hard and soft layers forms what is commonly referred to as an exchange spring.

The concept of a magnetic film consisting of a soft magnetic layer in close proximity to a hard magnetic layer was first considered by Goto *et al.* [37]. In this work a single bi-layer system is considered whereby a soft and a hard magnetic layer are ferromagnetically coupled together. This coupling between layers tends to cause parallel alignment of the neighbouring spins. These authors found that as a critical "bending field" ($\mathbf{B}_B$) was approached, the magnetization of the hard magnetic layer remained pinned whilst the soft layer's magnetization was able to rotate by an amount proportional to the depth (**d**) along the thickness of this soft layer, with $\mathbf{B}_B \propto \frac{1}{\mathbf{d}^2}$. Thus the concept of "exchange springs" was born. A schematic of an exchange spring multilayer showing a hard ferromagnetic layer coupled to a soft antiferromagnetic layer (as in the case of $DyFe_2$ / YFe_2 samples studied within this work) is presented in Figure 2.9.

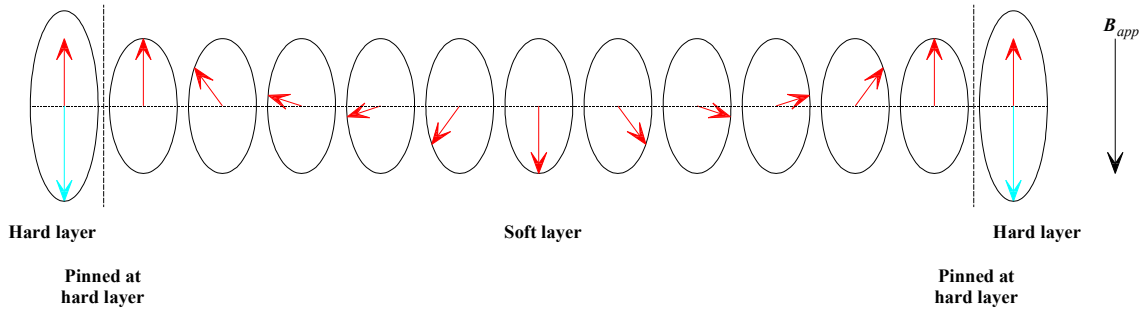

Figure 2.9: Schematic representation of a multilayer exchange spring. Here the soft layer (*e.g.* YFe_2) is pinned at its extremes by an antiferromagnetically coupled hard layer (*e.g.* $DyFe_2$). The red arrows represent the direction of magnetization of the Fe spins whilst the blue arrows represent that of the Dy (*c.f.* Figure 2.8).

An example hysteresis loop of an exchange spring system studied within this work (measured using a vibrating sample magnetometer) is given in Figure 2.10. This measurement is of an "as grown" sample, *i.e.* it has not been modified in any way post-growth. At point 1, the Fe spins of *both* the soft and the hard layers align in the direction of the applied field, whilst the spins of the Dy align antiparallel to this (since they are antiferromagnetically coupled to the Fe, see section 2.4.3). As the field is reversed to point 2 the Fe spins in the *soft* layer (YFe_2) align parallel with the field, whilst those in the *hard* layer ($DyFe_2$) remain aligned in the original direction, pinned by the Dy spins – this is the case illustrated in Figure 2.9. The field at which this reversal begins to occur is known as the *bending* field ($\mathbf{B}_B$). Here *exchange springs* are set up within the system which behave as two 180° Bloch domain walls (see section

2.6.3) and the magnetization curve is reversible right up to 0.14 T. As the field is increased the Bloch domain walls gradually invade the hard layer, until eventually a critical field value is reached whereby the hard layer magnetization is switched irreversibly, known as the irreversible field ($\mathbf{B}_{irr}$). This is the configuration illustrated at point 3 which is the mirror image of that at point 1. The whole process can then be repeated by reversing the applied field to traverse between points 3 and 1, again forming exchange springs within the system (at point 4). It should be noted that this is a simplified (yet usually adequate) explanation of the exchange spring system's behaviour under the application of a magnetic field; the applied field itself causes a rotation of the magnetization of the sample out of the film plane.

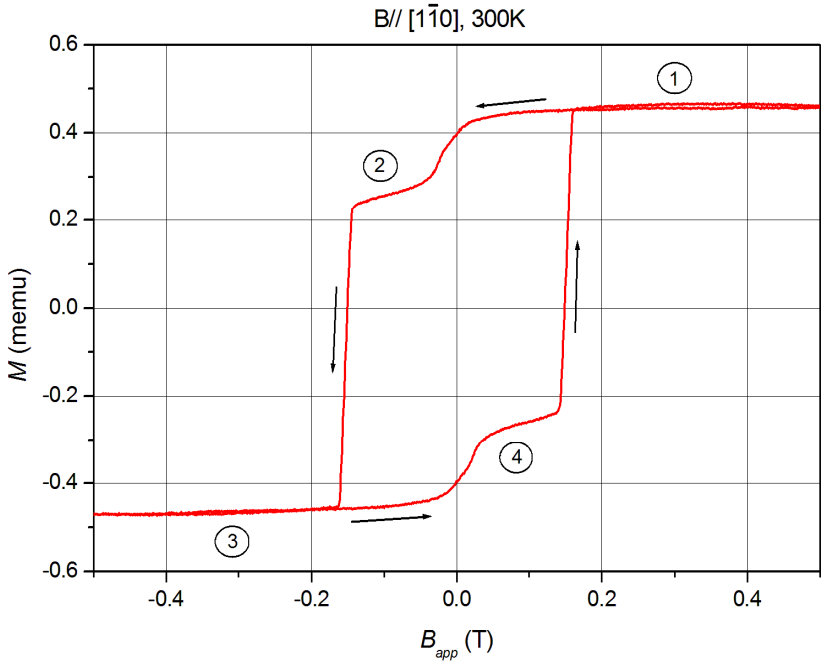

Figure 2.10: VSM hysteresis loop of an YFe_2 / $DyFe_2$ multilayer exchange spring sample, taken with the magnetic field applied parallel to the easy axis of magnetization [1$\bar{1}$0] at room temperature. The arrows indicate the direction in which the field is being swept.

Modelling of such exchange spring systems has recently been conducted by Bowden *et al.* [38], using a combination of numerical and analytical methods to derive a simple formula. The result of the competition between Zeeman and exchange energies is that above $\mathbf{B}_B$, the soft Fe spins rotate gradually throughout the multilayer sample, pinned at the interfaces with the hard layers (*c.f.* Figure 2.9). Assuming N soft mono-layers within the system, the ratio between $\mathbf{B}_B$ and the exchange field $\mathbf{B}_{Ex}$ is given by

$$\frac{\mathbf{B}_B}{\mathbf{B}_{Ex}} = \left(\frac{\pi}{N}\right)^2 \tag{2.38}$$

which agrees well with the aforementioned $\frac{1}{d^2}$ ratio in Goto *et al.* [37].

Exchange spring systems have received much attention over the past 15 years with notable original papers by Kneller & Hawig [39], Skomski & Coey [40] and Fullerton *et al.* [41] which indicate their potential as hard permanent magnetic materials. Coupling the RE with a transition metal gives both a high coercivity and magnetic anisotropy (from the RE), and high magnetic remanence (from the transition metal, specifically Fe) thereby increasing $(BH)_{max} = \frac{1}{V}\int|\mathbf{B}\cdot\mathbf{H}|d\boldsymbol{r}$. Here V is the volume of the magnet, **B** the applied magnetic field and **H** the internal field (the sum of the applied field and the demagnetizing field). Thus $(BH)_{max}$ is a measure of the magnet's energy product. A further advantage of such an exchange spring system is that the RE content of the soft magnetic layer can be 0% [41], thereby significantly reducing the production costs.

The first systems with discrete hard and soft layers to be studied experimentally were sputter deposited bi-layers by Al-Omari & Sellmyer [42] in 1995, who demonstrated reversible hysteresis loops (a classic sign of an exchange spring) and an increased $(BH)_{max}$. Since then, the number of papers on the topic has increased dramatically due to the potential for inclusion of these materials in a number of applications, ranging from hard permanent magnets in MEMS [43], fundamental spin transfer torque studies [44] and data storage devices as early as the original work by Goto *et al.* in 1965 [37]. The latter is covered in greater depth in section 2.7.4.

2.6 Magnetization Reversal, Magnetic Domains and Micromagnetics

In order to describe much of the experimental data presented in this work, and to understand the technology supporting this research, it is useful to detail some of the magnetization reversal mechanisms. Two extreme limiting mechanisms will be described; coherent rotation and domain wall motion. It should be noted that these are ideal, model situations for which analytical solutions are available. Thus they do not fully describe real magnetic media, but they provide useful insights into different mechanisms of magnetization reversal and will aid with interpretation of experimental data. However, for more complex systems, such as the exchange coupled magnetic

multilayers used in this work, a detailed understanding of the magnetization dynamics is only possible by performing computationally aided numerical simulations. Accordingly, details of micromagnetic computational simulations are also included in this section, but first, a brief description of coercivity is given.

2.6.1 Coercivity

When a hard ferromagnetic material is magnetized by an applied field ($\mathbf{B}_{app}$), its magnetization (**M**) will not relax back to zero once that field is removed. A reverse applied field ($-\mathbf{B}_{app}$) is required in order to drive **M** back to zero. Examples of this behaviour are given in the hysteresis loops in Figure 2.6, Figure 2.10 and Figure 2.11. The magnitude of the field required to return to the **M** = 0 situation is the *coercivity* (or *coercive field*, H_C). The value of H_C depends strongly on the intrinsic magnetic properties, its microstructure and time. In the thin film samples studied in this work, the intrinsic properties include the anisotropy energies, the exchange energy and the Zeeman energy, whilst the microstructure of the sample is governed primarily by surface roughness and any post-growth lithographical processes. In this work, all magnetization reversal processes occur over similar time periods (minutes).

2.6.2 Coherent rotation of magnetization

The Stoner-Wohlfarth model [45, 46] gives a simple analytical description of the effect of a magnetic field on the reversal of magnetization in an ensemble of non-interacting, single-domain particles. As will be shown in section 2.6.4, this corresponds to particles that are typically tens of nm in diameter, whose magnetization can be assumed to be equivalent to the sum of all of the individual constituent magnetic moments.

Within the Stoner-Wohlfarth model, the assumption is made that all spins are aligned parallel with respect to each other (thus the exchange energy can be ignored), whilst subject to a uniaxial shape anisotropy. Accordingly, the total energy of the system along an easy axis of magnetization is given by equation (2.21), which may now be expressed as

$$E = E_A + E_Z = K \sin^2 \theta - M_S B \cos \theta \tag{2.39}$$

The stable energy state is found by minimizing E, *i.e.*

$$\frac{\partial E}{\partial \theta} = 2K \sin\theta \cos\theta + M_S B \sin\theta = 0 \qquad (2.40)$$

which has the (non-trivial) solution $\cos\theta = -\frac{\mathbf{M}_S \mathbf{B}_{app}}{2K}$. When the sample is magnetized along the easy axis, $\mathbf{M}_S$ points parallel to $\mathbf{B}_{app}$, giving $\theta = 0, \pi$ for $\pm\ \mathbf{B}_{app}$. Hence the coercive field is defined as

$$\mathbf{B}_C = \pm\frac{2K}{\mathbf{M}_S} \qquad (2.41)$$

Thus, as $\mathbf{B}_{app}$ is varied, $\mathbf{M}_S$ remains pinned in a stable regime by the anisotropy energy, until a certain critical field ($\mathbf{B}_{app} = \mathbf{B}_C$) is applied causing the abrupt rotation of $\mathbf{M}_S$ by 180° over the anisotropy energy barrier. This is characterized by a perfectly square hysteresis loop (easy axis hysteresis loop in Figure 2.11). For the hard axis of magnetization, equation (2.39) takes the same form but the E_A term is replaced by $K\cos^2\theta$. This has stable energy solutions given by $\mathbf{B}_{app} < -\frac{2K}{\mathbf{M}_S}$ and $\mathbf{B}_{app} > \frac{2K}{\mathbf{M}_S}$. But between these regions, $\mathbf{M}_S$ will not remain pinned in a direction opposite to $\mathbf{B}_{app}$, hence θ is a continuous variable. Thus between the two stable energy solutions exists a further relationship given by $-\frac{2K}{\mathbf{M}_S} < \mathbf{B}_{app} < \frac{2K}{\mathbf{M}_S}$, where $\mathbf{M}_S$ varies linearly with $\mathbf{B}_{app}$. This is characterized by a slanted hysteresis loop (hard axis hysteresis loop in Figure 2.11).

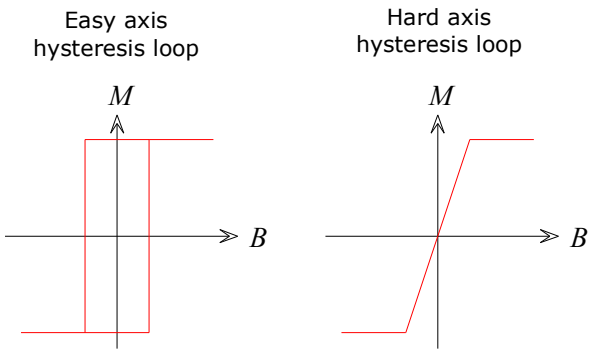

Figure 2.11: Example (ideal Stoner-Wohlfarth model) easy and hard axis hysteresis loops for a sample subject to a uniaxial shape anisotropy.

As an example of the success of the Stoner-Wohlfarth model, it is used to predict the coercivity of a 400 nm thick DyFe2 sample. The experimental data is given in Figure 2.12. Using values of K and $\mathbf{M}_S$ for $DyFe_2$ derived from Beaujour [9] (0.41 K ion^{-1} and 4.22 μ_B f.u.$^{-1}$) and equation (2.41) gives $\mathbf{B}_C$ = ±0.29 T. This is in reasonable agreement with the measured ±0.23 T from Figure 2.12. It should be noted that the easy axis of magnetization points out of the plane of the sample by ~15° [22], hence this in-

plane VSM measurement will give a reduced value of $\mathbf{B}_C$. Also, it is known from Brown's paradox [47, 48] that actual values of $\mathbf{B}_C$ lie well below theoretically calculated values, due to, for example the presence of domains (the subject of the following section) and the fact that the Stoner-Wohlfarth model is for zero temperature.

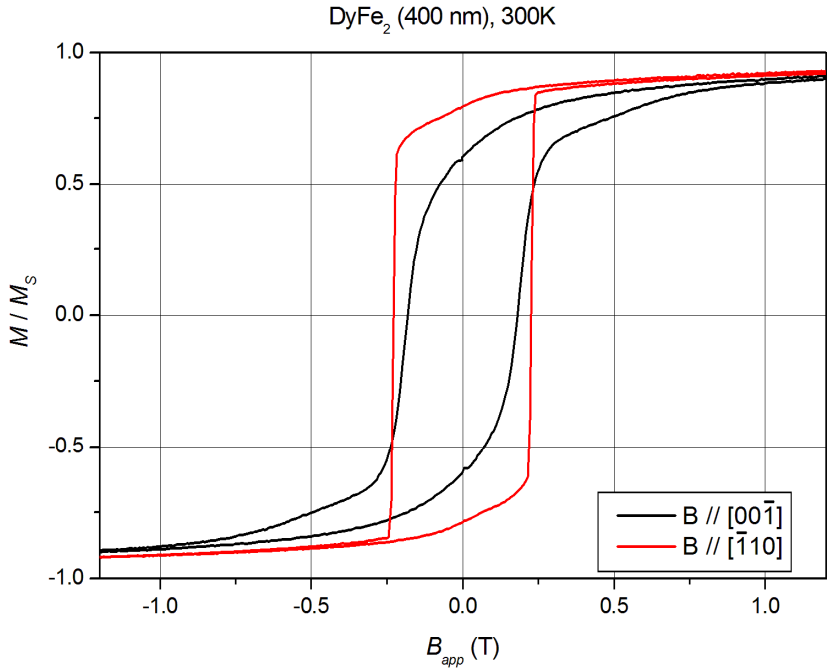

Figure 2.12: Easy and hard axis room temperature magnetization curves for a 400 nm $DyFe_2$ sample measured by VSM. The red loop is the easy axis [$\bar{1}$10] data and the black loop the hard axis [00$\bar{1}$] data.

2.6.3 Magnetic domains in thin films

Within the previous discussions the value of M has been assumed to be uniform throughout the sample. Realistically this is not accurate and domain walls (DW) or a spatial variation of M must be included to help account for Brown's paradox [49]. The formation of domains is the result of an attempt to reduce the magnetostatic energy (E_{MS}) of a uniformly magnetized finite sample. In a simple example the magnetic domains align antiparallel along the easy axis of magnetization, forming a 180° DW between them. If the wall was infinitely thin (neighbouring spins aligned 180° from each other) then there would be no anisotropy energy E_A (all spins along an easy axis of magnetization) but the exchange energy (E_{EX}) would be high. In practice there is a compromise between having an infinitely thin DW (large E_{EX}) and a thick DW (large E_A), thus the equilibrium thickness which minimizes their sum describes the typical DW width. This is typically ~ 200 nm in soft magnetic materials with low anisotropy energies and ~ 10 nm in hard magnetic materials which have a high anisotropy [2].

A further consideration is the effect that sample thickness has on DW formation. Typically within a thin film sample the magnetization of each domain will lie in the plane of the sample so as to reduce E_{MS}. The DW that forms between regions of opposite magnetization is generally *out* of the plane of the sample (Bloch wall). However, as the thickness of the sample decreases it becomes energetically favourable for the DW to form *in* the plane of the sample so as to reduce E_{MS} further. Such DWs are called Néel walls, with the transition between the two types occurring at film thicknesses of ~ 50 nm [2, 50].

The propagation and movement of DWs is the main candidate for magnetization reversal in epitaxially grown thin films such as those studied in this work [40]. Within such a model, reversed domains nucleate and abruptly propagate through the crystalline lattice, with surface defects impeding the DW movement. Example images of surface defects and the reasoning behind their appearance is given in section 3.2.3. The application of a magnetic field to the sample exerts a force on the "pinned" DW until this pressure is great enough to cause de-pinning, resulting in the DW accelerating through the sample until it encounters the next defect. Such discrete DW motion is commonly referred to as Barkhausen jumps [51]. There are two distinct regimes of DW pinning: weak DW pinning (WDWP) and strong DW pinning (SDWP) [52]. These were identified by Gaunt [53, 54] who described their behaviour as a combination of energies from the applied magnetic field and thermal excitations. Thermal excitations lead to a linear decrease of B_C with temperature in WDWP. In SDWP the walls are strongly pinned and "bow out" before overcoming a critical energy threshold and break away. Beaujour [9] has shown that in the epitaxially grown samples studied within this work that SDWP occurs.

2.6.4 Critical sizes of single domains

If a magnetic film is thin enough then a single domain state can be energetically favourable. In this case the total energy of the multi-domain state exceeds E_{MS} associated with a single large domain. This critical thickness t_c is given as [2]

$$t_c = 6.8\left(\frac{l}{w}\right)^2 \frac{\sigma_{dw}}{\mu_0 {M_S}^2}\left[\ln\left(\frac{4l}{w+t}\right) - 1\right]^{-2} \qquad (2.42)$$

where l, w and t are the film length, width and thickness respectively, σ_{dw} is the domain wall energy density and M_S is the saturation magnetization. This idea can be extended

to consider what the value for the critical radius r_c would be for a single magnetic nano-particle. The value for r_c is shown to be [2]

$$r_c = \sqrt{\frac{9A}{\mu_0 {M_S}^2}\left[\ln\left(\frac{2r_c}{a}\right) - 1\right]} \tag{2.43}$$

where A is the exchange stiffness constant[iv], a is the lattice constant. r_c has values ranging from tens to hundreds of nm in typical granular composite magnetic media such as Co / PdSi [55, 56, 57] (see section 2.7), above which the nano-particle tends to break into several magnetic domains.

2.6.5 Micromagnetic simulations

The concept of magnetic domains, domain walls and domain wall pinning were introduced in the previous sections in an attempt to explain and compensate for deviations from the Stoner-Wohlfarth model. These concepts permit the more accurate determination of magnetization properties, yet still only provide a solution for the magnetization characteristics of relatively simple systems. For example, equation (2.43) can be solved to determine r_c for samples with well defined geometries, *e.g.* an infinite cylinder, a sphere and an ellipsoid [58], but the real shapes of samples discussed within this work differ somewhat from those.

Often the most appropriate way to solve the complex problems associated with realistic samples is to use numerical simulations, whereby the temporal evolution of the dynamics of many interacting magnetic moments within a body can be accurately calculated. This subject is referred to as "micromagnetics" and forms a vast area of research within the magnetism community and beyond. As such, detailed descriptions of the calculation processes are outside the scope of this thesis. The reader is referred to a useful review by Fidler & Schrefl [59] and references therein for further information.

There are numerous micromagnetics software packages available. In this thesis, the software package `OOMMF` [60] has been used to provide numerical simulations of the magnetic properties of the materials investigated. The user interface of `OOMMF` was modified by Dr J. Zimmermann to permit accurate simulations of the strained epitaxial $REFe_2$ Laves phase materials studied in this work[v]. It should be noted that the `OOMMF`

[iv] The exchange stiffness constant is a measure of the strength of exchange coupling within the ferromagnetic system and is typically of the order $1 - 2 \times 10^{-11}$ Jm^{-1}.

[v] The author is grateful to Mr. D. Wang for assistance in utilising the software.

mesh utilised throughout this work was in the form of a purely one dimensional spin-chain so as to drastically reduce computational time. OOMMF is also inherently a zero temperature simulation; temperature dependence was introduced into the model through the anisotropy constants derived in section 2.3.3.

In OOMMF, the temporal evolution of the magnetic moments is calculated by solving the Landau Lifshitz Gilbert (LLG) equation. The LLG equation is an extension to the original Landau Lifshitz equation of 1935 [61], which includes a modified damping term introduced by Gilbert some years later [62, 63]. The LLG equation takes the form

$$\frac{d\mathbf{M}_i}{dt} = -\gamma_0 \mathbf{M}_i \times \mathbf{H}_{eff} - \frac{\alpha}{|\mathbf{M}_i|}\mathbf{M}_i \times \left(\mathbf{M}_i \times \mathbf{H}_{eff}\right) \tag{2.44}$$

This gives the temporal evolution of each magnetic moment within the system $\mathbf{M}_i$. Here $\gamma_0 = \gamma(1+\alpha^2)$ is the modified gyromagnetic ratio and α is the Gilbert damping parameter. $\mathbf{H}_{eff}$ is an effective magnetic field given by $-\frac{\partial E}{\partial \mathbf{M}_i}$ where E is the total energy of the system given by equation (2.21). $\mathbf{H}_{eff}$ acts as a torque on $\mathbf{M}$ [62]. Equation (2.44) describes the precessional motion of the magnetization under the application of a magnetic field within a damped system, and is solved numerically for each magnetic moment in the defined system by the OOMMF package.

2.7 Magnetic Data Storage

The first magnetic hard disk drive (HDD) used to store data within a computing system was manufactured by IBM in 1956 under the name of RAMAC [64]. The principle of operation of this drive has remained virtually unchanged to date; a rotating medium (platter) containing magnetic bits of information is scanned under or over an actuator mounted read / write head which senses the direction of magnetization within various small regions of the platter. However, quite the contrary is true about the amount of data which is stored within such a magnetic disk drive. Original devices stored only megabytes (MB) of information whereas today's devices can store more than one terabyte (TB) of data [65]. This has been accompanied by a physical reduction in device size, culminating in the common 3½" Ø drives found in desktop computers, 2½" Ø drives in laptops and even smaller drives in personal media players *etc*. These two factors result in a substantial increase in data storage *density* (commonly measured in bits in^{-2}). The original IBM system stored 5 MB of data on a total area of fifty 24" Ø

platters whereas modern drives store 1 TB over five 3½" Ø platters, translating to a greater than 100,000,000 fold increase in density over the past 55 years. This trend cannot continue indefinitely due to manufacturing limits within the current technology and, more fundamentally, due to the superparamagnetic limit.

Within this section, the physics behind magnetic data storage is discussed with a particular focus on the superparamagnetic limit. Existing magnetic data storage technologies are described, from which it will be seen that for HDDs to remain the non-volatile data storage device of choice, substantial technological developments are needed. These developments are likely to be in the form of "patterned" magnetic data storage media, of which an overview is given in this section, with reference to the materials used throughout this work.

2.7.1 The Physics of Magnetic Data Storage

A plot of log aerial density (MB in^{-2}) versus time (years) results in a general linear trend showing that data storage density has roughly doubled every one to two years for HDDs. This trend is known as a "Moore's Law", which was originally designed to predict the increase in the number of transistors in electronic circuitry, and later used as a roadmap for industry [66, 67]. However, this continual growth cannot proceed indefinitely due to fundamental physical limitations, the most predominant and famous of which is known as the superparamagnetic effect.

Equation (2.43) suggests that below a critical radius, r_c, a magnetic nano-particle will behave as a single domain element. At first glance this appears very appealing for the prospect of magnetic data storage since it suggests that there are no lower bounds on the size of individual magnetic elements. This in turn would suggest that an infinite data storage density could be achieved. Unfortunately it is not possible to reduce r_c indefinitely since the remnant magnetization will not remain fixed in a specific, anisotropy dictated direction. This is because when r_c reaches a critical value, the thermal energy ($E_T = k_B T$) can be large enough to overcome any potential energy barriers associated with the anisotropy, causing the magnetization to switch to a different stable orientation. In terms of data storage this would correspond to the loss of the binary data stored on that magnetic nano-particle. The probability P that the magnetization of a nano-particle may switch out of one metastable state and into a different, more stable state is given by the simple Arrhenius-Néel equation

$$P = \nu_0 \exp\left(-\frac{KV}{k_B T}\right) \tag{2.45}$$

with υ_0 an "attempt frequency" and KV the energy barrier which the nano-particle must overcome to switch states. Here K and V are the magnetic anisotropy and volume of the nano-particle respectively. Typically $\upsilon_0 = 10^9$ s^{-1} and P = 10% are used for drawing rough estimates of dimensions and timescales.

Equation (2.45) clearly shows that P is exponentially proportional to V which explains why random thermal switching is irrelevant for large, un-patterned magnetic films with large-scale ensembles of interacting grains. Equation (2.45) can be rearranged to give a simple approximation for the nano-particle radius which is stable against ambient thermal demagnetization (r_0) as

$$r_0 = \left[-\frac{3k_B T}{4\pi K} \ln\left(\frac{P}{\upsilon_0}\right)\right]^{\frac{1}{3}} \tag{2.46}$$

Defining probability as $P < 10\%$ and assuming $K = 10^5$ Jm^{-3} for a spherical particle [68] gives $r_0 = 6$ nm for a magnetization retention timescale of 1 s, $r_0 = 7$ nm for 1 year and $r_0 = 8$ nm for 100 years. This weak dependence of r_0 with time is a result of the $\ln\left(\frac{1}{\upsilon_0}\right)$ relationship and therefore it is *not* a significant challenge to extend the lifetime over which data can be stored using magnetic nano-particles, rather it is reducing the *size* of said particles. The minimum value of r_0 sets a fundamental limit on the density at which data can be stored on magnetic recording devices and is referred to as the superparamagnetic limit. Referring back to equation (2.46) and assuming P, υ_0 and T all to be fixed by definition, the only remaining variable that can be used to affect the size of r_0 is K. Clearly fabrication of the nano-particle from a material with a larger anisotropy (shape, magnetocrystalline *etc.*) will reduce r_0.

2.7.2 Longitudinal media

Until recently the standard media used in magnetic data storage was *longitudinal* media. In longitudinal media the magnetization of the recorded bit of information lies *in* the plane of the disk. The media were fabricated from a Co based alloy which typically included a combination of Pt and Cr with B or Ta [69], grown on a complex under-layer in order to promote the required magnetocrystalline anisotropy and grain orientation. The granular nature of the media had dimensions of 10 nm upwards, with the smaller dimensions present in only the more modern examples. Figure 2.13 shows AFM and

MFM images of a HDD sample from the mid 1990s where grains of average diameter 30 nm can clearly be seen.

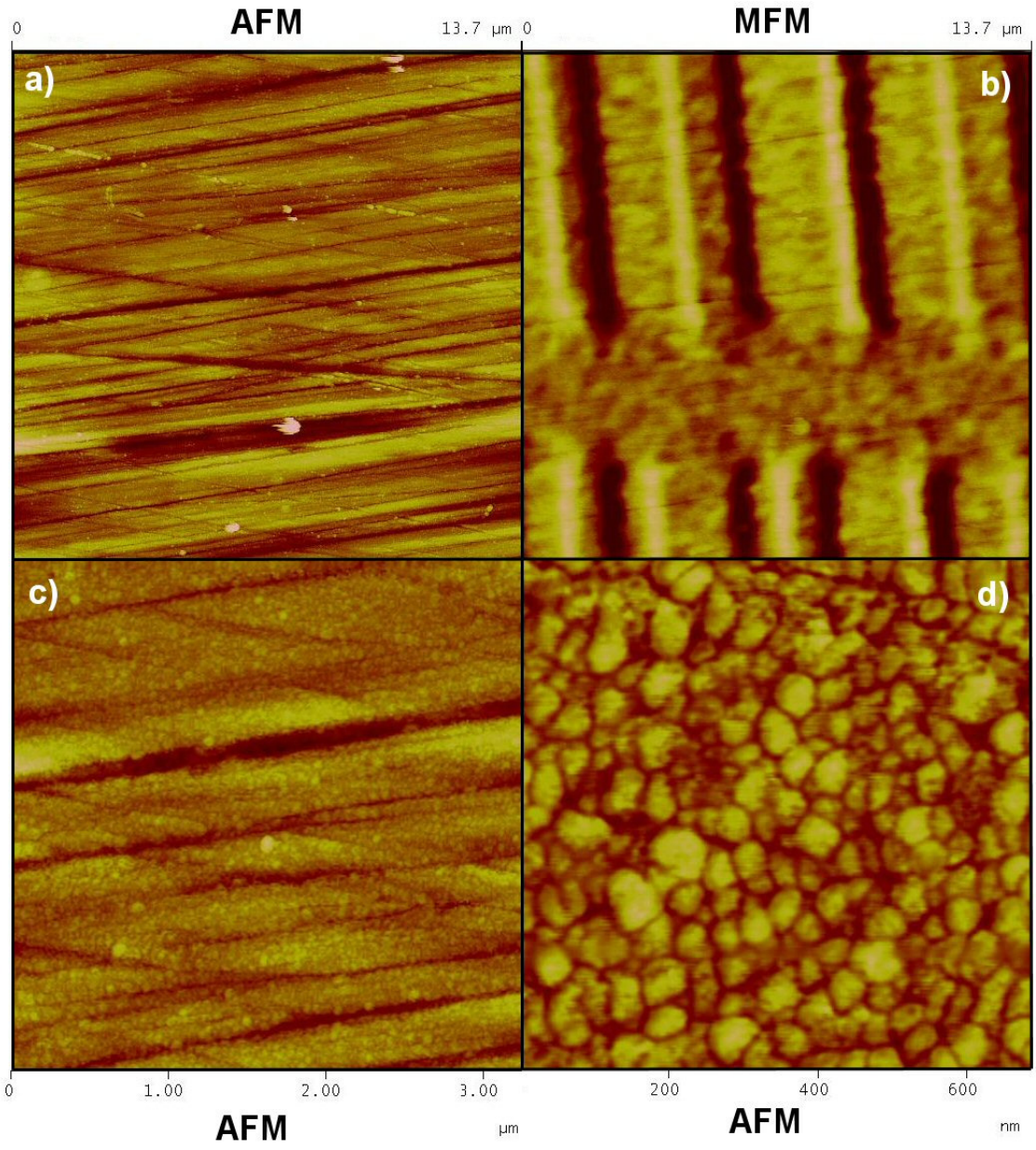

Figure 2.13: AFM and MFM micrographs of a conventional granular magnetic data storage media. The MFM data (image b)) shows discrete bits of magnetic data corresponding to binary information (light and dark contrast) – the bit *length* (*B*) is in fact the *short* side of a high contrast region whilst the bit *width* (*W*) is the *long* side since the HDD read / write head passes roughly horizontally across this area. Image a) shows the long-range, generally smooth nature of the magnetic media (vertical scale is 50nm) whilst the granular nature becomes more apparent as magnification is increased in images c) and d) (vertical scales of 40 and 10 nm respectively). The average surface feature size is approximately 30 nm.

Whilst the ultimate limit on density is governed by the grain size *i.e.* 1 bit of data per magnetic grain, to achieve an adequate signal-to-noise ratio (SNR) for reliable operation, the magnetization corresponding to 1 bit of information is averaged over

many grains, greatly reducing the media's data storage density. Thus each grain behaves as a single magnetic dipole, with the region of magnetization corresponding to 1 bit of information forming a larger single domain-like state comprised of many smaller grains. For example, 1 bit of information may be encoded in a total of 50 or more of the individual smallest surface features depicted in Figure 2.13.

The last generation of longitudinal media used an inductive write head (*i.e.* an electromagnet) to change the direction of magnetization of the grains. The write head had two poles (a write pole and a collector pole) which together with the magnetic media form a magnetic fringing field as depicted in Moser *et al.* [71]. Reading of the data was accomplished by a magneto resistance sensor[vi]. The read and the write head are separate entities but are in close proximity on an actuator arm within the HDD, hence are commonly referred to as a read / write head.

In order to keep the SNR constant, all dimensions of the media must be scaled accordingly, *i.e.* a reduction in the bit length (B), the "magnetic thickness" ($M_R t$), the grain radius (r_0) and the read and write head sizes (W_r). Zhou & Bertram [70] and Moser *et al.* [71] show that

$$\mathrm{SNR} \propto \frac{B^2 W_r}{\alpha^2 {r_0}^3 (1+\sigma^2)} \tag{2.47}$$

with $\alpha = {}^{a}/_{r_0}$. Here a is a transition parameter describing the noise associated with the change from one magnetization direction to another [72] and σ is the normalized grain size distribution. $M_R t$, a measure of magnetic flux, is a useful quantity derived in [71] which gives a relationship between the product of the remanence magnetization (M_R) of the film and its thickness (t) and will be useful in describing more complex systems. Reducing $M_R t$ reduces both a and r_0. Clearly from equation (2.47), reducing r_0 significantly improves the SNR. However, a strict limit on the lowest value for r_0 has already been described (equation (2.46)). In order to minimize r_0, it was proposed in the previous section that a media with a high anisotropy (K) be used. This can be achieved by using materials richer in Pt (*e.g.* FePt, CoPt) or RE compounds. The magnetic field required to switch the magnetization direction H_w is [71]

[vi] Within the magnetic media from which the sensor is fabricated there are two separate magnetic layers, a pinned layer and a free layer. Under the application of a magnetic field, the magnetization of the pinned layer remains fixed whilst that of the free layer rotates. The electrical resistance depends on the relative orientation of the two layers, therefore can be used as a probe to sense the direction of magnetization.

$$H_w \approx \frac{K}{M_S} \tag{2.48}$$

where M_S is the saturation magnetization. Therefore K cannot be arbitrarily increased, as the field required to switch the magnetization to write a bit of information to the media would become prohibitively large. Clearly increasing M_S helps reach a larger H_w, illustrating the distinct potential for exchange spring media as data storage elements due to the intrinsically large K *and* M_S.

By the turn of the century, the write head material in longitudinal media had been optimised with saturation magnetization values close to those of the media with the highest known M_S [73], thereby limiting the maximum achievable value of H_w. Improvements to the bit-length B by reducing the bit-aspect-ratio (BAR) also had improved SNR by this time, but at the expense of increasing the complexity of the read / write heads. As a stop-gap to these problems, longitudinal magnetic recording media saw two significant developments.

1. Oriented media where the grains no longer have a random distribution of easy axes throughout the media. This reduces what was before a free parameter, serving to lower the overall noise level of the media. In oriented media, all grains per bit contribute to the magnetic signal, whereas in standard media those grains with easy axes aligned perpendicular do not contribute to the signal yet still contribute to noise [71, 74]. The result is the reduction in grain size and bit length and therefore an increase in data storage density.
2. Antiferromagnetically coupled (AFC) media. In AFC media there is an effective magnetic thickness, $M_R t_{eff}$, given by the difference between $M_R t$ of the two AFC layers. At remanence the layers are AFC, so $M_R t_{eff}$ is greatly reduced (thereby reducing the field required to reverse the magnetization of the media), yet the large physical thickness of the structure leads to a high thermal stability. Careful control of the composition and thickness of the layers delivers the opportunity for precise control of the media's thermal stability and SNR characteristics.

Both oriented and AFC media benefit from requiring no changes in the read / write head design of the HDD and minimal changes in disk fabrication technologies.

It has been shown that novel alterations to longitudinal media allowed it to remain competitive for a long period of time. However, these alterations offered only a small increase in density, hence new technologies required development. The most

fundamental of these was the shift from magnetization *in* the plane of the media to magnetization *out* of the plane of the media.

2.7.3 Perpendicular media

The present media used for HDDs is *perpendicular* media, where the magnetization of the individual bits of information points *out* of the plane of the disk. Perpendicular recording was first demonstrated on a useful density scale (~50 GB in^{-2}) in 2000 by Takano *et al.* [75] and since approximately 2005 has gradually become the standard technology employed in HDDs. In short, it offers a reduction in the medias' aerial grain diameter by using thicker magnetic materials [76]. Dipole interactions between neighbouring bits of information are reduced since there are no longer head-to-head and tail-to-tail regions of magnetization, serving to increase the overall data storage density. The method of data storage utilised in perpendicular media is fundamentally the same as that used in longitudinal media, therefore aspects governing SNR in section 2.7.2 still apply. However a key difference between the two media lies in the method of writing. The perpendicular media cannot be used as part of the fringing field as for longitudinal media. To prevent stray fields from the write head which might erroneously switch surrounding grains, a soft under-layer (SUL) is incorporated into the media to act as a flux return mechanism. Reading is still accomplished by a magneto resistance (MR) type sensor employing either giant MR (GMR) [77] or tunnelling MR (TMR) [78] with the latter becoming the norm. Detailed images of this and the longitudinal read / write heads are given in a review by Moser *et al.* [71], whereas the SUL is discussed in depth in Richter [79].

Similar to longitudinal recording media, current perpendicular media is based upon Co. The first demonstration of perpendicular magnetic data storage used a granular media in the form of CoCrPt [75]. Granular media is an attractive technology due to the expertise in its deposition which has arisen from the fabrication techniques employed in longitudinal media. In order to promote the required magnetic easy axis out of plane of the material, various seed and growth layers are deposited to promote specific crystalline orientations and narrow grain size distributions, whilst reducing crystalline lattice mis-match in much the same way as the epitaxial films studied in this thesis are grown (see section 3.2). Current HDDs with granular perpendicular media have an average grain size of 8 nm [79]. Substantial and useful reviews of

perpendicular magnetic recording media can be found by Richter [79] and Piramanayagam [80].

2.7.4 Composite perpendicular media

Despite the clear advantage in data storage density achievable by using perpendicular granular media over longitudinal, it incurs a significant disadvantage in writability. Writing to highly anisotropic perpendicular granular media requires a large magnetic field from the write-head, a problem in itself since current write-heads already utilise some of the highest saturation magnetization materials [73]. This large write-field limits the potential data storage density due to stray fields emanating from the write-head. This is especially problematic in perpendicular granular media, which tends to switch magnetization direction at lower fields if the magnetic field is applied at an angle [81], which is exactly the case when bits of information are written from stray fields. The reduction in switching field (H_{SW}) when the field is applied at an angle has been explored in perpendicular granular media, with an easy axis of magnetization tilted to 45°. This is the optimal condition which reduces the required write-field to only half of that in the perpendicular granular media case (due to the exchange interaction) [55, 56]. Unfortunately, the fabrication of such media remains excessively complex and ultimately prohibitively costly [82]. Therefore it is desirable to design new types of magnetic media that are economically viable to fabricate, yet retain the desirable characteristics of the tilted media. These media are referred to as *composite* media. Composite media consists of two different magnetic layers with significantly different properties. One layer is a soft magnetic material and the other hard. Theoretical work by Victora & Shen [83] has shown that the magnetic properties of composite media should vary with the volume ratio of the two materials as well as the magnetization ratio, the exchange coupling and the anisotropy ratio.

In composite media, the soft layer magnetization is easily rotated by the application of a small magnetic field. Since the soft layer is exchange coupled to the hard layer, the rotation from the small applied field changes the angle of the exchange field applied to the hard layer. This in turn alters the angle of the effective field applied by the write-head. This reduces the field at which the magnetization of the hard layer switches [55], similar to tilted perpendicular granular media. The thermal stability of composite perpendicular media is commonly obtained by the Sharrock equation [84], which provides an estimation of a volume which must switch magnetization direction in

order to overcome a potential thermal energy barrier ΔE. It is essentially an extension to the Arrhenius-Néel equation (2.45), assuming a distribution of magnetic properties over a range of particles of differing volumes, providing a more reliable estimate on switching probability P. The ratio of this thermal stability to H_{SW} is given as [83]

$$\xi = \frac{2\Delta E}{H_{SW} M_S V} \tag{2.49}$$

with M_S the saturation magnetization. A value of $\xi = 1$ is given for typical perpendicular granular media where the write-field is aligned perfectly with the volume to be switched. A larger value of ξ means a higher thermal stability and small H_{SW} for a given value of M_S and V. For 45° tilted perpendicular granular media, $\xi = 2$, which gives half the value of H_{SW} for a given thermal stability. Wang *et al.* [57] find that their composite system gives $\xi = 1.5$ which, whilst not as high as for the 45° tilted media, is a significant improvement over the standard perpendicular granular media. Thus they demonstrate a composite media with high anisotropy from the hard layer (and therefore the potential for small magnetic grains and high data storage density) with good thermal stability, which can still be written to using an easily attainable H_{SW}.

Further positive benefits of composite media have also been realised. Both Victora & Shen [83] and Suess *et al.* [85] show in their theoretical papers that the switching of composite media is substantially more tolerant to variations in easy axis orientation than granular perpendicular media. This is demonstrated experimentally in Wang *et al.* [57] and Takahashi *et al.* [86]. The outcome of this is that unlike in granular perpendicular media where a small deviation in angle (± 10°) between the applied field and the easy axis results in a *reduction* in H_{SW} by a factor of 0.68 [81], in composite media this deviation actually gives almost *no change* in H_{SW} (a factor of 1.01). A large deviation in angle ($\gtrsim$ 50°) leads to a significant *increase* in H_{SW} (a factor of $\gtrsim$ 1.5) [83, 85], as shown experimentally in FePt multilayer structures by Takahashi *et al.* [86]. This results in a major reduction in erroneously written bits of information on adjacent tracks thus improving the SNR, reducing the bit size and permitting an increase in data storage density. Further interesting experimental work regarding composite media may be found in Okamoto *et al.* [87] and Suess [88]. The latter shows that the coercivity of the media is inversely proportional to the number of repeats of a multilayer system whilst the thermal energy barrier remains constant. This strongly suggests that materials such as the exchange coupled multilayer $DyFe_2$ / YFe_2 systems investigated in this thesis are excellent candidates for magnetic data storage media.

There are however clear limits to perpendicular granular and composite media since the grain sizes cannot be made infinitely small. Already novel designs in media have been introduced to compensate for this, so efforts are intensely focussed on new methods to increase data storage density. Of greatest importance is the use of patterned media which will be discussed in the following dedicated sections (2.7.5 and 2.7.6), but two other emerging technologies should be noted. These are heat assisted magnetic recording (HAMR) and microwave assisted magnetic recording (MAMR). HAMR employs local heating of the media over time periods of order of the write-time to momentarily reduce the anisotropy, write the information with a small magnetic field, and then return the media to the original thermal stability level [89]. Recent work by Şendur & Challener [90] combines patterned media and HAMR, where the isolation of the patterned bits not only helps localise the write-field, but also the dissipation of heat. MAMR uses the phenomenon of ferromagnetic resonance, applied over nano-second timescales to assist in the precession of the rotation of spins to aid magnetic switching by using energy gained from the AC microwave field to reduce the effective H_{SW} [91].

It is without doubt that both technologies are novel and potentially promising candidates to improve data storage density. However, at the present time both require the implementation of significantly different manufacturing techniques from the current technology. The implementation of composite media over tilted media has already been welcomed due to the similarities in the media growth techniques, thus at present the use of HAMR and MAMR outside of laboratory demonstrations looks unlikely. New technologies focussing on patterned magnetic media avoid some of these issues since perpendicular media similar to that which already exists are used. But this is in conjunction with some very different technologies which give rise to their own problems, for example the method by which an individual bit of patterned data may be addressed, thus the path toward patterned media still requires significant development.

2.7.5 Discrete Track Media

In conventional magnetic media, whether it be longitudinal or perpendicular, antiferromagnetically coupled or composite in nature, the bit length (B) and width (W) are always defined by the write-field from the read / write head. The read / write head traverses many individual tracks on the platter, which are located using pre-written servo masks. Due to the nature of the arc subtended by the head as it traverses the platter and the mechanical misplacement it encounters in doing so, there is a finite

element of misalignment between the head and the bit on the platter being addressed. Ever increasing data storage densities require successive reductions in bit dimensions and read / write head widths. However, maintaining a suitably high and suitably localized magnetic field to switch even the composite media becomes problematic as track widths of < 50 nm are reached (required for 1 Tb in^{-2}) [92]. Physically defining the track positions on the platters, a technology known as "discrete track media" (DTM) will change the read / write head positioning from purely mechanical to a more accurate, lithographically defined method, but it does still require some physical means of placing the head on the track.

Lithographically defined tracks of magnetic media result in reduced noise since the read / write head is essentially positioned more accurately. Accordingly, Soeno *et al.* [93] showed that DTM results in less erroneous read / writes from stray head fields (adjacent track erasure) which is a major problem in perpendicular granular media as already discussed. The media used in DTM is very similar to the thin film media already discussed, except clearly there are non-magnetic regions between adjacent tracks. This has the benefit of increasing the relative dimensions of the write head (*i.e.* can be larger than the track width) which improves SNR as demonstrated in Roddick *et al.* [94]. Numerical simulations by Soeno *et al.* [93] also demonstrate this effect; they show that the magnetic flux from the write head is significantly more concentrated in the DTM than the bulk media, *i.e.* there is less circulation of the flux. This is explained by a difference in permeability of the material surrounding a bit of information in the two instances.

There are however issues regarding the fabrication of DTM. Whilst lithographically patterning small, laboratory scale samples is perfectly achievable, the alignment required to pattern *both* sides of a complete 3 ½ in platter at a scale of better than 50 nm is non-trivial. Moreover the step to lithographically defined media requires a great deal of manufacturing implementations. This significantly reduces throughput by introducing many more complex steps in fabrication. Clearly this will have a detrimental effect on costs, but in a similar vein to perpendicular granular media, this may be absorbed if overall production is great enough. Other technical obstacles include planarization of the disk and protection against corrosion at the edges of the patterned media. The disk surface needs to be smooth on the scale of one nm since the read / write head fly-height is as small as 10 nm in current media. Soeno *et al.* [95] have successfully demonstrated a fly-height of 20 nm on DTM. Planarization of the

disk surface is clearly still in its infancy and requires significant development, but other routes to patterned media which do not require planarization are being developed. These will be covered in Chapter 5 where their potential benefits to simplifying the fabrication process will be discussed and demonstrated in light of the author's experimental results.

2.7.6 Bit Patterned Media

It has already been shown in the case of granular media, that in order to increase the density of data storage, the volume per bit (V) must be reduced. Without advances in signal processing, this would require the number of individual grains making up V to remain approximately constant to retain a satisfactory SNR. Overall, this has resulted in the introduction of high anisotropy (K) materials since the product KV must remain constant to avoid reaching superparamagnetism where the ratio $\frac{KV}{k_BT}$ becomes too small. Even considering the recent significant advances in composite perpendicular media and the potential of DTM, there will be a limit reached whereby the data storage density cannot feasibly be increased further. New technologies must be therefore explored and prototype devices fabricated. Bit patterned media (BPM), where the idea of one "magnetic island" for one bit of information rather than an ensemble of grains is a likely candidate to advance data storage density. Since the number of magnetic islands is reduced to just one, the SNR considerations in BPM are completely different to granular and DTM – there is no statistical averaging over many magnetic grains in order to increase the SNR. Since the volume of magnetization to be switched is now equal to the individual bit size, each bit can occupy a significantly smaller *total* volume whilst still remaining thermally stable, *e.g.* one 10 nm magnetic island rather than one hundred 10 nm magnetic grains.

To realise BPM, the orientation of the anisotropy axis of each magnetic island – or bit – with the read / write head needs to be identical. To achieve this using longitudinal media would require *circumferential* alignment of the magnetic easy axes of the bits, something which has never been demonstrated. Far simpler is the use of perpendicular media whereby alignment of the easy axis of magnetization is out of the plane of the disk. It is also important to note that for the flux return mechanism to function correctly, the SUL will need to remain continuous within the BPM, therefore only the magnetic layers on top of this will require patterning. Very similar fabrication

techniques have been successfully demonstrated in this work and are described in Chapter 6.

Naturally with BPM the same economic considerations apply as with the introduction of perpendicular granular, composite and DTM. However, it has already been demonstrated that perpendicular granular media has led the way to composite perpendicular media, and similar trends are expected for the introduction of DTM. Therefore combining the novel materials used in composite perpendicular media with the extension of the fabrication technologies employed in DTM should lead to the eventual economic viability of BPM. Unfortunately, although only one magnetic island is required for one bit of information, the dimensions of this island are incredibly small, beyond present lithography limits when one considers densities over 1 Tbit in^{-2} (see Table 2.1, Khoury & Ferry [96] and Vieu *et al.* [97]). In order to maximise the smallest lithographically defined feature on BPM, it is beneficial to change the bit aspect ratio (BAR) to 1, unlike in current media where it is much larger, typically 6 (for example, see Figure 2.13). Obviously this will be at the expense of read / write head design, but as detailed when describing DTM, lithographical patterning of the platters helps increase the tolerances on the head since the individual bits are superimposed on a non-magnetic background. It is also possible to preferentially align the individual magnetic islands in BPM to ensure that their entire volume is beneath the head, unlike in continuous media and DTM.

Density (bit in-2)	**Bit size (BAR = 1) (nm)**
5 T	5.5
1 T	12
500 G	17
100 G	40
10 G	125
1 G	400

Table 2.1: Approximate bit sizes (assuming a square bit (BAR = 1) and equal bit spacing) required to meet data storage density targets using BPM.

Whilst the bit sizes detailed in Table 2.1 are at (and in the case of > 1 Tb in^{-2}, beyond) current lithographical limitations, this need not pose a significant problem. It is a logical step to look to the International Technology Roadmap for Semiconductors (ITRS) [98] (used to predict lithographic resolutions in the semiconducting industry) to provide a guide towards when the appropriate lithographic resolution will be available.

The 2008 ITRS suggests that a "DRAM half-pitch" (analogous to the bit size detailed in Table 2.1) will not reach 17 nm until 2018, moreover not reaching 12 nm until 2021! This is significantly later than the projected date of 2014 for reaching 1 Tb in^{-2} magnetic data recording densities [99]. However, it is important to realise that the lithographic requirements of the semiconductor industry involved in fabricating computer memory, processors and solid state drives are significantly more severe than those required to produce BPM. The current lithographic records [96, 97], where the structures fabricated more closely resemble BPM than semiconductor devices, provide a more accurate guide towards the data storage densities which could be met, rather than simply following the ITRS.

It was noted in section 2.7.5 that the requirements of the magnetic materials used in DTM were similar to those already in use on perpendicular granular bulk media. The requirements for BPM are different and sometimes more stringent [99]. BPM must always maintain a single domain remnant state *i.e.* obey the Stoner-Wohlfarth model described in section 2.6. Media below a certain critical size (see section 2.6.4 and equation (2.46)) should automatically favour a single domain remnant state, where the energy required to create a domain wall is greater than the reduction in energy associated with the formation of a multi-domain state. However, it is commonly evidenced that magnetic islands with dimensions of the order ~ 100 nm and below exhibit single domain properties in BPM [99, 100] (the exact value being dependent on the magnetic media in question), with all of the constituent grains behaving as one larger, single domain. BPM must also have an even smaller switching field distribution (SFD) than current granular media. This is a direct result of losing the averaging performed in the granular media. In granular media, non-uniformities on the nm scale result in a small continuous SFD, whilst in BPM these non-uniformities result in discrete bit-to-bit variations in the SFD. Obtaining a small SFD has proved troublesome and is the subject of much research in both granular and BPM. A small SFD is a key parameter in obtaining good device performance by reducing the effect the write-field has on neighbouring magnetic islands [101, 102, 103, 104, 105, 106]. Finally, all elements of the BPM must be as close to identical in size and shape as possible and have a high degree of exchange coupling. Whilst using a technology of 1 bit per magnetic island will eliminate traditional "jitter", that is the noise due to grain irregularities, it will in turn introduce lithographic jitter (also referred to as lithographic noise). This is a direct result of lithographic irregularities [107]. It is independent of

the number of magnetic islands in the media [108] since they are independent elements. Assuming a 5 – 10% jitter in centre-to-centre spacing or island size, the chances of mis-reading or writing a bit increase by one order of magnitude [109, 110], a fact which is especially alarming when studying Table 2.1 – a 5% error in 500 GB in^{-2} media corresponds to a lithographic tolerance of just 850 pm!

Referring to a key consideration regarding the increase in data storage density in longitudinal granular media, the concept of an effective magnetic thickness ($M_R t_{eff}$) was introduced. The value of $M_R t_{eff}$ was significantly smaller for AFC media than the value of $M_R t$ for standard media. Piramanayagam *et al.* [111] have extended the concept of patterned composite media to include AFC composite media using similar arguments. The authors show that the large SFD is due in part to a large demagnetizing field (they use closely spaced bits to further improve data storage densities), which in turn is determined by a large M_R. Thus reducing M_R reduces the SFD but without reducing the saturation magnetization due to the AFC (for example, see the hysteresis loop in Figure 2.10), therefore avoiding the associated increase in H_C from equation (2.48).

A further noteworthy point is that lithography is not the only route to the fabrication of bit patterned media. Many different polymer-based self-assembly methods are the subject of intense research. A useful, detailed review can be found in Terris & Thomson [99], whilst Yang *et al.* [112] have recently reviewed one of the most promising self-assembly methods in comparison with lithographic techniques. However, these self assembly methods are by no means applicable to the fabrication of BPM from the samples studied in this thesis. That, coupled with the author's view that they present even more significant challenges for mass-scale fabrication than lithographical processes, means that these fabrication processes will be discussed no further in this work.

2.7.7 Concluding remarks on magnetic data storage

Within recent years there have been significant advances in the media used for magnetic data storage. Of these, the most significant is undoubtedly the transition from longitudinal to perpendicular media, a topic which is extensively reviewed in Moser *et al.* [71] and Richter [79]. Also of significant note is the introduction of the GMR read-head [113, 114] and the implementation of composite granular media [83]. The common goal of all of these advances has been to increase the data storage density of HDDs whilst maintaining their competitive cost within a closely fought market.

Whilst there are certainly obstacles to be overcome with regard to the implementation of patterned media, the current composite granular media is again rapidly approaching the superparamagnetic limit, therefore it is of great relevance and interest to focus research efforts onto patterned magnetic data storage. This is expected to be especially fruitful when exploited in conjunction with many of the recent advances in composite exchange coupled media, especially considering the benefits highlighted with AFC media. The $DyFe_2$ / YFe_2 AFC exchange spring systems studied in this work provide an excellent model system. Thus the essence of this thesis is to explore the fundamental magnetic properties of such materials when their dimensions are artificially structured. This can be achieved by using "traditional" lithographical patterning techniques, or by the novel process of energetic ion implantation, whereby the internal crystalline structure is directly modified on the atomic scale.

2.8 Interactions between Energetic Ions and Target Materials

From the point of magnetic data storage there is significant interest in developing both discrete track and bit patterned media with the aim of improving HDD data storage density. One possible route is via the post-patterning of high quality films, grown by sputtering or molecular beam epitaxy. Patterned arrays are transferred to the media using ion milling as a tool to remove material from selected areas only, providing physical changes to the external dimensions of the media. This is covered in sections 3.6.3 – 3.6.6.

Assuming elastic collisions between the incident energetic Ar^+ ion and the target material, if an ion imparts enough energy (K) to a surface atom (bound to the surface with some energy (E_b)), then if $K > E_b$ the recoiling atom would be removed from the surface. Thus if the sample is bombarded by enough ions with energy $\geq K$, the target will be gradually milled away [115], hence the terminology "ion milling". However, if $K < E_b$ all of the ion's energy is absorbed by the target material. This simplistic view was shown to be inadequate to fully describe the interaction between an energetic ion and a target material [116], but it immediately begs the question of what physically happens when $K < E_b$. Clearly there will be changes in the *internal* crystalline structure of the target material as it accommodates these implanted ions, even though this may not be immediately apparent in the topological characteristics of the sample in

question. However it does offer a second method by which to change the magnetic properties of the media by altering its internal rather than its external structure. Throughout the literature this process is largely referred to as "ion implantation". The rather broad title of "ion implantation" will be broken into two sub-categories in this thesis. The first is *ion irradiation*, which will be used to discuss processes where the energetic ions simply pass *through* the magnetic media. The second is *ion implantation*, which will be used exclusively to define processes where the ions pass into *and* are *stopped within* the magnetic media.

This section describes both ion irradiation and ion implantation, providing a brief literature overview to familiarise the reader with what is likely a new topic. Computational modelling is used extensively throughout in order to offer further insight into the interactions between energetic ions and the target material. The details contained within this section are invaluable to interpreting Chapter 5 where the effects of energetic Ar^+ ions implanted into a range of $REFe_2$ materials are presented and discussed.

2.8.1 Modelling the interactions between ions and solids

Throughout this thesis the Monte Carlo-based `SRIM` software package [117] has been used to model the effects between ions and target material. Specifically, the `TRIM` code (transport of ions in matter) has been used, which itself forms part of the overall `SRIM` package. `SRIM` allows the modelling of the effect of any ion incident on any solid target through a complete range of angles from normal through to grazing incidence. The incident ion energy can span many orders of magnitude, from approximately 100 eV through to several GeV. Furthermore, the target material can be relatively complex, allowing for the use of multilayer materials and alloys *etc.* For example a $DyFe_2$ / YFe_2 sample with 40 repeats of 2 / 8 nm thick individual layers can be modelled, as well as a complex mask material such as PMMA ($C_5O_2H_8$). Densities can be calculated or manually input and "compound corrections" applied. A correction is necessary for compounds comprised of light elements ($Z \lesssim 13$) (with Z the atomic number) where the

stopping power differs from that of purely elemental matter[vii]. SRIM calculates the incident ion depth distribution throughout the target in 3D, as well as following any resultant cascade effects. Other kinetic phenomenon associated with ion energy losses are also computed, including the number of backscattered ions and sputtered atoms (and their associated energies) as well as further energy losses due to ionization, vacancy creation and phonon production.

SRIM provides a very powerful means of calculating ion interactions within a target (solid, gas and liquid targets are possible), but unfortunately there are some limitations to its capabilities. Whilst complex targets can be modelled, they must be amorphous. There have been reports of "channelling" of implanted ions in single crystal structures [115,118, 119, 120]. Here, incident ions that are approximately parallel to crystalline planes experience additional interatomic forces, causing them to execute oscilliatory motion as they propagate through the lattice [121]. This reduces the number of collisions between the ions and atoms thereby reducing sputtering yields [122], but increasing implantation depth and associated damage. This is likely to be relevant for the materials studied throughout this work since they are single crystal structures. SRIM also assumes that each ion interacts with the solid in its virgin state, neglecting any material that may have already been implanted with ions. Accordingly changes to the crystalline quality of the film due to ion implantation cannot be modelled. In general it is acceptable to neglect such effects when considering light ions [123] (such as Ar^+ used throughout this work). This is especially apparent when considering the fact that the sample is continuously rotated which significantly reduces the effect of channelling (since the incident ions are very rarely exactly parallel to atomic planes) thereby increasing sputtering yield and reducing ion implantation damage.

2.8.2 Ion irradiation

The first report of ion irradiation used to directly modify magnetic properties in well defined locations was by Chappert *et al.* [124] who, in 1998, irradiated Pt / Co / Pt

---

[vii] In a compound the outer electrons, which are responsible for absorbing much of the incident ion energy, have different orbitals to the corresponding elemental matter. The compound correction separates the stopping contributions from the bonding and core electrons and is automatically applied to common materials such as PMMA by the SRIM software.

"sandwiches" and Pt / Co multilayers with 30 keV He^+ ions. These samples are characterized by a perpendicular magnetic anisotropy. This anisotropy can be rotated into the plane of the material by varying amounts due to He^+ ion irradiation over a range of fluences (10^{15} – 10^{16} ions cm^{-2}). In section 2.3 it was shown that the magnetic anisotropy of a material is directly related to an asymmetrical atomic environment, the source of which can be described as being due to shape, crystalline or elastic anisotropies, or a combination thereof. This concept can be extended further to include what is commonly referred to within the literature as "interfacial anisotropy". At the interface between the layers of two different materials the local environment experienced by the surface atoms is altered. This may, for example, locally modify the crystal field interactions, leading to a significantly different magnetic response. In a system constructed from very thin layers these surface atoms will constitute a considerable proportion of the material and thus this altered anisotropy at the interface may become dominant. In the Pt / Co layers (with a thin Co layer) this interfacial anisotropy is great enough to overcome the magnetostatic anisotropy (which usually acts to keep the magnetization *in* the film plane), causing the magnetization to point *out* of the plane. By irradiating these samples with He^+ ions, Chappert *et al.* [124] were able to reduce this interfacial anisotropy by mixing the layers together. The less abrupt the interface between the Pt and Co layers, the lower the interfacial anisotropy [125, 126]. Similar results were obtained by the same researchers using much more massive Ga^+ ions [127]. The bulk of research, regarding modifications to magnetic materials by high energy ions, has been carried out on similar, thin, perpendicularly magnetized films. However, much of the underlying physics in these samples is analogous to that in samples with in-plane, or near in-plane magnetization such as those studied in this thesis.

Irradiation of Pt / Co multilayers and Pt / Co / Pt sandwiches by high energy ($\gtrsim$ 10 keV) He^+ ions has been shown to be ballistic in nature [128] with correspondingly few atomic cascades. Due to the dissimilar masses between the tightly bound target atoms and the incident ions, the atoms recoil almost exclusively by only one lattice constant or less. As a result there is no overall change to the underlying crystalline structure of the material. Since displacements are confined so rigidly, in general the only rearrangements to the material's structure can be the substitution of Pt by another Pt atom, Co by another Co, Pt by a Co and Co by a Pt. Thus there is no change in the material's topography and no ions are implanted in the magnetic layers, travelling

through them and into the substrate [124, 129]. Devolder [130] has shown that for low fluences ($< 5 \times 10^{16}$ ions cm^{-2}) ion irradiation is responsible for relaxing strain in the films, whilst higher fluences cause intermixing of the layers in a Pt / Co / Pt structure. This intermixing may be seen later in Figure 2.14, showing the author's SRIM modelling of this Pt / Co / Pt structure after implantation by 30 keV He^+ ions.

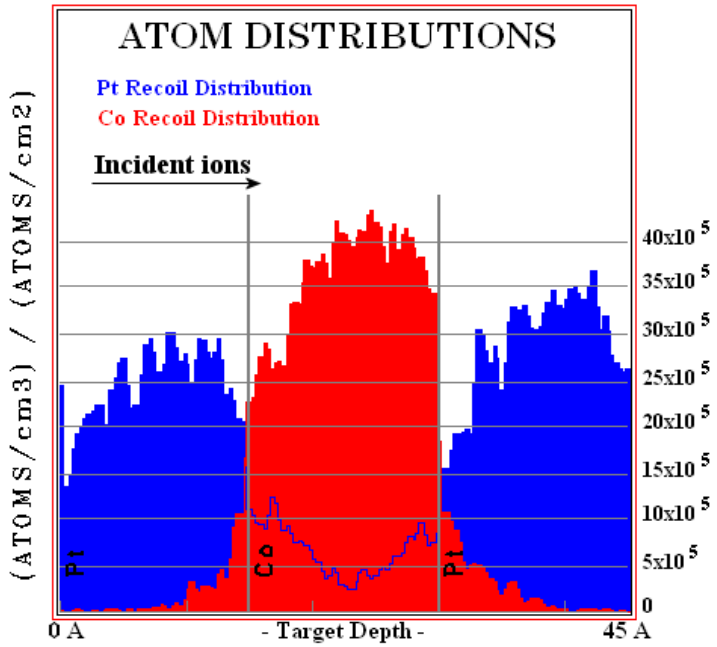

Figure 2.14: SRIM modelling showing the distribution of recoiled Pt and Co atoms in a sandwich structure after irradiation by 30 keV He^+ ions. The area under the blue lines within the red regions (*i.e.* Pt atoms recoiling into Co lattice sites) is greater than the areas of red within the blue regions (*i.e.* Co atoms recoiling into Pt lattice sites) hence the formation of a Pt rich structure within the Co layers.

Figure 2.14 shows that the penetration depth of Pt into Co is greater than Co into Pt since the path of Co in Pt is smaller than that of Pt in Co. This intermixing-induced change to the structural anisotropy of the material induces a change from magnetization perpendicular to the plane of the film to magnetization parallel to the plane. Intermixing at the interface between two different films is also shown in Figure 2.15.

In passing it is worthwhile noting that there was a small reduction in the Kerr rotation angle in the He^+ ion implanted Pt / Co / Pt sandwich structures [131]. This is characteristic of Pt rich, disordered films [130], confirming the intermixing of the layers. This was accompanied by a reduction in Curie temperature (T_C) [129]. At very high fluences the sample became paramagnetic at room temperature. This reduction in T_C becomes more pronounced for sandwiched structures with thinner Co layers since more intermixing of the layers occurs. This alters both the spin-orbit interaction and the exchange integral thus inducing a change in the magnetic anisotropy [129]. On the

contrary, multilayer structures of Pt / Co irradiated by N^+ ions show an increase in Kerr rotation angles and correspondingly no reduction in T_C [132]. This is attributed to alloying of the sample occurring at higher fluences ($\sim 2 \times 10^{16}$ ions cm^{-2}) (see Figure 2.15). Indeed, the corresponding PtCo alloy is well known for increased magneto-optical activity [133]. Ion irradiation has also been studied in Cu / Ni / Cu sandwich structures [134]. This was achieved using very high energy (1 MeV) C^+ ions. With reference to sections 2.3.4 & 3.2.2, and the early work by Lee *et al.* [135], the degree of perpendicular anisotropy in Cu / Ni / Cu films is shown to be constant over a large range of Ni layer thicknesses. It is strongly dependent on the magnetoelastic anisotropy energy associated with the strain in the Ni layer, due to the mis-fit between the Cu and Ni lattices [136, 137]. Further research regarding C^+ ion implantation into these films [138] has shown that the dominant change in anisotropy energy was in fact a reduction in the interfacial anisotropy. This is analogous to the intermixing of layers in Pt / Co systems as described earlier. A final noteworthy point is the observation of both an increase in the interfacial roughness between the Ni and Cu *and* an increase in the sharpness of the boundary between the two elements after 1 MeV C^+ ion irradiation [134]. This can be explained in terms of the heat of mixing associated with the reaction[viii]. The Cu / Ni system has a positive heat of mixing (endothermic reaction) resulting in a de-mixing process causing the atomic planes to be separated out. But for the Pt / Co system, which possesses a negative heat of mixing (exothermic reaction), the reverse is true and an inter-mixed layer is created between the multilayers. These two systems are illustrated in Figure 2.15. Further useful discussions regarding the effect of ion irradiation and heat of mixing can be found in Veres *et al.* [139].

[viii] Heat of mixing, often referred to as heat of formation or enthalpy of formation, describes the change in enthalpy when one product is formed from its constituent elements, *i.e.* it is equal to the change in internal energy of the system plus the work done on that system to form the product.

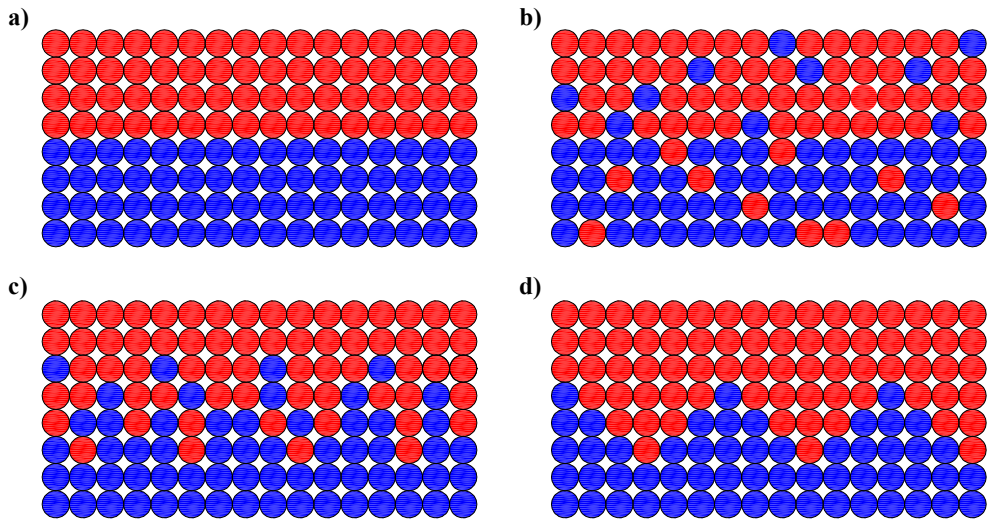

Figure 2.15: Schematic diagram showing different mixing occurring at an atomic interface. Image a) shows the interface of a bi-layer in its as-deposited state. Image b) shows an alloy interface where the respective atoms have been displaced by large distances. Image c) shows the rough interface which results from ion irradiation of a sample with positive heat of formation (*e.g.* Pt / Co) whilst image d) shows the atomically sharp "rough" interface which forms from ion irradiation of a sample with negative heat of formation (*e.g.* Cu / Ni).

2.8.3 Ion implantation

As the energy and / or atomic number (Z) of ions is increased, the induced damage to the target surface is magnified, often leading to significant changes to the material's internal crystalline structural. Terris *et al.* [140, 141] irradiated Pt / Co multilayers and $L1_0$ ordered Fe / Pt superlattices with 2.3 MeV He^+, 700 keV N^+ and 1.2 MeV Ar^+ ions. Every experiment showed similar effects; a significant reduction in coercivity at a well defined ion dose, plus a rotation from an out of plane to an in plane easy axis of magnetization. The authors noted that there were also topographical changes to the material, most specifically an increase in surface roughness. Given the very high energy ions used, the authors attribute the topographical changes to swelling or compression of the substrate due to the large amount of incident ion energy deposited within this region. Within the substrate the ions experience elastic collisions with the target atoms and are said to be *implanted* within this region. The ions have passed through the magnetic film, only *irradiating* it [142].

When ions are *implanted* into a material they deposit *all* of their energy to the surrounding atoms as they are retarded. As the ions pass quickly and completely through the thin metallic layers they impart only a small proportion of their kinetic energy to these metallic materials, causing them to be displaced by typically only one atomic site (see section 2.8.2). Within the much thicker substrate this effect is

magnified many times. As the ions continue to slow down they undergo many successive collisions with atoms, resulting in many changes of trajectory due to the dissimilar masses involved. Thus the damage due to high energy ions is far from localised. Accordingly, when considering the ion bombardment throughout the *entire* sample's thickness, the motion of the ions is only ballistic towards the upper surface (through which it entered), becoming more and more diffuse as it penetrates further into the sample. This is illustrated in Figure 2.16 for Al_2O_3, where ion trajectories can clearly be seen to be ballistic towards the left (top of the substrate), gradually becoming more diffuse as they penetrate deeper. Figure 2.17 shows the corresponding atomic recoil events, showing typically very small atomic displacements. For comparison, polymethylmethacrylate (PMMA) can be seen in Figure 2.18 and Figure 2.19. Here the atoms are much less tightly bound with a significantly reduced average Z, the result of which is many atomic displacements by multiple lattice constants (note the increased scale of the graph). Note that, for visual clarity, only 250 incident ions are shown, but for the numerical calculations and modelling, simulations were performed with tens of thousands of incident ions to improve statistics.

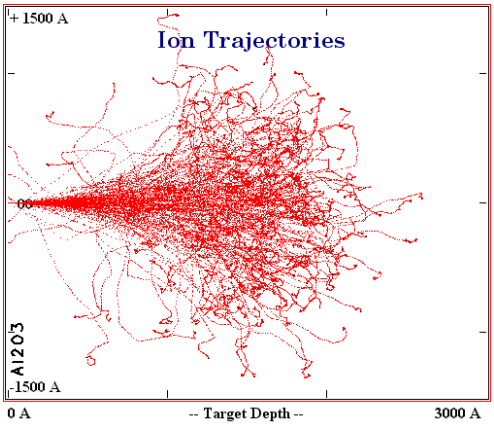

Figure 2.16: SRIM calculation showing 30 keV He^+ ion penetration into a 300 nm sapphire (Al_2O_3) substrate.

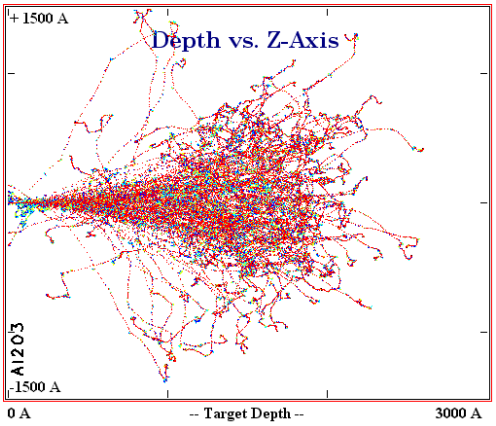

Figure 2.17: SRIM calculation showing atomic recoils associated with Figure 2.16; stopped and moving Al atoms are represented by yellow and green whilst stopped and moving O atoms are represented by blue and cyan respectively.

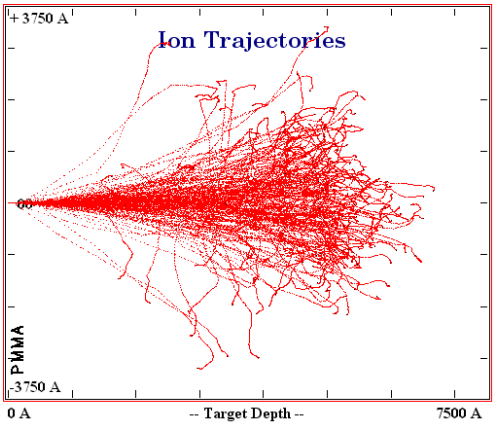

Figure 2.18: SRIM calculation showing 30 keV He^+ ion penetration into 750 nm of PMMA.

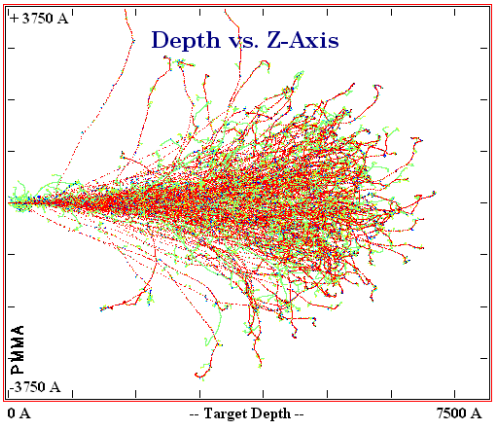

Figure 2.19: SRIM calculation showing atomic recoils associated with Figure 2.18; stopped and moving H atoms are represented by yellow and green, stopped and moving C atoms by blue and cyan and stopped and moving O atoms by dark blue and black respectively.

Combining the work of Terris *et al.* [140] and the SRIM modelling above, significant structural changes can clearly occur within the target material when energetic ions are *implanted*. Over such a large scale this may well induce a change in implanted materials' dimensions. In the case of the work by Terris *et al.* [140, 141] and Chappert *et al.* [124, 129, 131, 143] where high energy ions are implanted into the substrate (only irradiating the metallic layers on top of this), this will induce a stress / strain in the metallic material deposited onto the substrate by creating a lattice mismatch. In the work of Terris *et al.*, where ions of higher energy and larger *Z* were

used, this effect was significantly more pronounced as evidenced by an enlarged surface roughness [140].

SRIM calculations showing the dependence of ion penetration depth and recoil collisions on ion energy can be seen in Figure 2.20 through to Figure 2.23, whilst Figure 2.24 through to Figure 2.27 illustrates this dependence on ion species. All of the data are shown for the present example of a Pt / Co / Pt sandwich structure.

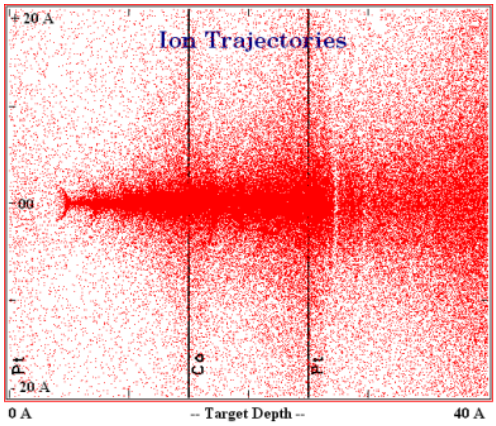

Figure 2.20: 3 keV He^+ ions incident on a Pt / Co / Pt sample. At 3 keV, the straggling of the ions is very pronounced and their propagation through the sample is diffuse.

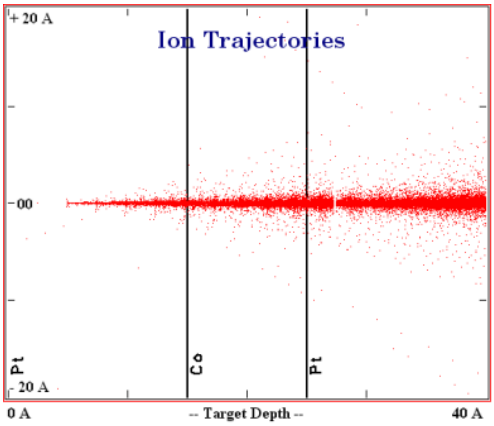

Figure 2.21: 300 keV He^+ ions incident on the same sample. At higher energies, the incident ions suffer less strtaggling and experience a more ballistic motion through the sample.

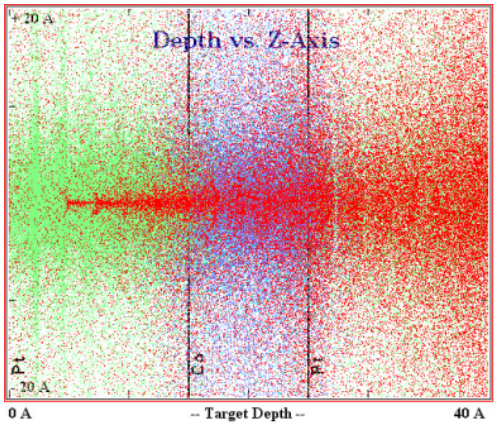

Figure 2.22: Recoil collisions due to 3 keV He^+ ions incident on the Pt / Co / Pt sample. Due to the diffuse nature of the motion of the ion (Figure 2.20), there are many recoil collisions. Red represents the He^+ ions and Green and blue represent recoiled Pt and Co atoms respectively.

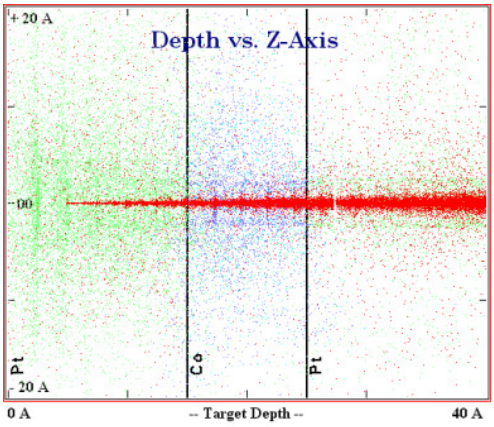

Figure 2.23: Recoil collisions due to 300 keV He^+ ions incident on the same sample. Due to the ballistic motion of the ion through the sample (Figure 2.21), there are fewer recoil collisions. Same colour convention as Figure 2.22.

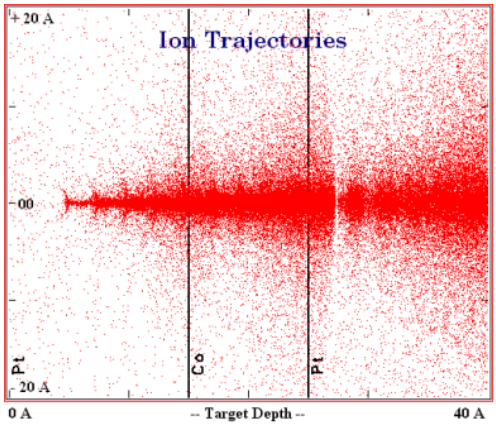

Figure 2.24: 30 keV N^+ ions incident on a Pt / Co / Pt sample.

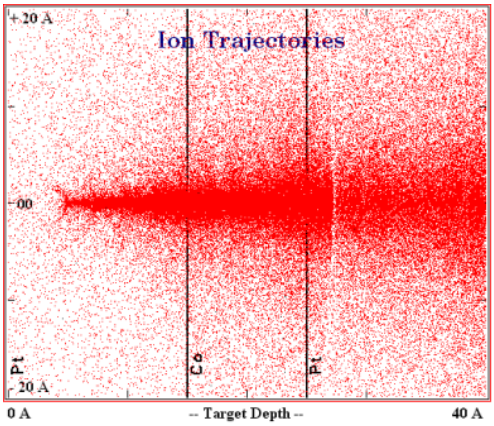

Figure 2.25: 30 keV Ar^+ ions incident on the same sample. Clearly as the atomic number of the incident ions increases the path of the ion becomes more impeded. This leads to a broader ion distribution.

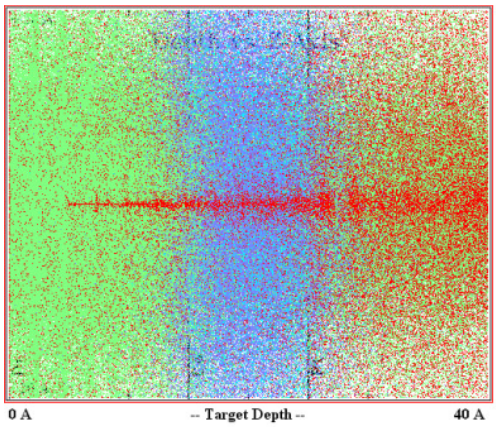

Figure 2.26: Recoil collisions for 30 keV N^+ ions incident on the Pt / Co / Pt sample. Again, red represents the ions and Green and blue represent recoiled Pt and Co atoms respectively.

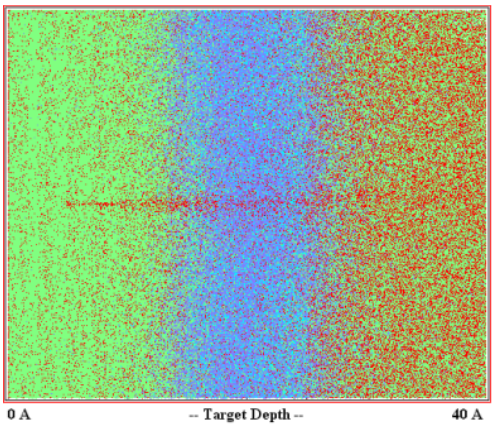

Figure 2.27: Recoil collisions for 30 keV Ar^+ ions incident on the same sample. Due to the broader distribution of incident ions, more disorder is induced within the sample leading to a greater number of recoil collisions. Same colour convention as Figure 2.26

From Figure 2.20 through to Figure 2.23 it is clear that as the incident ion energy is increased, the ions penetrate further into the film. Figure 2.24 through to Figure 2.27 shows that as the masses of the incident ions are increased, the ions penetrate less distance into the film. Therefore the use of lower energy ions and / or a heavier ion species results in the energy being deposited wholly within the film, rather than within the substrate. Consequently structural changes to the crystalline structure of the film itself can be expected. For the samples studied in this thesis this is indeed the case; Ar^+ ions with energy in the keV range are used. These Ar^+ ions penetrate a very small distance into the $REFe_2$ samples, typically only 10 nm. The penetration depth is derived

from SRIM calculations, example outputs from which are shown in Figure 2.28 and Figure 2.29. Since all of the samples studied in this work have a thickness greater than 10 nm, the Ar^+ ions are always *implanted* into the metallic layers, losing *all* of their energy within these layers and transmitting *nothing* to the Al_2O_3 substrate. The majority of the Ar^+ ion transport within the sample is clearly diffuse, resulting in the aforementioned elastic collisions between the Ar^+ ions and the target atoms and the associated recoil collisions. This is expected to cause significant changes to the crystalline lattice of the material. These effects may become even more pronounced due to the regular, single-crystal nature of the materials used in this work.

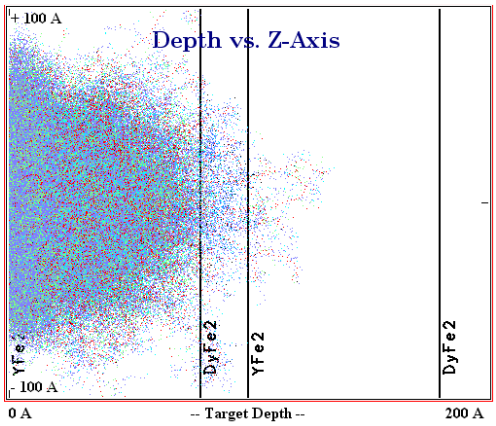

Figure 2.28: SRIM model showing the depth distribution of recoiled atoms in the top 2 repeats of a [2 nm $DyFe_2$ / 8 nm YFe_2] × 40 multilayer sample, due to 3.25 keV Ar^+ ion implantation at 68° to the sample plane.

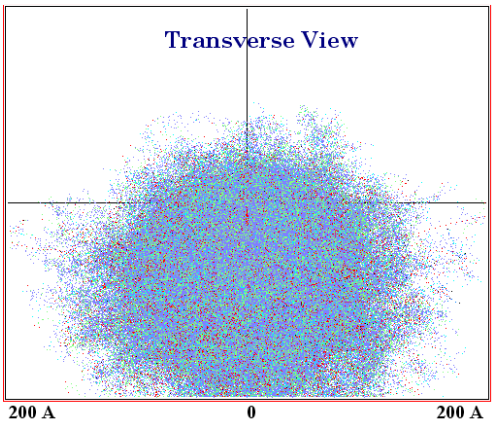

Figure 2.29: SRIM model showing the distribution of recoiled atoms in the film plane for the same irradiation conditions as in Figure 2.28.

There is a significant sputtering yield associated with the implantation of Ar^+ ions especially at lower incident ion energies whereby the ion motion is predominantly diffuse close to the sample surface. Therefore material is removed from these samples via ion milling and eventually the film will become thin enough to be considered as only being *irradiated* by the incident Ar^+ ions, *i.e.* they pass completely through it, ending their motion in the substrate. However, in the patterned sample, the remaining magnetic material will still include implanted ions as this is an inevitable transition stage between bulk and patterned films when using Ar^+ ions in the 1 – 5 keV range. From this, a further noteworthy point concerning ion milling as a tool for target material removal arises. Expensive, commercial ion milling equipment [144] typically uses higher fluences of lower energy Ar^+ ions than that used in this work. For example, at an energy of 400 eV, Ar^+ ions travel by almost a purely diffuse nature throughout a very

small volume close to the top of the target material. Thus the crystalline lattice of the target material is disrupted significantly within this region, but this region is very quickly eliminated from the sample due to the large sputtering yield associated with the high ion fluence. In the experimental set-up used here, the volume of material damaged by the ion milling process is considerably larger and it is removed at a much reduced rate, leading to a larger proportion of damaged material remaining after the ion milling process.

Finally it is worthwhile noting that over recent years a small but significant amount of research regarding ion implantation into films other than Pt / Co sandwiches and multilayers has emerged. To date, this work has been primarily centred around two different magnetic films: NiFe (80:20 wt. % – "Permalloy"®) [145] and Ni [146]. Naturally, since ion implantation is investigated, the films studied are significantly thicker than those used by Chappert *et al.* [124, 129, 131], Terris *et al.* [132, 140, 141, 147] and Sung, Kim and Lee *et al.* [134, 135, 148 respectively] and have used higher energy ions and / or heavier ion species such as Ar^+, Kr^+, Ga^+ and Xe^+. Ozkaya *et al.* [145] implanted Ga^+ ions into Permalloy films and found an increased coercivity in the ion implanted regions. This was explained by the fact that the implanted Ga^+ ion physically changes the lattice parameters of the Permalloy film. Common to ion implantation research in general, these authors found that there are no appreciable changes in the magnetic properties of the film for ion fluences of 10^{14} ions cm^{-2}, but significant changes when the fluence reaches 10^{16} ions cm^{-2}, *i.e.* when the implanted ions start to contribute to a significant proportion of the aerial density of atoms at the sample surface[ix]. For ion implanted Permalloy films, it can generally be concluded that the most dominant effect is that due to changes in the stress / strain of the film's structure as a result of the displacements induced in the crystalline lattice by the implanted ions [145, 149, 150]. Similar implantation work was reported by Zhang *et al.* [146] whereby Ni films were irradiated by high energy Xe^+ ions. As the Xe^+ ion fluence was increased the tensile strain in the Ni film was observed to decrease, in good agreement with previous results for other metallic films. However, as the ion fluence was increased past a critical value the tensile strain was observed to evolve into a

[ix] Assuming a typical atomic density of 10^{23} atoms cm^{-3}, there is an approximate aerial density of 10^{15} – 10^{16} atoms cm^{-2}.

compressive stress, attributed to increased damage from elastic recoil collisions and the inclusion of non-soluble Xe atoms within the film [146]. Ion implantation was also used to explain the departure of the easy axis of magnetization from perpendicular to in-plane. The perpendicular magnetization is attributed to a large magnetoelastic anisotropy energy [138, 151], hence reducing the tensile strain by ion implantation reduces this contribution to the film's anisotropy, causing the magnetization to rotate into the plane of the film.

The effects of energetic Ar^+ ions implanted into various epitaxial $REFe_2$ films will form the contents of Chapter 5, where the effects of implanted ions will be seen to drastically alter the magnetic and crystalline properties of these materials.

References

[1] N. Bohr, *Phil. Mag.*, ser. 6, vol. **26**, pp. 1 – 24, 1913.

[2] R. C. O'Handley, *Modern Magnetic Materials, Principles and Applications*, John Wiley & Sons Inc., 2000.

[3] P. Zeeman, *Phil. Mag.*, ser. 5, vol. **43**, pp. 226 – 239, 1897

[4] G. E. Uhlenbeck & S. A. Goudsmit, *Naturwiss*, vol. **13**, pp. 953 – 954, 1925.

[5] A. Landé, *Z. Phys.*, vol. **5**, n. 4, pp. 231 – 241, 1921.

[6] P. A. M. Dirac, *Proc. R. Soc. Lond. A*, vol. **123**, no. 792, pp. 714 – 733, 1929.

[7] E. C. Stoner, *Proc. R. Soc. Lond. A*, vol. **165**, no. 922, pp. 372 – 414, 1938.

[8] J. C. Maxwell, *Phil. Trans. Royal Soc. Lond*., vol. **155**, pp. 459 – 512, 1865.

[9] J-. M. L. Beaujour, *Ph. D. Thesis*, University of Southampton, UK, 2003.

[10] H. B. Callen & E. Callen, *J. Phys. Chem. Sol.*, vol. **27**, no. 8, pp. 1271 – 1285, 1966.

[11] U. Atzmony & M. P. Dariel, *Phys. Rev. B*, vol. **13**, no. 9, pp. 4006 – 4014, 1976.

[12] K. N. Martin, P. A. J. de Groot, B. D. Rainford, K. Wang, G. J. Bowden, J. P. Zimmermann & H. Fangohr, *J. Phys.: Condens. Matt.*, vol. **18**, pp. 459 – 478, 2006.

[13] J. P. Zimmermann, *Ph. D. Thesis*, University of Southampton, UK, 2007.

[14] A. Mougin, C. Dufour, K. Dumesnil, N. Maloufi, Ph. Mangin & G. Patrat, *Phys. Rev. B*, vol. **59**, no. 8, pp. 5950 – 5959, 1999.

[15] J. P. Zimmermann, G. Bordignon, R. P. Boardman, T. Fischbacher, H. Fangohr, K. N. Martin, G. J. Bowden, A. A. Zhukov & P. A. J. de Groot, *J. Appl. Phys.*, vol. **99**, p. 08B904, 2006.

[16] J. P. Zimmermann, K. Martin, G. Bordignon, M. Franchin, R. C. C. Ward, G. J. Bowden, P. A. J. de Groot & H. Fangohr, *J. Mag. Mag. Mater.*, vol. **321**, pp. 2499 – 2507, 2009.

[17] J. Joule, *Sturgeon's Ann. Elec.*, vol. **8**, p. 219, 1842.

[18] E. W. Lee, *Rep. Prog. Phys.*, vol. **18**, pp. 184 – 229, 1955.

[19] V. Oderno, C. Dufour, K. Dumesnil, Ph. Bauer, Ph. Mangin & G. Marchal, *Phys. Rev. B*, vol. **54**, no. 24, pp. R17375 – R17378, 1996.

[20] A. Mougin, C. Dufour, K. Dumesnil & Ph. Mangin, *Phys. Rev. B*, vol. **62**, no. 14, pp. 9517 – 9531, 2000.

[21] G. J. Bowden, P. A. J. de Groot, B. D. Rainford, K. Wang, K. N. Martin, J. P. Zimmermann & H. Fangohr, *J. Phys.: Condens. Matt.*, vol. **18**, pp. 5861 – 5871, 2006.

[22] A. A. Zhukov, G. J. Bowden, J-. M. L. Beaujour, B. D. Rainford, P. A. J. de Groot, R. C. C. Ward, M. R. Wells & H. Küpfer, *J. Mag. Mag. Mat.*, vol. **270**, pp. 312 – 320, 2003.

[23] N. Singh, *Physica B*, vol. **270**, pp. 298 – 306, 1999.

[24] G. J. Bowden, D. St. P. Bunbury, A. P. Guimarães & R. E. Snyder, *J. Phys. C*, vol. **1**, pp. 1376 – 1387, 1968.

[25] K. H. J. Buschow, *Rep. Prog. Phys.*, vol. 40, pp. 1179 – 1256, 1977.

[26] R. L. Cohen, *Phys. Rev.*, vol. **134,** no. 1A, pp. A94 – A98, 1964.

[27] Reproduced from a free application on the US Naval Research Laboratory website,

http://cst-www.nrl.navy.mil/lattice/struk/c15.html.

[28] J. C. Slater, *Phys. Rev.*, vol. **36**, pp. 57 – 64. 1930.

[29] C. Zener, *Phys. Rev.*, vol. **81**, no. 4, pp. 440 – 444, 1951.

[30] M. A. Ruderman & C. Kittel, *Phys. Rev.*, vol. **96**, no. 1, pp. 99 – 102, 1954.

[31] T. Kasuya, *Prog. Theor. Phys.*, vol. **16**, no. 45, pp. 45 – 57, 1956.

[32] K. Yosida, *Phys. Rev.*, vol. **106**, no. 5, pp. 893 – 898, 1957.

[33] M. B. Stearns, *Phys. Rev.*, vol. **147**, no. 2, pp. 439 – 453, 1966.

[34] M. B. Stearns, *Phys. Rev. B*, vol. **8**, no. 9, pp. 4383 – 4398, 1973.

[35] J. Jensen & A. R. Mackintosh, *Rare Earth Magnetism, Structures and Excitations*, Clarendon Press, Oxford, 1991, p. 11

[36] I. A. Campbell, *J. Phys. F: Metal Phys.*, vol. **2**, pp. L47 – L50, 1972.

[37] E. Goto, N. Hayashi, T. Miyashita & K. Nakagawa, *J. Appl. Phys.*, vol. **36**, no. 9, pp. 2951 – 2958, 1965.

[38] G. J. Bowden, J-. M. L. Beaujour, S. Gordeev, P. A. J. de Groot, B. D. Rainford & M. Sawicki, *J. Phys.: Condens. Matt.*, vol. **12**, pp. 9335 – 9346, 2000.

[39] E. F. Kneller & R. Hawig, *IEEE Trans. Mag.*, vol. **27**, no. 4, pp. 3588 – 3600, 1991.

[40] R. Skomski & J. M. D. Coey, *Phys. Rev. B*, vol. **48**, no. 21, pp. 15812 – 15816, 1993.

[41] E. E. Fullerton, J. S. Jiang, M. Grimsditch, C. H. Sowers & S. D. Bader, *Phys. Rev. B*, vol. **58**, no. 18, pp. 12193 – 12200, 1998.

[42] I. A. Al-Omari & D. J. Sellmyer, *Phys. Rev. B.*, vol. **52**, no. 5, pp. 3441 – 3447, 1995.

[43] P. Sharma, J. Waki, N. Kaushik, D. V. Louzguine-Luzgin, H. Kimura & A. Inoue, *Acta Mat.*, vol. **55**, pp. 4203 – 4212, 2007.

[44] M. Franchin, G. Bordignon, T. Fischbacher, G. Meier, J. Zimmermann, P. de Groot & H. Fangohr, *J. Appl. Phys.*, vol. **103**, p. 07A504, 2008.

[45] E. C. Stoner & E. P. Wohlfarth, *Phil. Trans. Royal Soc. Lond. A*, vol. **240**, no. 826, pp. 599 – 642, 1948.

[46] E. C. Stoner & E. P. Wohlfarth, *IEEE Trans. Mag.*, vol. **27**, no. 4, pp. 3475 – 3518, 1991.

[47] W. F. Brown, *Rev. Mod. Phys.*, vol. **17**, no. 1, pp. 15 – 19, 1945.

[48] A. Aharoni, *Rev. Mod. Phys.*, vol. **34**, no. 2, pp. 227 – 238, 1962

[49] H. Zijlstra, *IEEE Trans. Magnet.*, vol. **MAG-15**, no. 5, pp. 1246 – 1250, 1979.

[50] M. R. Scheinfein, J. Unguris, R. J. Celotta & D. T. Pierce, *Phys. Rev. Lett.*, vol. **63**, no. 6, pp. 668 – 671, 1989.

[51] H. Barkhausen, *Zeit. Phys.*, vol. **20**, p. 401, 1919.

[52] P. Gaunt, *IEEE Trans. Mag.*, vol. **MAG-19**, no. 5, pp. 2030 – 2032, 1983.

[53] P. Gaunt, *J. Appl. Phys.*, vol. **43**, no. 2, pp. 637 – 638, 1972.

[54] P. Gaunt, *IEEE Trans. Mag.*, vol. **MAG-9**, no. 3, pp. 171 – 173, 1973.

[55] J-. P. Wang, W. K. Shen, J. M. Bai, R. H. Victora, J. H. Judy & W. L. Song, *Appl. Phys. Lett.*, vol. **86**, p. 142504, 2005.

[56] W. K. Shen, J. M. Bai, R. H. Victora, J. H. Judy & J-. P. Wang, *J. Appl. Phys.*, vol. **97**, p. 10N513, 2005.

[57] J-. P. Wang, W. Shen & J. Bai, *IEEE Trans. Mag.*, vol. **41**, no. 10, pp. 3181 – 3186, 2005.

[58] A. Goncharov, *Ph. D. Thesis*, University of Southampton, UK, 2004.

[59] J. Fidler & T. Schrefl, *J. Phys. D:, Appl. Phys.*, vol. **33**, pp. R135 – R156, 2000.

[60] M. J. Donahue & D. G. Porter, NIST, Gaithersburg, USA, `OOMMF` software freely available at http://math.nist.gov/oommf.

[61] L. Landau & E. Lifshits, *Phys. Zeitsch. Sow.*, vol. **8**, pp. 153 – 169, 1935, reprinted in *Ukr. J. Phys.*, vol. **53**, pp. 14 – 22, 2008.

[62] T. L. Gilbert & J. M. Kelly, *Conf. Mag. Mag. Mater.*, Pittsburgh, PA, 1955, New York: *American Institute of Electrical Engineers*, pp. 253 – 263, 1955.

[63] T. L. Gilbert, *IEEE Trans. Mag.*, vol. **40**, no. 6, pp. 3443 – 3449, 2004.

[64] IBM 350 Disk Storage Unit, Historical Details Available at http://www-03.ibm.com/ibm/history/exhibits/storage/storage_350.html

[65] Hitachi Deskstar 7K1000, Product Specifications Available at http://www.hitachigst.com/tech/techlib.nsf/techdocs/67A68C59B27368FC862572570080FC70/$file/Deskstar7K1000_010307_final.pdf

[66] G. E. Moore, *Electronics*, vol. **38**, no. 8, 1965.

[67] G. E. Moore, *Proc. IEEE 1975 International Electron Devices Meeting*, vol. **21**, pp. 11 – 13, 1975.

[68] R. C. O'Handley, *Modern Magnetic Materials, Principles and Applications*, John Wiley & Sons Inc., 2000.

[69] B. D. Terris & T. Thomson, *J. Phys. D: Appl. Phys.*, vol. **38**, pp. R199 – R222, 2005.

[70] H. Zhou & H. N. Bertram, *IEEE Trans. Mag.*, vol. **35**, no. 5, pp. 2712 – 2714, 1999.

[71] A. Moser, K. Takano, D. T. Margulies, M. Albrecht, Y. Sonobe, Y. Ikeda, S. Sun & E. E. Fullerton, *J. Phys. D: Appl. Phys.*, vol. **35**, pp. R157 – R167, 2002.

[72] H. N. Bertram, H. Zhou & R. Gustafson, *IEEE Trans. Mag.*, vol. **34**, no. 4, pp. 1845 – 1847, 1998.

[73] N. X. Sun & S. X. Wang, *IEEE Trans. Mag.*, vol. **36**, no. 5, pp. 2506 – 2508, 2000.

[74] W. R. Bennett, B. Zhang & H. J. Richter, *IEEE Trans. Mag.*, vol. **34**, no. 3, pp. 743 – 749, 1998.

[75] H. Takano, Y. Nishida, A. Kuroda, H. Sawaguchi, Y. Hosoe, T. Kawabe, H. Aoi, H. Muraoka, Y. Nakamura & K. Ouchi, *J. Mag. Mag. Mater.*, vol. **235**, pp. 241 – 244, 2000.

[76] X. Shen, M. Kapoor, R. Field & R. H. Victora, *IEEE Trans. Mag.*, vol. **43**, no. 2, pp. 676 – 681, 2007.

[77] S. S. P. Parkin, C. Kaiser, A. Panchula, P. M. Rice, B. Hughes, M. Samant & S-. E. Yang, *Nature Mat.*, vol. **3**, pp. 862 – 867, 2004.

[78] S. Mao, Y. Chen, F. Liu, X. Chen, B. Xu, P. Lu, M. Patwari, H. Xi, C. Chang, B. Miller, D. Menard, B. Pant, J. Loven, K. Duxstad, S. Li, Z. Zhang, A. Johnston, R.

Lamberton, M. Gubbins, T. McLaughlin, J. Gadbois, J. Ding, B. Cross, S. Xue & P. Ryan, *IEEE Trans. Mag.*, vol. **42**, no. 2, pp. 97 – 102, 2006.

[79] H. J. Richter, *J. Phys. D: Appl. Phys.*, vol. **40**, pp. R149 – R177, 2007.

[80] S. N. Piramanayagam, *J. Appl Phys.*, vol. **102**, p. 011301, 2007.

[81] D. Suess, T. Schrefl, S. Fähler, M. Kirschner, G. Hrkac, D. Dorfbauer & J. Fidler, *Appl. Phys. Lett.*, vol. **87**, p. 012504, 2005.

[82] T. J. Klemmer & K. Pelhos, *App. Phys. Lett.*, vol. **88**, p. 162507, 2006

[83] R. H. Victora & X. Shen, *IEEE Trans. Mag.*, vol. **41**, no. 2, pp. 537 – 542, 2005.

[84] M. P. Sharrock, *J. Appl. Phys.*, vol. **76**, no. 10, pp. 6413 – 6418, 1994.

[85] D. Suess, T. Schrefl, R. Dittrich, M. Kirschner, F. Dorfbauer, G. Hrkac & J. Fidler, *J. Mag. Mag. Mater.*, vol. **290**, pp. 551 – 554, 2005.

[86] Y. K. Takahashi, K. Hono, S. Okamoto & O. Kitakami, *J. Appl. Phys.*, vol. **100**, p. 074305, 2006.

[87] S. Okamoto, O. Kitakami, N. Kikuchi, T. Miyazaki, Y. Shimada & T-. H. Chiang, *J. Phys.: Condens. Matt.*, vol. **16**, pp. 2109 – 2114, 2004.

[88] D. Suess, *Appl. Phys. Lett.*, vol. **89**, p. 113105, 2006.

[89] T. W. McDaniel, W. A. Challener & K. Sendur, *IEEE Trans. Mag.*, vol. **39**, no. 4, pp. 1972 – 1979, 2003.

[90] K. Şendur & W. Challener, *Appl. Phys. Lett.*, vol. **94**, p. 032503, 2009.

[91] J-. G. Zhu, X. Zhu & Y. Tang, *IEEE Trans. Mag.*, vol. **44**, no. 1, pp. 125 – 131, 2008.

[92] S. Takenoiri, *J. Mag. Mag. Mater.*, vol. **321**, pp. 562 – 565, 2009.

[93] Y. Soeno, M. Moriya, A. Kaizu & M. Taki, *IEEE Trans. Mag.*, vol. **41**, no. 10, pp. 3220 – 3222, 2005.

[94] E. Roddick, D. Wachenschwanz & W. Jiang, *IEEE Trans. Mag.*, vol. **41**, no. 10, pp. 3229 – 3231, 2005.

[95] Y. Soeno, M. Moriya, K. Ito, K. Hattori, A. Kaizu, T. Aoyama, M. Matsuzaki & H. Sakai, *IEE Trans. Mag.*, vol. **39**, no. 4, pp. 1967 – 1971, 2003.

[96] M. Khoury & D. K. Ferry, *J. Vac. Sci. Technol. B*, vol. **14**, no. 1, pp. 75 – 79, 1996.

[97] C. Vieu, F. Carcenac, A. Pépin, Y. Chen, M. Mejias, A. Lebib, L. Manin-Ferlazzo, L. Couraud & H. Launois, *Appl. Sur. Sci.*, vol. **164**, pp. 111 – 117, 2000.

[98] International Technology Roadmap for Semiconductors reports are updated annually and freely available online at http://public.itrs.net/reports.html.

[99] B. D. Terris & T. Thomson, *J. Phys. D: Appl. Phys.*, vol. **38**, pp. R199 – R222, 2005.

[100] B. D. Terris, M. Albrecht, G. Hu, T. Thomson & C. T. Rettner, *IEEE Trans. Mag.*, vol. **41**, no. 10, pp. 2822 – 2827, 2005.

[101] C. Haginoya, S. Heike, M. Ishibashi, K. Nakamura, K. Koike, T. Yoshimura, J. Yamamoto & Y. Hirayama, *J. Appl. Phys.*, vol. **85**, no. 12, pp. 8327 – 8331, 1999.

[102] J. W. Lau, R. D. McMichael, S. H. Chung, J. O. Rantschler, V. Parekh & D. Litvinov, *Appl. Phys. Lett.*, vol. **92**, p. 012506, 2008.

[103] E. Chunsheng, V. Parekh, P. Ruchhoeft, S. Khizroev & D. Litvinov, *J. Appl. Phys.*, vol. **103**, p. 063904, 2008.

[104] R. Sbiaa, K. O. Aung, S. N. Piramanayagam, E-. L. Tan & R. Law, *J. Appl. Phys.*, vol. **105**, p. 073904, 2009.

[105] M. Takahashi & S. Saito, *J. Mag. Mag. Mater.*, vol. **320**, pp. 2868 – 2873, 2008.

[106] R. Sbiaa, R. Gandhi, K. Srinivasan, S. N. Priamanayagam & R. M. Seoh, *J. Mag. Mag. Mater.*, vol. **321**, pp. 2682 – 2684, 2009.

[107] H. J. Richter, A. Y. Dobin, O. Heinonen, K. Z. Gao, R. J. M. van der Veerdonk, R. T. Lynch, J. Xue, D. Weller, P. Asselin, M. F. Erden & R. M. Brockie, *IEEE Trans. Mag.*, vol. **42**, pp. 2255 – 2260, 2006.

[108] M. Albrecht, C. T. Rettner, A. Moser, M. E. Best & B. D. Terris, *Appl. Phys. Lett.*, vol. **81**, no. 5, pp. 2875 – 2877, 2002.

[109] G. F. Hughes, *IEEE Trans. Mag.*, vol. **35**, no. 5, pp. 2310 – 2312, 1999.

[110] H. J. Richter, A. Y. Dobin, R. T. Lynch, D. Weller, R. M. Brockie, O. Heinonen, K. Z. Gao, J. Xue, R. J. M. van der Veerdonk, P. Asselin & M. F. Erden, *Appl. Phys. Lett.*, vol. **88**, p. 222512, 2006.

[111] S. N. Piramanayagam, K. O. Aung, S. Deng & R. Sbiaa, *J. Appl. Phys.*, vol. **105**, p. 07C118, 2009.

[112] X. Yang, L. Wan, S. Xiao, Y. Xu & D. K. Weller, *ACS Nano*, vol. **3**, no. 7, pp. 1844 – 1858, 2009.

[113] M. N. Baibich, J. M. Broto, A. Fert, F. Nguyen Van Dau, F. Petroff, P. Eitenne, G. Creuzet, A. Friederich & J. Chazelas, *Phys. Rev. Lett.*, vol. **61**, no. 21, pp. 2472 – 2475, 1988.

[114] R. L. White, *IEEE Trans. Mag.*, vol. **30**, no. 2, pp. 346 – 352, 1994.

[115] A. D. G. Stewart & M. W. Thompson, *J. Mat. Sci.*, vol. **4**, pp. 56 – 60, 1969.

[116] P. Sigmund, *Appl. Phys. Lett.*, vol. **14**, no. 3, pp. 114 – 117, 1969.

[117] J. F. Ziegler, M. D. Ziegler & J. P. Biersack, `SRIM-2008.04`, PC software available at http://www.srim.org

[118] G. R. Piercy, F. Brown, J. A. Davies & M. McCargo, *Phys. Rev. Lett.*, vol. **10**, no. 9, pp. 399 – 400, 1968

[119] W. L. Chan & E. Chason, *J. Appl. Phys.*, vol. **101**, p. 121301, 2007

[120] R. A. Minamisawa, D. Buca, H. Trinkaus, B. Holländer, S. Mantl, V. Destefanis & J. M. Hartmann, *Appl. Phys. Lett.*, vol. **95**, p. 034102, 2009.

[121] G. Carter, *J. Phys. D: Appl. Phys.*, vol. **34**, pp. R1 – R22, 2001.

[122] M. T. Robinson & O. S. Oen, *Appl. Phys. Lett.*, vol. **2**., no. 2, pp. 30 – 32, 1963.

[123] J. Fassbender, D. Ravelosona & Y. Samson., *J. Phys. D: Appl. Phys.*, vol. **37**, pp. R179 – R196, 2004.

[124] C. Chappert, H. Bernas, J. Ferré, V. Kottler, J-. P. Jamet, Y. Chen, E. Cambril, T. Devolder, F. Rousseaux, V. Mathet & H. Launois, *Science*, vol. **280**, pp. 1919 – 1922, 1998.

[125] G. A. Bertero, R. Sinclair, C-. H. Park & Z. X. Shen, *J. Appl. Phys.*, vol. **77**, no. 8, pp. 3953 – 3959, 1994.

[126] J. Fassbender & J. McCord, *J. Mag. Mag. Mater.*, vol. **320**, pp. 579 – 596, 2007.

[127] C. Vieu, J. Gierak, H. Launois, T. Aign, P. Meyer, J. P. Jamet, J. Ferré, C. Chappert, T. Devolder, V. Mathet & H. Bernas, *J. Appl. Phys.*, vol. **91**, no. 5, pp. 3103 –

3110, 2001.

[128] T. Devolder, *Phys. Rev. B*, vol. **62**, no. 9, pp. 5794 – 5802, 2000.

[129] H. Bernas, T. Devolder, C. Chappert, J. Ferré, V. Kottler, Y. Chen, C. Vieu, J. P. Jamet, V. Mathet, E. Cambril, O. Kaitasov, S. Lemerle, F. Rousseaux & H. Launois, *Nuc. Instrum. Meth. Phys. Res. B*, vol. **148**, pp. 872 – 879, 1999.

[130] T. Devolder, *Phys. Rev. B*, vol. **62**, no. 9, pp. 5794 – 5802, 2000.

[131] J. Ferré, C. Chappert, H. Bernas, J-. P. Jamet, P. Meyer, O. Kaitasov, S. Lemerle, V. Mathet, F. Rousseaux & H. Launois, *J. Mag. Mag. Mater.*, vol. **198**, pp. 191 – 193, 1999.

[132] D. Weller, J. E. E. Baglin, A. J. Kellock, K. A. Hannibal, M. F. Toney, G. Kusinski, S. Lang, L. Folks, M. E. Best & B. D. Terris, *J. Appl. Phys.*, vol. **87**, no. 9, pp. 5768 – 5770, 2000.

[133] D. Weller, H. Brändle & C. Chappert, *J. Mag. Mag. Mater.*, vol. **121**, pp. 461 – 470, 1993.

[134] T. G. Kim, Y. H. Shin, J. H. Song, M. C. Sung, I. S. Kim, D. G. You, J. Lee, K. Jeong, G. Y. Jeon & C. N. Whang, *Appl. Phys. Lett.*, vol. **81**, no. 21, pp. 4017 – 4019, 2002.

[135] J. Lee, G. Lauhoff, & J. A. C. Bland, *Phys. Rev. B*, vol. **56**, no. 10, pp. R5728 – R5731, 1997.

[136] B. Schulz & K. Baberschke, *Phys. Rev. B*, vol. **50**, no. 18, pp. 13467 – 13471, 1994.

[137] P. Rosenbusch, J. Lee, G. Lauhoff & J. A. C. Bland, *J. Mag. Mag. Mater.*, vol. **172**, pp. 19 – 25, 1997.

[138] J-. S. Lee, K-. B. Lee, Y. J. Park, T. G. Kim, J. H. Song, K. H. Chae, J. Lee, C. N. Whang, K. Jeong, D-. H. Kim & S-. C. Shin, *Phys. Rev. B*, vol. **69**, p. 172405, 2004.

[139] T. Veres, M. Cai, R. W. Cochrane & S. Roorda, *J. Appl. Phys.*, vol. **87**, no. 12, pp. 8504 – 8512, 2000.

[140] B. D. Terris, L. Folks, D. Weller, J. E. E. Baglin, A. J. Kellock, H. Rothuizen & P. Vettiger, *Appl. Phys. Lett.*, vol. **75**, no. 3, pp. 403 – 405, 1999.

[141] B. D. Terris, D. Weller, L. Folks, J. E. E. Baglin, A. J. Kellock, H. Rothuizen & P. Vettiger, *J. Appl. Phys.*, vol. **87**, no. 9, pp. 7004 – 7006, 2000.

[142] W. Primak & R. Kampwirth, *J. Appl. Phys.*, vol. **39**, no. 12, pp. 5651 – 5658, 1968.

[143] D. Ravelosona, C. Chappert, V. Mathet & H. Bernas, *J. Appl. Phys.*, vol. **87**, no. 9, pp. 5771 – 5773, 2000.

[144] *Ion Beam Etch Rates and Sputter Yields*, Intlvac, Ontario, data available at http://www.intlvac.com/wp

[145] D. Ozkaya, R. M. Langford, W. L. Chan & A. K. Petford-Long, *J. Appl. Phys.*, vol. **91**, no. 12, pp. 9937 – 9942, 2002.

[146] K. Zhang, K. P. Lieb, D. G. Merkel, M. Uhrmacher, N. Pilet, T. V. Ashworth & H. J. Hug, *Nuc. Instrum. Meth. Phys. Res. B*, vol. **257**, pp. 379 – 382, 2007.

[147] C. T. Rettner, S. Anders, J. E. E. Baglin, T. Thomson & B. D. Terris, *Appl. Phys. Lett.*, vol. **80**, no. 2, pp. 279 – 281, 2002.

[148] M. C. Sung, D. G. You, H. S. Park, J. C. Lee, S. Y. Le, I. S. Kim, J. Lee, C. N.

Whang, S. Im, K. Jeong, T. G. Kim, J. S. Yang & J. H. Song, *J. Appl. Phys.*, vol. **90**, no. 4, pp. 2036 – 2038, 2001.

[149] R. Gupta, K. P. Lieb, Y. Luo, G. A. Müller, P. Schaaf & K. Zhang, *Eur. Phys. J. B*, vol. **63**, pp. 501 – 506, 2008.

[150] S. I. Woods, S. Ingvarsson, J. R. Kirtley, H. F. Hamann & R. H. Koch, *Appl. Phys. Lett.*, vol. **81**, no. 7, pp. 1267 – 1269, 2002.

[151] O. Song, C. A. Ballentine & R. C. O'Handley, *Appl. Phys. Lett.*, vol. **64**, no. 19, pp. 2593 – 2595, 1994.

Chapter 3

Experimental Methods

The results presented in this thesis focus on the creation of artificial patterned elements in rare earth – iron ($REFe_2$) materials on the nano-scale. In order to fabricate nano-scale patterned elements in these materials, a range of experimental steps are required, whilst characterization of the media requires the use of further specialised equipment. This chapter aims to describe the specific equipment used in fabrication and characterization the $REFe_2$ media.

The $REFe_2$ materials are prepared using molecular beam epitaxy (MBE). MBE, along with two other, more common thin film deposition processes (sputtering and thermal evaporation) are described in section 3.1. This describes the full complement of deposition techniques used in this work. The $REFe_2$ materials are subject to both lattice mismatch and thermally induced strains. This is detailed in section 3.2, which provides a description of both how these strains act and how they are minimized during sample growth. The $REFe_2$ materials are patterned using electron beam lithography (EBL), a process which permits the definition of patterns in a material sensitive to electron radiation down to a scale of tens of nm. EBL is conducted using a scanning electron microscope (SEM); the SEM used for the vast majority of the work described in this thesis underwent substantial development and improvement throughout the time it was used, therefore its operation is described in detail in section 3.3. The process of EBL and advances in this technique are described in the subsequently in section 3.4. The patterned polymer can provide a *soft* mask or a template for a *hard* mask (section 3.5) for the following ion milling process (section 3.6) in order to transfer the pattern into the $REFe_2$ material. To characterize the patterned $REFe_2$ media in terms of topographical and elemental composition, a range of techniques have been used: SEM and energy dispersive X-ray analysis (EDX) (section 3.3), X-ray diffraction (XRD) (section 3.7), He^+ ion microscopy (section 3.8) and atomic force microscopy (AFM) (section 3.9). Magnetic characterization was performed using magnetic force microscopy (MFM), the magneto optical Kerr effect (MOKE) and vibrating sample magnetometry (VSM) as described in sections 3.9, 3.10 and 3.11 respectively.

The experimental methods chapter is substantial since a significant amount of the author's time was devoted to developing and implementing these techniques. As such this chapter also provides comprehensive literature review on the related topics. EBL, whilst a well developed technology, was a new process to the School of Physics and Astronomy at the University of Southampton, and indeed provided the only such installation at the Institution after the devastating fire of 2005 [1]. The author's input to developing the EBL system has been an invaluable tool in continuing the School's research in nanotechnology, whilst other techniques new to the School such as ion milling and MFM (new to the University as a whole) have complimented this development. It is therefore timely and relevant to include details regarding the development and implementation of these new experimental techniques which hopefully will help to leave a long lasting legacy in nanofabrication and characterization within the School of Physics and Astronomy at the University of Southampton.

3.1 Deposition Methods

The growth of the $REFe_2$ magnetic media and the deposition of hard mask materials for ion milling were achieved using a range of techniques. MBE is used to accurately deposit ultra-thin layers of material to fabricate the metallic superlattice structures investigated in this work. MBE is discussed before the more standard thin film deposition techniques of sputtering and thermal evaporation are briefly described. The latter are used primarily to fabricate metallic masks for use in the ion milling pattern transfer process described in section 3.6.

3.1.1 Molecular beam epitaxy

MBE was first used in the 1960s by Arthur and Cho [2, 3] as a method to deposit thin films of semiconductor materials. A decade later MBE was applied to metallic systems, permitting highly epitaxial growth of magnetic films and multilayers with interfaces that are almost atomically sharp. The most famous use of MBE to grow epitaxial magnetic multilayers was in 1988 with the discovery of giant magneto resistance in Fe / Cr superlattices [4] which subsequently led to the 2007 Nobel Prize in physics. The growth of the $REFe_2$ samples discussed in this thesis was performed by Dr Roger Ward and co-workers at the Clarendon Laboratory, Oxford, using a *Balzers UMS 630 UHV* MBE device as described by Bentall *et al.* [5,6].

MBE is a generic term given to the deposition of atomic elements onto a substrate at an elevated temperature in ultra-high vacuum (UHV). The MBE device used at the Clarendon Laboratory (schematically shown in Figure 3.1) is able to heat the sample stage to a range of temperatures; those most commonly used for the samples studied within this work are between 450 and 750°C. The device has two main chambers; a deposition and a transfer / load-lock chamber, which permits the exchange of samples without bringing the entire system up to atmospheric pressure, allowing the system to remain at a constant base pressure of ~ 10^{-11} mbar. This helps ensure the high purity of the deposited films and multilayers, but it is also worthwhile noting that the material sources are of the highest purity, more so than that typically used in sputtering and thermal evaporation. In MBE there are two distinct sources for material deposition; effusion cells and electron beam guns

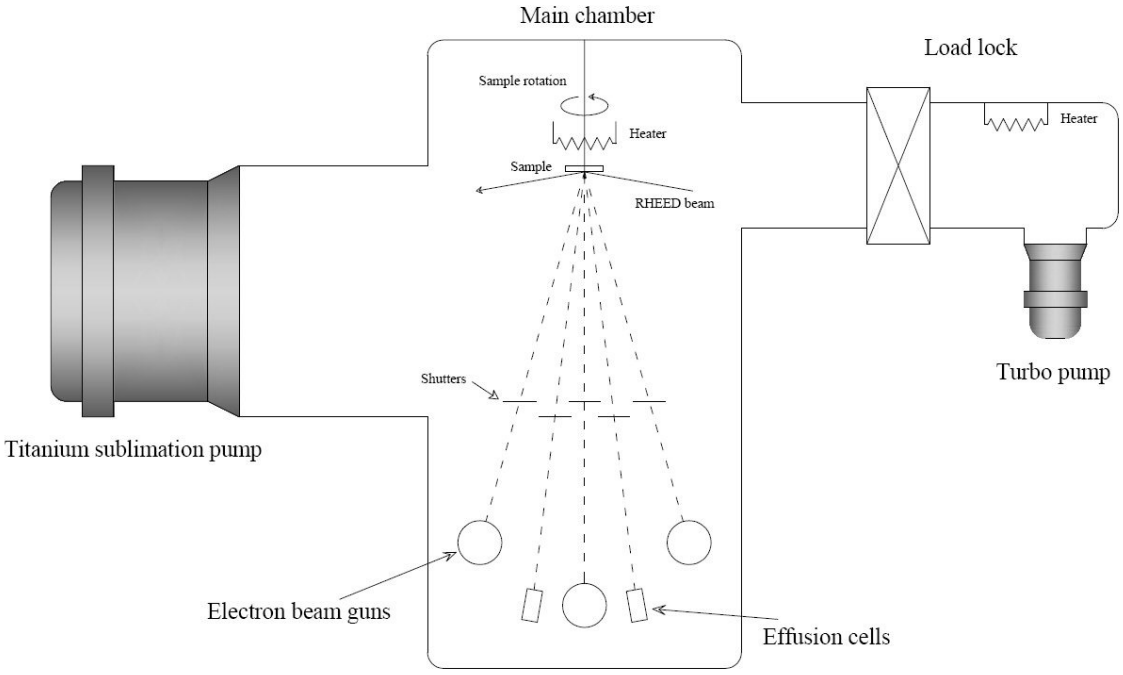

Figure 3.1: Schematic drawing of the *Balzers UMS 630 UHV* MBE system.

Effusion cells use a process analogous to thermal evaporation. They are heated resistively to cause the material contained within them to evaporate. Effusion cells are suitable for depositing metallic materials which evaporate at temperatures below 1300°C at a vapour pressure of ~ 10^{-8} mbar (*e.g.* Fe which evaporates at ~ 850°C). For materials that have a higher evaporation temperature for a similar vapour pressure, a beam of electrons is directed at and bombarded onto the material in order to directly and

locally heat it to high temperatures (*e.g.* for Nb which evaporates at ~ 1750°C). The base pressure rises to a working pressure of ~ 4×10^{-8} mbar during deposition.

Co-deposition of elemental fluxes is responsible for the $REFe_2$ film composition, but within the system there are shutters which isolate sources that are not being used (but which can be opened and closed in a fraction of a second) which allows for very precisely controlled layer-by-layer deposition when required. *In-situ* sample analysis can be performed using reflection high energy electron diffraction (RHEED) to gain an insight into the real time evolution of surface crystallography[i].

For the samples studied in this work, high quality single crystal Laves phase intermetallic layered systems have been grown on an Al_2O_3 (sapphire) substrate. The reasoning behind this process is described in section 3.2, where detail is given regarding lattice mismatch and thermal strains induced during the growth process. The Nb and Fe are deposited at a rate of 50 pms^{-1} and the $REFe_2$ layers at a rate of 100 – 200 pms^{-1}.

3.1.2 Magnetron sputtering

Sputtering can be most simply considered as the process whereby a target material is transformed into its vapour phase via physical bombardment by energetic ions. The basic process of magnetron sputtering has been around for many years (traditional, balanced magnetrons have been widely used since the 1970s), but with the introduction of the unbalanced magnetron in the late 1980s and early 1990s came the transformation of the sputtering technique from a niche process to the widely used process that it is today. A substantial review of recent advances in sputtering technology is given by Kelly & Arnell [7].

At the onset of deposition, a small flow of process gas (typically Ar) is leaked into the sputtering chamber. When a bias voltage is applied to the target, a discharge plasma of process gas ions forms in front of it and bombards the target surface. Atoms of the target material and secondary electrons are knocked off. The atoms can travel to and condense on the sample surface. There are magnets mounted behind the target which confine the secondary electrons. When one of these electrons strikes the process gas a positive ion is created which can then cause the whole sputtering process to start-over without the addition of further process gas. This cascade process is advantageous since

[i] Such *in-situ* methods of sample characterization are usually precluded from sputtering (and often thermal evaporation) due to the presence of process gasses and generally higher background pressures.

the rate of sputtering is increased whilst keeping the working pressure as low as possible (The typical working pressure is 10^{-3} mBar), and therefore the quality of the deposited films as high as possible. Despite this, sputtering clearly is not a directional process, resulting in the deposition of the material across a very large area (often the entire vacuum chamber). It is also important to realise the difference between DC and RF sputtering. DC sputtering uses a metallic target and therefore there is no build up of charge, but with an insulating target the plasma must be driven at a radio frequency (RF) to avoid charge build up.

Within the scope of the work discussed here, sputtering has been used to deposit a wide range of films with the primary focus on the deposition of metallic films through lithographically defined masks. The sputtering apparatus (shown schematically in Figure 3.2) is manufactured by *Kurt J. Lesker* and has four magnetrons; two designed for DC sputtering and two for RF sputtering. These are in a *confocal* arrangement, that is, they all face the sample stage simultaneously, which permits the co-deposition of target material and thereby the formation of alloy films from elemental targets. The apparatus is evacuated with a roughing pump and a cryo-pump, reaching a typical base pressure of 1×10^{-7} mbar. It is also equipped with a quartz crystal microbalance to accurately determine the thickness of the deposited film (± 0.1 nm) and a rotating sample stage to provide uniform film growth which can also be varied in temperature from ~ –175°C through to ~ 500°C.

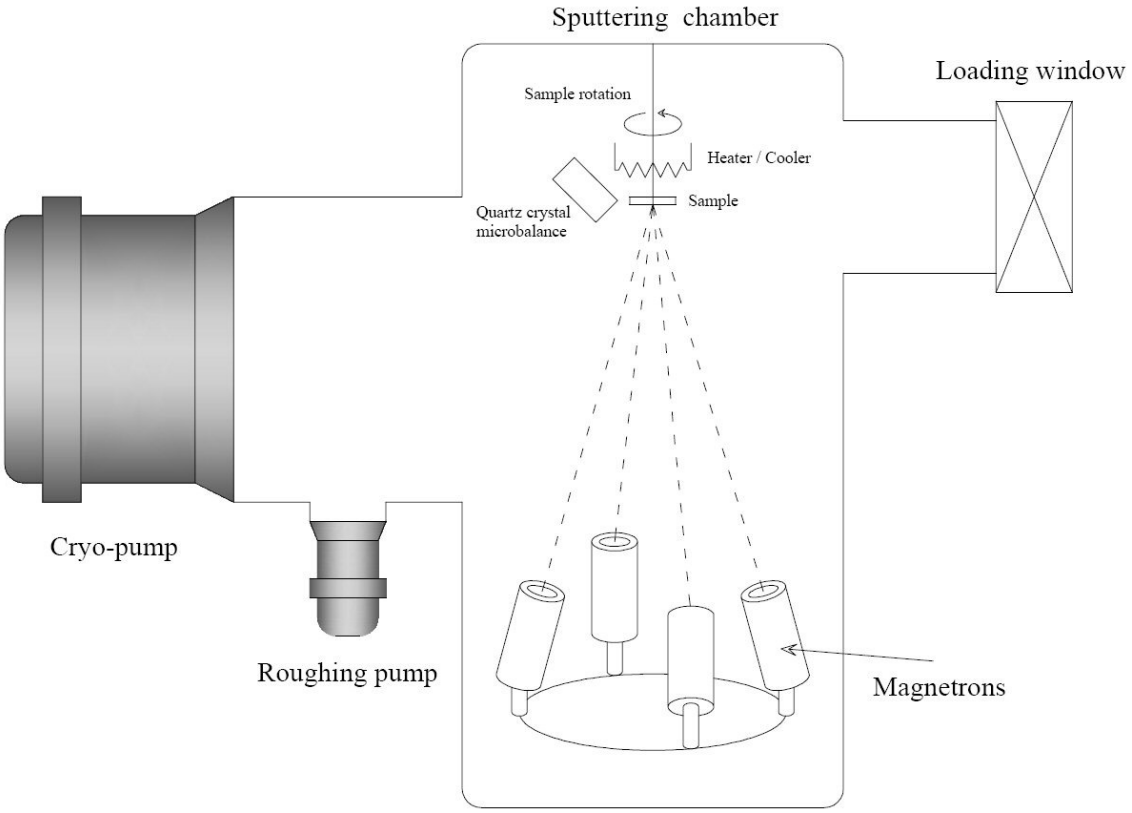

Figure 3.2: Schematic drawing of the *Kurt J Lesker* sputtering apparatus with 4 magnetrons arranged confocally with respect to the sample.

The confocal arrangement of the magnetrons limits the usefulness of the system for depositing materials through a lithographically defined mask. This occurs since the target material is not aligned parallel to the sample (see Figure 3.2) and therefore significant deposition can occur at the edges of the mask, *i.e.* it is not a *line of sight* system. Deposition against the side of the mask is responsible for an effect known as "rabbit ears", shown schematically in Figure 3.3 and illustrated in the SEM micrograph in Figure 3.5.

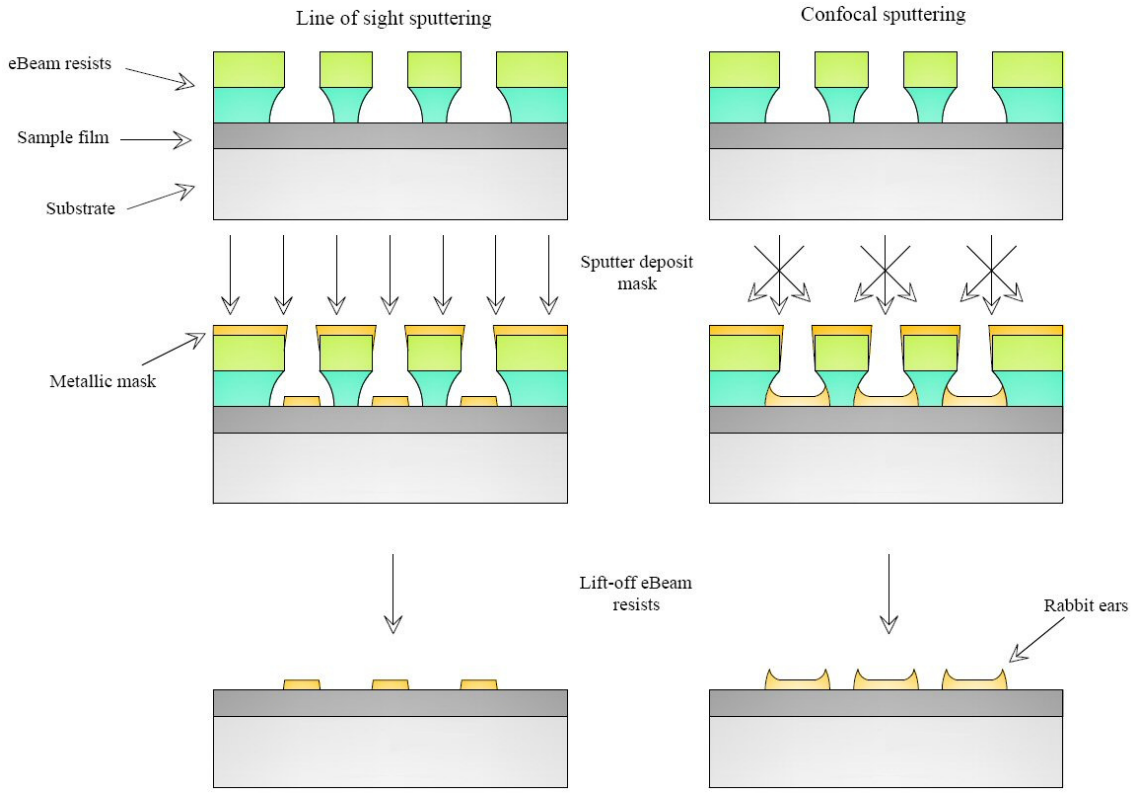

Figure 3.3: Schematic diagram comparing line of sight and confocal sputtering, and the associated formation of rabbit ears.

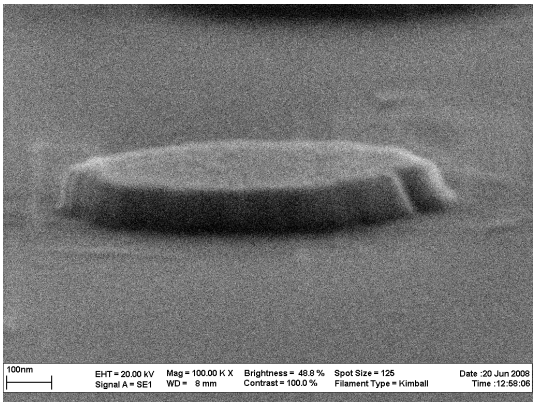

Figure 3.4: 100,000 × tilted magnification SEM micrograph of thermally evaporated Au on Si through a lift-off mask.

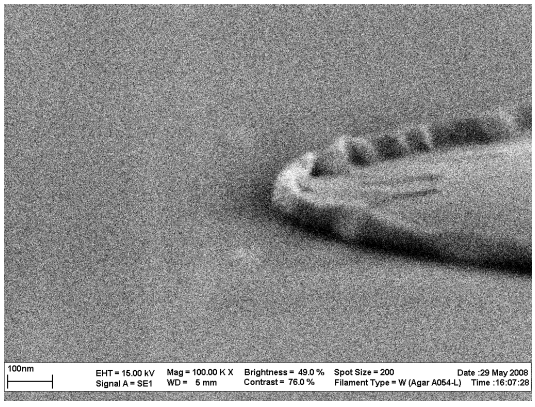

Figure 3.5: 100,000 × tilted magnification SEM micrograph of sputtered Au on Si through a lift-off mask showing rabbit ears.

To overcome this effect the sample can be mounted on an in-house designed holder which positions the sample parallel to the magnetrons and targets. This creates a line of sight arrangement. However, with this arrangement the sample cannot be rotated and therefore the uniformity of the film suffers and as such it is preferable to use a true line of sight deposition technique for metallic mask fabrication. Sputtering has however still been regularly used to create thin metallic layers to aid in electron microscopy.

3.1.3 Thermal evaporation

As previously noted, the process of thermal evaporation is very closely related to MBE with effusion cells, that is, the source metal is placed into a container that is resistively heated, causing it to evaporate and travel to and condense on the sample. Thermal evaporation takes place in a high vacuum chamber rather than a UHV chamber, therefore the precise control over film crystalline structure cannot be readily achieved. It does however provide a rapid and simple way to deposit thin films of non-refractory metals with evaporation temperatures below ~ 1,000°C at a vapour pressure of 10^{-6} mbar using a line of sight technique. Thermal evaporation therefore alleviates any problems associated with rabbit ears (section 3.1.2), thus has been used in this work to deposit metallic masks for use in ion milling (see section 3.6)

The thermal evaporator used in this work is an *Edwards Coating System E306A*. It is pumped down to a base pressure of typically 2×10^{-6} mbar using rotary and diffusion pumps. The typical working pressure is 4×10^{-6} mbar. Metallic masks for ion milling are fabricated from Cr which is evaporated from source material placed in "baskets". More details regarding the choice of metallic mask may be found in section 3.5.2. The *Edwards Coating System E306A* is also equipped with a quartz crystal microbalance thickness monitor which permits accurate measurement of film thickness to ± 0.1 nm.

3.2 Strains Induced During the Growth of $REFe_2$ Thin Films and Multilayers

When depositing films using the *Balzers UMS 630 UHV* MBE device, *in-situ* RHEED measurements show that the first stage of film growth is island-like, that is 3D growth rather than 2D growth. This growth mechanism is confirmed in other similar systems [8]. Island-like growth is a classic signature of a growth mechanism that is evolving in an attempt to reduce the strain within the system [9]. This strain is due to a mismatch in the lattice parameters of the substrate and the film and can be alleviated by including various inter-layers between the substrate and the film and by altering the growth temperature. The effect of lattice mismatch between the substrate and the film, the effect of the mismatch between the different layers within a multilayer, and the effects of growth temperatures are described in this section. In addition, the combined effects of the different strain terms are discussed and compared to experimental results.

Together, these sections provide the basis from which many of the experimental observations of Chapter 5 are derived.

3.2.1 Film and substrate lattice mismatch strain

The $REFe_2$ grows in a cubic Laves phase structure with 8 RE atoms and 16 Fe atoms (see section 2.4.1). The Laves phase $DyFe_2$ and YFe_2 have bulk lattice parameters of 0.7324 nm and 0.7362 nm respectively. There is a large mismatch between the lattice parameters of the $REFe_2$ $\left(\langle a_{REFe_2}\rangle \approx 0.733 \text{ nm}\right)$ and Al_2O_3 substrate $\left(a_{Al_2O_3} = 0.4758 \text{ nm} \,\&\, c_{Al_2O_3} = 1.2991 \text{ nm}\right)$ which prevents the growth of an ordered Laves phase. The lattice mismatch strain ε_l is given by

$$\varepsilon_l = \frac{a_f - a_s}{a_s} \tag{2.50}$$

with a_f and a_s the lattice parameters of the film and substrate respectively.

In order to reduce this large lattice mismatch, a (110) Nb buffer layer [10] is first deposited onto the Al_2O_3 before growth of the Laves phase film. The body centred cubic (BCC) Nb $(a_{Nb} = 0.3317 \text{ nm})$, when orientated along (001), has an effective lattice parameter of $a_{Nb_{eff}} = \frac{\sqrt{3}}{2} a_{Nb} = 0.2873 \text{ nm}$. When orientated along $(11\bar{2}0)$ (the orientation of the substrates), the Al_2O_3 has an effective lattice parameter of $a_{Al_2O_{3_{eff}}} = \sqrt{2{a_{Al_2O_3}}^2(1 - \cos 120°)} = 0.8241 \text{ nm}$ as shown schematically in Wildes *et al.* [11]). Therefore three (001) Nb unit cells combine with one $(11\bar{2}0)$ Al_2O_3 unit cell with the epitaxial relationships $[1\bar{1}1]$ Nb || $[0001]$ Al_2O_3 and $[\bar{1}12]$ Nb || $[10\bar{1}0]$ Al_2O_3 [8] with a lattice mismatch of 4.4%. In addition to providing strain relief, the Nb layer also acts as a buffer to prevent interdiffusion between the substrate and the reactive $REFe_2$. ε_l between the $REFe_2$ and the Nb can be calculated using the difference between the lattice parameters of the Laves phase and two BCC Nb cells

$$\varepsilon_l = \frac{a_{REFe_2} - 2a_{Nb}}{2a_{Nb}} \tag{2.51}$$

which gives an average value of ~ 11.3% [8]. In an effort to reduce this, an additional Fe seed layer is incorporated between the Nb and the $REFe_2$ [12]. The Fe reacts with the Nb to form a NbFe alloy with a 2D rectangular mesh (r.m.) with lattice parameters $a_{r.m.} = 0.70 \text{ nm}$ along $[001]$, and $b_{r.m.} = 0.48 \text{ nm}$ along $[1\bar{1}0]$. Along $[001]$ the two

lattices align parallel, and along $[1\bar{1}0]$ the Laves phase aligns at 45° to two NbFe rectangular meshes. Thus the mismatch strains are given by

$$\varepsilon_l[001] = \frac{a_{\mathrm{REFe_2}} - a_{\mathrm{r.m.}}}{a_{\mathrm{r.m.}}}$$
$$\varepsilon_l[1\bar{1}0] = \frac{(\sqrt{2}a_{\mathrm{REFe_2}}) - 2b_{\mathrm{r.m.}}}{2b_{\mathrm{r.m.}}} \quad (2.52)$$

giving average values corresponding to 5.5% and 8.8%. This is small enough to permit the growth of the required cubic Laves phase structure, growing with the epitaxial relationships $[1\bar{1}0]$ $\mathrm{REFe_2}$ || $[1\bar{1}0]$ Nb and $[001]$ $\mathrm{REFe_2}$ || $[001]$ Nb [13].

3.2.2 Lattice mismatch strain

In systems with one $\mathrm{REFe_2}$ grown onto another $\mathrm{REFe_2}$, for example $\mathrm{DyFe_2}$ / $\mathrm{YFe_2}$, there is a mismatch between the lattice parameters of the layers. Indeed it has been shown that varying the strain within a system of (001) Cu / Ni / Cu can vary the critical thickness for perpendicular magnetic anisotropy [14], thereby providing a useful way for tailoring the magnetic properties of thin film samples. Given that both $\mathrm{REFe_2}$ layers in these samples are grown in the Laves phase, the lattice mismatch can be calculated using equation (2.50), substituting a_f and a_s with values for the lattice parameters for the two $\mathrm{REFe_2}$ films to give

$$\varepsilon_{lm} = \frac{a^1_{\mathrm{REFe_2}} - a^2_{\mathrm{REFe_2}}}{a^2_{\mathrm{REFe_2}}} \quad (2.53)$$

which, using values from section 3.2.1 for the lattice parameters for $\mathrm{YFe_2}$ and $\mathrm{DyFe_2}$, gives a value of ε_{lm} = 0.52% for $\mathrm{DyFe_2}$ / $\mathrm{YFe_2}$ bi-layer sample. It should be noted however that in a *multilayer* system the "substrate" and "film" ($a^1_{\mathrm{REFe_2}}$ and $a^2_{\mathrm{REFe_2}}$) are constantly alternating materials, therefore the above argument only holds true for a bi-layer system. In almost all of the systems studied in this work, there are multiple layers, therefore equation (2.53) must be used twice, varying the lattice parameters for ($a^1_{\mathrm{REFe_2}}$ and $a^2_{\mathrm{REFe_2}}$). This gives a value of ε_{lm} = –0.52% for $\mathrm{YFe_2}$ / $\mathrm{DyFe_2}$. Combining these values gives an average strain value of < 0.01% for $\mathrm{DyFe_2}$ / YFe2 multilayers, small enough to be considered negligible.

3.2.3 Thermal strain

For the successful MBE growth of Laves phase $\mathrm{REFe_2}$ intermetallics, the deposition temperature must be approximately 600 °C in order to ensure regular 2D growth. Below this temperature a film exhibiting 3D growth and characteristic islands like those

shown in Figure 3.6 occurs. For comparison, a successfully grown $REFe_2$ sample is shown in Figure 3.7. Note that the growth of $ErFe_2$ is expected to be very similar to $DyFe_2$ due to their very similar lattice parameters (section 2.4.1). During deposition there are no thermal stresses between the films and the substrate as the film is clamped to the substrate at the interface. When the sample is cooled down to room temperature (RT = 20 °C), the Al_2O_3 substrate contracts at a different rate to the metallic films due to their very different coefficients of thermal expansion (α) as shown in Table 3.1.

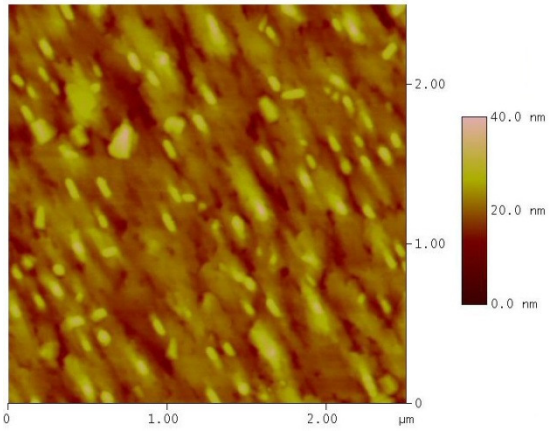

Figure 3.6: Atomic force microscopy (AFM) micrograph of a [5 nm $ErFe_2$ / 10 nm YFe_2] × 20 exchange spring sample grown below the optimum temperature of 600 °C. Preferential island growth along $[1\bar{1}0]$ is consistent with results reported in Mougin *et al.* [8]. Similar AFM results are obtained for samples with a total thickness < 50 nm where island growth also dominates.

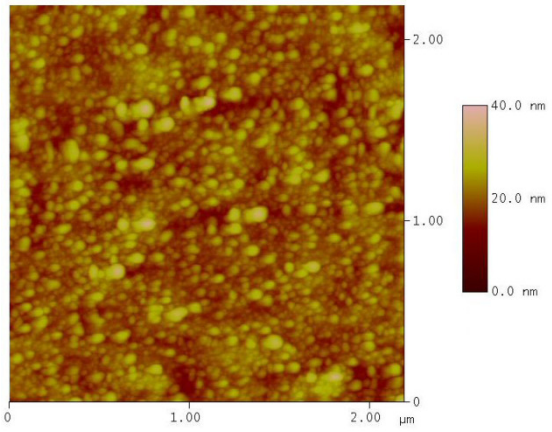

Figure 3.7: AFM micrograph of a [5 nm $DyFe_2$ / 10 nm YFe_2] × 20 exchange spring sample grown at 600 °C. There is an overall roughness to the film due either to the underlying island growth or post-growth sample oxidation, however this shows no preference along any crystalline axis.

Temperature	**Al_2O_3 (α_s)**	**$REFe_2$ (α_f)**
T_{RT} = 20 °C	5.4×10^{-6}	12×10^{-6}
T_d = 600 °C	8.9×10^{-6}	16×10^{-6}

Table 3.1: Thermal expansion coefficients for substrate and $REFe_2$ films at room and deposition temperatures.

The in-plane thermal strain $\varepsilon_{t||}$ due to differential thermal contraction can be calculated using

$$\varepsilon_{t||} = -(\alpha_f - \alpha_s)(T_{RT} - T_d) = -\Delta\alpha\Delta T \qquad (2.54)$$

with α_f and α_s the thermal expansion coefficients of the $REFe_2$ film and Al_2O_3 substrate and T_{RT} and T_d room temperature and deposition temperature respectively [15]. Using

the data from Table 3.1 (and assuming a linear relationship between the thermal expansion coefficient and temperature) this gives a value of $\varepsilon_{t||} = 0.39\%$. This *in-plane thermal expansion* is accompanied by a *perpendicular thermal contraction* $\varepsilon_{t\perp}$ which can be derived using [8];

$$\varepsilon_{t\perp} = -\left(\frac{2C_{12}}{C_{11}}\right)\varepsilon_{t||} \tag{2.55}$$

with C_{ij} the elastic constants of the Laves phase, which gives a value of $\varepsilon_{t\perp} = -0.13\%$. Mougin *et al*. [8] use the aforementioned fact that the dominant strain term is ε_{xy} (see section 2.3.4) and calculate the strain in the thin film samples using

$$\varepsilon_{xy} = \frac{a_\perp - a_\parallel}{2\langle a\rangle} \tag{2.56}$$

with $a_\perp = a + \varepsilon_{t\perp}a$, $a_\parallel = a + \varepsilon_{t\parallel}a$ and $\langle a\rangle = \frac{a_\perp + a_\parallel}{2} = a + \frac{a(\varepsilon_{t\perp} + \varepsilon_{t\parallel})}{2}$ and a the lattice parameter, to find a value of $\varepsilon_{xy} = -0.5\%$, *i.e.* an in-plane shear. This is in agreement with X-ray diffraction (XRD) data taken by Mougin *et al.* [8, 16], Bentall *et al.* [17] and this author (see sections 5.1.5 and 5.2.5), which confirms an in-plane lattice expansion and corresponding contraction along the (perpendicular) growth direction. Note that this is relatively constant across the complete Laves phase $REFe_2$ series due to the very similar lattice parameters as mentioned above. Note also that Bentall *et al.* [17] go further to show that the strain is not isotropic in the plane of the sample, rather it is anisotropic due to symmetry of the sapphire lattice in the (110) film plane. The result is that the value of α_s described above actually varies by some 10% along the two in-plane sample directions which are incorrectly assumed to be equivalent in Mougin *et al.* [8]. Whilst this fact is clearly important, the present work focuses on XRD measurements taken only in the growth direction so will be considered no further.

3.2.4 Combinations of strain terms and experimental data

Experimental results by Mougin *et al.* show that the $REFe_2$ in-plane strains are 0.6% and the perpendicular strains are –0.4% [8], *i.e.* there is an *in-plane expansion* and *perpendicular contraction*. These values are independent of the $REFe_2$ compound (see section 3.2.3) and therefore independent of the mismatch between the Laves phase $REFe_2$ compound and the r.m. NbFe alloy lattice parameters, and they are considerably smaller than those predicted by the lattice mismatch calculations (equations (2.50) – (2.52)). In addition to this, the $REFe_2$ Laves phase's average lattice parameter is

$\langle a_{\mathrm{REFe_2}} \rangle \approx 0.733$ nm which is larger than $a_{\mathrm{r.m.}}$, and $\sqrt{2}\langle a_{\mathrm{REFe_2}} \rangle$ is also larger than $2b_{\mathrm{r.m.}}$ (see section 3.2.1). Therefore an in-plane contraction of the Laves phase and a corresponding perpendicular expansion should be expected. This is *opposite* to the aforementioned experimental results.

Returning to equations (2.54) and (2.55), it is noted that they too are independent of the $REFe_2$ and crucially, have their sign in *agreement* with the experimental values (although they do underestimate these values slightly). Thus the thermal strain terms, $\varepsilon_{t||}$ and $\varepsilon_{t\perp}$, give values that are in far better agreement with the experimental data than the lattice mismatch strain terms ε_l. This leads to the conclusion that *the measured strains are thermal in nature*. In good agreement with this is the fact that as film growth progresses and its type alters from 3D to 2D, the lattice mismatch strain decreases significantly (as evidenced by *in-situ* RHEED, and *ex-situ* XRD and AFM measurements), thus the initial 3D growth compensates for almost the entirety of the lattice mismatch strain [18]. However in the thicker samples, which are dominated almost entirely by 2D growth, there is still a measured strain, a strain which can therefore only be thermal in its origin. Therefore it is concluded that there is an *in-plane expansion* and *perpendicular contraction* of the Laves Phase, depicted in Figure 3.8.

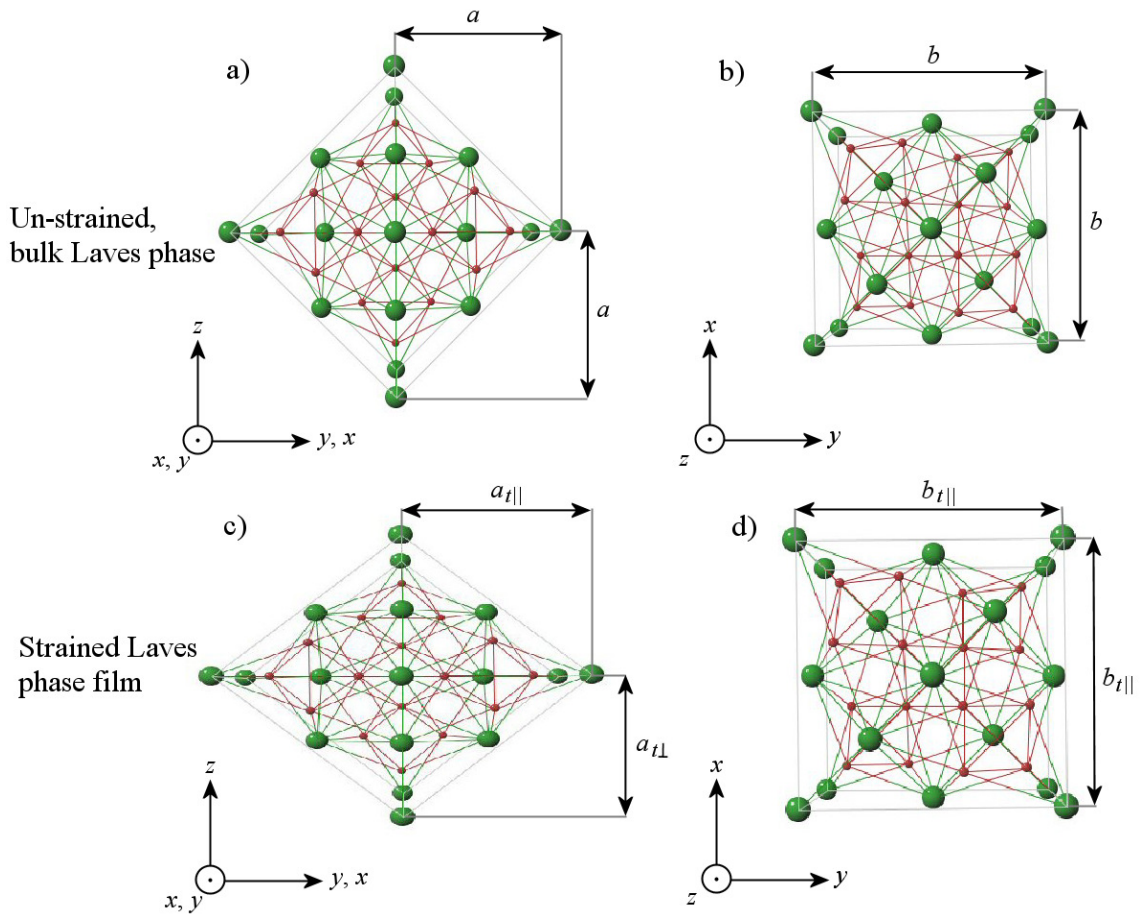

Figure 3.8: Schematic representation of the Laves phase structure in its bulk (images a) & b)) and strained (images c) & d)) configurations [19]. The sample growth is in the z-direction ([110] axis) thus the x- and y-directions form the sample plane. Image c) shows the thermally strained Laves phase with $a_{t\perp} < a$, *i.e.* contraction in the z-dimension, and $a_{t||} > a$, *i.e.* expansion in the y- (and x-) dimension. Image d) shows the corresponding x-y plane of the trained Laves phase, illustrating the lattice expansions in the x-y plane with $b_{t||} > b$.

3.3 Electron Microscopy

Since its conception in the 1930s the electron microscope has undergone continual extensive development, reaching a design similar to those used routinely to this day in the 1950s [20]. There are fundamentally two types of electron microscopy; scanning electron microscopy (SEM) and transmission electron microscopy (TEM). The vast majority of the sample patterning and analysis experiments conducted in this work is based upon SEM but for completeness an outline of TEM is also presented.

Common to all electron microscopes is the basic operational functionality of the microscope "column" – a high vacuum region in which electrons are emitted, accelerated and focussed. Electrons are emitted from a point-like source and then accelerated by a high voltage. The beam of electrons is then demagnified and focussed

to form the required beam diameter ($Ø_b$) using electromagnetic condenser lenses. The beam then passes through a mechanical aperture which controls its spread and collimation. The beam is then finally focussed on the sample surface with an objective electromagnetic lens. The resolution of the electron microscope is limited ultimately by the smallest value of $Ø_b$ which still offers a workable signal to noise ratio (SNR). The trade-off between small $Ø_b$ and high SNR can be understood in terms of the number of electrons arriving at the sample surface – "current density" or more commonly "source brightness".

A significant amount of the work presented in this thesis has been conducted using electron microscopes, most specifically an *LEO 1455 VP*. This work has required the input of considerable time and effort to improve and optimize the equipment available (assisted on occasions by Prof. Alan Fox). The result of this has been an increase in brightness of nearly two orders of magnitude and the subsequent significant improvement in both resolution and throughput of electron beam lithography (see section 3.4). A detailed description of electron microscopy is presented in this section in order to fully describe the work undertaken, covering topics including the available sources of electrons, the key components relating to the focussing of these electrons, descriptions of the interactions between electrons and samples, and the types of electron microscope and detection methods available.

3.3.1 The electron source

There are several sources of electrons employed in electron microscopes which can be conveniently grouped into two main categories. Traditional *thermionic* emitters which offer relatively low brightness but are exceptionally stable and cheap to operate, and *field* emitters which offer a large gain in brightness but can be less stable and are considerably more costly to operate.

The earliest electron microscopes used a thin tungsten wire bent into a hairpin shape (known as a filament) as a source of electrons. A relatively large current (typically 2 – 3 A) is passed through the W filament causing it to heat up to ~ 3000°C, giving the electrons enough energy to overcome the work function and be thermally emitted from the small, point-like source which is the apex of the hairpin. In reality this source is neither symmetric nor point-like (typically a 50 μm^2 emission area) but it does offer exceptional thermal stability (± ~ 1% $hour^{-1}$). This is the main reason why W filaments are still found in many commercial instruments to this day. At the onset of

the fabrication work discussed in this thesis, the *LEO 1455 VP* SEM was equipped with a W filament. In order to improve the ultimate resolution and SNR in an electron microscope a smaller $Ø_b$ and a higher beam current (I_b) is required. Decreasing $Ø_b$ will improve resolution but once values of ~ 15 nm are reached the SNR becomes too small, resulting in characteristically "grainy" images. Increasing the acceleration voltage will help alleviate this problem but can lead to a reduction in contrast due to the larger beam-sample interaction volume (described in section 3.3.5). To further increase the resolution an improved, more coherent source of electrons is required. Therefore the *LEO 1455 VP* SEM was upgraded to operate with a higher brightness lanthanum hexaboride crystal (LaB_6) electron source.

The LaB_6 source is a single crystal with a truncated ⟨100⟩ surface. This is held in place by a carbon ferrule which is mounted onto a single-piece carbon rod [21]. This in turn is mounted onto a ceramic sub-base and then on a further base tailored to the specific microscope. The carbon and ceramic elements are intended to minimise thermal expansion and contraction of the LaB_6 crystal during its operation. Compared to the W filament, electron emission from the LaB_6 crystal requires heating to only 1,600°C as the work function is lower, therefore smaller currents of 1.5 – 2 A are used. An SEM micrograph of a LaB_6 crystal manufactured by *Kimball Physics Inc.* installed in the *LEO 1455 VP* SEM is shown in Figure 3.9. The uniformity of the micro-flat coupled with its small size compared to the equivalent region of the W filament offers a much more point-like source with nearly equal thermal stability (± ~ 3% $hour^{-1}$). In realistic working terms the brightness of the LaB_6 crystal is roughly an order of magnitude improvement over the W filament (~ 4×10^4 $Acm^{-2}sr^{-1}$ for W filament [22] and ~ 4×10^5 $Acm^{-2}sr^{-1}$ for LaB_6 crystal [23]). This permits easier, higher SNR imaging with a decreased $Ø_b$ of ~ 5 nm. It should be noted that the LaB_6 crystal requires a much higher vacuum environment in the gun region than the W filament in order to assure a satisfactory operational lifetime [24] and as such column pumping and column isolation had to be employed on the *LEO 1455 VP* SEM.

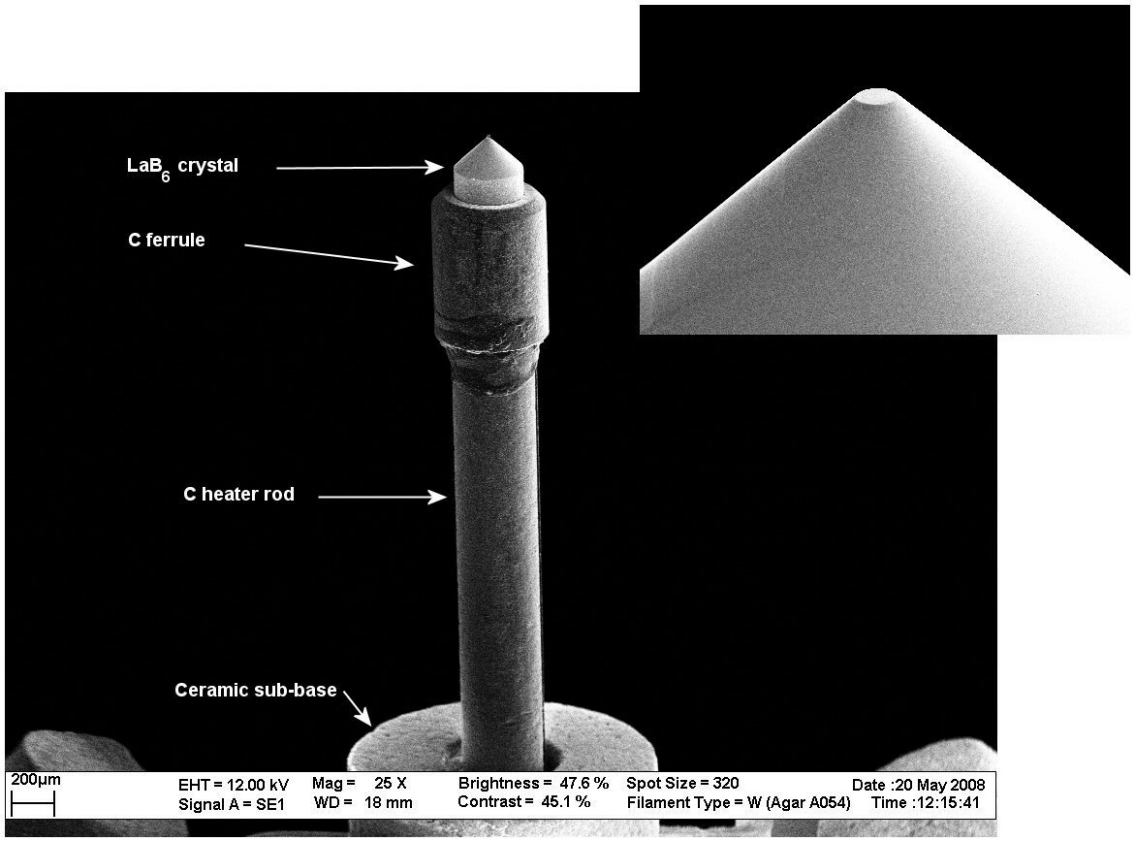

Figure 3.9: 25 × magnification SEM micrograph showing the LaB_6 crystal assembly for use in an *LEO 1455 VP* SEM. Inset: 500 × magnification of the LaB_6 crystal micro-flat. Cone angle 90°, diameter 15 μm.

In contrast to the aforementioned W filament and LaB_6 crystal thermionic electron sources, a much brighter source can be obtained by exploiting field emission of electrons. This can be in conjunction with thermionic emission (the Schottky effect), or on its own (*high* field emission). All field emission gun (FEG) electron sources have a single crystal W tip sharpened electrochemically [25] down to a diameter of hundreds of nm – the benefits of which are described in Crewe *et al.* [26]. The Schottky effect [27] relies on the application of a small positive potential (hundreds of V) to an electrode placed near to a thermally heated metallic surface. For a Schottky FEG, the W tip is coated with ZrO_2 which decreases the work function of the W further still, thereby increasing the electron yield. If the W tip is held at an even higher negative field with respect to the electrode, the potential barrier will be diminished further. This permits the quantum tunnelling of electrons, effectively reducing the work function of the tip to zero. This effect is known as *high* field emission and is employed in both thermally assisted and cold FEG electron sources. Typical thermal stabilities associated with the

FEG sources are: Schottky FEG ± ~ 1% $hour^{-1}$, thermal FEG ± ~ 6% $hour^{-1}$ and cold FEG ± ~ 5% ¼ $hour^{-1}$. Therefore a cold FEG would be an unsuitable source of electrons for electron beam lithography. It does however have a significantly smaller energy spread ($\Delta E \approx 1$ eV) and therefore reduced chromatic aberration (see section 3.3.3) making it especially suited to high resolution transmission electron microscopy (TEM) (see section 3.3.6). The FEG electron sources offer typical brightnesses of 5×10^7 $Acm^{-2}sr^{-1}$ [28] and hence a smaller $Ø_b$ can be achieved with an acceptable SNR giving improved resolution (SEM down to ~ 1 nm). Crewe *et al.* [26] offer an interesting direct comparison between W filaments and cold FEGs showing that for $Ø_b < 100$ nm the aforementioned increase in brightness holds true, but for $Ø_b > 200$ nm the W filament in fact offers increased brightness. This is due to the FEG brightness being limited by the operating aperture as described in Chang [29] and Broers [30]. In practice all experiments described in this work are conducted using $Ø_b < 35$ nm hence a FEG provides the brightest source of electrons. A *JEOL JSM 6500 F* Schottky FEG SEM is used for energy dispersive X-ray spectroscopy. For analysis of sample growth performed at the University of Oxford, a *JEOL 4000 EX* (LaB_6) TEM and *JEOL 3000 F* (FEG) TEM were used [31].

3.3.2 The Wehnelt

In both instances above, the electrons are accelerated to high voltages. This is provided by a "Wehnelt". A Wehnelt is essentially an anode held at a high potential with respect to the electron source which causes the electrons to be accelerated away from the source. A Wehnelt for a LaB_6 installation is shown in Figure 3.10. Readers are referred to Sewell [32] for more information regarding traditional thermionic Wehnelts and Crewe *et al.* [26] for further discussions and designs of FEG Wehnelts.

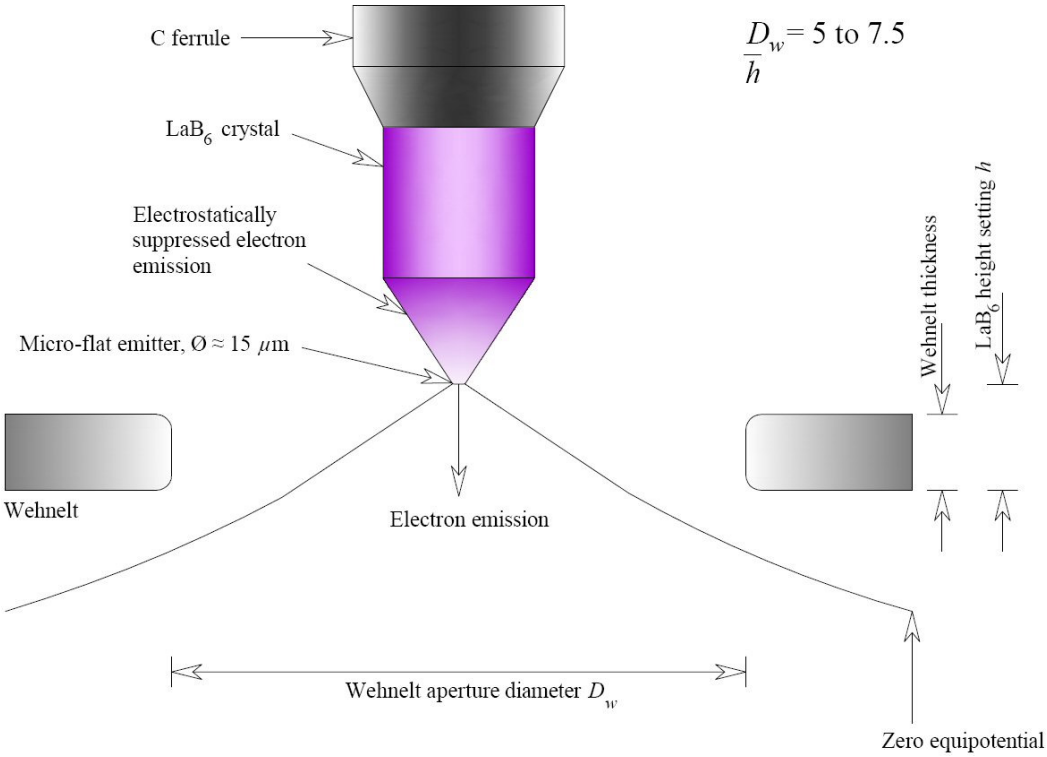

Figure 3.10: Schematic diagram of a typical Wehnelt design for a LaB_6 electron emitter.

There are two principal adjustments concerning the positioning of the electron emitter (cathode) within the Wehnelt: the centring of the cathode within the Wehnelt aperture (D_w), and the height (h) adjustment of the cathode within this aperture ($\frac{D_w}{h}$ ratio), which must be adjusted to give optimal electron emission whilst avoiding space charging at the cathode tip. Both are performed manually using a series of adjustment screws and threaded mechanisms while viewed with an optical microscope. It should also be noted that during operation the cathode will expand forwards as it heats up so $\frac{D_w}{h}$ should be adjusted accordingly.

A calibration curve showing the beam current (I_b) for different beam diameters ($Ø_b$) is shown in Figure 3.11 for the *LEO 1455 VP* SEM, comparing the thermal W and LaB_6 electron sources. This graph also illustrates the need for proper emitter alignment within the Wehnelt in order to maximise performance.

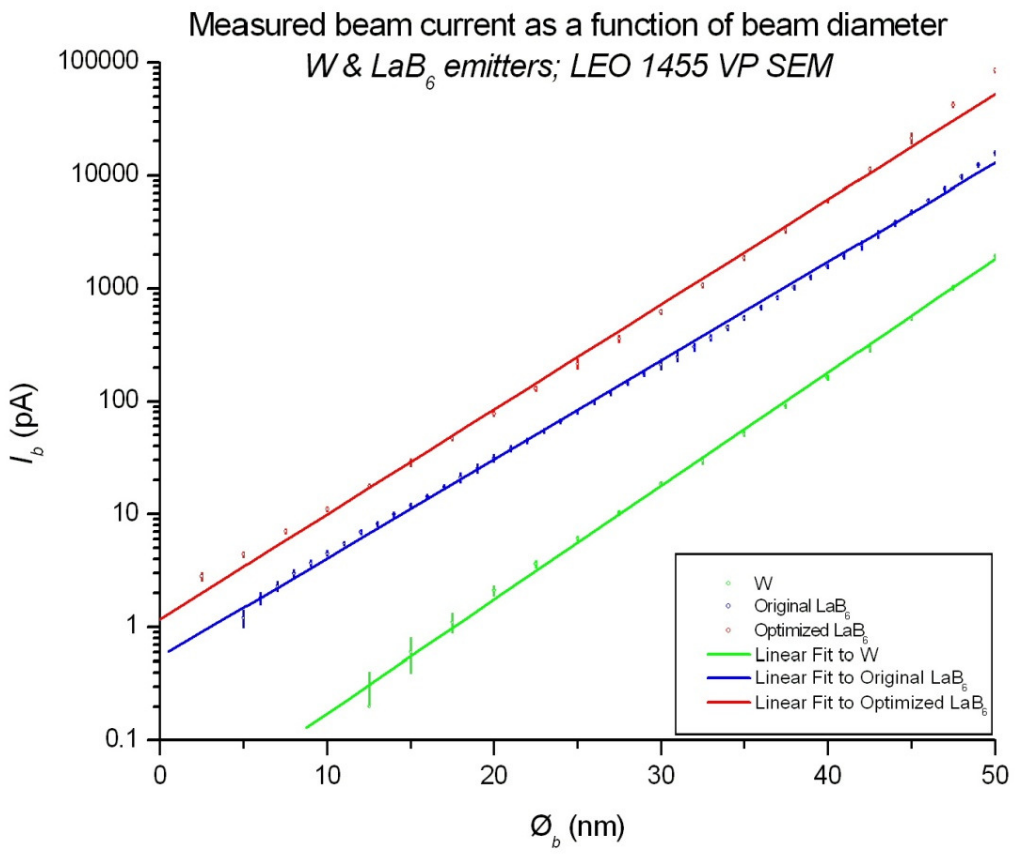

Figure 3.11: Log / Linear calibration graph for W and LaB_6 electron emitters in the *LEO 1455 VP* SEM. The data for the original thermal W filament are shown in green. The blue data are measurements made after initial setting up of LaB_6 emitter, and the red after full Wehnelt adjustment including compensating for thermal expansion. Correct Wehnelt adjustment permits a gain of 3 – 5 × in I_b whilst also allowing for the use of smaller $Ø_b$ (25 nm *c.f.* 50 nm). It is also clear that the fully optimized LaB_6 crystal emitter gives an increase of nearly two orders of magnitude in I_b over the thermal W filament. Accelerating voltage = 20 keV.

3.3.3 Electron microscope optics

After acceleration to a high voltage the beam of electrons requires focussing on the sample surface. After the beam is demagnified, the focal lengths of the electromagnetic condenser lenses are adjusted in order to define the required $Ø_b$. In order to ensure good resolution, the value of $Ø_b$ needs to be at least ½ that of the smallest feature size to be resolved, and for electron beam lithography typically ¼ is recommended [29]. There are two types of aberration which reduce the real value of $Ø_b$ and ultimately the achievable resolution; spherical and chromatic.

1. Spherical aberrations are ascribed to a deviation from perfect refraction of the incident electrons by the lens, *i.e.* those electrons not exactly on the optic axis will undergo an increase in refraction, thereby not producing a single focal *point*, rather one with a *waist*, increasing the real value of $Ø_b$ and therefore reducing

resolution. It was shown by Scherzer [33] that a perfect, spherical aberration corrected lens cannot be manufactured for electron optics. However, some modern TEMs have functionality to correct for spherical aberrations using two crossed sets of quadrupoles and octupoles [34, 35]. Such aberration correction is also utilized in the He^+ ion microscope described in section 3.8

2. In terms of visible light, chromatic aberrations manifest themselves as the under-focussing of long wavelengths compared to shorter wavelengths since the lens has a specific dispersion. Therefore in terms of electron microscopy, electrons with different energies, will be focussed to a different point, thereby causing $Ø_b$ to have a waist rather than be point-like. This can be overcome by ensuring a very small spread of electron energies (ΔE). This is achieved either by using an electron source with small ΔE – preferably a cold FEG electron source – or by employing energy filtering. Chromatic aberration is only a noticeable issue in electron microscopes with post specimen lenses (TEMs) and therefore is not of concern in SEMs (and thus the majority of this work).

3.3.4 Electron beam alignment

When the electron source is installed within the Wehnelt it is conducted using an optical microscope. In order to centralise the electron beam more accurately, a further series of electromagnetic coils are utilised, referred to as alignment coils, or more commonly "shift" and "tilt" adjustment. Alignment is performed with the electron microscope operating in "emission" mode where a virtual image of the electron source is viewed. Here, the electron beam can be made symmetric (tilt) and centralised (shift), creating a more collimated, brighter source of electrons. Further beam alignment methods include using a "focus wobble" technique whereby the focus is continuously automatically varied in order to perform fine aperture alignment and stigmation correction[ii].

[ii] If, as the focus is adjusted, the electron beam does not pass through the centre of the aperture, the image will move laterally since the beam is not centred on the optic axis. Similarly, if the beam is non-circular (*i.e.* stigmated), the image will change shape asymmetrically as the focus is adjusted.

3.3.5 Electron interactions

When an electron enters a solid sample, a certain amount of that sample is irradiated directly below the electron's point of entry. This is characterized by one of four possible interactions:

1. Inelastic collisions with electrons.
2. Elastic collisions with an atom.
3. Inelastic collisions with an atom.
4. Elastic scattering by the crystal.

These interactions are described in detail below, but first a schematic of this irradiated region – hereafter referred to under the more common nomenclature of "interaction volume" – is presented in Figure 3.12. Some typical values associated with both the penetration depths of electrons (D) and the associated resolutions (R) are given in Table 3.2, which should be viewed in conjunction with Figure 3.12.

Property	Typical range	Comments
R_{SE}	2 – 5 nm	Approximately independent of beam voltage
R_{BSE}	~ 100 nm	
R_X	1 – 5 μm (depending on sample)	
D_{AE}	~ 1 nm	Strongly dependent on beam voltage; typical values given for 20 keV
D_{SE}	5 – 50 nm	
D_{BSE}	50 – 200 nm	
D_X	> 200 nm	
D_e		
E_e	Typically 5 – 30 keV	
$Ø_b$	Typically 1 – 50 nm depending on resolution and SNR required	

Table 3.2: Some typical depths and resolutions associated with the electron interaction volume.

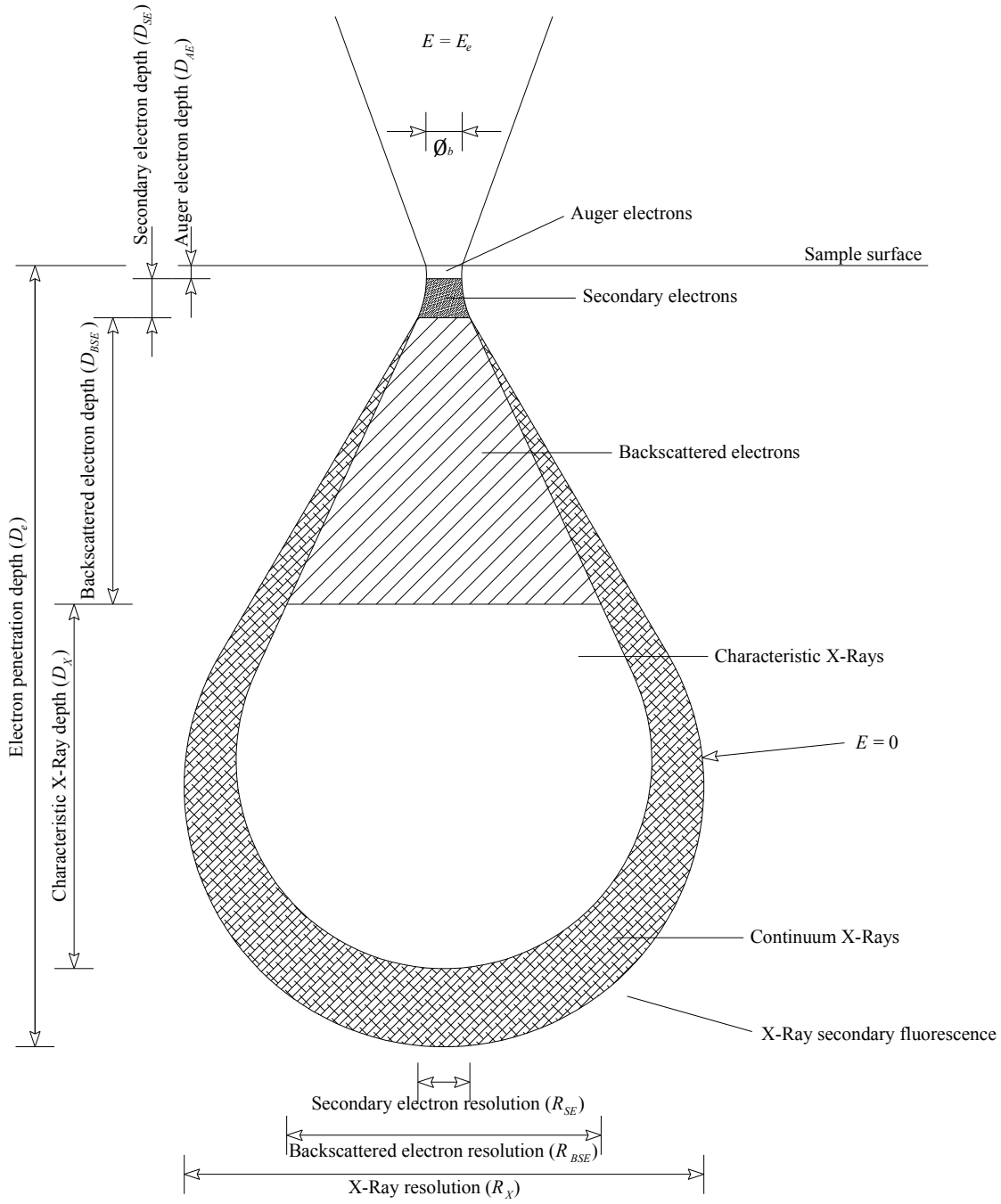

Figure 3.12: Schematic of the electron interaction volume within a solid sample. $E = e\Delta V$ with E = electron energy, e = electron charge and V = accelerating voltage.

When the incident high energy electron suffers an inelastic collision with a bound electron within the solid it transfers much of its energy to the bound electron, promoting it to a much higher, unbound state. This is the source of secondary electrons (SE) which are emitted from near the sample surface and give details of the sample topography. The vacancy which this electron leaves (at energy level E_1) is filled by another electron from a higher energy level (E_2), losing an amount of energy ΔE

characteristic to the irradiated region of the sample, $\Delta E = E_2 - E_1$, causing the emission of either a characteristic X-ray or Auger electron. Since ΔE is specific to each individual element it is simple to see how information about the sample composition can be found by detecting ΔE (or $\Delta\lambda$, with λ = wavelength) using energy dispersive X-ray analysis (EDX), wavelength dispersive X-ray analysis (WDX) or Auger electron detection. EDX is the most common elemental detection method in electron microscopy and has been used on occasion in this work to define sample composition (see section 3.3.7).

When the beam of electrons interacts with the atom as a whole it is far more likely to be with the massive nucleus rather than the small electrons. Since the charge on the nucleus is opposite to that on the electron, the electron is attracted to it, but as the electron is moving very quickly (typically 5 – 30 keV in an SEM) it is not "captured" by the nucleus but rather it is deflected, causing elastic scattering. Elastic scattering angles range from a few degrees up to 180°, with electrons scattered through the largest angles re-emerging from the sample known as back scattered electrons (BSE). It is worth noting that an incident electron can elastically scatter off of several different nuclei before re-emerging from the sample – a key reason behind the "proximity effect" (section 3.4.5). It is clear that this angle depends on the size of the nucleus, *i.e.* the atomic number *Z*, and therefore an image can be obtained which corresponds to the sample composition via BSE detection. Low *Z* elements will cause only a small amount of the incident beam to be backscattered whilst high *Z* elements will cause large amounts of electron backscattering.

If the collision between the electron and the nucleus is in fact inelastic (< 1% occurrence), an X-ray is emitted, known as bremsstrahlung. Bremsstrahlungen form a continuous background and have a dependence on electron beam energy, sample atomic number *Z* and also on electron beam incident angle. The latter is due to the fact that unlike inelastic electron – electron collisions where a characteristic X-ray is emitted some time later and thus has no angular dependence, the bremsstrahlungen are emitted at the instant the beam is inelastically scattered by the nucleus.

Finally, the electron beam can experience Bragg diffraction due to interactions with the bulk crystalline lattice. Valuable information regarding the crystalline structure of the sample can be obtained by exploiting this technique. However, this will not be discussed further as it is outside of the scope of the work described here. Readers are referred to Jones for further information [36].

3.3.6 Types of electron microscope

Until now no real distinction has been made between SEMs and TEMs. In short the SEM is more readily available, easier to use, has far simpler sample preparation and is considerably cheaper both to purchase and operate. The TEM however is preferable when ultimate resolution is at stake. In its most simple form, SEM users are looking *at* the sample and TEM users *through* the sample.

In an SEM, the beam of electrons is scanned across the sample surface in a raster fashion using electromagnetic scanning coils positioned in front of the objective electromagnetic lens, causing the beam to be deflected in both the *x*- and *y*-directions. Information from the sample is therefore built up in this raster fashion with typical acquisition times ranging from a few tenths of seconds through to a few minutes. SEM sample preparation is simple and straightforward. As long as the sample will physically fit into the sample chamber and can be traversed via the use of an automated stage it can usually be imaged. The simplest samples to image are metallic since these are good conductors and prevent charge accumulation on the sample surface. If a sample is only metallic on one face and insulating on the other (typical arrangement for metallic films analysed within this work) either a metallic contact or conductive adhesive tape can be placed on its conducting surface to electronically ground it to the sample holder. For samples which are non-metallic, a thin coating of a metallic element (typically Au) can be sputtered or evaporated onto the sample surface to form a thin conductive layer.

In a TEM, the sample sits on or within the objective lens rather than on a separate stage. The standard mode of operation is with a fixed beam, thus forming the whole image at once without the aid of scanning coils. Some TEMs can also work in scanning mode (STEM), in which the beam is rastered across the sample surface. Since the beam of electrons must penetrate through the sample, the sample must be "electron transparent". There are several processes whereby this can be achieved, but summarised here is that used by Wang [31] to prepare the MBE grown Laves Phase samples studied in this work. Cross-sections of thin film samples on Al_2O_3 substrates are mechanically ground down to ~ 10 μm using diamond coated lapping films and a dimple grinder. Following that, Ar^+ ion milling is used to reduce the thickness to hundreds of nm (electron transparent) using beam energies ranging from 5 keV for coarse machining down to 1 keV for the removal of the final few layers. Ar^+ ion beam milling is discussed at length in sections 3.6.3 to 3.6.6. Whilst TEM provides a realistic

means of visualising the atomic world, it is outside the scope of the work covered in this thesis, thus shall be discussed no further.

3.3.7 Detector types

Sample topography in SEMs is provided by SE detection. The SEs are attracted to a positively charged Faraday cage and accelerated towards a scintillator. This gives off photons which traverse along a light guide and are then converted back to electrons before being multiplied by a photomultiplier. Note that due to the typical placement of the SE detector (away from the sample, towards a corner of the vacuum chamber), it can be used to image the sample when it is tilted, providing useful insights into the sample thickness. A BSE detector is usually placed directly above the sample surface in an SEM, concentric with the electron beam. BSE detectors are of the scintillator or semiconductor type, providing sample composition information. In the case of the *LEO 1455 VP* SEM, this detector has 4 equal quadrants which can be activated independently thus permitting the collection of topographical information as well. Further information on SE and BSE detectors is available in Bozzola and Russell [37].

The principle behind EDX is the absorption of X-rays and the subsequent creation of photoelectrons which are then swept to electrodes by a large applied electric potential. This electric signal is then amplified and collated in a multichannel analyser. Many thousands of these events build up a spectrum which is characteristic of the elements present in the sample, with the peaks in signal amplitude attributed to characteristic X-rays and the background to bremsstrahlungen. WDX uses Bragg diffraction to resolve information regarding the elements present in the sample. X-rays from the sample are incident onto a crystal and then diffracted through a known angle θ onto a detector. Bragg's law, $n\lambda = 2d \sin\theta$ then allows for the X-ray wavelength λ to be calculated and the sample composition built up via varying θ. Since θ has to be varied to obtain a spectrum, WDX is a much slower process than EDX but the resolution is much greater and the background noise much smaller.

3.4 Electron Beam Lithography

Lithography is a collective term used to describe a number of closely related processes which include coating the sample with a "resist" that is sensitive to radiation, exposing this sample to radiation in well defined areas and then developing the sample. Electron

beam lithography (EBL) is the process by which a focussed beam of electrons (the source of radiation) is drawn across the sample surface in a manner corresponding to a pattern desired by the user. More correctly this process is known as "direct write" EBL since other, non-serial processes such as "projection printing" are possible [38]. Whilst these processes are useful in device replication, they are not suitable for the prototype fabrication required here. EBL is analogous to conventional photolithography but offers a reduction in minimum feature size of two or more orders of magnitude.

In order to realise where the beam of electrons has or has not been on the sample surface, *i.e*. the ability to define a pattern in the required regions *only*, the sample must first be coated with a thin polymer film (~ 100 nm – 1 μm thick) which is sensitive to electron radiation – "eBeam resist". After electron irradiation the sample is then developed to remove the unwanted material, leaving a pattern representative of that which the user initially desired. Devices of 1 μm were described as early as 1967 by Larkin and Matta [39], whilst features smaller than 10 nm were demonstrated in Khoury and Ferry [40] three decades later. Shortly after this Vieu *et al.* [41] demonstrated 3 – 5 nm structures; amongst some of the smallest devices fabricated using eBeam lithography. The aim of section 3.4 is to describe the fundamental aspects of EBL including its implementation, optimization and the "proximity effect".

3.4.1 Implementation of electron beam lithography

Whilst it is true that EBL is a direct descendant of SEM there are several issues which need to be addressed before an SEM can be used for EBL. There are two types of EBL systems available, complete systems and "inserts". Inserts are EBL systems which are added onto an existing SEM at a later date. The *LEO 1455 VP* SEM used in this work has an *ELPHY Quantum* insert by *Raith* [42].

In EBL, the total area over which the electron beam is scanned is referred to as the *write field* (WF). The area in which the individual *patterns* are defined is the *working area* (WA) (see Figure 3.13).

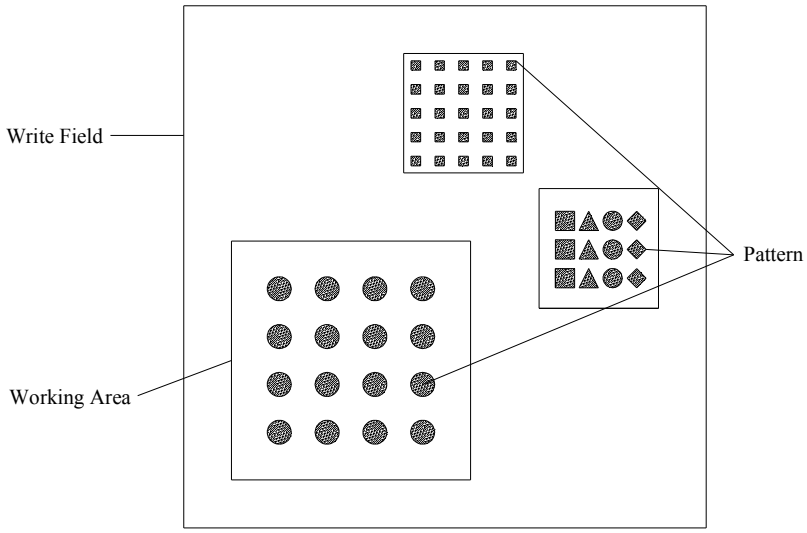

Figure 3.13: Schematic diagram of a write field, several working areas and many individual pattern elements.

In order to position different WAs within a WF, and different pattern elements within a WA, the EBL system requires a "beam blanker". This is typically in the form of an electrostatic or electromagnetic plate to which a potential of approximately hundreds of V can be applied many hundreds of times a second. This has the effect of deflecting the electron beam away from the optical axis and thus off the sample surface allowing regions to remain unexposed to the electron beam.

The individual pattern elements can be less than 10 nm [40, 41]. In order to achieve this resolution, the overall WF is typically ~ 10 – 100 μm. To achieve this resolution over a larger area, individual WFs may be stitched together. Their locations are defined in a "position list" and the sample stage is driven automatically to this location. Standard SEM sample stages are accurate to ~ ± 1 μm. For more accurate positioning a piezoelectric stage is coupled to a laser interferometer to achieve stitching accuracies of 20 nm or better.

The beam of electrons can be scanned across the sample surface in one of two ways: a raster scan or a vector scan. In the raster scan the beam is scanned across the entire WF and switched on and off in the relevant pattern regions (see Figure 3.13). This method was employed in early lithography systems whereby a flying spot scanner [43] was used to read the mask data from a scanned cathode ray tube, but has been superseded by digital computer controlled methods. In the vector scan method, the EBL computer scans the electron beam across only the WA. This method is far more

efficient and is employed in *Raith* systems. Further details describing both processes can be found in Ozdemir [44], Chang [45] and Tseng *et al.* [38].

3.4.2 Electron beam resist chemistry

eBeam resists can be grouped into two main categories: *positive* and *negative*. In both instances the resist material is a polymer consisting of long chains of hydrocarbons which are sensitive to electron radiation. In the case of a *positive* resist, the electron induced radiation damage depolymerises the long hydrocarbon chains by eliminating component atoms [46, 47], thus decomposing the resist into *shorter* chains. The opposite is true for a *negative* resist; the incident electron energy is used to polymerise short hydrocarbon chains into *longer* chains, a process known as cross-linking. The key is that in both instances there is a *change* in molecular weight of the regions subject to the electron radiation. The interactions between the electron beam and the resist will be considered again in the proximity effect section (3.4.5).

After pattern definition, the samples are developed using a solution which provides a differential development rate, *i.e.* a development rate dependent on molecular weight [48]. In both cases, the regions with the lower molecular weight (increased solubility) are preferentially developed (*i.e.* removed from the sample surface more quickly). The developer used in this work is methyl isobutyl ketone (MIBK), a solvent manufactured from acetone. This is typically combined with isopropyl alcohol (IPA) which is a development stopper. Hence by combining the two, the development rate is slowed, increasing potential resolution (but at the expense of throughput). After development, a pattern defined in a positive resist takes the form of a "hole" within the bulk resist, whilst one defined in a negative resist takes the form of a "pillar" on the sample surface.

3.4.3 Under-cut and bi-layer resist combinations

Referring back to Figure 3.12, an imaginary line can be drawn across this interaction volume at a value of $D \approx 100$ nm corresponding to the typical resist thickness used in this work. It is immediately clear that the value of $Ø_b$ at the bottom of the resist layer will be bigger than it is at the top. This serves to reduce the ultimate resolution (see the proximity effect section 3.4.5) but provides an "undercut"; that is a non-vertical sidewall profile to the exposed regions, akin to the eBeam resist interactions described in Heidenreich *et al.* [49] and Thompson et *al.* [50].

The undercut is advantageous for the process of "lift-off" (see section 3.5.2) since it helps prevent the formation of a continuous, impermeable layer when a material is deposited onto the lithographically defined pattern. However this undercut is typically very small, of the order of ~ 1 – 10 nm for a thin resist layer, so the deposition of more than a few nm of material will negate this effect leading to the formation of a continuous layer and the failure of lift-off. To overcome this effect, the author has developed a process in-house based on using two different molecular weight positive eBeam resists; Polymethylmethacrylate (PMMA) and methylmethacrylate – methacrylicacid (MMA-MAA). This is a similar technique to that used by Grundbacher *et al.* [51], Chen *et al.* [52] and Gritz *et al.* [53] but uses different resists and processing techniques. MMA-MAA is a "copolymer" to PMMA and has a higher dissolution rate, *i.e.* a larger amount is depolymerised per given amount of incident radiation than the PMMA. When MMA-MAA is applied to the sample below the PMMA layer, significantly more undercut is achieved (an example of this is shown in Figure 3.14). This facilitates lift-off which is easier and more reliable for thicker films, with successful results demonstrated for films with a thickness greater than 100 nm.

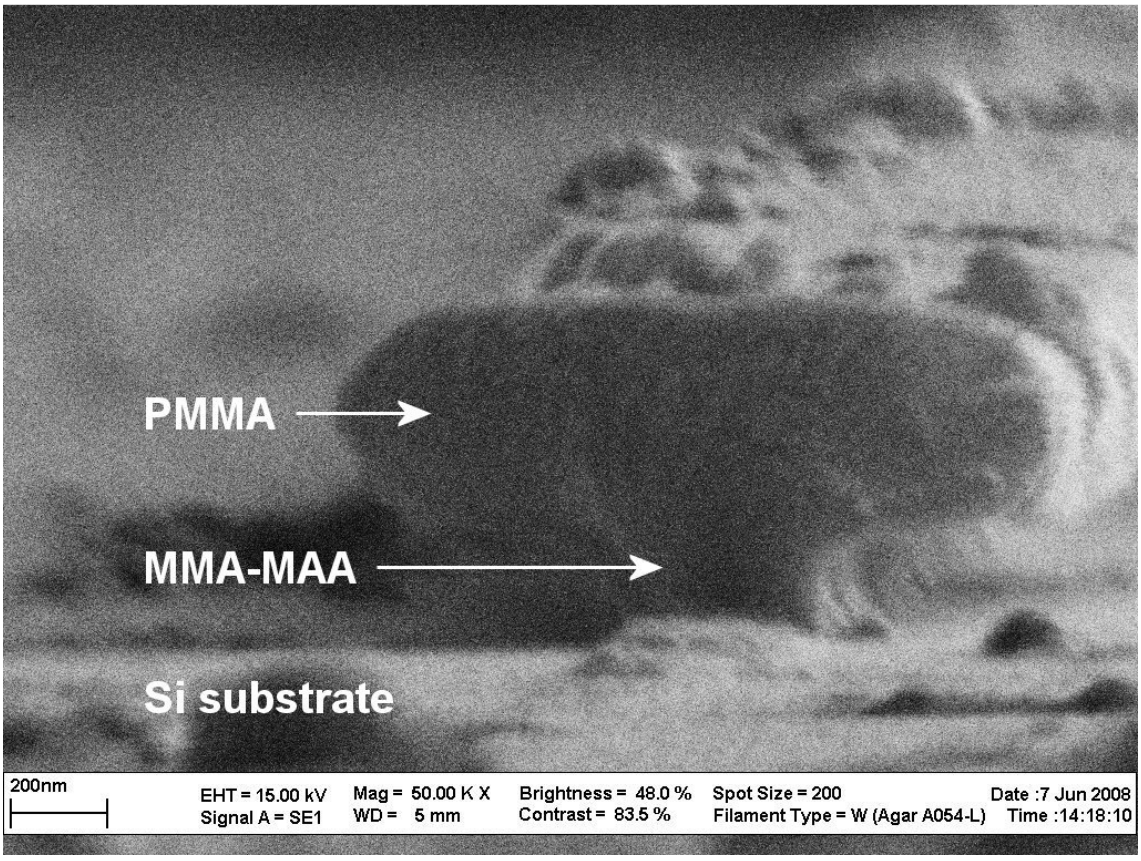

Figure 3.14: Cross-sectional SEM micrograph showing a T-gate structure. The top (PMMA) layer clearly suffers less under-cut than the bottom (MMA-MAA) layer. When material is deposited onto this structure, the shadow formed from the T-shape facilitates easy lift-off.

3.4.4 Resist application and lithography process

The two resists used to form the bi-layer combination are both supplied by *Microchem Corp.* [54]. The PMMA is "PMMA 950k A3"; it has a molecular weight of 0.95 gcm^{-3}, diluted to 3% in anisole. This is a higher dilution than is often used. A higher dilution results in a less viscous resist so a thinner layer can be applied to the sample, permitting higher resolution pattern definition. The MMA-MAA is standard "MMA(8.5)-MAA EL6"; 8.5% MMA, 91.5% MAA, diluted to 6% in ethyl lactate.

After resist application (see Appendix) the sample is loaded into the SEM and the relevant alignment, calibration and focussing procedures conducted. Sample alignment entails recording the sample position in *x*-, *y*- and *z*-axis SEM coordinates and translating this to the *u*-, *v*- and *w*-axis of the eBeam system. Calibration is the application of shift, rotate and zoom commands in order to ensure the correct positioning and scaling of the patterns to be defined on the sample surface. Focussing is achieved by "burning" contamination dots[iii] on the sample surface. Next the patterns to be applied to the sample are placed in the position list (and processed by proximity effect correction software if necessary (see section 3.4.5)). The position list is then executed and the patterns are defined on the sample surface. The time required to expose each pattern is defined by software calculations based upon values for the beam current (I_b), dose (d), step size (s) and dwell time (t). Patterns are executed in terms of "areas" (2D), "lines" (1D) and "dots" (0D, single pixel elements), indicated by a subscript a, l or p respectively. I_b is either measured directly using a Faraday cup or inferred from calibration data (see Figure 3.11, typically $I_b \approx 10$ pA ($Ø_b = 10$ nm)). d is a function of the accelerating voltage of the electron beam and the resist properties, typically set as $d_a = 100\ \mu Ccm^{-2}$, $d_l = 300$ $pCcm^{-1}$ and $d_p = 0.08$ pC. s is adjusted to be a negligible fraction of the pattern element size, typically 0.02 μm. t is calculated by the *Raith* software according to equations (3.1).

[iii] When PMMA or MMA-MAA are exposed to ~ 10 × the energy required to depolymerise the bonds, re-polymerization occurs (cross-linking of the bonds, creating an area resistant to further exposure (*i.e.* a negative resist)). When the SEM is operated in "spot" mode this forms a contamination dot on the sample which can be used to adjust and improve focus, beam alignment and astigmatism.

$$fd_a = \frac{I_b t_a}{{s_a}^2}$$
$$fd_l = \frac{I_b t_l}{s_l} \quad (3.1)$$
$$fd_p = I_b t_p$$

The pre-factor *f* is called the dose-factor. This is an experimentally defined factor used to find the optimum dose parameters, ranging typically from 0.4 through to 1.5, with the majority of successful patterns created with $f = 0.8 - 1.2$. It is found by conducting a "dose test". This is the simplest parameter to vary via the software since it is purely a scaling factor. It is optimised on each occasion a new pattern is desired using test samples.

Once exposure is complete, the samples are developed to leave the lithographically defined patterns on the sample surface. The development technique is also covered in the Appendix. All variables described within this section were extensively investigated and adjusted during this work to optimise the EBL process. The author has routinely achieved EBL resolutions of ~ 50 nm, although this is reduced to ~ 100 nm when using the bi-layer resist combination. This marks an improvement in resolution of between one and two orders of magnitude over the prior work conducted using this equipment.

3.4.5 The proximity effect

As described in section 3.3.5, when an electron undergoes an elastic collision with an atom its direction is altered, often by large angles leading to backscattering. Due to the elastic nature of these collisions, the backscattered electrons (BSE) have enough energy to cause the depolymerization (polymerization) of the positive (negative) resist. However, the BSE interact with the resist in locations that differ from the original beam position (recall that the electron can undergo many elastic collisions), leading to a spreading of the beam and the subsequent definition of patterns larger than those originally defined. This effect is termed "beam broadening". Beam broadening is dependent on the electron beam acceleration voltage, the resist molecular weight and thickness, and also the substrate material. This is generally not an issue for isolated line- and dot-like structures since the resist dose can be varied to account for this, but when patterns are more intricate (*e.g.* squares, hexagons *etc.*) or are placed in close proximity to each other ($\lesssim 2$ μm [55]), the beam broadening can enlarge intricate features and affect the exposure of neighbouring elements. This is the proximity effect.

It is defined as either the *inter* proximity effect, for the loss of resolution in intricate pattern elements, or the *intra* proximity effect, when pattern features are affected by their neighbours.

In general the proximity effect can be regarded as the overall effect of the dose received at each individual point (pixel) used to make up the entire pattern. For example, consideration should be given to two points on the resist surface, *P* & *Q* (separated by a distance *r*), which make up two independent pattern elements (intra proximity effect). The beam of electrons is incident first on *P*. Due to beam broadening, there is a rotationally symmetric distribution of radiation around *P* that is a function of *r*. Next the beam of electrons is incident on point *Q*, where the same distribution of radiation occurs. Now in the region between *P* & *Q* the sample has received a non-zero dose (the "reciprocity effect" [55]). If the dose received in this intermediate region is above the polymerizing (depolymerising) threshold, the positive (negative) resist will also be chemically altered, leading ultimately to the two patterns merging into one. Consideration should now be given to the above effect occurring for each pixel that makes up a larger pattern (inter proximity effect), *e.g.* one formed from 10 × 10 pixels (see Figure 3.15). The vast majority of the pattern (the central 9 × 9 pixels (*M* in Figure 3.15)), to a first order approximation, will be unaffected by neighbouring *M* other than to reduce the overall dose required for successful exposure. However, towards the edges (*E*) and corners (*C*), a higher dose will be required since pixels *M* have 8 neighbours, *E* only 5, and *C* just 3. Therefore the doses for successful exposure of pixels *E* and *C* will be larger than those for *M*. The first order approximation, that *M* is constant throughout the pattern, is in fact invalid since depending on the position of *M* it experiences a different total dose due to *all* of its neighbours (some of which are *E* and / or *C* in Figure 3.15), leading to a rather complex calculation. This is computed using Monte Carlo simulations of electron trajectories in proximity effect correction software (PECS). Figure 3.15 shows a schematic of the first order approximation of the proximity effect. It can be considered for either an array of 10 × 10 patterns (intra proximity effect) or a single pattern element consisting of 10 × 10 pixels (inter proximity effect). Figure 3.16 shows the result of *Raith* PECS on an array of 1 × 1 μm squares for 20 keV electrons where the intra proximity effect dominates, whilst Figure 3.17 shows an array of 2 × 2 μm squares for 10 keV electrons where the inter proximity effect is dominant.

C E E E E E E E E C
E M M M M M M M M E
E M M M M M M M M E
E M M M M M M M M E
E M M M M M M M M E
E M M M M M M M M E
E M M M M M M M M E
E M M M M M M M M E
E M M M M M M M M E
C E E E E E E E E C

Figure 3.15: Schematic diagram of the first order approximation of the proximity effect. The dose received at point *C* is lower than at point *E*, which itself is lower than at point *M*, due to different numbers of neighbouring elements.

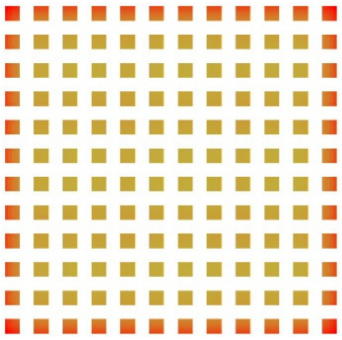

Figure 3.16: 1 × 1 μm squares corrected by PECS for 20 keV electrons – intra proximity effect dominant. Red = highest dose, yellow = lower dose.

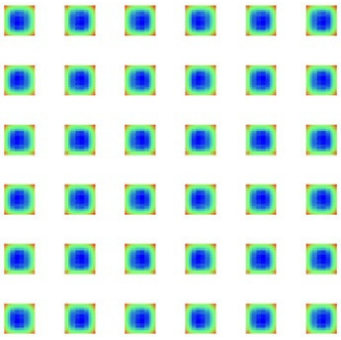

Figure 3.17: 2 × 2 µm squares corrected by PECS for 10 keV electrons – inter proximity effect dominant. Red = highest dose, blue = lowest dose.

Work has been ongoing since the mid 1970s [55, 56] to correct for both proximity effects. In essence each pixel that a pattern compromises is analysed and assigned a specific dose in order to minimise both inter and intra proximity effects and increase the overall resolution achievable. This is clearly illustrated by the varying colours in Figure 3.16 and Figure 3.17. For patterns with features smaller than 2 μm (other than lines and circles) described within this work, *Raith* PECS based on the above method has been used. Examples of 1 μm squares fabricated in PMMA both before and after implementation of PECS are given in Figure 3.18 and Figure 3.19 respectively. Recently work has been conducted by Lee and Anbumony [57] to model this effect in three dimensions, taking into account the resist thickness in order to improve resolution further still. A substantial review of EBL (and other related lithography techniques for nanoscale fabrication) is given in Martín *et al.* [58].

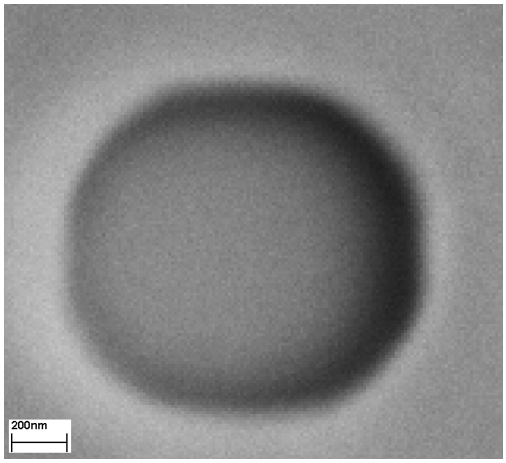

Figure 3.18: 1 μm square fabricated in PMMA using the *Raith ELPHY Quantum* insert in the *LEO 1455 VP* SEM without PECS. The radius of curvature to the corners is approximately 400 nm.

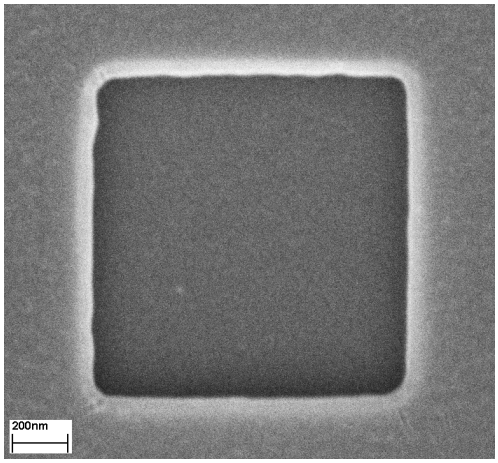

Figure 3.19: 1 µm square fabricated on the same equipment as Figure 3.18 but using PECS. The radius of curvature to the corners is less than 50 nm.

3.5 Mask design

Once the desired pattern is successfully defined in the polymer resist on a $REFe_2$ sample, it requires transfer down into the magnetic material below. This is achieved by etching, of which there are several different methods, discussed in section 3.6. All of these etching processes rely on one fundamental idea; to use a *mask* to remove material only in certain regions. The mask may be constructed from either a polymer (usually the eBeam resist directly) or a metallic material. Examples of different mask designs are presented in Figure 3.20.

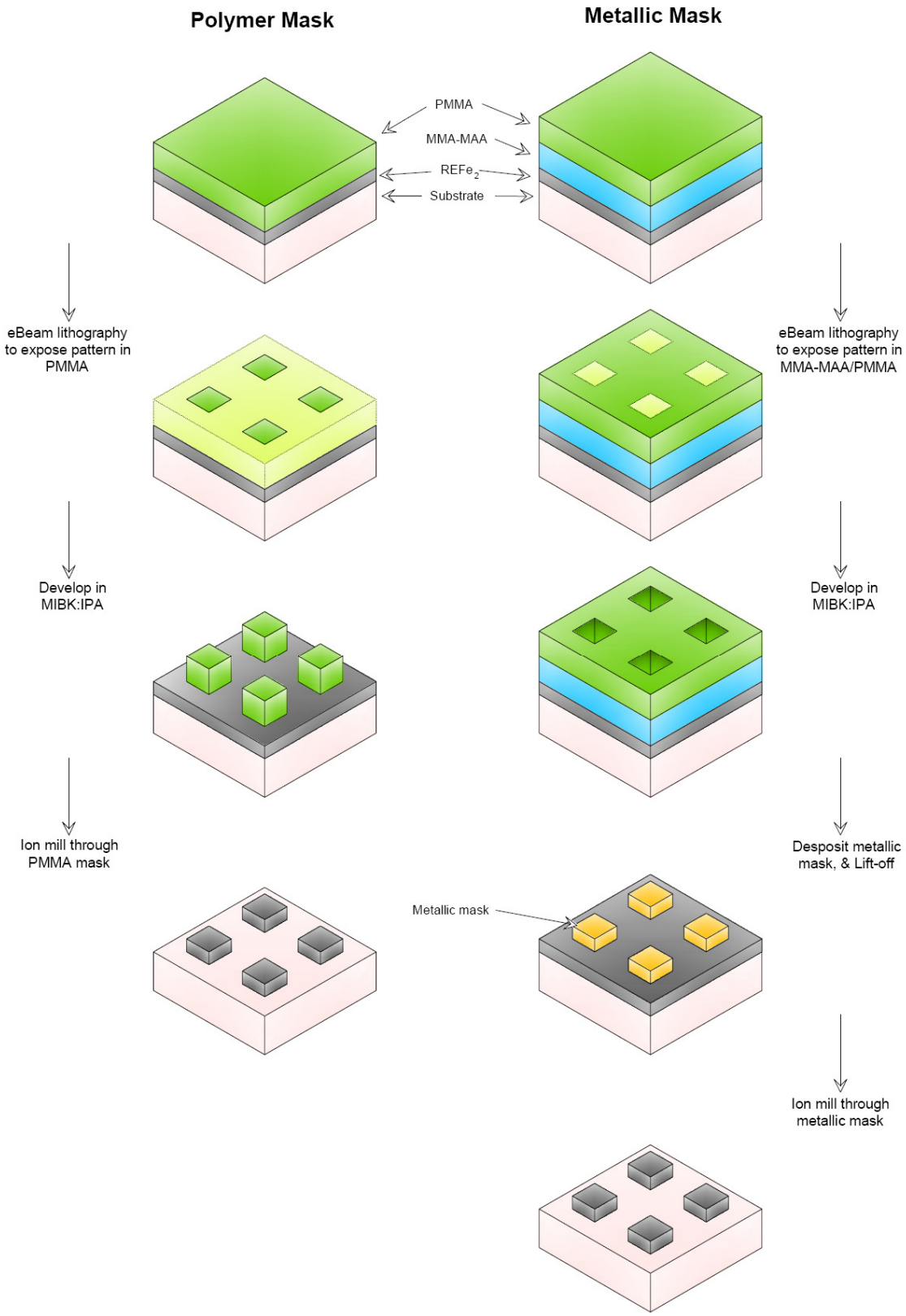

Figure 3.20: Schematic illustration showing the fabrication of (and etching through) a polymer and a metallic mask. In the PMMA / MMA-MAA, exposed regions are indicated by a light green colour. Note the requirement for a negative of the pattern to be exposed in the metallic mask process in order to achieve the same end result.

3.5.1 Polymer masks

The most basic mask which has been used in the work discussed here is a polymer resist mask (PMMA) that was patterned during the lithography steps detailed in section 3.4. In this instance, only a single layer of resist is required, permitting higher resolution and more closely packed patterns.

During early work the author found that the PMMA mask was not resilient enough to permit the removal of a significant amount of the $REFe_2$, that is, the mask was removed at a much greater rate than the underlying magnetic material (see section 3.6.3). Whilst polymer masks have been successfully employed in this manner before [59, 60, 61, 62], the $REFE_2$ films used in this work are significantly thicker. Therefore a far thicker polymer mask would be required to remove all of the material. This high rate of PMMA removal made for the etching through of more than ~ 25 nm of $REFe_2$ impossible (corresponding to only $^1/_{16}$ of a typical [2 nm $DyFe_2$ / 8 nm YFe_2] × 40 multilayer sample). However, for thin $REFe_2$ samples, *e.g.* bi-layer systems like those used in applications such as MRAM, the polymer mask process may still be of use (*c.f.* the thin materials mentioned above). Accordingly the polymer mask process was not disregarded and the results of patterns created using a polymer mask are presented in section 4.2.3. However, in order to define patterns in thick, high quality epitaxial multilayers of $REFe_2$, a more resilient mask material was required.

3.5.2 Metallic masks

Metallic masks have been successfully used in material etching processes on many occasions [63, 64, 65, 66, 67]. This work forms the first report of using metallic masks and energetic Ar^+ ions to define patterns in epitaxially grown $REFe_2$ media. Metals with a high atomic density, N, tend to perform well as masks since they are characteristically hard and thus more resilient to energetic ion bombardment. Some of these metals are summarised in Table 3.3.

Element		Atomic density N ($\times 10^{22}$ atoms cm^{-3})	Ion etching rate (nm min^{-1}) (@ 500 eV Ar^+, 1 mAcm^{-2}) [68]
Beryllium	Be	12.3	13
Osmium	Os	7.12	31
Vanadium	V	7.05	31
Titanium	Ti	5.69	33
Tungsten	W	6.34	34
Iron	Fe	8.48	35
Molybdenum	Mo	6.41	41
Tantalum	Ta	5.53	42
Cobalt	Co	9.10	45
Nickel	Ni	9.13	53
Chromium	Cr	8.34	53

Table 3.3: Atomic densities and typical etching rates for some elemental metals.

The metallic mask is deposited using thermal evaporation (section 3.1.3) through a lithographically defined pattern in a bi-layer resist structure so as to facilitate easy lift-off (section 3.4.3). Using this bi-layer method the mask material can be significantly thicker than would be possible using a single polymer layer which results in a structure more resilient energetic Ar^+ ions. Out of the elements given in Table 3.3, Os, V, Ti, W, Mo and Ta are difficult or impossible to thermally evaporate due to their high melting point. Fe, Co and Ni can be evaporated thermally but there have been issues achieving this reliably using the *Edwards Coating System E306A*, therefore Be and Cr must be turned to as mask materials. Be is toxic, corrosive to the skin and expensive, making Cr the optimal choice of mask material.

Note that it is not possible to simply grow the epitaxial $REFe_2$ media directly through a lithographically defined mask, removing the need for the fabrication of a metallic mask and the subsequent etching processes (a lift-off based nano-structuring process). Whilst it is true that lift-off processes been used to successfully fabricate nano-structured magnetic films and multilayers, *e.g.* refs. [69, 70, 71, 72], it is not possible to grow high quality epitaxial films on substrates with polymer masks using MBE. In MBE the sample surface needs to be ultra-clean (even after the resist is removed some residue can remain [73]) and the polymer mask would not remain stable at the elevated temperatures used for the growth of these materials. Thus some form of etch-back process is always required for nano-structuring these media.

3.6 Etching processes

There are three categories of etching readily available for the selective removal of the $REFe_2$ through a lithographically defined mask:

1. Wet etching, using chemical or electrochemical processes to dissolve the unwanted material.
2. Reactive ion etching (RIE), which creates volatile compounds by a chemical reaction between the material to be etched and the etch gas.
3. Physical dry etching (ion milling), which bombards the material to be etched with energetic ions.

All of these processes are covered in this section, with particular focus on the process of choice; ion milling.

3.6.1 Wet etching

Wet etching is inherently isotropic in nature; it etches in all directions at the same rate [58]. Therefore a large under-cut is formed during the etch process, which can be up to 400 nm laterally when etching through a complete 400 nm thick superlattice $REFe_2$ structure, *i.e.* the ultimate resolution achievable is limited by the thickness of the material being etched. Wet etching has been performed on similar $REFe_2$ films and multilayers to those discussed within this work by Wang *et al.* [74, 75, 76, 77]. This work was successful in structuring these materials on the scale of several μm, but nano-scale structuring was not possible due to the aforementioned issues. A brief review of this patterning process is presented in section 4.1, where this early research will be seen as a starting point for this work where nano-scale structuring of the media is demonstrated.

3.6.2 Reactive ion etching

Reactive ion etching relies on a chemical reaction between the material to be etched (sample) and the etch gas, binding the sample atoms into a volatile compound. Attractive properties of RIE are its anisotropic nature and high etch selectivity. RIE therefore has the potential for high resolution etching.

Estimations can be made as to whether etching will occur by investigating the boiling points of the sample. Typical etch gases are fluorine and chlorine. When combined with ferromagnetic materials (in this instance Co and Ni) they form the

compounds CoF_2 and $NiCl_2$ respectively, with very high boiling points of 1400°C and 1049°C [78]. These compounds are non-volatile and therefore do not easily enable RIE[iv]. Coupled with this issue, even if a suitable etchant was found for YFe_2 for example, it is not guaranteed that it would be able to successfully etch $DyFe_2$ and *vice-versa*. This makes RIE an unsuitable process for etching prototype designs into magnetic *multilayer* materials since significant development of the process is required well beyond the scope of this work. It should however be noted that some successful attempts have been reported in the literature; Zhang *et al.* [64] used $CBrF_3$ to RIE CrO_2 and Aziz *et al.* [79] used SF_6 to RIE Pt / Co / Pt trilayers.

3.6.3 Ion milling

When an energetic ion is incident on the sample surface it will penetrate into that surface provided its energy is high enough to overcome any repulsive potential barrier presented by the surface atoms. The ion will lose energy due to collisions with atoms and change its trajectory, before undergoing subsequent collisions and eventually coming to rest within the solid. This causes the surface atoms to deviate from their equilibrium positions, creating a vacancy and a recoil atom (which itself can go on to cause further deviations from equilibrium – a cascade effect), and if the energy transferred to these atoms is large enough, it can cause them to be ejected from the bulk material. This is a process almost identical in nature to sputtering (discussed in section 3.1.2). As such ion milling is also referred to as ion beam sputtering. It should be noted that energetic ions are implanted into the side-walls of the lithographically defined structure. This process, ion implantation, will be covered at depth in Chapter 5, but in summary the outer most ~ 5 nm of each patterned region suffers edge damage. Within these regions the chemical composition and crystalline structure of the sample can differ drastically. Clearly this effect becomes very much more apparent once the lithographically defined features reach a scale of ~ 100 nm. This places a clear constraint on the ultimate resolution achievable in ion milling.

Ion milling is an anisotropic process that provides a useful and cost-effective technique for the transfer of lithographically defined patterned structures into a material. It avoids many of the drawbacks associated with both RIE and wet etching. As such ion

---

[iv] *c.f.* materials that are etched easily, *e.g.* W and Si, which form WF_6 & SiF_4 with boiling points of 17.5°C and –86°C respectively.

milling with Ar^+ has been chosen to transfer nano-scale patterned elements into $REFe_2$ films and multilayers. The implementation and optimization of the Ar^+ ion milling process is detailed in the remaining sub-sections of section 3.6.

3.6.4 Optimising ion milling

Etch rates in ion milling are determined by the current density of ions at the sample surface, the angle of incidence of the ions (which itself is a function of the ion energy, the process gas and the material being etched) and the sputtering yield of the material being etched. The sputtering yield describes the number of atoms that sputtered from the sample surface per incident ion. Thus a material with a high sputtering yield is etched at an accelerated rate compared to a material with a low sputtering yield.

A fundamental factor regarding the etch rate (R) is the current density of ions (J_I) at the sample surface. This is illustrated in results by Yuba *et al.* [80] who show a linear relationship between R and J_I. It is a simple result of the fact that more ions arriving per unit area results in more atoms being ejected from the sample surface.

The effect of the angle of incidence of the ion beam plays a significant role in determining R. For example, a beam of ions normally incident on the sample surface ($\theta = 0°$) may subtend a circular interaction area A_1, corresponding to a sputtering yield S_1. If the sample is tilted away from normal incidence ($\theta \neq 0°$) this interaction area increases, subtending an ellipse with area $A_2 > A_1$, with a correspondingly increased sputtering yield $S_2 > S_1$. As θ is increased further, the sputtered atoms escape directly from the surface without generating any further recoils, thus S decreases. Finally as the angle approaches grazing incidence ($\theta = 90°$) no ions can penetrate the surface so S = 0. The optimum angle of incidence θ_o for maximum S is given in Stewart & Thompson [81] as

$$\theta_o = \frac{\pi}{2} - \sqrt{\frac{5\pi {R_0}^2 n^{2/3} Z_1 Z_2 E_R}{({Z_1}^{2/3} + {Z_2}^{2/3})E}} \tag{3.2}$$

Here R_0 is the Bohr radius, n is the density of atoms per unit volume, Z_1 & Z_2 are the atomic numbers of the ion and the atom respectively, and E_R & E are the Rydberg energy and ion energy respectively. Thus θ_o varies for different sample materials, process gasses and ion energies. Using $Z_1 = Z_{\mathrm{Ar}} = 18$, defining $Z_2 = Z_{\mathrm{DyFe_2}} = \frac{Z_{\mathrm{Dy}} + 2Z_{\mathrm{Fe}}}{3} \approx 39$ and $n_{\mathrm{DyFe_2}} \approx \left(\frac{1}{0.7324^3}\right) \times 24 = 61.1$ nm^{-3} (see section 3.2), for an ion energy E = 3 keV gives $\theta_{o_{\mathrm{DyFe_2}}} = 70.2°$. Similarly $\theta_{o_{\mathrm{YFe_2}}} = 71.8°$. Clearly careful

consideration must be paid to the design of the ion milling geometry in order to optimise the rate of material removal. It should also be noted that in order to maintain a uniform etch across the entire sample surface, rotation of the sample is performed. The result of this is an effective mean angle of incidence $\langle\theta_o\rangle$ which differs significantly from θ_o [82, 83]. There are two further, intimately related, points of note concerning ion milling angle of incidence; "faceting" and re-deposition. Faceting is the name given to the process whereby the mask material will always be removed at an accelerated rate along the optimal angle of incidence (θ_o). By aligning the sample and ion source at θ_o, faceting can be compensated for by promoting even wear across the mask. The effect of a faceted mask on the sample can also be reduced by increasing the mask thickness, but the thicker the mask the more it blocks the escape of sputtered material. This leads to increased sticking of sputtered material on the mask sidewalls (re-deposition) and the formation of features analogous to the "rabbit ears" presented in section 3.1.2. It is impossible for ion milling to be a truly anisotropic process, but provided θ_o is chosen wisely, making the undercut and re-deposition minimal, it by far out-performs wet etching processes. Thus in ion milling there is a trade-off; a compromise between a thick mask to ensure maximum etch selectivity (and to reduce the effect of faceting) and a thin mask to reduce re-deposition. The correct choice of θ_o and the use of a thin, hard metallic mask provides an attractive solution. The success of this solution will be presented in Chapter 4, but it will be made clear that the effects of re-deposition can never be completely eliminated.

Finally it is important not to over-look the inverse relationship between the etching rate R and the cohesive energy per atom U_c in the sample being etched. U_c is given by [84]

$$U_c = \frac{U_f - U_s}{N_s} \tag{3.3}$$

with U_f the energy of a free atom, U_s the total energy of the solid and N_s the number of atoms in the solid. Clearly R will vary depending on the material being etched (giving rise to the differential rates of mask erosion mentioned previously) but also on the nature of the material, with the bond type determining U_s and the nature of the recoil collisions as discussed in Sigmund [85]. U_c is the parameter responsible for the materials sputtering yield.

Given the complex nature of the combination of the processes at play during ion milling, attention is turned to computer simulations to help predict the amount of

material etched from the sample surface. This is achieved using the SRIM code [86]. SRIM can also predict ranges of ions in matter and track energetic atomic recoils and vacancies (based upon famous original works by Lindhard *et al.* [87]). This will be very useful when analysing the effects of energetic ion implantation (Chapter 5), and as such SRIM is described in more detail in section 2.8.1.

3.6.5 Development and implementation of an ion milling source

To ensure the effective removal of sputtered material from ion milling, there must be a mean free path long enough to ensure that this material does not return directly to the sample surface. Clearly then ion milling needs to be undertaken in a high vacuum chamber. The *Kurt J Lesker* sputtering apparatus described in section 3.1.2 has a suitable vacuum system and several spare 2¾" Ø ports, aligned at 68° to the sample holder normal. Based upon the information in section 3.6.4, this provides an ideal mounting point for a 2 ¾" Ø *Oxford Applied Research IG5* ion gun. The sputtering apparatus also includes the relevant gas supplies (Ar for ion milling), *mass-flo* gas controllers, sample stage rotation and feed-throughs to permit the measurement of current at the sample surface.

The *Oxford Applied Research IG5* was custom fitted to keep the gun to sample separation at 10 cm (as per manufacturers specifications) to ensure the maximum current collected at the sample surface. Unfortunately *in-situ* monitoring of the current collected at the sample is not possible[v], therefore measurements must be based on previous calibration runs. It should also be noted that some ion milling systems have end point detection [88]. This is not available in this system, therefore calibration runs of milling rates are also made, from which process times are derived. It should also be noted at this point that in the work conducted here, no faceting of the mask has been observed which is attributed to θ_o = 68°, which is very close to the optimal values described in section 3.6.4 and Yamauchi *et al.* [89].

3.6.6 Ion beam milling rates

The *Oxford Applied Research IG5* ion gun has a relatively low beam current density J_I with typical values of 1 μAcm^{-2}. This is approximately three orders of magnitude lower

[v] Due to the stage rotation required to ensure even removal of material, electrical contacts to measure the current at the sample cannot be successfully made during the etching process.

than more expensive commercial systems [80, 81, 88]. The Ar^+ ion energy can be varied between 0.5 and 5 keV, whilst the commercial systems are commonly operated in the 0.2 – 1 keV range. In such systems the milling rate R is typically between 1 – 10 μm hour^{-1} [80, 88, 90] and is linearly dependent on J_I [80]. Thus it is clear that the *IG5* system will remove material at a slower rate. However, the milling rate is also affected by the energy of the ion beam, therefore consideration should be given to SRIM calculations and experimental calibration runs to provide a better estimate of the reduction of R.

Standard Ar^+ ion milling rates for the materials are taken as R_{Dy} = 110 nm min^{-1}, R_Y = 95 nm min^{-1} and R_{Fe} = 35 nm min^{-1} (E = 500 eV, J_I = 1 mAcm^{-2}) [68]. From these data, approximate values can be derived for $R_{DyFe_2} \approx 60$ nm min^{-1} and $R_{YFe_2} \approx 55$ nm min^{-1}. Assuming the linear dependence in Yuba *et al.* [80], these values for R can be divided by 1,000 to account for the difference in J_I, to give $R_{DyFe_2} \approx R_{YFe_2} \approx 0.06$ nm min^{-1}. SRIM calculations for E = 500 (5,000) eV Ar^+ ions into $DyFe_2$ at an angle of 68° give sputtering yields of S = 2.20 (9.37) atoms ion^{-1}, a difference of a factor of 4.3. Therefore the rates can be modified to $R_{DyFe_2} \approx R_{YFe_2} \approx 0.26$ nm min^{-1} for the *IG5* ion gun using Ar^+ ions with a beam energy of 5 keV. Assuming a standard multilayer $REFe_2$ sample thickness of 400 nm, the time to etch through the entire sample would be approximately 26 hours. SRIM calculations for 5 keV Ar^+ ions into PMMA 950k return a sputtering yield of 10.05 atoms ion^{-1}, 7% higher than that for $DyFe_2$, corresponding to $R_{PMMA} \approx 0.28$ nm min^{-1}. In practice, experimental calibration runs (not presented) suggest that this etch rate is considerably faster[vi]. Therefore to remove the entire 400 nm $REFe_2$ multilayer, a PMMA thickness far greater than 400 nm would be required. This unacceptable since it would be near impossible to define nano-scale features in such a thick polymer layer. However, taking the etch rate of Cr as 53 nm min^{-1} [68] and scaling as before, gives $R_{Cr} \approx 0.24$ nm min^{-1}. The reduced etch rate of the Cr compared to the PMMA (and the $REFe_2$) suggests that Cr is indeed a more suitable mask material.

[vi] SRIM provides a reliable estimate for the etching rate of metals at a range of voltages but calculated values for PMMA are significantly underestimated at higher voltages. This may be due to "compound correction" and "bond correction" within the software which attempts to correct for deviations in ion stopping potential and sputtering yield for light elements such as H, C and O as found in PMMA.

A concern with regard to the choice of a metallic mask is its removal after pattern transfer to the underlying $REFe_2$ material. It is not possible to use wet etching processes to remove the mask material since almost all of the relevant chemical etchants, especially those for Cr, contain perchloric acid ($HClO_4$) or ceric ammonium nitrate ((NH_4) $[Ce(NO_3)_6]$) [91, 92], both of which are oxidising agents which would severely damage the $REFe_2$. Therefore it is desirable to tailor the mask thickness to be such that it is completely removed during the ion milling process. This has been successfully employed when defining nano-scale patterns in bi-layers of $REFe_2$ (section 4.2.6).

3.7 X-ray Diffraction

It has already been shown when discussing electron microscopy (section 3.3) that the diameter of the beam of electrons is the factor that ultimately governs the resolution attainable. When considering light (photons) rather than electrons, it is the wavelength that dictates the smallest feature size that can be resolved. Clearly visible light is only suited to resolving features of $\gtrsim 400$ nm. Thus to resolve details on length scales significantly smaller than this, for example the spacing between atoms within a crystalline lattice or the atom diameter itself, light with a shorter wavelength must be used. Atoms have a typical diameter of ~ 0.1 nm, approximately $^{1}/_{4000}{}^{\text{th}}$ of the wavelength of the visible light. X-rays on the other hand have wavelengths on the scale of ~ 0.1 nm, and can therefore be used to resolve structural features on the atomic scale.

X-rays which are incident on a sample will interact with the constituent atoms and be scattered in various directions. These collisions between the X-rays and the atoms produce an array of spherical waves that are cancelled out in almost all directions due to destructive interference, but add constructively along a few directions according to Bragg's law

$$n\lambda = 2d \sin\theta \tag{3.4}$$

Here, n is an integer, λ is the wavelength of the incident light, d is the spacing between the objects responsible for scattering the X-rays and θ is the angle the incident X-rays make with the sample surface. Considering only X-rays that are scattered elastically by the atoms, the incident and scattered X-rays have the same wavelength, only a different direction of propagation. Thus some X-rays incident on the sample will emerge from it

unaltered in all but direction after suffering scattering from the sample's underlying crystalline structure. Provided there is a regular array of scattering objects, the pattern of diffracted X-rays can be recorded directly onto a photographic film or by other means to build a diffraction pattern characteristic of the sample's crystalline structure. This diffraction pattern can then be recombined mathematically to form an accurate 3D representation of the crystal structure. This process, commonly referred to as X-ray diffraction (XRD), was famously first conducted by W. H. Bragg [93] and W. L. Bragg [94], both in 1913. Useful reviews of XRD can be found in Warren [95] and Clegg [96].

Within this work the crystalline lattice parameters rather than the known crystalline structure is the parameter of interest, since this reveals details about the growth conditions of the material, for example the extent to which it suffered strain during growth (see section 3.2). XRD data is acquired using a *Philips PW1050* diffractometer at the University of Oxford. The author is grateful for assistance from Dr Roger Ward in using this equipment. In this equipment, the X-ray detector position can be accurately controlled by the use of a goniometer. The angle subtended by the detector with respect to the sample, 2θ, is varied in typically 0.01° steps via a computer controlled mechanism. As 2θ is varied the number of diffracted X-rays is recorded, thus forming a dataset of the form X-ray counts versus angle 2θ. Accordingly this dataset will exhibit peaks at very specific angles characteristic of the spacing of the diffraction planes (d) within the crystal according to equation (3.4). A typical scan range covers 10° and takes approximately 45 minutes to complete. It is important to note that there will be several diffraction peaks present in a typical MBE grown epitaxial $REFe_2$ sample. This is because the X-rays penetrate further into the sample than the $REFe_2$ film thickness, thus peaks from the NbFe alloy layer and the Al_2O_3 substrate are also present. A clear peak due to the Al_2O_3 substrate can be seen in Figure 3.21 at 37.89 ± 0.005°, with the peak representative of the $DyFe_2$ film deposited on top of this apparent at 34.92 ± 0.005°. The NbFe alloy is apparent as the broad peak below the well defined Al_2O_3 peak.

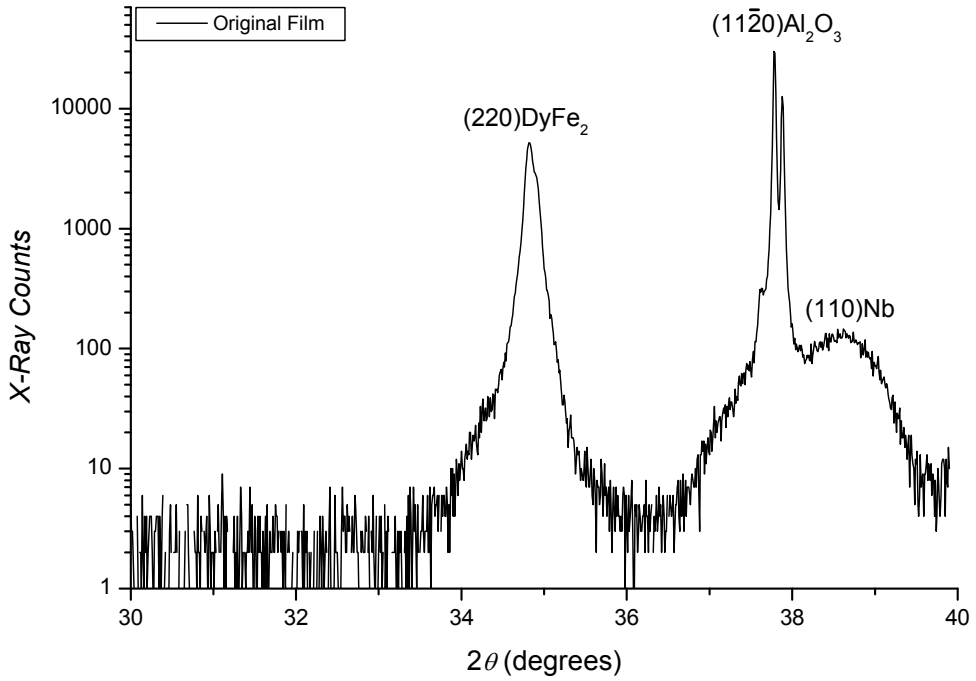

Figure 3.21: Example XRD data for a 400 nm $DyFe_2$ sample. Note that the graph has a $\log_{10}$ scale for X-ray counts and thus demonstrates the very good SNR present in the XRD data. The Al_2O_3 substrate peak at $2\theta = 37.78°$ acts as a fixed reference point for calibration.

The X-ray source employed is of the rotating anode Cu Kα_1 type which corresponds to X-rays with λ = 0.1541 nm. First order diffractions are in general detected (a path length difference of one between successively scattered X-rays), thus n = 1, hence d can be easily determined from equation (3.4). Data for d can then be translated into values for the crystalline lattice parameters provided the crystallographic reflection (given by integers h, k & l, known as Miller indicies) and the crystalline structure (cubic, hexagonal, orthorhombic *etc.*) are known. For the present cubic Laves phase structure, the lattice parameter a is given by [95]

$$a = d\sqrt{h^2 + k^2 + l^2} \tag{3.5}$$

The (110) reflection is forbidden so results are obtained for the (220) reflection [, 97], thus equation (3.5) is simplified to $a = 2\sqrt{2}d$ for the cubic Laves phase $REFe_2$ samples, with diffraction at normal incidence providing data for the lattice parameter perpendicular to the film plane (*i.e.* in the sample growth direction). The diffractometer has been equipped with a curved graphite monochromator which filters out unwanted wavelengths corresponding to X-ray fluorescence from the sample (*c.f.* section 3.3.5 and Figure 3.12) and Cu Kβ radiation. Whilst unwanted wavelengths are filtered out,

the efficiency of the graphite crystal is very high and as such the peak intensities remain unaltered which leads to results with a significantly improved SNR [98]. The resulting resolution, in terms of measured angle 2θ, is accurate to 0.01°, with a SNR between 10,000:1 and 100:1 depending on the film thickness and position in the sample cross-section. Note that the Al_2O_3 peak appears as one central main peak with two sub-peaks, one on either side. The doublet (central and right peaks) are due to the Cu Kα_1 and Cu Kα_2 doublet in the characteristic Cu radiation, with Kα_2 roughly half the intensity of Kα_1. The third, smaller peak on the low angle side is an escape peak, again characteristic of the Cu target. These peaks are present because the Al_2O_3 substrate is thick and of very high crystalline quality. The thick metallic layers also show signs of a doublet (hence the slightly asymmetric shape to the $DyFe_2$ peak in Figure 3.21). Whilst the graphite monochromator successfully filters out the unwanted Cu Kβ radiation, it is not efficient enough to eliminate the Cu Kα_1 radiation.

XRD has been employed at various stages throughout this work to determine if the patterning processes as a whole affects the composition and / or the underlying crystalline structure of the epitaxial $REFe_2$ films. XRD has also been used on occasion to determine if any Cr mask material remains after the Ar^+ ion milling process, thus providing a useful tool, in conjunction with EDX (see section 3.3.7), to check whether the entirety of the mask material has been removed.

3.8 Helium Ion Microscopy

In section 3.3 it was noted that reductions in the electron beam diameter ($Ø_b$) and accelerating voltage (E) diminish the electron interaction volume, improving the overall resolution attainable. However, this also led to a decrease in the SNR of the data obtained. Recently, a new method [99] permitting atomic scale resolution has been developed which uses He^+ ions rather than electrons to image samples at near TEM resolution [100] yet without the complicated sample preparation. A *Zeiss ORION Plus* He^+ ion microscope has recently been installed at The University of Southampton and has been used by the author with the assistance of Dr S. Boden to characterize some $REFe_2$ samples.

The source of He^+ ions is from a metallic tip which has been fabricated into an atomically sharp pyramid. Neutral He gas is fed into the tip region. Under the application of a high positive electric field to the metallic tip, the neutral He is ionized

and accelerated away from the tip. Since the tip is atomically sharp, emission occurs from only the top-most atom of the pyramid, permitting a very high beam current with intrinsically small $Ø_b$. In the He^+ ion microscope the source brightness is ~ 1×10^9 $Acm^{-2}sr^{-1}$, over an order of magnitude better than a cold FEG (section 3.3.1) whilst maintaining a similarly small energy spread of ~ 1 eV [101]. The He^+ ions also have an intrinsically higher momentum p than electrons, thus have a much shorter de Broglie wavelength λ ($\lambda = \frac{h}{p}$, with h Plank's constant) and are diffracted less. The combination of high source brightness and small wavelength results in He^+ ions producing an imaging beam which can be smaller in diameter yet brighter than that possible with electrons.

When a He^+ ion interacts with a sample, typically two to eight secondary electrons (SE) are generated [101] as opposed to an electron hitting the surface generating only one SE (section 3.3.5). The He^+ ions have a higher energy than electrons ($E \propto \frac{1}{\lambda}$) and thus penetrate further into the sample, but suffer little straggling and thus a smaller interaction volume is formed. Therefore the SEs are emitted from a region much smaller than that due to the irradiation from electrons. This corresponds to the formation of a much higher resolution image with vastly improved contrast. Moreover, He^+ can also be backscattered from the target nucleus, the number of which is strongly dependent on Z. This is analogous to the case of backscattered electrons and therefore similar conclusions can be drawn from the data, allowing the user to obtain qualitative information regarding the sample composition.

3.9 Scanning Probe Microscopy

Since its conception in 1981 by Binning and Rohrer [102], scanning tunnelling microscopy (STM) has taken on many different guises proving that it is a truly versatile analysis (and in some instances fabrication) technique. For this they won the Nobel Prize for Physics in 1986. STM is the founding invention of a class of microscopy techniques known collectively as scanning probe microscopy (SPM). In general SPMs scan, in a raster fashion, an ultra-sharp mechanical tip (commonly referred to as a "cantilever" with a "probe" attached at one end) across a sample surface. At each point on the sample surface information is collected regarding the probe-sample interaction,

thereby creating of a 3D representation of the sample. In an STM this is charge density as a function of position on the sample's surface.

It was such an STM that was taken by Binning *et al.* [103] in 1985 and developed to form the first atomic force microscope (AFM). In an AFM, the atomic force dependent motion of a probe as it traverses the surface is precisely measured in order to build up a 3D image of the sample topography (see section 3.9.1). The versatility of the SPM can be extended further by measuring other characteristics such as spin polarization (SPSM), electrostatic forces (EFM) and magnetic forces (MFM) (section 3.9.4). The SPM can also act as a nanofabrication tool where it is used to locally modify the sample surface. A comprehensive review of SPM (including nano-fabrication) is given in Wiesendanger [104].

3.9.1 Atomic force microscopy

The combination of atomic dipole – dipole forces are collectively known as van der Waals (VDW) forces. They are due to interactions between polar molecules (orientation forces), a polar and a neutral molecule (induction forces) and neutral molecules (dispersion forces). At separations of a few nm or less, VDW forces (F_{VDW}) are attractive and grow strongly as the displacement between bodies decreases, but for separations larger than a few nm these forces become repulsive.

A device called a "surface force apparatus" has been in use since the late 1960s [105] to measure F_{VDW} using a sprung cantilever assembly and piezoelectric motors. From the deflection of a spring, F_{VDW} can be derived to an accuracy of ~ 10^{-8} N. A further device, called a "surface profilometer" has been in use since the 1930s [106], consisting of a mechanical probe that is in contact with the sample surface. This probe is then scanned across the surface in a raster fashion in order to build a 3D representation of the surface. The probe has a large diameter (~ 1 μm) since the device operates under a constant, relatively large force of 10^{-4} N; any larger force may damage the sample surface. This limits the resolution to ~ 1 μm. The AFM in many ways is a combination of the surface force apparatus and the surface profilometer.

The Binning *et al.* [103] AFM used a diamond probe mounted on a Au foil cantilever with an STM probe in close proximity to detect the deflection of the cantilever as the probe was rastered across the sample surface. The deflection of the cantilever is a simple implementation of Hooke's law; $F = -k\Delta z$, with F the force, k the spring constant and Δz the vertical displacement. By keeping F constant (by means

of a feedback loop), Δz can be varied via a piezoelectric motor and thus the raster scan will result in a 3D topographical representation of the sample surface[vii]. The sensitive detection methods of the cantilever displacement permit AFM to detect small changes in force (~ 10^{-8} N as per the surface force apparatus) using a probe with a small diameter (between ~ 5 and ~ 50 nm) and therefore a spatial resolution that is greatly improved over the surface profilometer. This process can be used on any sample surface thus is one of the most versatile forms of microscopy. An example of a modern, mass-produced AFM cantilever and probe assembly is shown in Figure 3.22.

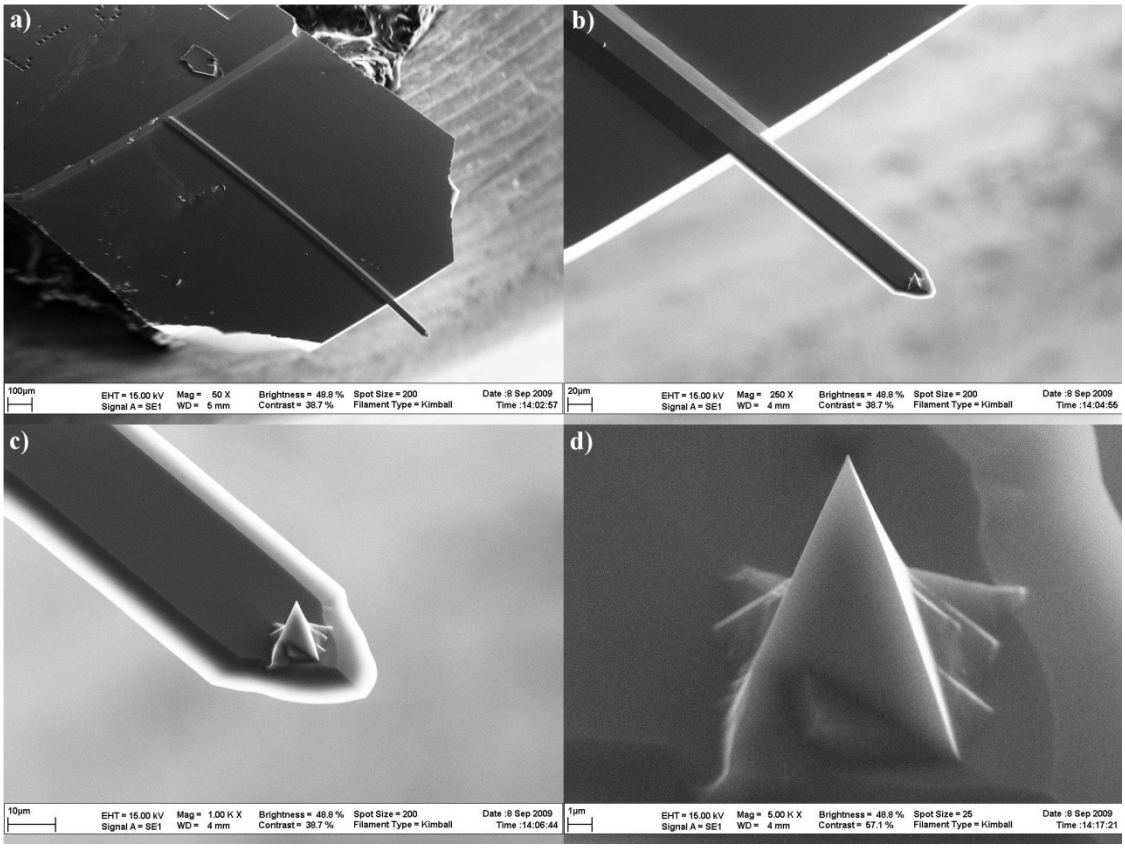

Figure 3.22: Images a), b), c) & d) show 50 ×, 250 ×, 1,000 × and 5,000 × magnification SEM micrographs of a standard AFM cantilever and probe assembly respectively. Image a) shows the entire bulk assembly which is manually inserted into the SPM. The cantilever (the arm protruding from the bulk material) is just visible with the unaided eye, having a width of ~ 30 μm. Images b), c) & d) show the cantilever and the probe magnified further. At the tip of the probe the diameter is less than 100 nm.

The AFM used throughout this work (and also implemented in the MFM measurements in section 3.9.4) is a *Digital Instruments* (now *Veeco*) *Multimode* SPM. The *Multimode* SPM uses an optical technique to determine the magnitude of the

[vii] Similarly Δz can be held fixed whilst measuring changes in F, but this method runs the risk of causing damage by colliding the cantilever into the sample surface.

cantilever deflection. A laser is reflected off the back of the cantilever, onto a mirror and then onto a quadrant position sensitive photo-detector (PSD). When the cantilever is deflected, the direction of the reflected laser beam changes which in turn induces an increase or decrease in voltage induced by the PSD. Opposed to other methods of deflection detection (for example the STM tip described above), the laser exerts negligible force on the cantilever and as such permits excellent resolution, routinely of the order 10 nm in *x*- and *y*- dimensions and < 1 nm in the *z*-dimension. In order to obtain the *x*-*y* positioning of the cantilever the *sample* is scanned underneath the *fixed* cantilever using piezoelectric motors; *x*-*y* scan regions range from ~ 100 μm to ~ 100 nm. The position of the cantilever is varied in *z* by a further, independent, piezoelectric motor which forms part of the aforementioned feedback loop and has a range of approximately 0 – 5 μm.

3.9.2 Contact mode atomic force microscopy

In traditional "contact mode" AFM the cantilever deflection is kept constant, *i.e.* it experiences a constant force. This is achieved by means of a feedback circuit that continuously varies the *z*-axis piezoelectric motor. In contact mode the dominant force is not the relatively speaking long-range F_{VDW}, but actually a combination of the force originating from the Coulomb repulsion between the ion cores, F_i (short-range), and the interaction of valence electrons with these ion cores, F_e (medium-range). In most contact regimes $|F_i| > |F_e|$ which results in the contact mode AFM being sensitive to the repulsive Coulomb interaction which provides high spatial resolution due to the force's short-range. Typical values of F_i and k are 10^{-8} N and 1 Nm^{-1} respectively. This corresponds to a cantilever deflection of 10 nm which can be easily measured using any one of the techniques in section 3.9.1.

3.9.3 Tapping mode™ / non-contact atomic force microscopy

Throughout this work, the *Digital Instruments Multimode SPM* is operated exclusively in "tapping mode" (TM). TM (also called "semi-contact mode" and "van der Waals microscopy") is a form of non-contact AFM whereby the cantilever is driven to vibrate near its resonant frequency, at an amplitude of ~ 100 nm, at a distance of approximately 0 – 100 nm above the sample surface. Throughout this ~ 100 nm region, if the sample is electrically neutral and non-magnetic the van der Waals force will be dominant. Since the cantilever is oscillating, the process of TM-AFM is sensitive to force *gradients*,

$F' = \frac{\partial F_z}{\partial z}$, which in turn modifies the spring constant k of the cantilever; $k' = k - F'$. Taking the standard equation of motion $mg - kz = m\frac{d^2z}{dt^2}$, with m the mass of the cantilever, g the acceleration due to gravity and time t, and using a standard solution of the form $z = \alpha \sin(\omega t - \varphi) + \beta$ gives

$$mg - k\{\alpha \sin(\omega t - \varphi) + \beta\} = m\{-\alpha\omega^2 \sin(\omega t - \varphi)\} \tag{3.6}$$

with the resonant frequency, ω given by

$$\omega = \sqrt{\frac{k}{m}} \tag{3.7}$$

Substituting k' into equation (3.7) gives

$$\omega' = \sqrt{\frac{k-F'}{m}} = \omega\sqrt{1 - \frac{F\prime}{k}} \approx \omega\left(1 - \frac{F\prime}{2k}\right) \tag{3.8}$$

with the latter approximation from a Taylor expansion since $F' \ll k$. It can now clearly be seen that a change in F' felt by the cantilever causes a change in the resonant frequency $\Delta\omega$;

$$\Delta\omega = \omega' - \omega \approx -\frac{\omega F\prime}{2k} \tag{3.9}$$

which is the measured quantity in tapping mode AFM. Throughout this work, $\Delta\omega$ was detected using a method known as *phase* detection, where a phase shift in the cantilever's vibration is detected using a lock-in method. It is also possible to measure amplitude shift (although not as accurately) and $\Delta\omega$ directly (using specialist lock-in to the feedback loop methods).

Using a similar cantilever and probe assembly as for the contact mode AFM, *i.e.* k = 1 Nm^{-1}, a scan height of 10 nm and assuming that the minimum detectable force gradient is of the order 10^{-4} Nm^{-1} [104], this would correspond to a force of order ~ 10^{-12} N, or a deflection of just 1 pm which is at the limit of most interferometer systems. Clearly TM-AFM offers a clear improvement in sensitivity over standard contact AFM.

For the AFM measurements included in this work, the cantilevers are fabricated from, n-type doped Si. They have a tip diameter of < 100 nm and a resonance frequency of 70 ± 5 Hz, with a spring constant between 1 – 3 Nm^{-1}.

3.9.4 Magnetic force microscopy

The *Digital Instruments Multimode SPM* is a very versatile device which can perform almost all types of SPM described in Wiesendanger [104] with relatively simple

hardware and software modifications. Such modifications were made to permit magnetic force microscopy (MFM). The most notable modification was the use of a magnetized probe so as to detect magnetic force gradients, and the installation of an additional cantilever z-axis piezoelectric motor to perform lift-mode™ scanning.

MFM was first demonstrated shortly after AFM by Martin and Wickramasinghe [107] in 1987. Like TM-AFM, MFM is also based upon operation in the non-contact regime. Magnetic forces (F'_M) can be attractive or repulsive and therefore create difficulties with the continued successful maintenance of a feedback circuit. Fortunately the attractive F'_{VDW} is always present in the same regime as F'_M which can be used to stabilise the feedback circuit. However the result of this is that it is very difficult to then separate the sample's magnetic information from its topographical information since the measured force gradient F' is now $F' = F'_M + F'_{VDW}$. Early work by Martin and Wickramasinghe [107] and Sáenz *et al.* [108] show results for F' but note that the magnitude of their detected signals increase with increasing probe – sample separation, a clear sign of magnetic interactions [109]. All of these early works use a relatively large probe-sample separation, 100 nm on average, to ensure that the dominant signal in F' was F'_M, but this is at the expense of resolution which is limited to approximately this separation.

Early work by Hobbs *et al.* [110] used a "terrain following" feedback loop to increase the MFM resolution by a factor of 4. This is the same principle that is used in lift-mode™ scanning in the *Multimode SPM*. A standard TM-AFM topography scan is first made which is then used as a reference to make a further pass. The cantilever is *lifted* above the topography scan by a user defined amount, typically 10 – 50 nm, and a subsequent scan is made. This process is shown schematically in Figure 3.23. Since this subsequent scan follows directly the topography information from the first scan, it is virtually devoid of any contributions from F'_{VDW}, thus the force gradient measured in lift-mode™ is $F' \approx F'_M$. Clearly this leads to data that are not only of a higher resolution, but are much easier to interpret.

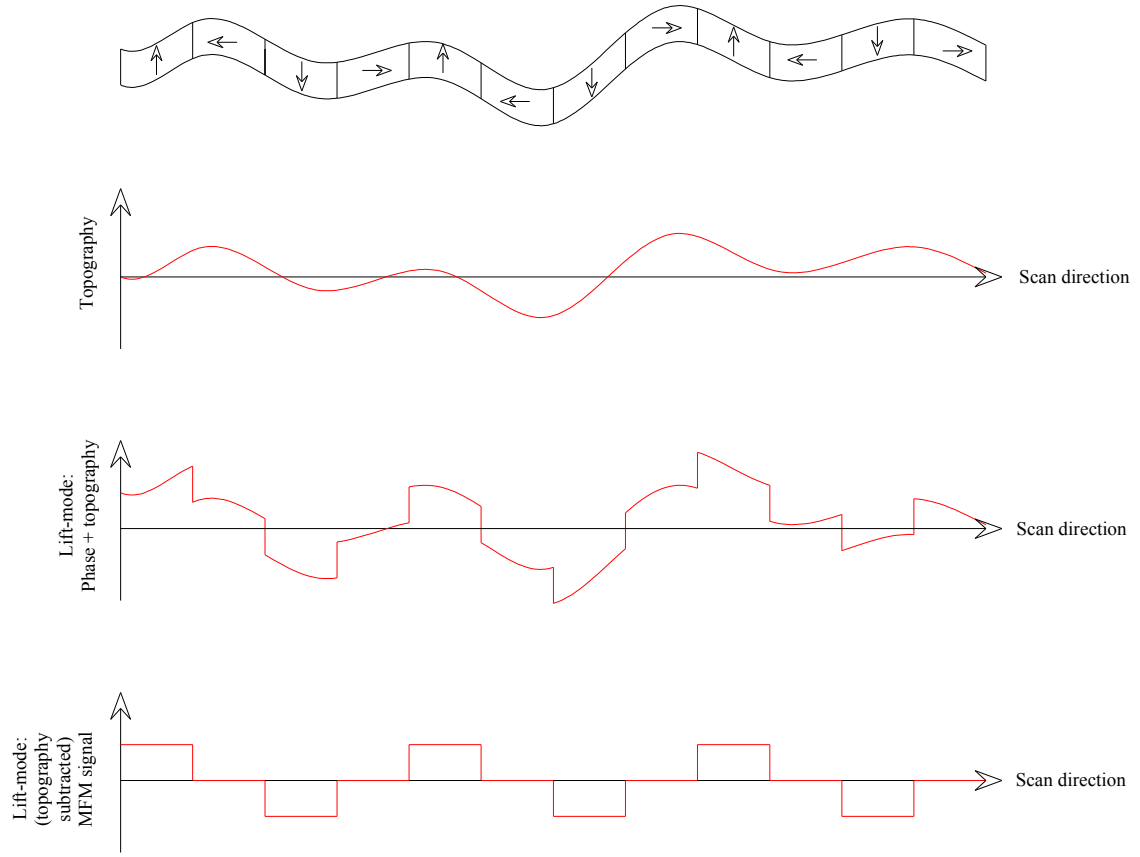

Figure 3.23: Schematic representation of AFM and MFM data acquisition. The top image represents a magnetized sample surface. The illustration below this shows the standard tapping mode AFM topography scan (van der Waals force). Below this is the raw data for the lift mode scan, in this instance detecting changes in phase of the cantilever's vibration due to magnetic domains. In the lift mode scan, the cantilever follows the topography scan directly, being deflected only due to longer range forces (*e.g.* magnetic), thus leaving only the lift-mode MFM signal shown in the bottom illustration.

Amos *et al.* [111] recently improved MFM resolution further by investigating the use of multi-domain probes rather than the standard single-domain probes, reaching a resolution better than 10 nm which is critical for imaging individual bits in the latest magnetic recording media. Very recent work by Endo *et al.* [112] has used MFM as a spectroscopic tool. The MFM probe is kept in a constant position and used to detect changes in local magnetization as the applied magnetic field is swept (MFS-MFM), in this instance locally probing vortex core movement and chirality of a NiFe disk. Novel methods such as these further reinforcing the versatility of MFM and SPM as a whole.

For the MFM measurements in this work, the cantilevers are single-domain type, constructed from Sb n-type doped Si and have a high-reflectivity coating of Cr / Co / Cr. The tip diameter is < 100 nm, the resonance frequency is 75 ± 5 Hz and the spring

constant is between 1 – 5 Nm^{-1}. The probes are always magnetized along the long axis (*i.e.* the *z*-axis). Using coated, rather than bulk magnetic probes[viii], the influence of the sample stray field on the probe magnetization (and *vice-versa*) is substantially reduced. This permits small sample-probe separations and therefore high spatial resolution.

3.9.5 Magnetic force microscopy as a probe for patterned magnetic media

Whilst MFM provides superb nano-metre scale resolution of magnetic landscapes, its inability to provide quantitative information is often a drawback. Whilst some success has been enjoyed from creating hysteresis loops from MFM data of switching field distributions of patterned elements via elementary counting processes [113, 114, 115, 116], it remains difficult to directly compare data from one measurement to the next. This problem is due, amongst other things, to the very large number of input parameters that are varied from the acquisition of one set of data to another, and the MFM tip shape and composition *etc.* Such input parameters include, but are by no means limited to, the cantilever tip to sample separation, the cantilever drive amplitude and frequency, and the proportional, integral and differential (PID) feedback controls. In order to obtain high quality data for good image reconstruction it is necessary to optimise each of these parameters from one experiment to another, making the quantitative comparison of different sets of data exceptionally difficult.

In an attempt to overcome this problem, the author has limited the range over which the variables are adjusted. For example, using only a small range of tip to sample separations (typically 50 nm), a single make and design of cantilever (see section 3.9.4) and a constant PI(D)[ix] ratio of 3:2. By keeping these variables as close to constant as possible, the author was able to relate the effect of the vertical component of the stray magnetic field ($\mathbf{B}_S$) on the change in phase of the MFM cantilever's oscillations ($\Delta\varphi$) from one set of data to another. In particular, if the easy axis of magnetization lies in or close to the sample plane (as in the case of the $REFe_2$ materials studied here), the presence of a patterned element will induce many surface magnetic poles at its edges.

[viii] The stray magnetic field from the MFM probe falls off much more rapidly with distance for probes with a thin magnetic coating when compared to bulk magnetic probes due to the significant reduction in magnetic material and the overall reduction in probe magnetization.

[ix] The *Digital Instruments Multimode SPM* software does not include control for a differential (D) feedback, but the term PID is in common use to indicate the type of feedback mechanism utilised.

The surface poles are responsible for $\mathbf{B}_S$, thus the phase change ($\Delta\varphi$) will also be strongly affected by the presence of patterned elements. MFM therefore provides a local probe of magnetic surface poles which were induced by the patterning process. This is demonstrated schematically in Figure 3.24, with the "+" and "–" signs representing the surface poles.

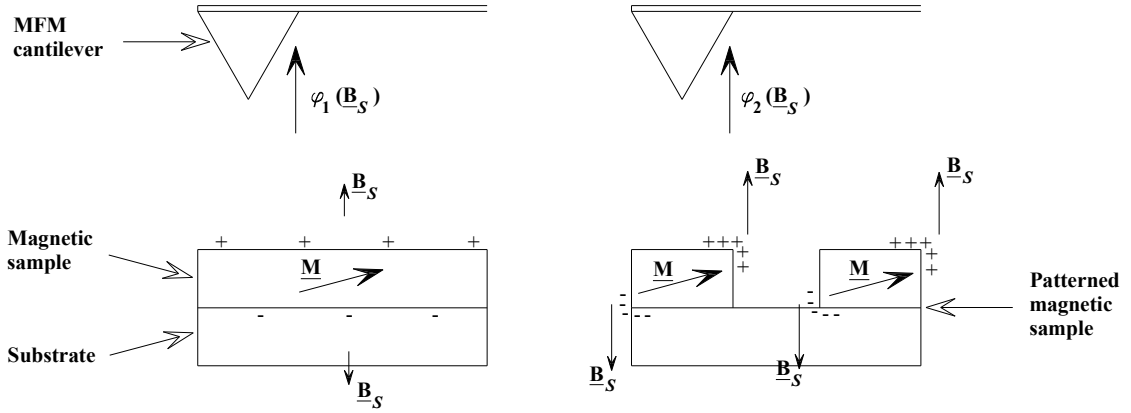

Figure 3.24: Schematic representation of the acquisition of MFM data. Left-hand image: easy axis of magnetization lying predominantly in the sample plane and associated stray magnetic field ($\mathbf{B}_S$). Right-hand image: patterned region in the same sample, leading to an accumulation of surface poles and hence more prominent $\mathbf{B}_S$ in specific regions. The MFM cantilever senses $\mathbf{B}_S$ which is detected as a change to the phase angle φ during data acquisition, hence $\varphi(\mathbf{B}_S)$.

From Figure 3.24 it is can be seen that, for the un-patterned sample (left-hand image), $\mathbf{B}_S$ is very small due to the sample's multi-domain structure. This is characteristic of very few surface poles, due to the predominantly in-plane sample magnetization (the reader should assume that the sample extends to infinity at its edges). In the patterned sample (right-hand image), many more surface poles are present at the edges of the patterned region, leading to a much larger and more localized $\mathbf{B}_S$. Clearly then, the deflection experienced by the cantilever ($\Delta\varphi$, a function of $\mathbf{B}_S$) will be large at the edges of the patterned regions, such that $\Delta\varphi_2(\mathbf{B}_S) > \Delta\varphi_1(\mathbf{B}_S)$. This is experimentally verified in the MFM data presented in Figure 3.25.

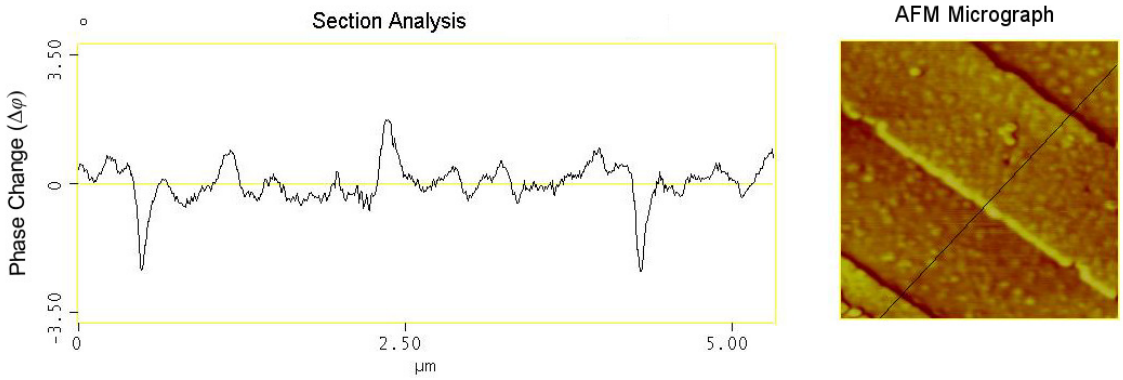

Figure 3.25: MFM cross-sectional analysis showing increased cantilever deflection ($\Delta\varphi$) at the edges of patterned regions, corresponding to an increase in $\mathbf{B}_S$ out of the plane of the sample (bright region, $+\Delta\varphi$) or into the sample plane (dark regions, $-\Delta\varphi$).

Comparing values of $\Delta\varphi$ from one sample to another provides a useful and rapid method for determining the local magnetic landscape, giving very useful insights into the effects that patterning has on the creation of stray magnetic fields and surface poles. It is not possible to directly quantify the sample magnetization using this method, but as most variables in the MFM data acquisition process are rigorously controlled, it is possible to make estimates of the magnitude of the pattern-induced stray magnetic field, either within the same sample, or from one sample to another. It should also be noted, that even if such a basic method could be extended to provide truly quantitative information regarding sample magnetization (from intricate knowledge of the MFM cantilever tip magnetization and stray field *etc.*), it would suffer serious flaws in the case of samples where patterned elements are present on a magnetic background, such as some of those detailed in Chapter 6.

3.10 Magneto Optical Kerr Effect

The interaction between the magnetic field of a medium and an electromagnetic wave is known as a magneto-optical effect, and in general serves to alter the speed at which electromagnetic waves of different polarizations propagate through the medium. There are two kinds of magneto-optical effects, the Faraday effect [117] and the Kerr effect [118] (MOKE). The Faraday effect is characterized by the rotation of the polarization of an electromagnetic wave when it is *transmitted* through the magnetic medium. The Kerr effect is characterized by the rotation in the polarization of an electromagnetic wave when it is *reflected* from the medium. In both instances, the change in polarization is proportional to the magnetization of the sample. This makes both the

Faraday and Kerr effects valuable tools for investigation the magnetic properties of samples. As expected, the origin of both of these interactions is the same and in short is traditionally related to the spin-orbit interaction of the electrons in the atoms under the application of a magnetic field. More recent models focus on the interaction of electromagnetic waves with surface plasmons. In this work the Kerr effect is used exclusively since this forms a simpler and more useful experiment; bulk samples as well as thin, transparent samples can be investigated, whilst analysis of these data is made somewhat simpler since there is no need to consider discontinuous changes in polarization across multiple interfaces.

3.10.1 Magnetic birefringence and magnetic dichroism

There are two key effects which must be considered when investigating the interaction between light and the orbital magnetic moments of electrons within the media: magnetic birefringence (MB) – polarization dependent refractive indices, and magnetic dichroism (MD) – polarization dependent absorption. These may be sub-divided further depending on the polarization of the light, namely circular (C) or linear (L), giving rise to the acronyms; MCB, MCD, MLB and MLD. Throughout this work the primarily concern is with linearly polarized light which is reflected off of the media hence MLD is the subject of interest.

When light is incident on a sample surface, in general a certain amount will be absorbed. If one considers the incident linearly polarized light to be composed of vertical and horizontally polarized components, each component will experience a different amount of absorption due to the effect of dichroism. The resultant reflected light R has two orthogonal components to its polarization; a large component from the standard Fresnel reflection coefficient r, and a small component called the Kerr coefficient k. Since r and k need not be in phase this leads not only to a rotation of the polarization of the reflected light, but also to light which is elliptically rather than linearly polarized. These effects are known as Kerr rotation (θ_K) and Kerr ellipticity (ε_K) respectively, both which serve to alter R.

3.10.2 Magneto optical Kerr effect geometries

The Kerr effect can be measured in three different configurations. These are known as polar, longitudinal and transverse MOKE. These are presented in Figure 3.26, from

where it can be seen that the terminology describes the relative orientation of the sample magnetization **M** and the incident and reflected light.

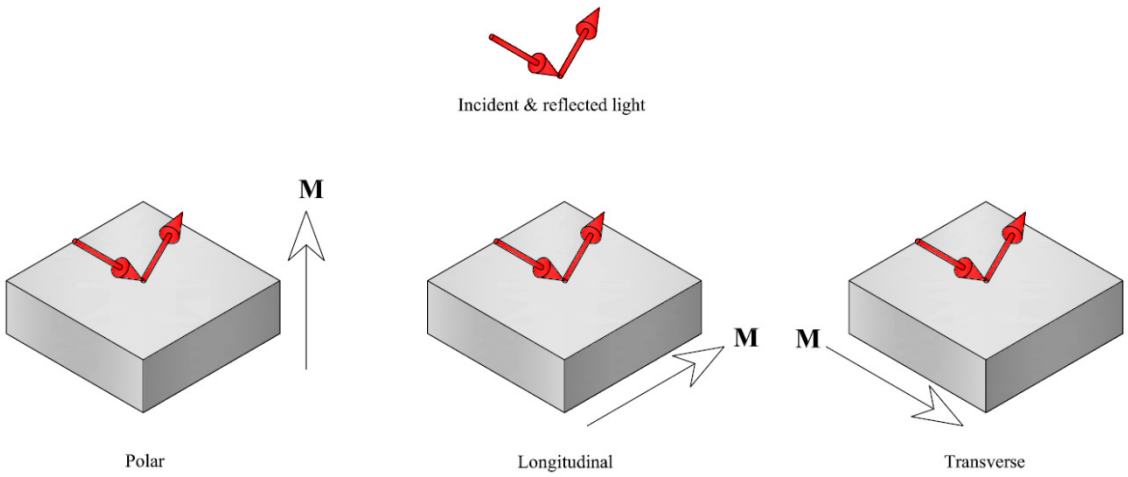

Figure 3.26: Schematic diagram showing the three orientations possible in MOKE measurements; Polar, longitudinal and transverse. Technically longitudinal and transverse MOKE require grazing incidence light. **M** = sample magnetization.

In the polar arrangement **M** is perpendicular to the sample surface thereby inducing θ_K and ε_K. In the longitudinal arrangement, provided there is a component of the incident light that is not normal to the sample surface this will again induce θ_K and ε_K. In the transverse arrangement there are no parallel components of **M** along the direction of the incident light so there is no induced θ_K or ε_K, only a change in the amplitude of the reflected signal $R = |r \pm k|^2$. No signal is obtained at normal incidence in longitudinal and transverse arrangements. An extensive review of magneto-optical effects and formal derivations of θ_K and ε_K are given in Wohlfarth & Buschow [119].

In this work longitudinal MOKE was used to characterize both bulk and patterned samples. A schematic of the longitudinal MOKE apparatus used is presented in Figure 3.27. The author is grateful for practical advice from Dr Chris Morrison and theoretical advice from Mr Daowei Wang, both of whom devoted much time to constructing and optimising this experimental arrangement.

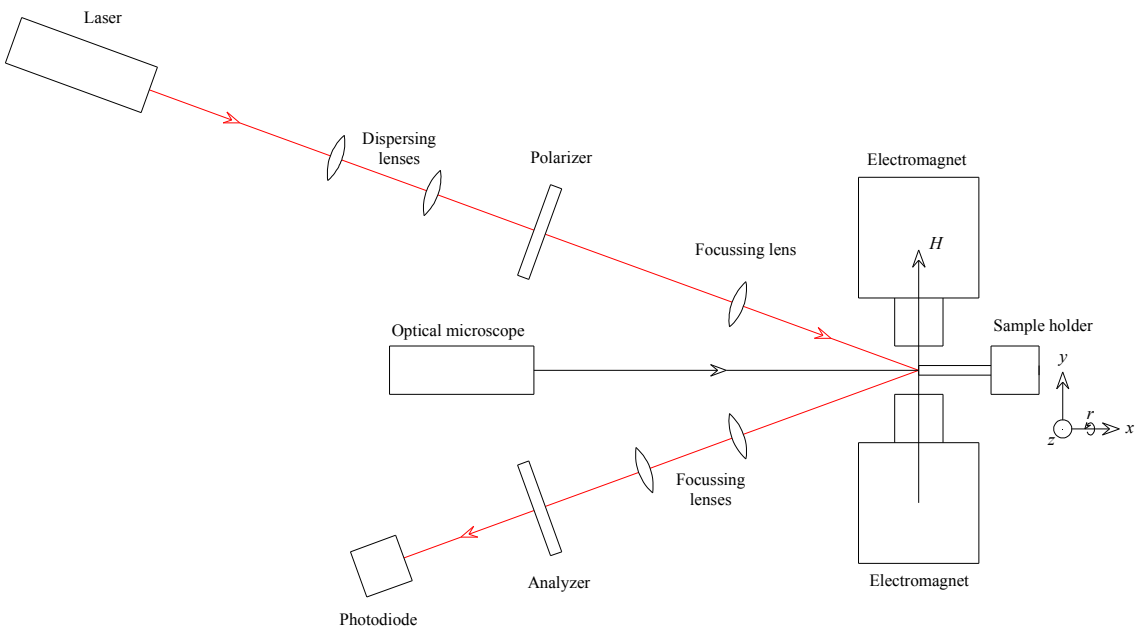

Figure 3.27: Schematic of the longitudinal MOKE experimental arrangment used in this work. The sample holder is continuously adjustable in *x*-, *y*-, *z*- and *r*- directions so that the laser can be accurately positioned onto a range of different areas on the sample surface.

The sample is placed between the poles of the electromagnet with the film plane perpendicular to the plane of the poles. The maximum applied field is ~ 0.35 T (recorded by a Hall probe positioned very close to the sample). The light source is a linearly polarized, intensity stabilized 15 mW 633 nm He-Ne laser. Dispersing and focussing lenses are included in the incident beam to minimize the laser spot diameter $Ø_l$ with the two-fold aim of reducing thermal damage to the sample and permitting the study of small regions. Typically $Ø_l$ = 200 μm. The focussing lenses in the reflected beam reduce the reflected $Ø_l$ so that it falls entirely on the photodiode. Two polarizers are used with angles almost perpendicular to each other; the reason they are not crossed is to improve the signal-to-noise ratio and to ensure a linear response in the photodiode. The author made modifications to include an optical microscope in this arrangement, the purpose of which is to aid the alignment of the sample and the laser spot so that the spot can wholly and accurately be placed onto small lithographically patterned regions. Finally, the electromagnet is driven by a power supply combined with a function generator and reversing unit, whilst data acquisition is performed using a computer to record the Hall probe and photodiode voltages within the `HPVEE` framework. In general, between 10 and 50 individual hysteresis loops are obtained over several minutes to several hours. These data are then mathematically combined and averaged in

order to create a relatively noise-free hysteresis loop. It should also be noted that in this MOKE arrangement, components of magnetization both in and out of the plane of the material are studied.

3.10.3 Skin depth and Kerr rotation angles

MOKE is considered to be a "surface sensitive" technique. Whilst this assumption is valid when compared with bulk magnetization measurements such as those made with a vibrating sample magnetometer (see section 3.11), the incident light does penetrate a finite depth into the sample surface. The depth of this penetration can be approximated using a skin depth calculation which gives the distance the light travels in a material before its amplitude decays to $1/e$ of its original value. The skin depth, δ is given by

$$\delta = \sqrt{\frac{\rho\lambda}{\pi\mu_0\mu_r c}} \tag{3.10}$$

with ρ the resistivity of the medium, λ the wavelength of the incident light, μ_0 the permeability of free space, μ_r the relative permeability of the medium and c the speed of light in a vacuum. Taking λ = 633 nm, $\mu_r \approx 1$ for optical wavelengths and $\rho_{DyFe_2} = 5.5 \times 10^{-7}$ Ωm [120], gives δ_{DyFe_2} = 17 nm. Similarly δ_{YFe_2} = 21 nm. The following conclusions regarding what exactly is sampled in MOKE measurements can be drawn:

1. In thin samples (where the total sample thickness is of the order 10 – 20 nm) the entire sample is probed.
2. In bulk films (where the total sample thickness is of the order hundreds of nm), only the top fraction of the sample (corresponding to δ) is probed.
3. In superlattice exchange spring samples (where there are many repeats of single nm thick layers making a sample which is hundreds of nm thick overall) only the top few repeats of these layers (corresponding to δ) are probed.

A final point to note regarding skin depth is that if the Cr metallic mask is not fully removed, the amplitude of the MOKE signal will be significantly reduced since δ_{Cr} = 8 nm. Thus MOKE may be used as a method to detect whether the metallic mask has been completely removed during Ar^+ ion milling.

The values for θ_K for $DyFe_2$ are given in Wohlfarth and Buschow [119] as $\theta_{K_{DyFe_2}} = 0.16°$ at an incident light wavelength of 633 nm. $\theta_{K_{YFe_2}} = -0.19°$ is given in Lange *et al.* [121]. This significant change in θ_K, coupled with the above calculations for δ leads to the interpretation of the amplitude of the reflected light R being non-trivial

in the case of multilayer samples. R will be dependent on the thickness of each layer, the orientation of the layers (*i.e.* which is the top layer) and on any interface reflections between the layers. In reality this does not pose a significant issue since only the *relative* amplitude of the signal for the *same* samples (before and after nano-scale structuring and ion implantation) will be considered. It is worth noting that samples with an YFe_2 top layer give bigger values for ΔR (*i.e.* larger amplitude in the MOKE hysteresis loops) due to its larger θ_K. Since $\theta_{K_{YFe_2}}$ is of the opposite sign to $\theta_{K_{DyFe_2}}$, the MOKE hysteresis loop is also reversed about the **B** = 0 axis. Results presented here are inverted so as to permit comparison between different data-sets; a process which does not affect the conclusions drawn.

3.11 Vibrating Sample Magnetometer

Since its conception in the 1950s [122, 123], the vibrating sample magnetometer (VSM) has gradually been adopted as a standard method for magnetic measurements. Two VSMs are used in this work, both based upon a design first proposed by Springford *et al.* [124]. The sample measured using the VSM technique must be small enough to be considered as a simple magnetic dipole. This is indeed the case for the samples studied in this work, measuring ~ 5 mm along each edge. This sample is mounted on a rod and placed within a highly homogenous magnetic field, within which there is a pair of pick-up coils at an equilibrium position $z = z_0$. The sample is then driven sinusoidally at a frequency of typically $\omega = 10 - 100$ Hz with an amplitude $z = z_a = 1$ mm. The movement of the magnetized sample results in a change of flux (φ) within the pick-up coils, which in turn induces an electromotive force (ε) given by $\varepsilon = -\frac{d\varphi}{dt}$. A full derivation of this sinusoidal motion used to define ε is given in Beaujour [13] to be

$$\varepsilon = z_a \omega m \sin(\omega t)\, G(z_0) \tag{3.11}$$

with m the magnetic moment of the sample and t the time. $G(z_0) = \left.\frac{d\left(\frac{\mathbf{B}}{\mathbf{I}}\right)}{dz}\right|_{z_0}$ defines the geometric sensitivity function which represents the dependence of the VSM signal output on the position of the sample along the z-axis [13, 125] (where **B** is the magnetic field which would be generated by a fictitious current **I** flowing within the pick-up coils). $G(z_0)$ is assumed to be constant over the whole sample volume and is calibrated

using bulk samples of known magnetic moments, thus meaning that the measurement of ε provides a direct measurement of the sample's magnetic moment, m.

Both VSMs used in this work are based upon an *Oxford Instruments Aerosonic 3001*. In one VSM, a superconducting magnet can be used to produce fields of up to 12 / 14 T within a sample space which can have its temperature varied between ~ 2 K and room temperature. In the other VSM, an electromagnet generated field of 1.1 T can be applied at room temperature only, to a sample which can be rotated within the field. In both VSMs, the applied field has a homogeneity of 0.1% over a ~ 10 mm Ø sample space. The superconducting-magnet based VSM has a sensitivity of ~ 2×10^{-6} emu (2×10^{-9} Am^2), and the electromagnet-based VSM has a sensitivity of ~ 5×10^{-5} emu.

The technique of VSM can be applied to bulk samples only, and therefore other "focussed" methods of analysis, such as the aforementioned MFM and MOKE techniques, must be used to characterise nano-scale patterned samples. However, as will become clear in the following chapters, the effects of implanted Ar^+ ions across the entire sample surface serve to alter its magnetic properties quite drastically. Thus VSM has been used to characterise samples both before and after Ar^+ ion implantation, providing a valuable insight into artificially induced atomic-scale changes within the sample's crystalline structure. Moreover, VSM, unlike MOKE and MFM, provides a calibrated measurement of the sample magnetization. Not only is this useful for basic magnetic characterization, it can also be used to provide a calculation of the volume of magnetic material present in a sample. An example of this calculation is provided in the Appendix.

References

[1] BBC News Article, *Fire Destroys Top Research Centre*, news article available online http://news.bbc.co.uk/1/hi/england/hampshire/4390048.stm, 2005.

[2] J. R. Arthur, *J. App. Phys.*, vol. **39**, pp. 4032 – 4034, 1968.

[3] A. Y. Cho & J. R. Arthur, *Phys. Rev. Lett.*, vol. **22**, no. 22, pp. 1180 – 1181, 1969.

[4] M. N. Baibich, J. M. Broto, A. Fert, F. Nguyen Van Dau, F. Petroff, P. Eitenne, G. Creuzet, A. Friederich & J. Chazelas, *Phys. Rev. Lett.*, vol. **61**, no. 21, pp. 2472 – 2475, 1988.

[5] M. J. Bentall, R. A. Cowley, W. J. L. Buyers, Z. Tun, W. Lohstroh, R. C. C. Ward & M. R. Wells, *J. Phys.: Condens. Matt.*, vol. **15**, pp. 4301 – 4330, 2003.

[6] M. J. Bentall, R. C. C. Ward, E. J. Grier & M. R. Wells, *J. Phys.: Condens. Matt.*, vol. **15**, pp. 6493 – 6512, 2003.

[7] P. J. Kelly, R. D. Arnell, *Vacuum*, vol. **56**, pp. 159 – 172, 2000.

[8] A. Mougin, C. Dufour, K. Dumesnil, N. Maloufi & Ph. Mangin, *Phys. Rev. B*, vol. **59**, no. 8, pp. 5950 – 5959, 1999.

[9] J. Tersoff & R. M. Tromp, *Phys. Rev. Lett.*, vol. **70**, no. 18, pp. 2782 – 2786, 1993.

[10] A. R. Wildes, R. A. Cowley, R. C. C. Ward, M. R. Wells, C. Jansen, L. Wireen & J. P. Hill, , *J. Phys.: Condens. Matt.*, vol. **10**, pp. L631 – L637, 1998.

[11] A. R. Wildes, J. Mayer & K. Theis-Bröhl, *Thin Sol. Film.*, vol. **401**, pp. 7 – 34, 2001.

[12] V. Oderno, C. Dufour, K. Dumesnil, Ph. Mangin & G. Marchal, *J. Cryst. Growth*, vol. **165**, pp. 175 – 178, 1996.

[13] J-. M. L. Beaujour, *Ph. D. Thesis*, University of Southampton, UK, 2003.

[14] J. Lee, G. Lauhoff, & J. A. C. Bland, *Phys. Rev. B*, vol. **56**, no. 10, pp. R5728 – R5731, 1997.

[15] C-. T. Wang, B. M. Clemens & R. L. White, *IEEE Trans. Mag.*, vol. **32**, no. 5, pp. 4752 – 4754, 1996.

[16] A. Mougin, C. Dufour, K. Dumesnil & Ph. Mangin, *Phys. Rev. B*, vol. **62**, no. 14, pp. 9517 – 9531, 2000.

[17] M. J. Bentall, R. C. C. Ward, E. J. Grier & M. R. Wells, *J. Phys.: Condens. Matt.*, vol. **15**, pp. 6493 – 6512, 2003.

[18] M. Huth & C. P. Flynn, *J. App. Phys.*, vol. **83**, no. 11, pp. 7261 – 7263, 1998.

[19] Reproduced from a free application on the US Naval Research Laboratory website, http://cst-www.nrl.navy.mil/lattice/struk/c15.html.

[20] C. W. Oatley, *The Scanning Electron Microscope*, Cambridge Press, 1972.

[21] Kimball Physics Inc. Technical Bulletin, *ES-423E Extended Life LaB_6 Cathode User Information*, Kimball Physics Inc., 2002.

[22] R. G. Murray & R. J. Collier, *Rev. Sci. Instrum.*, vol. **48**, no. 7, p. 872, 1977.

[23] V. Katsap, *Vacuum Electronics Conference 2006*, IEEE International, p.210, 2006.

[24]P. B. Sewell, Kimball Physics Inc. Technical Bulletin, *The Relationship Between LaB_6 Cathode Lifetime and Gun Vacuum*, Kimball Physics Inc., 1991.

[25] W. P. Dyke, J. K. Trolan, W. W. Dolan & G. Barnes, *J. App. Phys.*, vol. **24**, no. 5, 1953.

[26] A. V. Crewe, D. N. Eggenberger, J. Wall & L. M. Welter, *Rev. Sci. Instrum.*, vol. **39**, no. 4, pp. 576 – 583, 1968.

[27] W. H. Schottky, *Phys. Rev.*, vol. **28**, pp. 74 – 103, 1926.

[28] M. J. Fransen, M. H. F. Overwijk & P. Kruit, *Appl. Sur. Sci.*, vol. **146**, pp. 357 – 362, 1999.

[29] T. H. P. Chang, *IEEE Trans. Magnet.*, vol. **Mag-10**, no. 3, pp. 883 – 887, 1974.

[30] A. N. Broers, *5th International Conference on Electron and Ion Beam Science and Technology*, Electrochemical Society, pp. 3 – 25, 1972.

[31] C. Wang, *D. Phil. thesis*, University of Oxford, UK, 2008.

[32] P. B. Sewell, Kimball Physics Inc. Technical Bulletin, *General Guidelines for Operating ES-423E LaB6 Cathodes*, Kimball Physics Inc., 1991.

[33] O. Scherzer, *J. App. Phys.*, vol. **20**, no. 1, pp. 20 – 29, 1949.

[34] P. Nellist, *Phys. World*, vol. **18**, no. 11, pp. 24 – 29, 2005.

[35] P.E. Batson, N. Dellby & O. L. Krivanek, *Nature*, vol. **418**, pp. 617 – 620, 2002.

[36] I. P. Jones, *Chemical Microanalysis Using Electron Beams*, The Institute of Materials, 1992.

[37] J. J. Bozzola & L. D. Russell, *Electron Microscopy 2nd Ed.*, Jones & Bartlett Pub., 1998.

[38] A. T. Tseng, K. Chen, C. D. Chen and K. J. Ma, *IEEE Trans. Electron. Pack. Manuf.*, Vol. **25**, no. 2, pp. 141-149, 2003.

[39] M. W. Larkin & R. K. Matta, *Sol. State Electron.*, vol. **10**, pp. 491 – 496, 1967.

[40] M. Khoury & D. K. Ferry, *J. Vac. Sci. Technol. B*, vol. **14**, no. 1, pp. 75 – 79, 1996.

[41] C. Vieu, F. Carcenac, A. Pépin, Y. Chen, M. Mejias, A. Lebib, L. Manin-Ferlazzo, L. Couraud & H. Launois, *Appl. Sur. Sci.*, vol. **164**, pp. 111 – 117, 2000.

[42] Raith GmbH, *ELPHY Quantum*, details available at http://www.raith.com/?xml=solutions|SEM+%26+FIB+lithography+kits|ELPHY+Quantum.

[43] M. Hatzakis & A. N. Broers, *Record of 10th Symposium on Electron, Ion and Laser Beam Tech.*, San Francisco, p. 107, 1969.

[44] F. S. Ozdemir, Annual ACM IEEE Design Automation Conference; Proceedings of the 16th Conference Design Automation, San Diego, pp. 383 – 391, 1979.

[45] T. H. P. Chang, *IEEE Trans. Magnet.*, vol. **Mag-10**, no. 3, pp. 883 – 887, 1974.

[46] L. W. Hobbs, *Introduction to Analytical Electron Microscopy*, Plenum, New York, p.437, 1979.

[47] A. Charlesby, *Atomic Radiation and Polymers*, Pergamon Press, England, 1960.

[48] J. S. Greeneich, *J. Appl. Phys.*, vol. **45**, no. 12, pp. 5264 – 5268, 1974.

[49] R. D. Heidenreich, L. F. Thompson, E. D. Feit & C. M. Melliar-Smith, *J. Appl. Phys.*, vol. **44**, no. 9, pp. 4039 – 4047, 1973.

[50] L. F. Thompson, E. D. Feit, C. M. Melliar-Smith & R. D. Heidenreich, *J. Appl. Phys.*, vol. **44**, no. 9, pp. 4048 – 4051, 1973.

[51] R. Grundbacher, I. Adesida, Y-. C. Kao & A. A. Ketterson, *J. Vac. Sci. Technol. B*, vol. **15**, no. 1, pp. 49 – 52, 1996.

[52] Y. Chen, K. Peng & Z. Cui, *Micro Elec. Eng.*, vol. **73-74**, pp. 278 – 281, 2004.

[53] M. A. Gritz, J. González & G. D. Boreman, *Micromach. Technol. Micro-opt. Nano-opt.*, vol. **4984**, pp. 100 – 110, 2003.

[54] Micro Chem. Corp., *Nano™ PMMA and Copolymer*, product catalogue available at http://www.microchem.com, 2001.

[55] T. H. P. Chang, *J. Vac. Sci. Technol.*, vol. **12**, no. 6, pp. 1271 – 1275, 1975.

[56] D. F. Kyser & C. H. Ting, *J. Vac. Sci. Technol.*, vol. **16**, no. 6, pp. 1759 – 1763, 1979.

[57] S-. Y. Lee & K. Anbumony, *Micro Elec. Eng.*, vol. **83**, pp. 336 – 344, 2005.

[58] J. I. Martín, J. Nogués, K. Liu, J. L. Vicent & I. K. Schuller, *J. Magn. Magn. Mater.*, vol. **256**, pp. 449 – 501, 2003.

[59] R. Sbiaa, K. O. Aung, S. N. Piramanayagam, E-. L. Tan & R. Law, *J. App. Phys.*, vol. **105**, p. 073904, 2009.

[60] R. Moriya, L. Thomas, M. Hayashi, Y. B. Bazaliy, C. Rettner & S. S. P. Parkin, *Nature Physics*, vol. **4**, pp. 368 – 372, 2008.

[61] Y. Kitade, H. Komoriya & T. Maruyama, *IEE Trans. Magnet.*, vol. **40**, no. 4, pp. 2516 – 2518, 2004.

[62] A. Remhof, A. Schumann, A. Westphalen, H. Zabel, N. Mikuszeit, E. Y. Vedmedenko, T. Last & U. Kunze, *Phys. Rev. B*, vol. **77**, p. 134409, 2008.

[63] P. J. Hirst, T. G. Henrici, I. L. Atkin, J. S. Satchel1, J. Moxey, N. J. Exon, M. J. Wooliscoft, T. J. Horton & R.G.Humphreys, *IEEE Trans. Appl. Superdon.*, vol. **9**, no. 2, pp. 3833 – 3836, 1999.

[64] Q. Zhang, Y. Li, A. V. Nurmikko, G. X. Miao, G. Xiao & A. Gupta, *J. Appl. Phys.*, vol. **96**, no. 12, pp. 7527 – 7531, 2004.

[65] T. Seki, T. Shima, K. Yakushiji, K. Takanashi, G. Q. Li & S. Ishio, *J. Appl. Phys.*, vol. **100**, p. 043915, 2006.

[66] J. A. Katine, F. J. Albert, R. A. Buhrman, E. B. Myers & D. C. Ralph, *Phys. Rev. Lett.*, vol. **84**, no. 14, pp. 3149 – 3152, 2000.

[67] J. W. Lau, R. D. McMichael, S. H. Chung, J. O. Rantschler, V. Parekh & D. Litvinov, *App. Phys. Lett.*, vol. **92**, p. 012506, 2008.

[68] *Ion Beam Etch Rates and Sputter Yields*, Intlvac, Ontario, data available at http://www.intlvac.com/wp

[69] D. Tripathy & A. O. Adeyeye, *Phys. Rev. B*, vol. **79**, p. 064413, 2009.

[70] S. Jain & A. O. Adeyeye, *J. Appl .Phys.*, vol. **104**, p. 103914, 2008.

[71] P. Vavassori, D. Bisero, V. Bonanni, A. Busato, M. Grimsditch, K. M. Lebecki, V. Metlushko & B. Ilic, *Phys. Rev. B*, vol. **78**, p. 174403, 2008.

[72] S. Y. H. Lau, S. S. Kushvaha, Y. H. Wu, K. L. Teo & T. C. Chong, *Appl. Phys. Lett.*, vol. **93**, p. 122504, 2008.

[73] F. Magnus, G. Burnell, Y. Miyoshi, K. A. Yates, Y. Bugoslavsky, S. K. Clowes, P. W. Josephs-Franks, M. G. Blamire & L. F. Cohen, Physics of Semiconductors, 28th International Conference, *AIP Conf. Proc.*, **CP893**, pp. 1281 – 1282, 2007.

[74] K. Wang, K. N. Martin, C. G. Morrison, R. C. C. Ward, G. J. Bowden & P. A. J. de Groot, *Phys. Stat. Sol.*, vol. **203**, no. 15, pp. 3831 – 3835, 2006.

[75] K. Wang, C. Morrison, K. N. Martin, R. C. C. Ward, G. J. Bowden & P. A. J. de Groot, *J. Alloy. Comp.*, vol **440**, pp. 23 – 25, 2007.

[76] K. Wang, K. N. Martin, C. G. Morrison, R. C. C. Ward, G. J. Bowden & P. A. J. de Groot, *Appl. Phys. A*, vol **86**, pp. 325 – 328, 2007.

[77] K. Wang, K. N. Martin, C. Morrison, R. C. C. Ward, G. J. Bowden & P. A. J. de Groot, *J. Alloy. Comp.*, vol. **455**, pp. 31 – 34, 2007.

[78] M. E. Walsh, *M. Sci. Thesis*, Massachusetts Institute of Technology, USA, 2000.

[79] A. Aziz, S. J. Bending, H. Roberts, S. Crampin, P. J. Heard & C. H. Marrows, *J. Appl. Phys.*, vol. **98**, p.124102, 2005.

[80] Y. Yuba, K. Gamo, H. Toba, X. G. He & S. Namba, *Jap. J. Appl. Phys.*, vol. **22**, no. 7, pp. 1206 – 1210, 1983.

[81] A. D. G. Stewart & M. W. Thompson, *J. Mater. Sci.*, vol. **4**, pp. 56 – 60, 1969.

[82] N. Yamauchi, T. Yachi & T. Wada, *J. Vac. Sci. Technol. A*, vol. **2**, no. 4, pp. 1552 – 1557, 1984.

[83] M. Walter, H. M. Hütten, H. C. Scheer & J. Engemann, *Model. Simul. Mater. Sci. Eng.*, vol. **6**, pp. 251 – 260, 1998.

[84] P. Sigmund, *Phys. Rev.*, vol. **184**, no. 2, pp. 383 – 416, 1969.

[85] P. Sigmund, *Appl. Phys. Lett.*, vol. **14**, no. 3, pp. 114 – 117, 1969.

[86] J. F. Ziegler, M. D. Ziegler & J. P. Biersack, `SRIM-2008.04`, PC software available at http://www.srim.org

[87] J. Lindhard, M. Scharff & H. E. Schiøtt, *Mat. Fys. Medd. Dan. Vid. Selsk.*, vol. **33**, no. 14, 1963

[88] O. Wada, *J. Phys. D : Appl. Phys.*, vol. **17**, pp. 2429 – 2437, 1984.

[89] N. Yamauchi, T. Yachi & T. Wada, *J. Vac. Sci. Technol. A*, vol. **2**, no. 4, pp. 1552 – 1557, 1984.

[90] G. Carter, *J. Phys. D: Appl. Phys.*, vol. **34**, pp. R1 – R22, 2001.

[91] Microchemicals, *Chromium Etching Technical Information*, Microchemicals.eu, 2009.

[92] K. R. Williams, K. Gupta & M. Wasilik, *J. Microelectromech. Sys.*, vol. **12**, no. 6, pp. 761 – 778, 2003.

[93] W. H. Bragg & W. L. Bragg, *Nature*, vol. **91**, p. 557, 1913.

[94] W. L. Bragg, *Proc. Roy. Soc. A.*, vol. **89**, pp. 248 – 277, 1913.

[95] B. E. Warren, *X-Ray Diffraction*, Addison-Wesley Publishing Co., 1969.

[96] W. Clegg, *Crystal Structure Determination*, Oxford University Press, 2008.

[97] M. J. Bentall, R. C. C. Ward, E. J. Grier & M. R. Wells, J. *Phys., Condens. Matt.*, vol. **15**, pp. 6493 – 6512, 2003.

[98] Philips Service Technical Note, *Curved Graphite Monochromator PW 1752*, Philips.

[99] Carl Zeiss Press Release, *Carl Zeiss SMT Ships World's First ORION™ Helium Ion Microscope to U.S. National Institute of Standards and Technology*, PI no. 125/07, p. 4, 2007.

[100] Carl Zeiss Press Release, *Carl Zeiss Sets New World Record in Microscopy Resolution Using Scanning Helium Ions*, PI no. 0220-2008-ENG, p. 1, 2008.

[101] J. Morgan, J. Notte, R. Hill & B. Ward, *Microscopy Today*, vol. **14**, no. 4, pp. 24 – 31, 2006.

[102] G. Binning & R. Hohrer, *Ultramicroscopy*, vol. **11**, no. 2-3, pp. 157 – 160, 1983.

[103] G. Binning, C. F. Quate, Ch. Gerber, *Phys. Rev. Lett.*, vol. **56**, no. 9, pp. 930 – 933, 1986.

[104] R. Wiesendanger, *Scanning Probe Microscopy and Spectroscopy*, Cambridge University Presss, Cambridge, 1994.

[105] D. Tabor & R. H. S. Winterton, *Proc. Roy. Soc. A.*, vol. **312**, pp. 435 – 450, 1969.

[106] E. J. Abott & F. A. Firestone, *Mec. Eng.*, vol. **55**, p. 569, 1933.

[107] Y. Martin & H. K. Wickramasinghe, *Appl. Phys. Lett.*, vol **50**, no. 20, pp. 1455 – 1457, 1987.

[108] J. J. Sáenz, N. García, P. Grütter, E. Meyer, H. Heinzelmann, R. Weisendanger, L. Rosenthaler, H. R. Hidber & H-. J. Güntherodt, *J. Appl. Phys.*, vol. **62**, no. 10, pp. 4293 – 4295, 1987.

[109] Y. Martin, D. Rugar & H. K. Wickramasinghe, *Appl. Phys. Lett.*, vol. **52**, no. 3, pp. 244 – 246, 1988.

[110] P. C. D. Hobbs, D. W. Abraham & H. K. Wickramasinghe, *Appl. Phys. Lett.*, vol. **55**, no. 22, pp. 2357 – 2359.

[111] N. Amos, R. Ikkawi, R. Haddon, D. Litvinov & S. Khizroev, *Appl. Phys. Lett.*, vol. **93**, p. 203116, 2008.

[112] Y. Endo, I. Sasaki, R. Nakatani & M. Yamamoto, *Jap. J. Appl. Phys.*, vol. **48**, p. 066502, 2009.

[113] G. Hu, T. Thomson, M. Albrecht, M. E. Best, B. D. Terris, C. T. Rettner, S. Raoux, G. M. McClelland & W. M. Hart, *J. Appl. Phys.*, vol. **95**, no. 11, pp. 7013 – 7015, 2004.

[114] C. Haginoya, S. Heike, M. Ishibashi, K. Nakamura, K. Koike, T. Yoshimura, J. Yamamoto & Y. Hirayama, *J. Appl. Phys.*, vol. **85**, no. 12, pp. 8327 – 8331, 1999.

[115] J. W. Lau, R. D. McMichael, S. H. Chung, J. O. Rantschler, V. Parekh & D. Litvinov, *Appl. Phys. Lett.*, vol. **92**, p. 012506, 2008.

[116] E. Chunsheng, V. Parekh, P. Ruchhoeft, S. Khizroev & D. Litvinov, *J. Appl. Phys.*, vol. **103**, p. 063904, 2008.

[117] M. Faraday, *Phil. Trans. R. Soc.*, vol. **136**, pp. 1 – 20, 21 – 40 & 41 – 62, 1846.

[118] J. Kerr, *Phil. Mag. 5*, vol. **3**, no. 19, pp. 321 – 343, 1877.

[119] E. P. Wohlfarth & K. H. J. Buschow, *Ferromagnetic materials: a handbook on the properties of magnetically ordered substances vol. 4*, Amsterdam, 1988.

[120] E. Gratz, E. Bauer, H. Nowotny, A. T. Burkov & M. V. Vedernikov, *Sol. Stat. Comm.*, vol. **69**, no. 10, pp. 1007 – 1010, 1989.

[121] R. J. Lange, I. R. Fisher, P. C. Canfield, V. P. Antropov, S. J. Lee, B. N. Harmon & D. W. Lynch, *Phys. Rev. B*, vol. **62**, no. 11, pp. 7084 – 7092, 2001.

[122] S. Foner, *Rev. Sci. Instrum.*, vol. **27**, p. 548, 1956.

[123] S. Foner, *Rev. Sci. Instrum.*, vol. **30**, no. 7, pp. 548 – 557, 1959.

[124] M. Springford, J. R. Stockton & W. R. Wampler, *J. Phys. E: Sci. Instrum.*, vol. **4**, no. 12, pp. 1036 – 1040, 1971.

[125] K. N. Martin, *Ph. D. Thesis*, University of Southampton, UK, 2008.

Chapter 4

Nano-scale Patterned $REFe_2$ Laves Phase Intermetallics

The subject matter of this chapter is the first successful demonstration of patterning on the nano-scale in $REFe_2$ films and multilayer structures. It is intended to serve as a general guide towards the patterning process, bringing together many of the elements discussed in the experimental methods chapter. This work highlights the successes of the patterning process as well as detailing some of the drawbacks and problems encountered. Furthermore the benefits of the dry etching process over the wet etching techniques are emphasized.

The structure of this chapter is as follows. In section 4.1 a brief but comprehensive review is given on the creation of patterned structures in $REFe_2$ materials using a wet etching process. It will be argued that isotropic etch processes, whilst being relatively successful, possess severe resolution constraints rendering them essentially useless for inclusion in nano-scale patterned media technologies. Accordingly, dry etching techniques are described in section 4.2, highlighting the benefits they possess over wet etching techniques. Finally in section 4.3 it is shown that even the dry etching techniques encounter some drawbacks, namely re-deposition and the implantation of the incident Ar^+ ions. However, the reader will learn that re-deposition can be readily tackled and overcome, or, in the case of ion implantation, be used to great benefit to investigate fundamental magnetic and material properties. This chapter is dedicated to describing the fabrication of patterned elements in the $REFe_2$ materials. The magnetic characterization of these materials is delayed a chapter in favour of describing the process of ion implantation. Consequently the magnetic properties of patterned $REFe_2$ media are presented in Chapter 6.

4.1 Wet Etching to Pattern $REFe_2$ Films and Multilayers

Patterned elements have previously been fabricated in samples of epitaxially grown $REFe_2$ films and multilayer structures using a wet etching process [1, 2, 3, 4]. Here, the term "wet etching" refers to a process which uses liquid chemicals rather than the "dry" gases used in reactive ion etching and ion milling. A short description of these processes can be found in section 3.6. At the outset it should be noted that the wet etching process, when applied to $REFe_2$ materials, is rather isotropic. These materials are easily etched by chemical methods and as such the etching is hard to control, resulting in an overwhelming tendency for the etching to proceed in all directions at the same rate [5]. In general, this results in a large undercut to the patterned structure, thereby providing a constraint on the ultimate resolution achievable. Moreover, the wet etching process is very sensitive to local sample imperfections, for example small regions of surface oxides can result in exaggerated etching at these positions. This reduces the ultimate resolution still further. Example scanning electron microscope (SEM) micrographs showing the rough edges associated with this accelerated etching can be seen in Figure 4.1 and Figure 4.2.

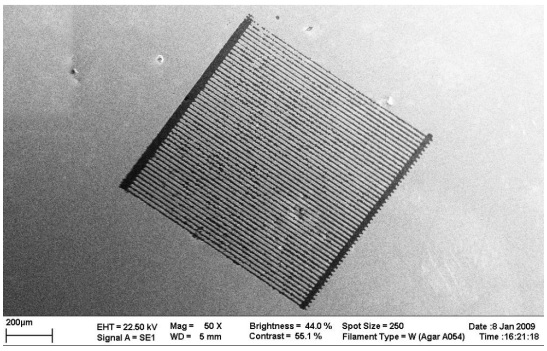

Figure 4.1: 50 × magnification SEM micrograph of ~ 10 μm lines with a pitch of ~ 15 μm in a [2 nm $DyFe_2$ / 8 nm YFe_2] × 40 multilayer sample. The lines have their major axis along the material's easy axis of magnetization.

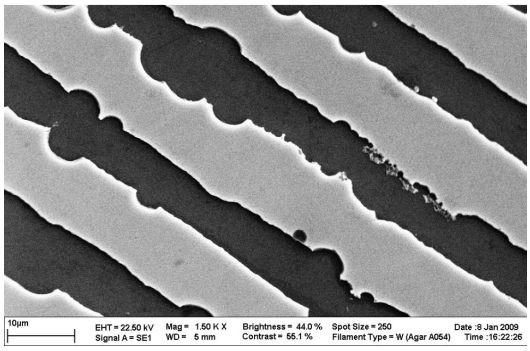

Figure 4.2: 1,500 × magnification SEM micrograph, zoomed in on an arbitrary patterned region of Figure 4.1. The enhanced etching at sites of imperfections is clearly visible, leading to very jagged edges.

Despite these drawbacks, patterns defined via the wet etching process display some interesting results. These are highlighted, for different $REFe_2$ materials, in the remainder of section 4.1.

4.1.1 Review of micron-sized patterns in $REFe_2$ materials defined by wet etching

The first demonstration of patterned structures in epitaxial $REFe_2$ samples was given in 2006 by Wang *et al.* [1], who reported results on patterned lines in a thick (400 nm) sample of magnetically soft YFe_2. Lines of width 6.5 μm with a period of 20 μm were fabricated over a total area of 1 × 1 mm. The lines were patterned along two directions, parallel to the $[\bar{1}11]$ and $[001]$ axes, corresponding to directions believed to be close to the easy and hard axis of magnetization respectively [6, 7]. The reported hysteresis loops [1] for the as-grown film are in good agreement with the author's own measurements for a 100 nm thick YFe_2 film[i]. The hysteresis loop is almost completely square when the magnetic field is applied along a direction close to the easy axis of magnetization, but when the field is applied along a direction close to the hard axis of magnetization the hysteresis loop reveals three distinct regimes (the reader is referred to the description in section 5.1.2 for further detail regarding hard axis hysteresis loops in materials with a cubic anisotropy). Of course these hysteresis loops display a reduced magnitude of the MOKE signal received for the patterned film when compared to the as-grown film, in keeping with the removal of material during the patterning process. When lines are patterned with their major axis parallel to the $[\bar{1}11]$ direction, the easy axis of magnetization remains the same as expected. The hard axis of magnetization however rotates from the $[001]$ direction to the $[1\bar{1}2]$ direction, *i.e.* it is reoriented so that it becomes perpendicular to the major axis of the lines. When lines are patterned with their major axis parallel to the $[001]$ direction, the easy axis of magnetization is reoriented so that it too lies in this direction, whilst the hard axis is oriented orthogonal to this along the $[\bar{1}10]$ direction. This shows that the process of patterning lines in an epitaxially grown YFe_2 film induces a shape anisotropy that is more dominant than the intrinsic magnetocrystalline and magnetoelastic anisotropies which govern the magnetic behaviour of the as-grown sample. The magnitude of this shape induced anisotropy (K_s) is calculated roughly to be $K_s = 1.1 \times 10^5$ erg cm^{-3}, which is close to the value of the samples intrinsic anisotropy $K_I = K_{MC} + K_{ME} = 1.4 \times 10^5$ erg cm^{-3} (with K_{MC} and K_{ME} the magnetocrystalline and magnetoelastic anisotropies respectively). Thus

[i] It should be noted that the author suspects some erroneous labelling of that data in ref. [1] with regard to which hysteresis loop corresponds to the magnetic field applied along which axes.

patterning rather large striped arrays in the sample can influence the easy and hard axis of magnetization. This, however, is not a surprising result given that K_{MC} and K_{ME} of YFe_2 thin film samples are relatively weak since only the Fe ions carry magnetic moments [6].

Striped arrays were also investigated in a magnetically hard epitaxial film of $DyFe_2$ [2]. In this work lines were patterned with their major axis along the close to easy axis direction of $[\bar{1}10]$ [8]. The arrays investigated had a width of 3.4 μm and a period of 18 μm. Again the sample was 400 nm thick and the patterned array covered 1 × 1 mm. It is worth noting that the MOKE hysteresis loops for this sample show no evidence of an out of plane component of magnetization. This is in contrast to the author's measurements of similar $DyFe_2$ samples (see section 5.2.2), which themselves are in good agreement with the work by Zhukov *et al.* [8] and D. Wang [9]. However the hysteresis loops of ref. [2] do show large amounts of noise, which may mask the appearance of the out of plane component of magnetization. On comparing the as-grown and patterned $DyFe_2$ samples, a slight increase in the measured coercivity is found when the magnetic field is applied along the $[\bar{1}10]$ direction. But, once again the signal-to-noise ratio (SNR) obtained from the patterned regions is *very* poor. K. Wang *et al.* [2] encounter similar problems to this author when attempting to characterize the $DyFe_2$ sample with the magnetic field applied along the $[00\bar{1}]$ direction – the field attainable by the MOKE set-up is insufficient to reverse the magnetization of this hard magnetic material. Using the same rough estimates for the aforementioned YFe_2 sample, the shape anisotropy is believed to be $K_S = 4.2 \times 10^5$ erg cm^{-3}. This is to be compared with the intrinsic anisotropy of the as-grown sample of $K_{I_{[\bar{1}10]}} = 9.2 \times 10^5$ erg cm^{-3} and $K_{I_{[001]}} = 3.4 \times 10^6$ erg cm^{-3}. Thus the magnitude of the intrinsic anisotropy along either the easy or hard axis of magnetization is significantly greater than that induced by patterning. This can provide an explanation for why the coercivity is increased slightly when the $DyFe_2$ sample is patterned with lines along the $[\bar{1}10]$ direction, since here the two anisotropies combine constructively. However the easy and hard axes of magnetization do not rotate to be parallel and perpendicular to the major axis of the striped array as in the magnetically soft YFe_2 film [1]. Here they remain fixed by the dominant intrinsic K_{MC} and K_{ME}.

Arrays of lines in an epitaxially grown exchange spring sample of [2 nm $DyFe_2$ / 8 nm YFe_2] × 40 were investigated [3]. The lines were patterned along the sample's

hard axis of magnetization ([001] direction) [10, 11]. The patterned array covered an area of 1 × 1 mm and individual elements had a width of 8.7 μm and a period of 20 μm. With the magnetic field applied along the [001] direction, *i.e.* parallel to the major axis of the lines, a slight increase in coercivity is observed. This is in keeping with the results for the $DyFe_2$ sample described in the previous paragraph. However when the magnetic field is oriented perpendicular to this (along the $[\bar{1}10]$ direction), the coercivity is reduced significantly to about ¼ of the value in the as-grown sample. The induced anisotropy due to shape effects from the patterned lines is shown to be approximately $K_s = 1.8 \times 10^4$ erg cm^{-3}, whilst the intrinsic anisotropy associated with the as-grown sample is estimated to be $K_{I_{[\bar{1}10]}} = 5.4 \times 10^4$ erg cm^{-3} and $K_{I_{[001]}} = 1.0 \times 10^4$ erg cm^{-3}. Thus with $K_s > K_{I_{[001]}}$ the coercivity is increased when the magnetic field is applied along the [001] direction, with the patterned elements acting to pin the sample magnetization parallel to their major axis. When investigated with the applied magnetic field perpendicular to this, no increase in coercivity is exhibited, which is in keeping with $K_s < K_{I_{[\bar{1}10]}}$.

Very similar results for a $Dy_{0.9}Tb_{0.1}Fe_2$ film were also reported [4]. The induced K_s is again not dominant over the intrinsic K_{MC} and K_{ME}, serving only to slightly increase coercivity when a magnetic field is applied parallel to the major axis of the lines, but with no effect when the magnetic field is applied perpendicularly. This sample will be considered in no further detail since that material is not investigated in the present work. It is however interesting to note that in this sample, K. Wang *et al.* [4] found an out of plane component of magnetization.

4.1.2 Concluding remarks on wet etching techniques

In summary, in the patterned arrays of lines investigated by Wang *et al.* [2, 3, 4], the anisotropy induced by shape effects was not sufficient to significantly alter the magnetic response of the samples, bar the magnetically soft YFe_2 films [1]. In the films of hard magnetic materials, the intrinsic magnetocrystalline and magnetoelastic anisotropies were more dominant than any effects induced by patterning. The shape induced anisotropy was noted as being responsible for a slight increase to the coercivity of the samples when subjected to a magnetic field parallel to the major axis of the lines. However no significant effects were observed with the magnetic field applied perpendicular to the major axis of the patterned elements. For example there was no

reorientation of the easy and hard axis of magnetization, suggesting that the induced shape anisotropy was only very weak.

From the results of patterned micron-scale structures in $REFe_2$ media, it is clear that the effects of shape anisotropy are limited by the size of the patterned features. Taking the standard expression for shape anisotropy (K_s) from equation (2.27), and taking $\Delta N = |N_x - N_y|$ as the difference in orthogonal (in-plane) demagnetizing factors, using the general ellipsoid model from Osborn [12] (described in section 6.2.4) where $N_x = 0$ and $N_y = \left(\frac{t}{t+w}\right)$, gives

$$K_s = \frac{\mu_0 {M_S}^2 t}{2(t+w)} \tag{4.1}$$

with *t* & *w* the film thickness and patterned line width respectively. Thus decreasing *w* will increase K_s, thereby improving the possibility for the shape to be the dominant anisotropy.

Whilst wet etching and photolithography processes provided useful information regarding the effects of shape anisotropy on epitaxially grown $REFe_2$ films, it is clear that significant improvements need to be made before shape effects will become dominant. The work by Wang *et al.* described in section 4.1.1 is conducted close to the ultimate resolution possible using standard optical lithography direct write techniques. This therefore highlights the need for the use of electron beam lithography and a dry etching process. This is especially evident when considering the rather high speed of the wet etching process (evident even when using highly diluted etchants) which gives rise to the isotropic nature of the process. In conclusion, reaching these resolution and technical limitations, combined with the obvious need to improve the general pattern definition (removal of rough edges *etc.*) provides the spur for the author's research and development of an electron beam lithography and ion milling process. This process will provide a cornerstone in the research towards nano-scale device fabrication in $REFe_2$ media, where general control over the fabrication processes required for a wide range of tasks will become further developed.

4.2 The First Demonstrations of Patterned $REFe_2$ Media on the Nano-scale

From the review in section 4.1 it is clear that in order to reliably and reproducibly pattern features on the nano-scale in epitaxially grown thin films and multilayers of

$REFe_2$ materials, new lithography and etching processes need development and implementation. The lithographic goal of this work therefore is to define nano-scale structures in these novel media using electron beam lithography and ion milling. Nano-structuring will provide useful insights toward the potential use of $REFe_2$ films and exchange spring media in patterned magnetic data storage, whilst also facilitating further research towards the development of additional exchange-spring nano-devices such as magnetoresistive random access memory (MRAM) [13], nano-scale permanent hard magnets for use in microelectromechanical systems (MEMS) [14] and nano-scale spin transfer torque pillars [15, 16]. This section draws together all of the author's work with regard to achieving this goal. Sample choice and the application of the lithography process are covered, before experimental verifications of various patterned elements on differing length scales are given.

4.2.1 Sample Choice and Preparation

It is well established that the epitaxially grown $REFe_2$ samples suffer from rapid oxidation and thus are prepared with Y capping layers in order to help prevent this [17, 18]. Whilst this does significantly stem the rate of oxidation, it does not completely prevent it. This is compounded by oxidation at the sample edges after cutting them into smaller pieces[ii], exposing a cross-section through the sample whereby the edges are not protected from oxidation. Accordingly the samples chosen for investigation throughout this work are limited to those which showed no noticeable signs of oxidation on the sample surface – checks were made by eye and with both optical and scanning electron microscope (SEM) systems. Example SEM micrographs, using both secondary electrons (SE) and backscattered electrons (BSE) showing a small region of oxidation on the surface of a [7.5 nm $DyFe_2$ / 15 nm YFe_2] × 18 exchange spring sample are presented in Figure 4.3. In order to obtain results which are both reliable and reproducible, it is imperative that the regions chosen for patterning are free from such surface defects.

[ii] Samples are cut into smaller pieces for two reasons: i). multiple experiments can be made on one sample whilst maintaining a reference sample, and ii). the sample space within certain experimental arrangements is severely limited.

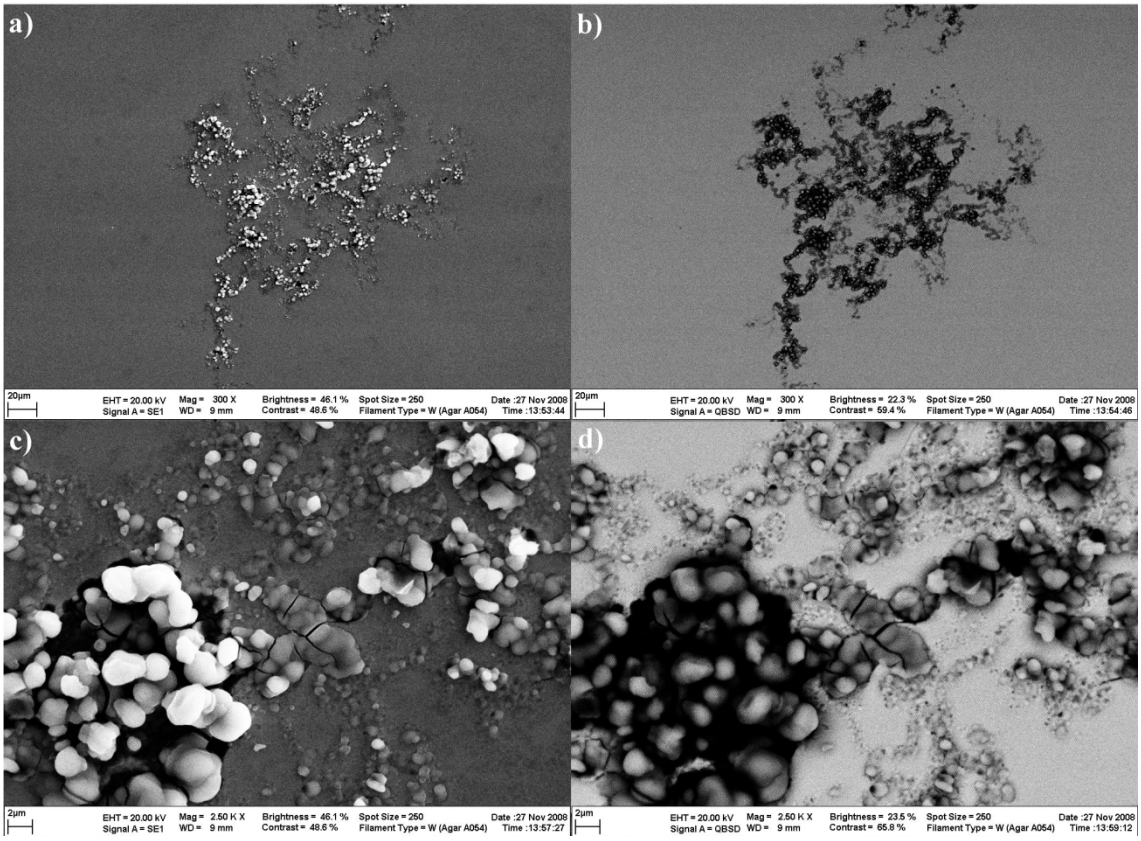

Figure 4.3: SEM micrographs of a [7.5 nm $DyFe_2$ / 15 nm YFe_2] × 18 sample showing an area of roughly 100 × 100 μm which has been subject to accelerated oxidation. Images a) and c) are SE micrographs showing the notable change in sample topography. Images b) and d) are BSE micrographs, showing a change in atomic number (Z) (presence of oxidised material and / or cracks through to the lower Z (darker) substrate). Images a) and b) are taken at 300 × magnification whilst c) and d) are taken at 2,500 × magnification.

The requirement for samples free from oxidation and other surface defects over large (~ mm^2) areas limits the number of different samples available for investigation. However, it is stressed that this work provides underpinning research into the use of epitaxially grown $REFe_2$ films and multilayers as model systems. Further material development can be expected in the future.

4.2.2 Lithography

Once an appropriate sample has been chosen, the desired patterns are lithographically defined using an electron beam direct-write system. This process is covered in depth in section 3.4. In short, multiple test runs were conducted using Si wafers coated with eBeam resist in order to find the optimal electron beam current, dose, step-size, dwell time and dose factor for a range of electron beam acceleration voltages over a variety of different feature sizes. It was found that for the bi-layer resist technology used throughout this work, the most reliable, high resolution patterns can be defined using an

electron beam accelerating voltage of 20 keV with an electron beam diameter of 10 nm. For patterns with dimensions less than approximately 2 μm (other than circles and lines), proximity effect calculations have been used in conjunction with the above parameters with the aim of improving the overall resolution. These calculations have proved successful in the definition of square elements which, for example, are essential to the future design and fabrication of bit patterned magnetic data storage media.

After exposure and development the lithographically defined pattern can only be checked by optical microscope to avoid destruction of the patterned region by electron microscopy techniques[iii]. Clearly, using standard optical microscopy techniques it is not possible to characterize with any precision the defined patterns, since they are often on a length scale less than the wavelength of the visible light used to illuminate the sample. For this reason the aforementioned Si test samples are sputter coated with a thin layer of Au and subsequently investigated via SEM. Four sample SEM micrographs, one showing 2 μm wide lines, two showing varying magnifications of an array of 1 μm squares, and one showing a dot with a diameter of approximately 85 nm can be seen in Figure 4.4, images a) – d) respectively. Once optimum lithography process parameters are found from images such as these the parameters are fixed and used for the fabrication of patterned $REFe_2$ samples. The processing of these $REFe_2$ samples is essentially "blind" at this stage, as the sputter coating would obviously interfere with the subsequent fabrication steps. However, in all patterned $REFe_2$ samples the author has chosen to include a larger region which *can* be checked using an optical microscope to assure complete development.

[iii] Atomic force microscopy (AFM) is a relatively non-destructive technique which can be used to check for pattern resolution and sample development, but it is a rather time consuming process to employ during fabrication. Nevertheless AFM has been used to confirm eBeam resist thicknesses.

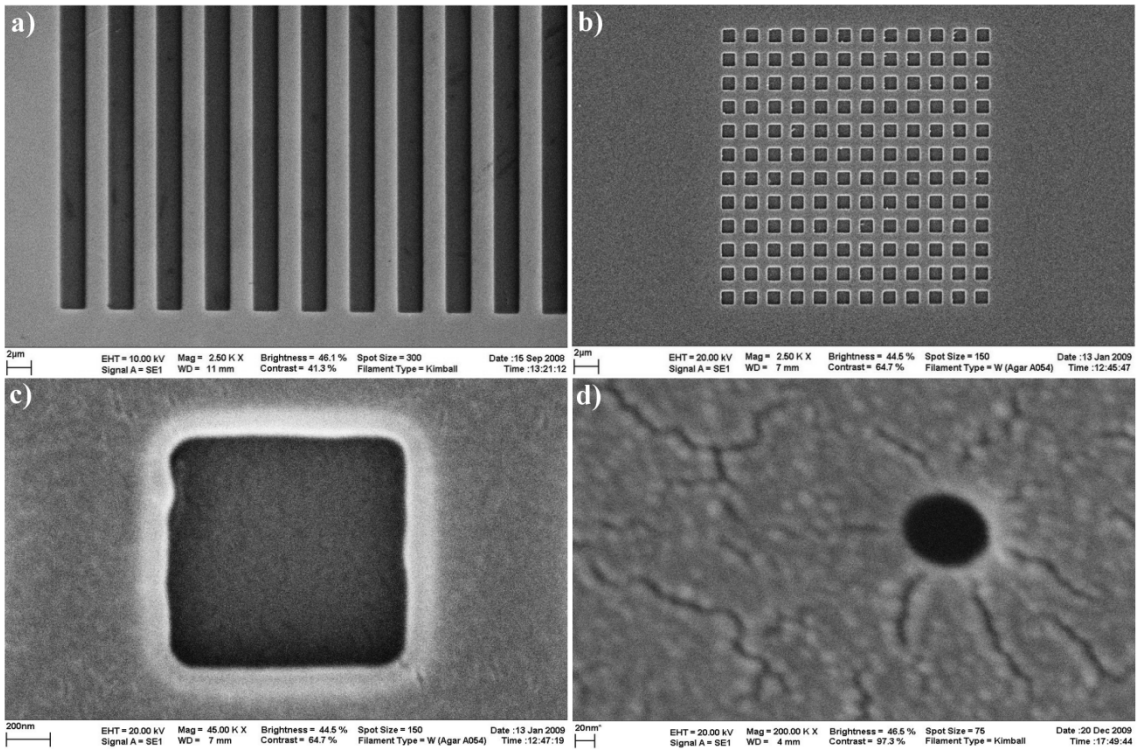

Figure 4.4: SEM micrographs of various patterned elements in a bi-layer resist stack of MMA-MAA and PMMA, sputter coated with a 5 nm Au layer. Image a) is a 2,500 × magnification micrograph of 2 μm wide lines with a pitch of 4 μm. Image b) a 2,500 × magnification micrograph of an array of 144 1 μm squares at a pitch of 2 μm and image c) is a 45,000 × magnification representation of the same region, displaying a radius of curvature to the corners of ~100 nm. A 200,000 × magnification micrograph of a dot with a diameter of 85 nm is presented in image d). Note that the cracks in image d) are most likely due to movement in the soft polymer and are expected to be present in all samples.

The SEM micrographs of Figure 4.4 show the first step in nano-scale pattern fabrication of epitaxial $REFe_2$ films and multilayers. The dark regions within these SEM micrographs represent "holes" which will be "filled" with the Cr mask material during the lift off process. These regions will become the areas of $REFe_2$ which remain after the ion milling process (recall Figure 3.20). The corners of the patterned regions in the lines and squares (images a), b) & c)) closely represent right-angles. This is due, in part, to the use of the small diameter electron beam ($Ø_b$ = 10 nm) permitted via the development and installation of a LaB_6 crystal electron emitter, and, for the case of the 1 μm squares, also the use of proximity effect correction software (PECS). Clear evidence for sub 100 nm pattern resolution is provided in images c) and d). This is the first demonstration of patterning on this scale using this lithography system.

The nano-scale patterned samples can subsequently be progressed to the next step of the patterning process whereby a thick metallic mask is deposited via lift-off.

However, before this is discussed in section 4.2.4, the concept of a polymer mask is revisited below since this offers *potential* for significant gains.

4.2.3 Polymer mask

It is clear from the preceding text that a metallic mask will be used to protect specific regions of the patterned $REFe_2$ material during the ion milling process. However, a discussion and demonstration of the drawbacks of a polymer mask is worthwhile, since if it were possible to use such a mask this would reduce process complexity. This in turn would increase throughput, with the goal of reducing costs in device fabrication.

In section 3.6, re-deposition of sputtered material was discussed with regard to the use of a thick mask. Put simply, a thicker mask results in an increased rate of re-deposition since there is more chance that the sputtered material will interact with the mask rather than being ejected completely from the sample. Further, the adhesion of the sputtered material to the mask material itself must be taken into consideration. If the mask is made out of a softer material such as PMMA (which has a high coefficient of adhesion), energetically sputtered atoms are more likely to be embedded into the side-walls than they would be with a hard mask (*e.g.* a metal with a low coefficient of adhesion). Thus the drawbacks of a polymer mask are twofold. Not only does the polymer mask have to be thicker than the equivalent metallic mask due to its increased rate of removal, it is made from a material more prone to re-deposition. Nevertheless, polymer masks for the use in fabrication of patterned $REFe_2$ media have been investigated, as the process time and throughput gains that they offer are significant, *provided* increased rates of removal may be accommodated and re-deposition made negligible.

SEM and AFM micrographs of nominally 500 nm squares, defined in a test sample of NiFe on Si after ion milling using a polymer (PMMA) mask are presented in Figure 4.5 and Figure 4.6 respectively.

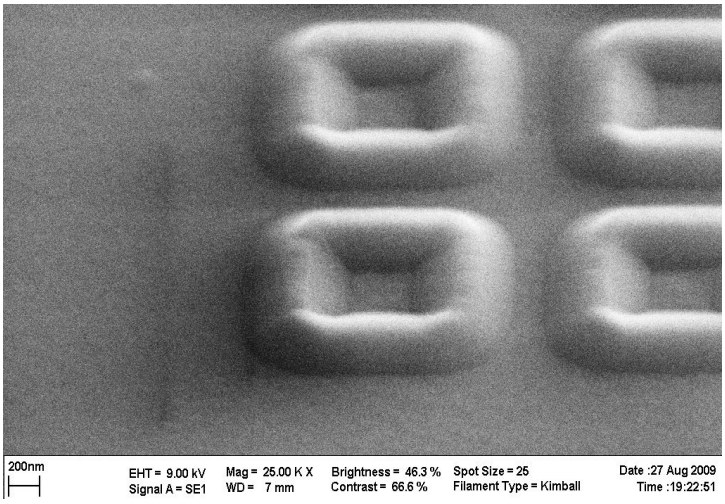

Figure 4.5: 25,000 × magnification SEM micrograph showing the effects of re-deposition. The centres of the squares are etched away compared to the bulk material surrounding them (*c.f.* Figure 4.6) but this material has been re-deposited at the sidewalls of the PMMA mask (now removed).

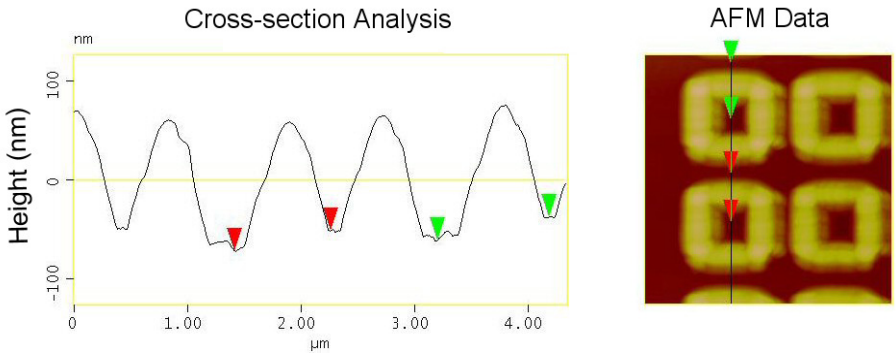

Figure 4.6: AFM micrograph and cross-section analysis showing the removal of material at the centre of the patterned squares with respect to the surrounding bulk material (indicated by the vertical distance between the markers). Note the significant re-deposition of material against the PMMA mask walls (PMMA mask now removed).

The central square corresponds roughly to the original "hole" in the mask and therefore to the region where material should have been removed. Material has indeed been removed from this position as evidenced by the AFM micrograph cross-section, where the markers placed inside the hole are lower than those to its side (on the material originally protected by the polymer mask). However, there is obvious evidence of re-deposited material. The NiFe film in the patterned regions has been removed from the sample surface by the energetic incident Ar^+ ions, but rather than being ejected completely from the sample it has been re-deposited on the side-walls of the polymer mask. The polymer mask has since been removed in order to leave what should be a film of NiFe patterned with an array of 500 nm squares. This leaves just the re-

deposited metallic material at the edge of the patterned region, tracing out a shape representative of the mask under-cut and thickness. The fact that the re-deposited material reaches a height far greater than the depth of the patterned region is confirmation that the polymer mask is removed by Ar^+ ion milling more rapidly than the metallic film, whilst the reduced pattern size (now approximately 300 nm squares *c.f.* nominal 500 nm squares) can also be attributed to the re-deposition process. This concept will be discussed further in section 4.3.1. Furthermore Figure 4.5 and Figure 4.6 appear to violate the obvious rule of conservation of material. One explanation for this could be that the re-deposited metallic film could form a thin layer over some polymer mask material, encapsulating it so that it is not removed along with the remainder of the mask.

Figure 4.5 and Figure 4.6, together with the accompanying text, provide a clear illustration that a polymer mask cannot be used to satisfactorily pattern thick $REFe_2$ films using the equipment available. In conjunction with these drawbacks a further problem may be identified. It will be seen in Chapter 5 that the Ar^+ ions used in the milling process are in fact implanted into the mask and $REFe_2$ layers. Due to the soft nature and low atomic density of the PMMA, the 3.25 keV Ar^+ ions used for milling have a range in PMMA significantly larger than that in most metals (12.5 nm in PMMA *c.f.* 2 – 3 nm in most metals[iv]). Therefore damage to the $REFe_2$ material below the polymer mask occurs sooner than if a metallic mask is used. This reduces the appeal of the polymer mask further still. Accordingly it is absolutely necessary to develop and implement the more complex metallic mask process.

4.2.4 Metallic mask deposition and lift-off

For reasons discussed in the preceding section, it has been necessary to develop a metallic mask based system for pattern transfer using Ar^+ ion milling. The most successful choice of material was shown to be Cr in section 3.5.2.

Cr has been successfully deposited as a metallic mask using thermal evaporation and lift-off. Cr is evaporated onto a sample which has had lithographic patterns defined and developed in the resist which covers it. The whole sample is then submerged in acetone, thus removing the entirety of the remaining resist. The removal of the resist

[iv] These values are obtained from `SRIM` simulations.

takes with it any metal deposited on top of it, leaving metal only in the regions where the sample surface was exposed, thereby creating a direct metallic replica of the pattern defined via the lithography process. This procedure is referred to as "lift-off". The Cr mask thickness is typically 100 nm as this provides a reasonably thick layer that is resilient to Ar^+ ion milling, yet remains thin enough to still facilitate the lift-off process. However as already noted in section 3.6.6, this metallic mask thickness may not be sufficient to permit the removal of the entirety of a nominally 400 nm thick Laves phase $REFe_2$ sample. The reader should also recall that the thickness of the resist layer is directly related to the resolution attainable in the lithography process. Accordingly there is a trade-off between mask thickness, resolution and amount of material to be removed. Thin resist layers and correspondingly thin (typically 100 nm) Cr masks have been used predominantly since the ultimate goal is to achieve patterning of $REFe_2$ films and multilayers at the nano-scale. Thin bi-layer samples of $REFe_2$ material have been specially developed and used to provide a proof of principle confirmation of the success of this fabrication process, before the procedure is extended to include a demonstration of the patterning process in the significantly higher quality yet thicker multilayer $REFe_2$ samples. This will be covered in sections 6.1 and 6.2 respectively.

Figure 4.7 and Figure 4.8 show an array of 1 μm lines patterned with a pitch of 2 μm. The lines are fabricated from Cr on top of a 7.5 nm $DyFe_2$ / 30 nm YFe_2 sample. The lines are created using a 100 × 100 μm write-field, thus there are 50 lines per patterned region, each with dimensions 1 × 100 μm. These write-fields are then stitched together to form a larger array, typically in the form of 5 × 5, to create a total patterned area of 500 × 500 μm. An array of this size may easily be analysed using the MOKE apparatus.

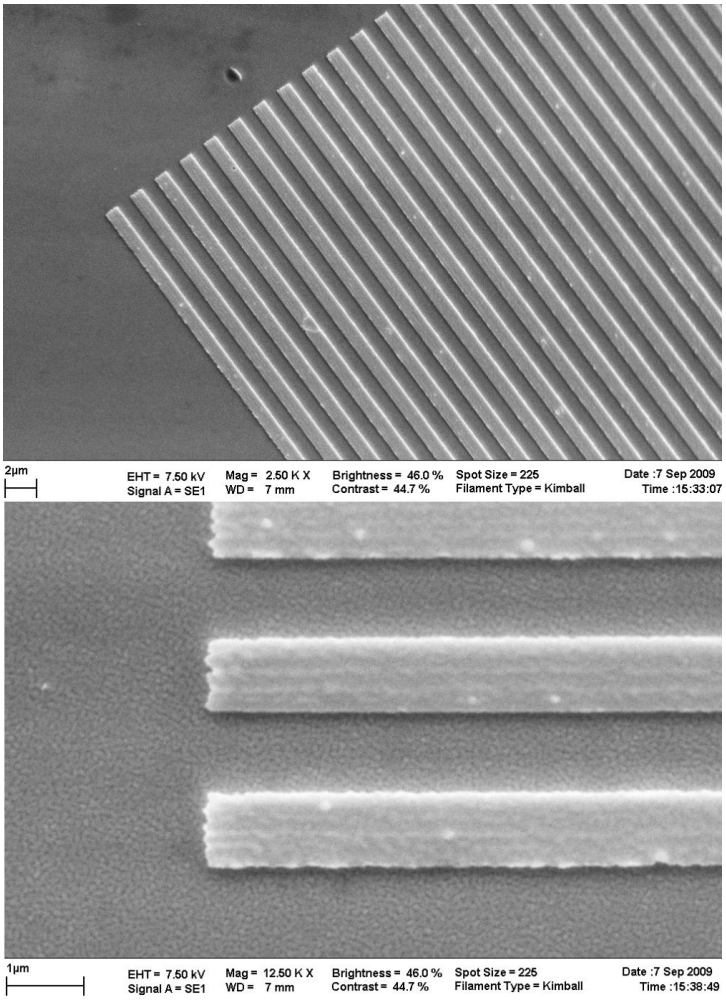

Figure 4.7: 2,500 × and 12,500 × magnification SEM micrographs of 1 μm wide, 100 μm long lines patterned with a pitch of 2 μm from the Cr mask material. The Cr lines are on top of a 7.5 nm $DyFe_2$ / 30 nm YFe_2 sample and show a horizontal edge smoothness of order 50 nm.

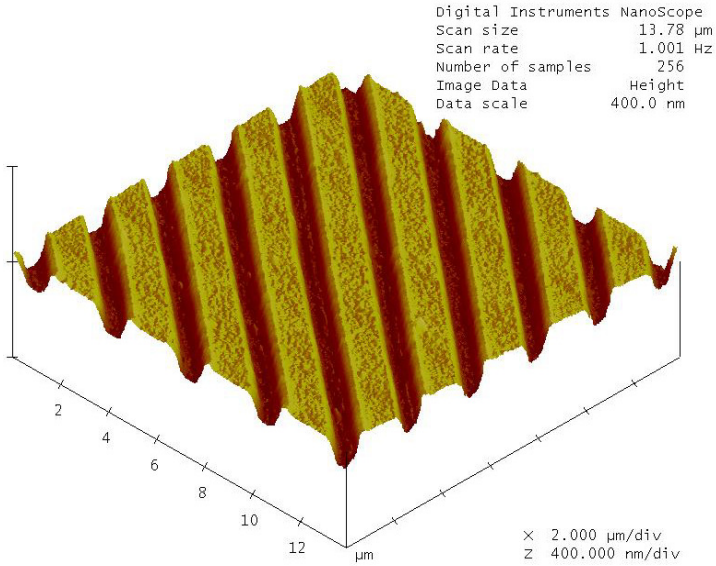

Figure 4.8: 3D AFM micrograph of the same 1 μm wide, 2 μm pitch lines as those shown in Figure 4.7. The lines have a height of 94 ± 2 nm.

The lower image in Figure 4.7 is an SEM micrograph taken at an increased magnification where defects at the edges of the patterned region are visible. The defects at the (vertical) ends of the lines are more prominent than those at the (horizontal) sides due to the rastering nature of the electron beam employed during the lithography process[v]. The horizontal sides exhibit a roughness of order 50 nm which is 5% of the patterned element's vertical dimension and only 0.01 % of its total horizontal dimension. The thickness of the Cr mask was found to be 94 ± 2 nm, from analysis of the data used to create the 3D AFM representation of the sample. This is very close to the intended nominal value of 100 nm. The side-walls to the patterned Cr elements appear to span a lateral distance of approximately 25 nm, corresponding to a taper angle of $\tan^{-1}\left(\frac{94}{25}\right) \approx 75°$. It is worthwhile noting that due to the finite dimensions of the AFM probe tip (see Figure 3.22), the side-wall taper angle is likely greater than this (*i.e.* more vertical side-walls). Together the data presented in Figure 4.7 and Figure 4.8 show the potential for high resolution metallic mask fabrication using electron beam lithography and lift-off processing over large areas.

In Figure 4.9 two SEM micrographs of an array of 1 μm squares are presented. The data again correspond to Cr mask material on a 7.5 nm $DyFe_2$ / 30 nm YFe_2 sample. The patterned elements closely represent squares with predominantly right-angled, rather than curved corners. This is attributed to the use of a small diameter electron beam and PECS. The radius of curvature of the corners to the squares is approximately 50 nm, and they exhibit an edge roughness of order 50 nm or less[vi]. Note the appearance of vertical side-walls in the tilted SEM micrograph. This confirms the AFM probe diameter is likely responsible for the aforementioned side-wall taper angle of 75° rather than the lift-off processing. Thus the measure of side-wall taper angle via AFM is not absolute, but it still offers the potential for comparison from one set of data to another.

---

[v] Lines with a width 1 μm are treated as rectangles, hence "areas" rather than "lines" are implemented in the lithography software for their fabrication. This results in a preferential beam rastering direction along the major axis of the pattern and accompanying smoother pattern edges).

[vi] In this instance both vertical and horizontal edges are equally well defined. This is because each element within the patterned array is created from a combination of individual "dots" (due to the PECS), thus the electron beam is not subject to a preferential rastering direction.

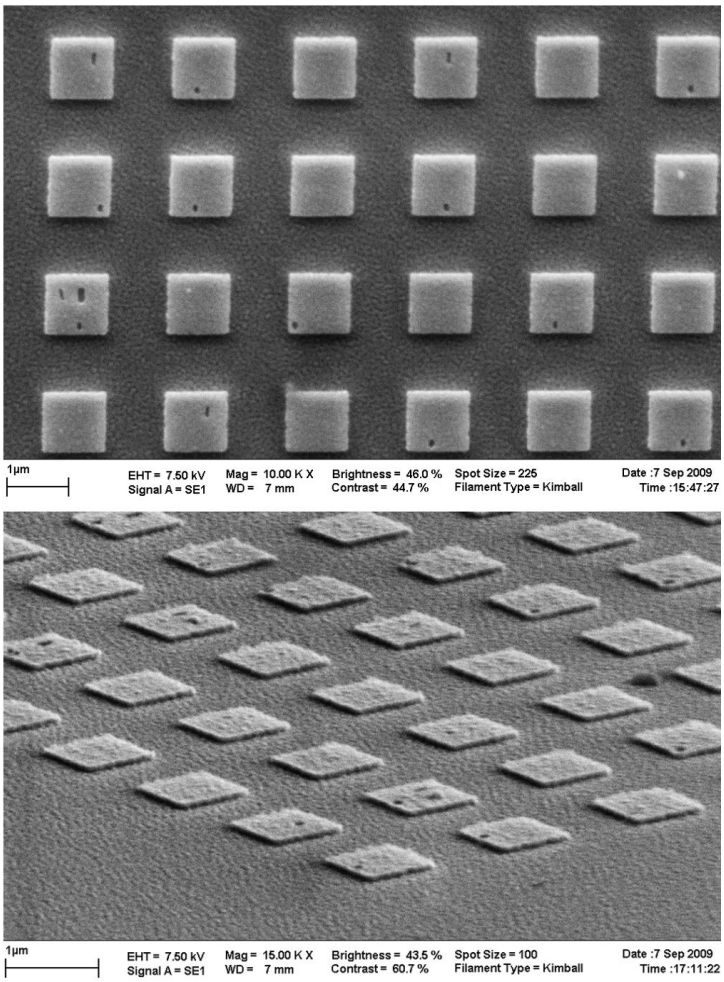

Figure 4.9: SEM micrographs showing a 10,000 × magnification (top) and 15,000 × magnification tilted (bottom) representation of an array of 1 μm squares, each fabricated in Cr on a 7.5 nm $DyFe_2$ / 30 nm YFe_2 sample. The corners of the patterned features exhibit a high degree of squareness, with a radius of curvature of approximately 50 nm. The vertical sidewalls to the patterned elements are clear in the bottom micrograph.

This sample has also been characterized using AFM. A 3D representation of the array of Cr squares on the 7.5 nm $DyFe_2$ / 30 nm YFe_2 sample can be seen in Figure 4.10. The near vertical side-walls of the patterned elements are clearly visible. The thickness of the Cr mask material is confirmed as 94 ± 2 nm.

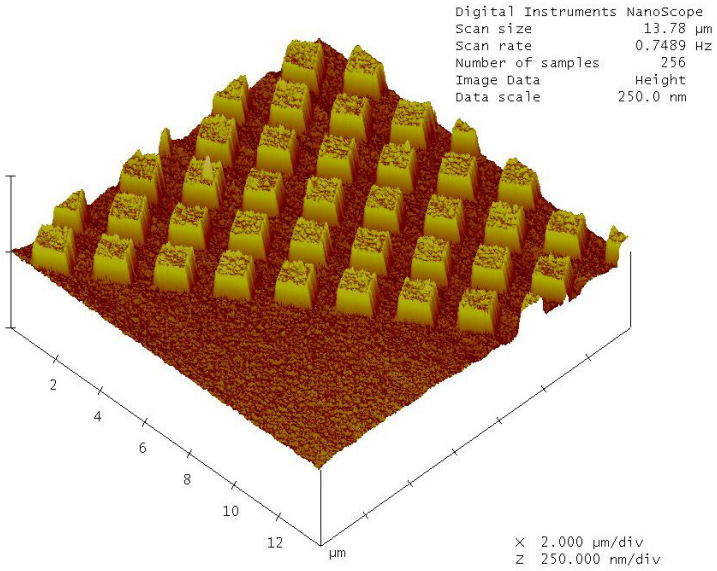

Figure 4.10: 3D AFM micrograph the same array of 1 μm squares featured in Figure 4.9. The Cr patterned elements have a thickness of 94 ± 2 nm.

500 nm square patterned Cr mask elements on a 7.5 nm $DyFe_2$ / 30 nm YFe_2 sample are presented in Figure 4.11. These elements also exhibit a radius of curvature to the corners of approximately 50 nm, plus edges that are smooth on the same scale. It is interesting to note that at this increased magnification the underlying roughness of the epitaxially grown $REFe_2$ film becomes visible.

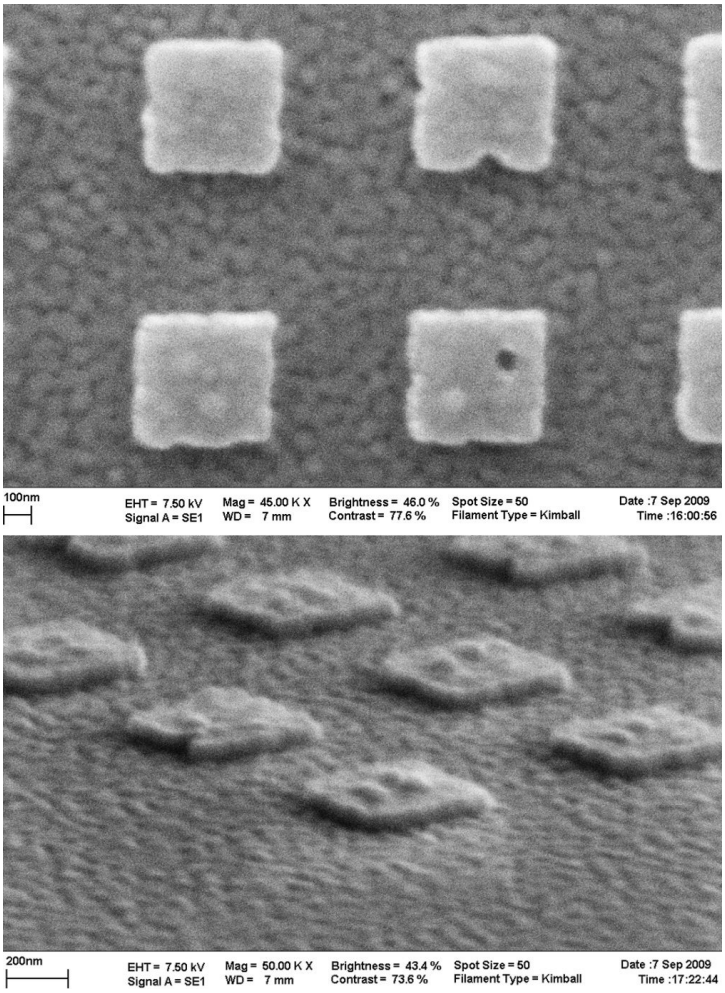

Figure 4.11: SEM micrographs showing a 45,000 × magnification (top) and 50,000 × magnification tilted (bottom) representation of an array of 500 nm squares fabricated in Cr on top of a 7.5 nm $DyFe_2$ / 30 nm YFe_2 sample. The vertical side-walls to the patterned elements are again clear in the lower micrograph.

Finally, a square mask array, fabricated from a near 100 nm thick layer of Cr on a 7.5 nm $DyFe_2$ / 30 nm YFe_2 sample, consisting of individual elements with lateral dimensions of just 200 nm can be seen in Figure 4.12. Whilst the 50 nm radius of curvature to the corners is more prevalent on patterns of this scale, there remains no question that the patterned elements closely represent squares. Note that the patterned elements are larger than the spacing between adjacent elements. This is likely due to over-exposure during the lithography process. The tilted SEM micrograph (lower image) shows that the patterned elements' side-walls remain vertical even when relatively high aspect ratio features are fabricated using this process. The 200 nm squares shown in Figure 4.12 represent the smallest *square* features that have been defined using the in-house electron beam lithography and metallic deposition

equipment. They represent the culmination of much calibration work and many trial runs in order to optimise the lithography, mask deposition and lift-off processes.

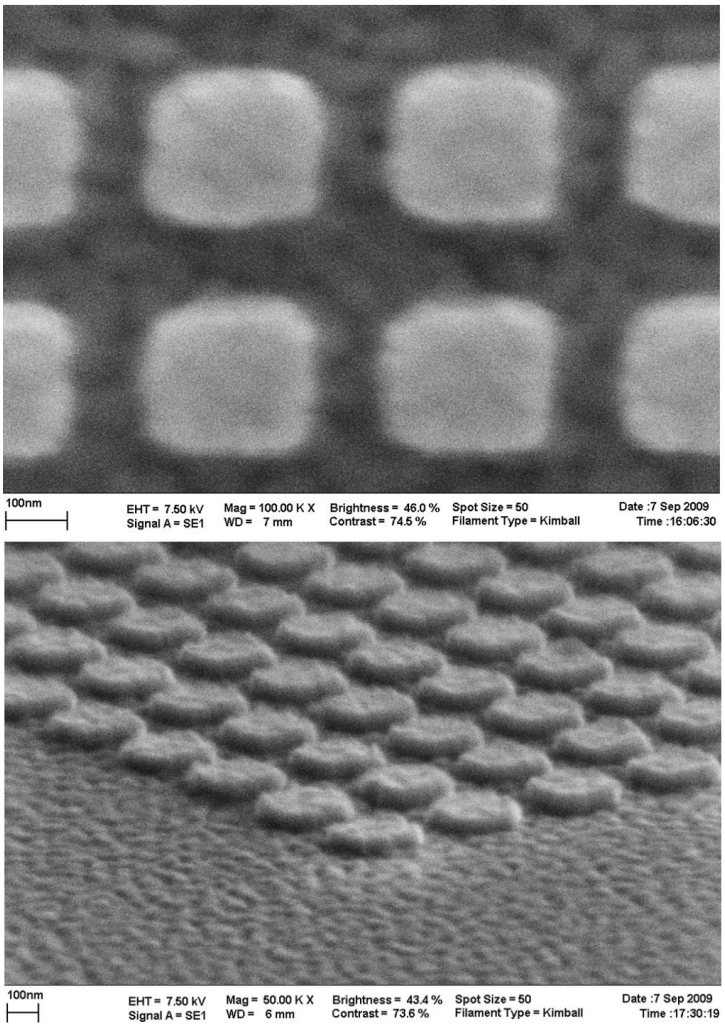

Figure 4.12: SEM micrographs showing a 100,000 × magnification (top) and 50,000 × magnification tilted (bottom) representation of an array of 200 nm squares, each fabricated in Cr on top of a 7.5 nm $DyFe_2$ / 30 nm YFe_2 sample. The patterned elements are approximately 100 nm thick.

In summary, the SEM and AFM micrographs presented in this section provide an illustration of the gains made in attainable resolution using the in-house lithography and metallic mask fabrication techniques. They represent an optimistic goal to reach and surpass for future work concerning nano-scale pattern definition with $REFe_2$ films and multilayers. These successfully patterned metallic masks can then be used in the Ar^+ ion milling process to selectively protect regions of the $REFe_2$ films and multilayers. Due to the anisotropic nature of the Ar^+ ion milling process these patterned elements should be directly transferred into the under-lying material, thus creating well defined nano-scale patterns in $REFe_2$ materials for the first time.

4.2.5 The self-mask process

The object of the metallic mask is to protect the region on which it is deposited from the Ar^+ ion milling process. In the previous section it was shown that nano-scale patterns in the Cr metallic mask material can be successfully fabricated. It is hoped that these patterns can be transferred into the underlying $REFe_2$ films and multilayers using the Ar^+ ion milling process.

Concerns regarding the similarity in material sputtering rates ("etch selectivity") between the Cr mask material and the $REFe_2$ films and multilayers were raised earlier in section 3.6.6, and the trade-off between mask thickness and ultimate resolution was re-visited in section 4.2.4. It is clear that the nominal Cr mask thickness of 100 nm (required to obtain nano-scale patterns) will be insufficient to permit the fabrication of features equal to the nominal thickness of the $REFe_2$ samples (400 nm). However it is important to note that most metallic films when used for technical applications are thinner than 400 nm, thus the development of *thin* $REFe_2$ films with excellent magnetic anisotropies is important. For these films the 100 nm Cr mask and the present ion milling process would be sufficient; successful examples are given in section 4.2.6. It must also be remembered that the Cr mask is not *the* optimal material, rather it is the optimal material that can be thermally evaporated using in-house equipment. The use of a metal with a considerably higher resistance to ion milling, such as Be, Os, V, Ti or W [19] would permit the definition of higher aspect-ratio structures in the thick $REFe_2$ multilayers.

The removal of the entire metallic mask does not have to mean the termination of the ion milling process. This is a local limit rather than a fundamental limit, *i.e.* the correct mask material (or a relevant RIE recipe, see section 3.6.2) for fabricating high aspect-ratio structures in 400 nm thick $REFe_2$ materials is not available. As a work-around to this problem the author has used a self masking process. Once the pattern is defined in the thick $REFe_2$ material, the $REFe_2$ material can act as a mask itself ("self-mask") if the ion milling process is continued. This is illustrated schematically in Figure 4.13 where the 100 nm thick metallic mask, and the 400 nm thick $REFe_2$ film are shown approximately to scale. Although there is absolutely no etch selectivity between the patterned and non-patterned regions, this self-mask process can be used to transfer the pattern through the entirety of the $REFe_2$ film or multilayer. The resulting patterned elements have a thickness proportional to the original etch selectivity between the

$REFe_2$ and Cr mask. The Cr mask is nominally 100 nm thick and removed at 90% the rate of $REFe_2$ (see section 3.6.6), thus the final $REFe_2$ patterned element will be approximately 110 nm thick. Patterned elements on a non-magnetic background are substantially easier to characterize using MOKE and MFM than those superimposed onto a magnetic background. However, the final use for the patterned media may not require the complete removal of the magnetic background (for example in magnetic data storage media where there is a continuous soft under-layer), eliminating the need for the self-mask process. Nevertheless, in order to aid MOKE and MFM characterization, the self mask process has been used on occasion to facilitate simpler and clearer interpretations of the patterned samples. A demonstration of the effects which this process has regarding the sample topography and pattern resolution can be seen in section 4.2.8, whilst the topic will be re-visited as a whole in Chapter 6.

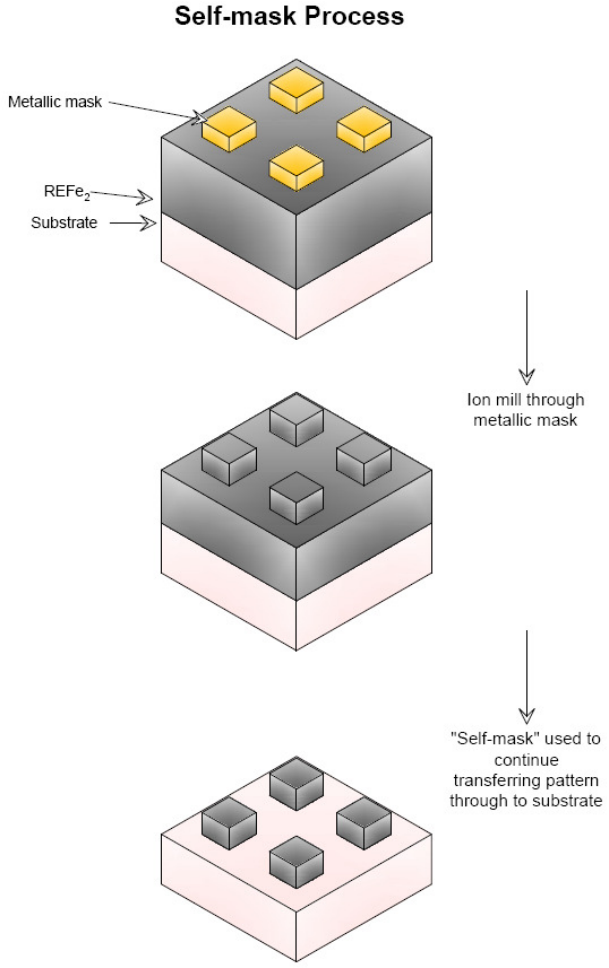

Figure 4.13: Schematic illustration of the self-mask process. A pattern defined in the $REFe_2$ material becomes the mask as the ion milling process proceeds, removing material beyond the thickness of the thermally evaporated metallic mask. This leaves $REFe_2$ structures on a non-magnetic background to make MFM and MOKE characterization simpler.

4.2.6 Ar^+ ion milling to transfer patterned arrays into a bi-layer $REFe_2$ film

To demonstrate the applicability of the Ar^+ ion milling process to readily define nano-scale elements in $REFe_2$ materials, arrays of lines and squares have been patterned in a bi-layer sample of $DyFe_2$ / YFe_2. The sample in question was 7.5 nm $DyFe_2$ / 30 nm YFe_2 and includes the standard NbFe alloy seed and buffer layer (7 nm) and the Y protective cap (3 nm), giving it a total thickness well below that typically used for the Cr mask (recall, 100 nm). Because of this the patterned elements may be transferred wholly through the $REFe_2$ material, leaving them superimposed on a non-magnetic background.

Due to the thinness of the sample, it suffered from island-like growth (detailed in section 3.2). Accordingly the sample has a relatively rough surface and poorly defined magnetic anisotropy. This is evident in the hysteresis loops which show little variation with the direction of the applied magnetic field. The hysteresis loops also have a poor SNR due to the small amount of magnetic material present and thus cannot be used to reliably interpret the magnetic characteristics of the sample. Nevertheless the sample does provide a useful demonstration, confirming proof of principle process of nano-scale patterning *throughout the entirety of a sample's thickness* using Ar^+ ion milling.

A 40 nm thick Cr mask was thermally evaporated onto this bi-layer sample in order to transfer the lithographically defined patterns into the $REFe_2$ film. The mask thickness was chosen so that it should be entirely removed by the time the pattern had been wholly transferred into the $REFe_2$ material. Results showing an array of 400 nm squares defined in this sample can be seen in the format of SEM and AFM micrographs in Figure 4.14 and Figure 4.15 respectively.

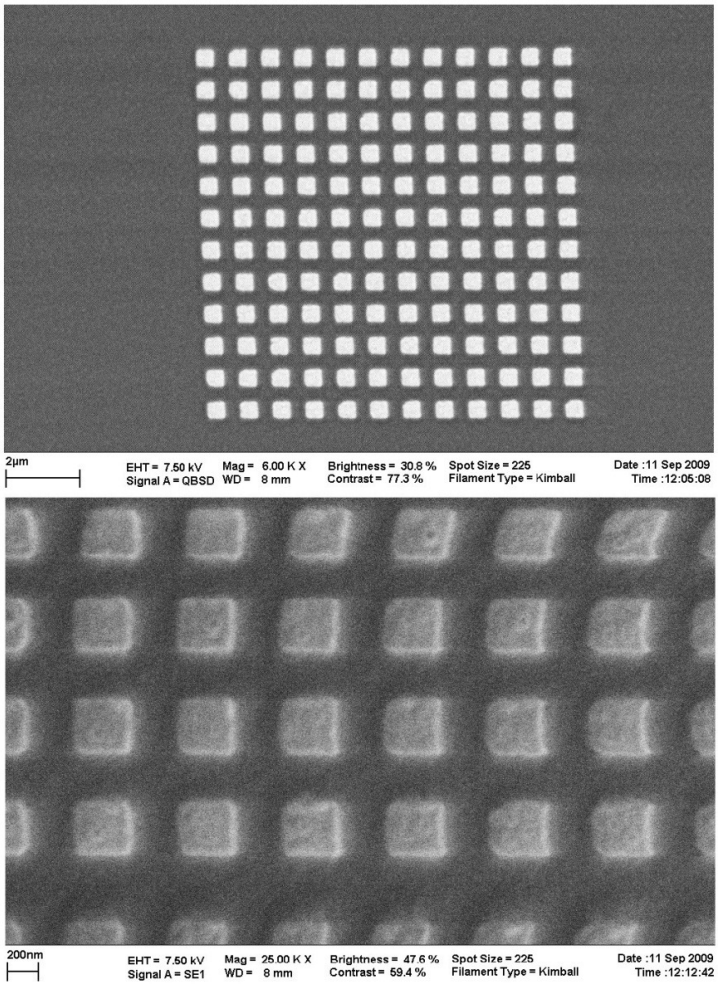

Figure 4.14: 6,000 × and 25,000 × magnification SEM micrographs of an array of 400 nm squares defined in the 7.5 nm $DyFe_2$ / 30 nm YFe_2 bi-layer sample. The top image is created from BSEs with the clear differences in contrast illustrating the metallic patterned elements (high Z = white) on a non-metallic background (low Z = dark). The slanted appearance to some elements within the images is attributed to accumulation of negative charge on the sample; it was not possible to ground the Al_2O_3 substrate.

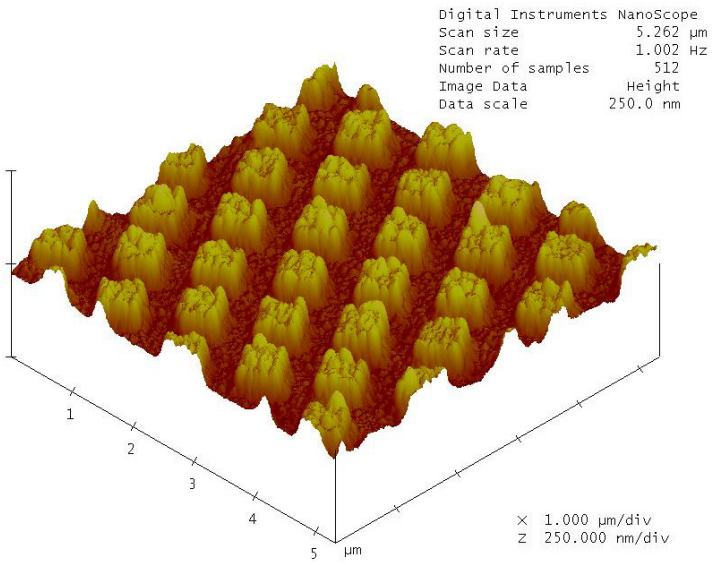

Figure 4.15: 3D AFM micrograph of the same array of 400 nm squares defined in the 7.5 nm $DyFe_2$ / 30 nm YFe_2 bi-layer sample depicted in Figure 4.14. The rough nature to the patterned elements is due to the island-like growth. The patterned elements have a thickness of 40 ± 2 nm.

The patterned elements have lateral dimensions that are almost exactly equal to those defined by the Cr mask. Neither the SEM data (Figure 4.14) nor the AFM data (Figure 4.15) show evidence of side-walls with a taper angle greater than those of the Cr mask, suggesting that the patterned elements have been faithfully reproduced in the $REFe_2$ bi-layer using Ar^+ ion milling.

4.2.7 Ar^+ ion milling transfer of patterned arrays into a multilayer $REFe_2$ sample

An array of 1 μm wide, 500 μm long lines with a pitch of 2 μm, covering a total area of 500 × 500 μm has been transferred into a [3 nm $DyFe_2$ / 12 nm YFe_2] × 27 multilayer exchange spring sample using Ar^+ ion milling. Figure 4.16 and Figure 4.17 show the corresponding SEM and AFM micrographs respectively. Not only does this mark the first successful demonstration of patterned elements created in a $DyFe_2$ / YFe_2 multilayer exchange spring sample using Ar^+ ion milling, it also provides the first demonstration of patterned elements on this length scale in these media. Note that in the case of this sample the self-mask process has not been used, thus the micrographs show patterned lines of $DyFe_2$ / YFe_2 on a $DyFe_2$ / YFe_2 background. As would be expected, the secondary electron contrast between patterned and non patterned regions is relatively weak and the lines appear invisible when characterized using back-scattered electron detection (not shown).

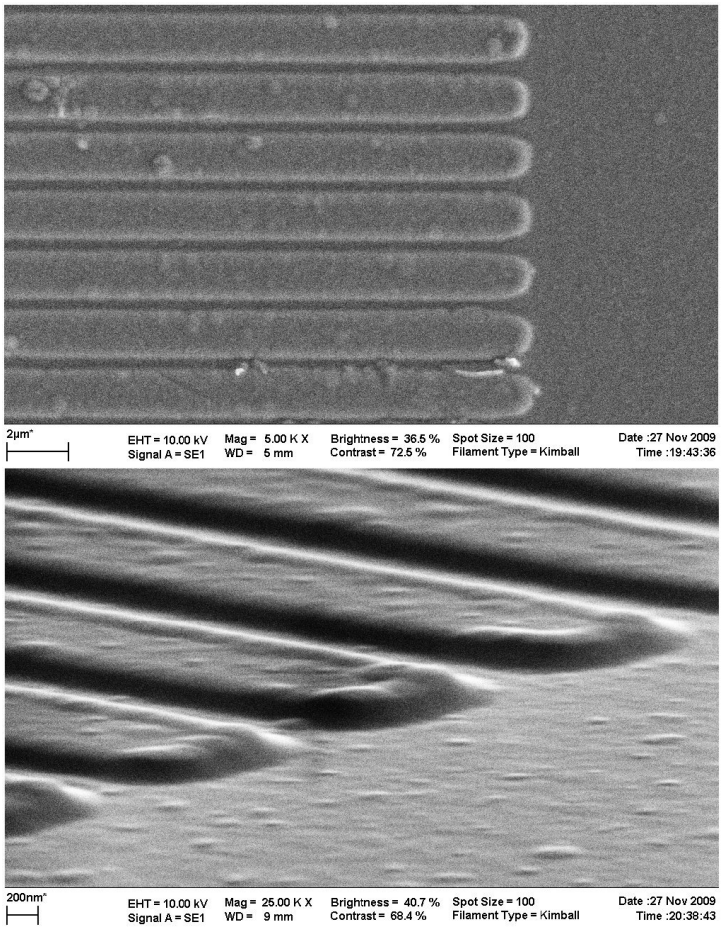

Figure 4.16: 5,000 × and 25,000 × (tilted) magnification SEM micrographs of lines defined in a [3 nm $DyFe_2$ / 12 nm YFe_2] × 27 multilayer sample. The width of the lines is 1.8 μm and their pitch is 2.0 μm. Note the sloped edges visible in the lower (tilted) SEM micrograph, responsible for increasing the line width to 1.8 μm from the 1.0 μm width of the Cr mask.

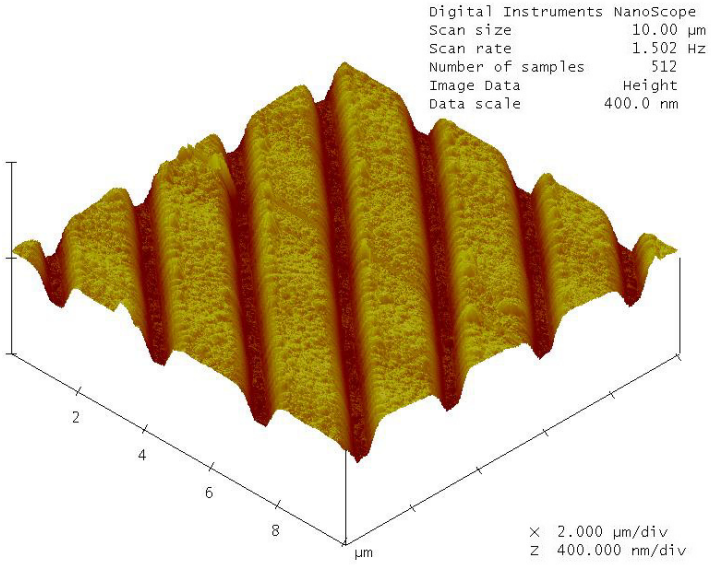

Figure 4.17: 3D AFM micrograph of the same array of 1.8 μm wide, 2.0 μm pitch lines defined in a [3 nm $DyFe_2$ / 12 nm YFe_2] × 27 multilayer sample as depicted in Figure 4.16. The lines have a height of 109 ± 2 nm and the sloped side-walls are clearly visible.

From these micrographs it is immediately clear that the patterned lines are now significantly wider than those defined in the Cr mask. Rather than a width of 1.0 μm and a pitch of 2.0 μm as intended, these lines now have a width of 1.8 μm whilst retaining the same pitch. Thus there is a spacing of just 200 nm between adjacent elements. In addition to this the tilted SEM micrograph (lower image in Figure 4.16) and the AFM micrograph (Figure 4.17) show that the lines exhibit sloped slide-walls and slightly raised edges. The data used to generate the AFM micrograph has been analysed in cross-sectional form to derive a thickness of 109 ± 2 nm for the patterned elements. This is in good agreement with the data calculated earlier whereby a 100 nm thick Cr mask was shown to be thick enough to permit the fabrication of 110 nm deep features in a typical $REFe_2$ film or multilayer. The side-walls of the patterned elements extend over approximately 250 nm; given the elements' height is 109 nm this corresponds to side-wall taper angles of $\tan^{-1}\left(\frac{109}{250}\right) \approx 25°$. Whilst for reasons discussed earlier (section 4.2.4) this may not correspond to an absolute value, it *is* substantially reduced from the apparent angle after mask deposition and lift-off. The raised edges to the patterned elements have a height of approximately 20 nm and extend over a width of roughly 250 nm. The sloped side-walls and increased edge height to the patterned elements are attributed to re-deposition of sputtered material. This will be discussed in more detail in section 4.3.1.

Arrays of squares have been successfully fabricated in the same [3 nm $DyFe_2$ / 12 nm YFe_2] × 27 multilayer sample. Corresponding SEM and AFM micrographs are presented in Figure 4.18 – Figure 4.21. Again the sample has not been subject to the self-mask etching process.

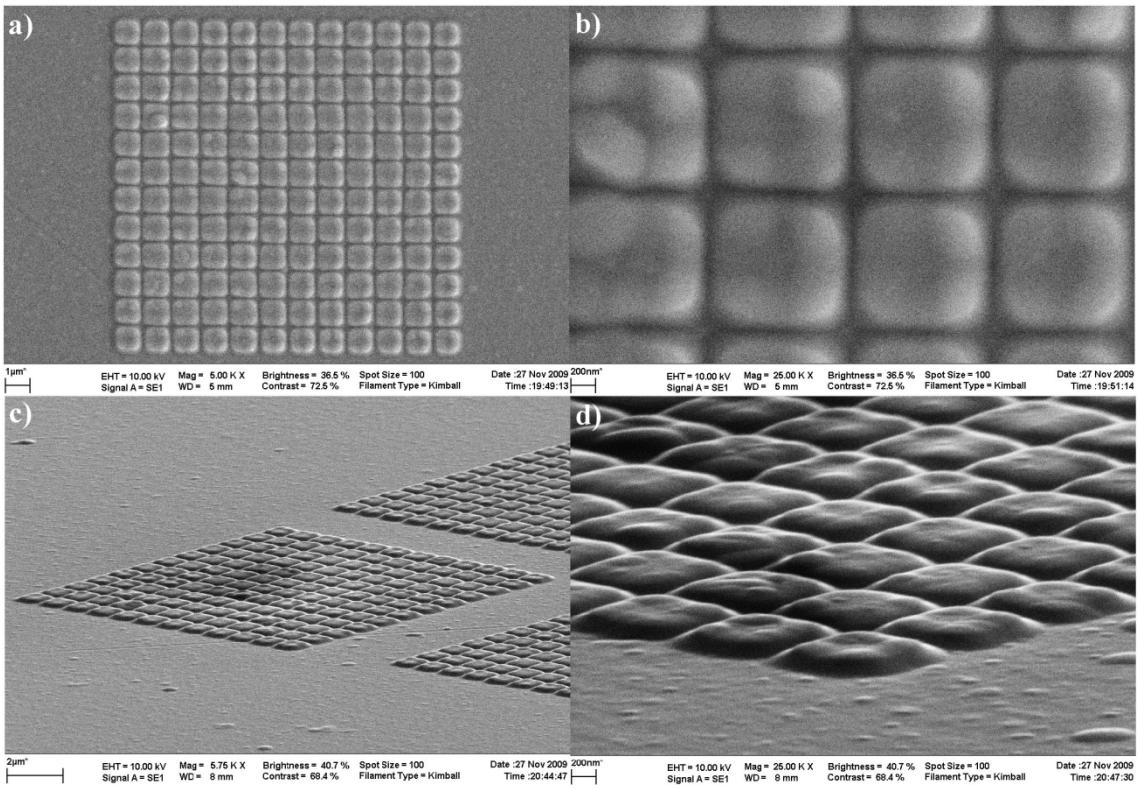

Figure 4.18: Images a) and b) provide 5,000 × and 25,000 × magnification SEM micrographs of squares defined in a [3 nm $DyFe_2$ / 12 nm YFe_2] × 27 multilayer sample. Images c) and d) provide tilted SEM micrographs of the same squares, taken at 5,750 × and 25,000 × magnification. Note the sloped side-walls.

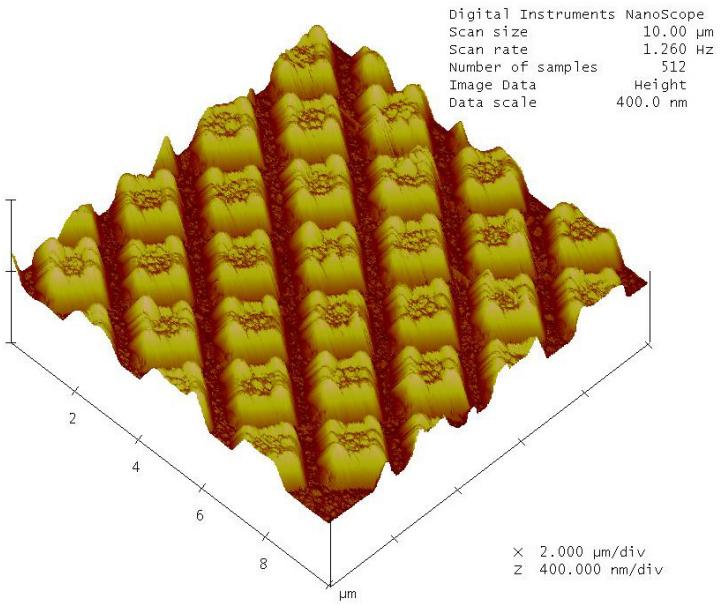

Figure 4.19: 3D AFM micrograph of the same array of 1.1 μm squares at a pitch of 1.2 μm defined in the same [3 nm $DyFe_2$ / 12 nm YFe_2] × 27 multilayer sample as that depicted in Figure 4.18. The squares have a height of 100 ± 2 nm.

Figure 4.18 shows squares which are approximately 1.1 μm in lateral dimensions, patterned at a pitch of 1.2 μm. Thus the spacing between adjacent patterned elements is just 100 nm. This patterned array was derived from a near 100 nm thick Cr mask, featuring 600 nm squares patterned at a pitch of 1.2 μm. The tilted SEM micrographs (Figure 4.18, images c) and d)) and the AFM micrograph (Figure 4.19) provide further evidence of sloped side-walls and increased height towards the edges and corners of the patterned elements. The raised edges have a height of approximately 20 nm, extending over a width of roughly 250 nm. At the corners this thickness of re-deposited material is roughly doubled to 40 nm. The sloped side-walls and raised edges to the patterned arrays are again attributed to re-deposition of sputtered material during the Ar^+ ion milling process. The higher magnification SEM micrographs (images b) and d) in Figure 4.18) and the AFM micrograph (Figure 4.19) show that the patterned elements, although only separated by 100 nm, remain as relatively well-defined individual items. This serves as a useful demonstration that the Ar^+ ion milling process can be used to pattern close-packed features in $REFe_2$ films and multilayers.

In Figure 4.20 and Figure 4.21 the first demonstration of nano-scale patterned arrays created in a $REFe_2$ film are presented in the form of SEM and AFM micrographs respectively. The square patterned elements have a lateral dimension equal to 700 nm and a pitch of 800 nm. The now familiar sloped side-walls and increased height to the patterned elements at their edges and corners are clear from the tilted SEM micrographs (images c) and d) within Figure 4.20) and the AFM micrograph (Figure 4.21).

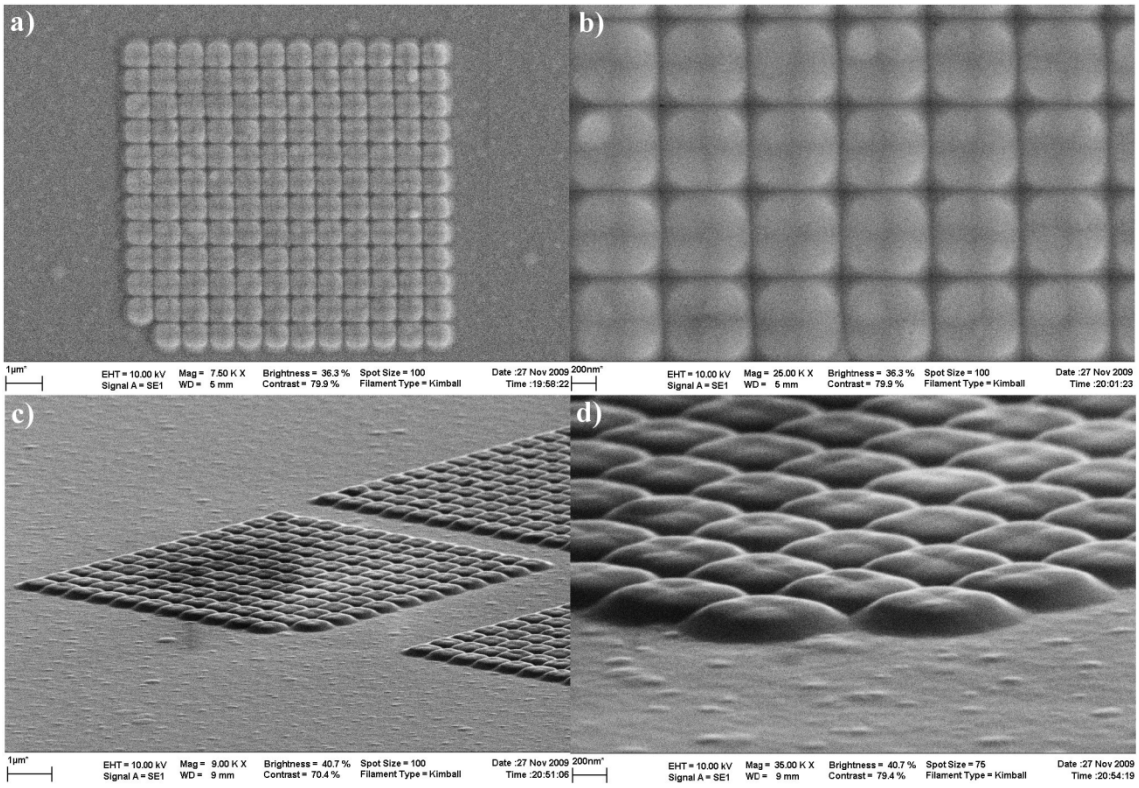

Figure 4.20: Images a) and b) provide 7,500 × and 25,000 × magnification SEM micrographs of squares defined in a [3 nm $DyFe_2$ / 12 nm YFe_2] × 27 multilayer sample. Images c) and d) are tilted SEM micrographs taken at 9,000 × and 35,000 × magnification respectively of the same regions. The lateral dimensions to the patterned elements are 700 nm and they have a pitch of 800 nm. The "missing" square is intended to aid sample recognition and orientation.

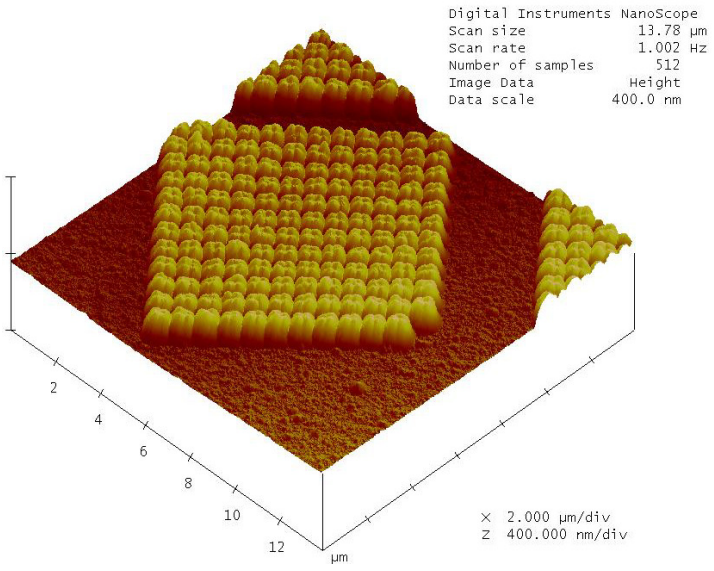

Figure 4.21: 3D AFM micrograph of the same array of 700 nm squares defined in a [3 nm $DyFe_2$ / 12 nm YFe_2] × 27 multilayer sample as depicted in Figure 4.20.

From Figure 4.20 and Figure 4.21 it is clear that the "individual" magnetic nano-elements have begun to merge together. This is illustrated most prominently in a cross-sectional scan of this AFM data, presented in Figure 4.22. The overall height of the patterned region, measured from the base of the sample (red markers and text) is 106 ± 2 nm, whilst the height between adjacent elements (green markers and text) is 19 ± 2 nm. Whilst this significant reduction in height can be attributed to the finite dimensions of the AFM probe tip (discussed earlier) in part, comparison of these data with that in Figure 4.15 strongly suggest that the originally individual patterned elements have begun to merge together.

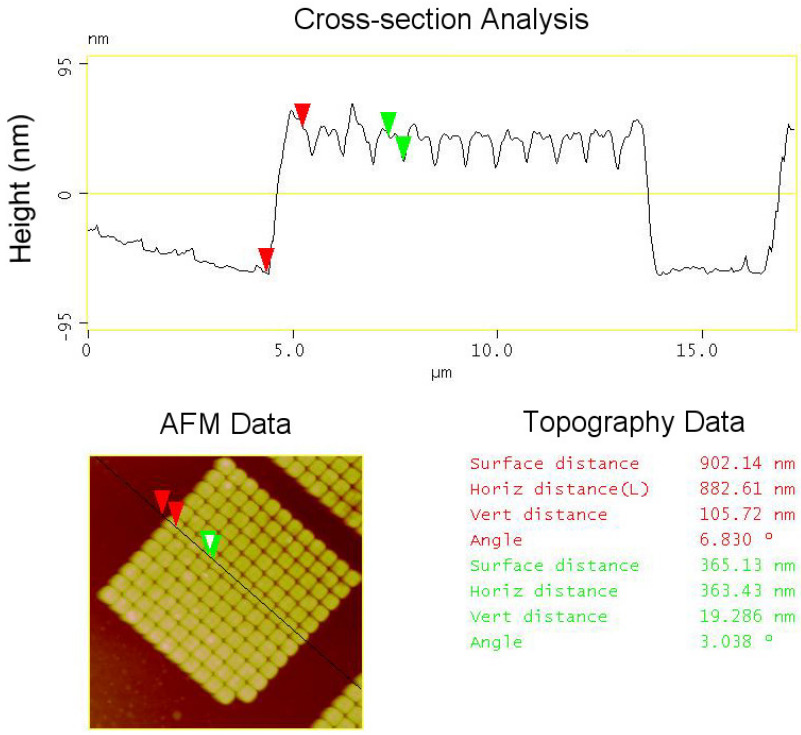

Figure 4.22: Cross-sectional AFM data of the 700 nm squares defined in the [3 nm $DyFe_2$ / 12 nm YFe_2] × 27 multilayer sample depicted in Figure 4.20 and Figure 4.21. The height of the patterned region is 106 ± 2 nm whilst the height of the individual elements is 19 ± 2 nm.

The successful transfer of patterned elements at the nano-scale into a thick epitaxial $REFe_2$ multilayer exchange spring sample has thus been demonstrated for the first time. However, the patterned elements are superimposed on a $REFe_2$ background due to the trade-off between mask thickness and nano-scale resolution and begin to merge together as smaller feature dimensions are reached.

4.2.8 Demonstration of the self-mask process

Following the successful fabrication of nano- and micro-scale patterned elements in the [3 nm $DyFe_2$ / 12 nm YFe_2] × 27 multilayer exchange spring sample described in the previous section, this sample has been subject to the self-mask process. This transfers the patterned elements further into the bulk of the material, removing the underlying background so as to facilitate simpler interpretation of both the MFM and MOKE data. An example AFM micrograph showing the nominally 1 μm wide lines (2 μm pitch) is presented in Figure 4.23.

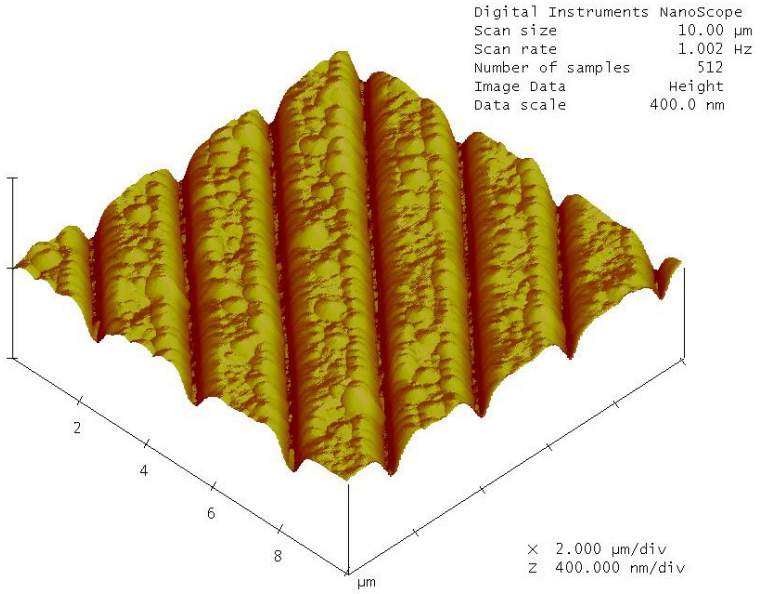

Figure 4.23: 3D AFM micrograph of an array of nominally 1 μm wide, 2 μm pitch lines defined in a [3 nm $DyFe_2$ / 12 nm YFe_2] × 27 multilayer sample. Due to the re-deposition associated with the self-mask process, the patterned lines now have a width of 1.9 μm whilst retaining the same pitch, hence have an intra-element spacing of 100 nm.

The lines are measured to have a width of 1.9 ± 0.02 μm whilst the pitch remains fixed at 2.0 ± 0.02 μm. The AFM micrograph shows clear evidence for a well defined un-patterned region between the adjacent elements, the width of which is approximately 100 nm. When comparison is made with Figure 4.17 it can be seen that the width of the lines has increased slightly from 1.8 to 1.9 μm (with the separation between adjacent elements reduced accordingly) as a result of further re-deposition of sputtered material. These lines have a height of 107 ± 2 nm which is the same (within the error) as data measured after Ar^+ ion milling with half of the incident fluence. This is to be expected since there is no etch selectivity in the self-mask process. The side-walls extend over approximately 275 nm, corresponding to a very similar taper angle of 20°. However given the incident Ar^+ ion fluence has doubled between these two sets of data (1.7 ×

10^{17} ions cm^{-2} *c.f.* 3.4 × 10^{17} ions cm^{-2}) the effects of further re-deposition are somewhat less pronounced than expected. One explanation for this is an altered sticking coefficient [20] between the sputtered $REFe_2$ material and the mask, with the $REFe_2$ self-mask having a smaller coefficient than the Cr mask. Further investigation of this effect is required to draw more conclusive answers. It is important to note at this point that there remains a certain amount of background material in this sample even after the self mask process has been executed for a fixed incident fluence of Ar^+ ions. Whilst clearly this is not ideal in terms of interpretation of MFM and MOKE data it is unavoidable since, due to re-deposition, further Ar^+ ion milling will cause unacceptable deterioration to the resolution of the patterned elements. This would result in the scenario evidenced for the nominally smaller features shown in Figure 4.22.

4.3 Drawbacks of Ion Milling

The drawbacks associated with wet etching and reactive ion etching processes have already been discussed in sections 3.6.1 and 3.6.2 respectively. To this end the process of ion milling was chosen to provide transfer of lithographically defined patterns onto epitaxially grown $REFe_2$ films and multilayers. Whilst ion milling avoids many drawbacks such as the isotropic nature of wet etching and the complex process gasses used in reactive ion etching, it inevitably suffers from some drawbacks of its own. The low etch selectivity between the mask material and the substrate is clearly one issue warranting some concern. This was addressed by the demonstration that harder mask materials (*e.g.* a metallic mask rather than a polymer mask) offer a useful and practically attainable way of overcoming the etch selectivity problem. There are however two further issues associated with the ion milling process which are evident in the results discussed above. These are re-deposition of sputtered material and the implantation of energetic ions. These points will briefly be considered in sections 4.3.1 and 4.3.2 respectively.

4.3.1 Re-deposition of sputtered material

The subject of re-deposition, touched upon in section 4.2.3, together with the increased etch selectivity, formed the incentive behind the utilisation of a metallic mask. In practice the use of a metallic mask does significantly reduce this problem, but from the

figures and accompanying text of section 4.2.4 it can be seen that the effects of re-deposition have not been eliminated entirely.

Whilst the metallic mask is significantly thinner and harder than its polymer counterpart it still remains susceptible to re-deposition and trenching. Re-deposition, as discussed previously, is the process whereby sputtered material lands on and sticks to the mask rather than being ejected entirely from the proximity of the sample [21]. This leads to a reduction in the resolution of the etch-transferred pattern, compared to that of the mask, and the loss of the strictly directional (anisotropic) etch process desired. Trenching, also referred to as reflected ion beam milling, occurs when the incident ions are reflected from one part of the sample surface onto another with enough energy to sputter material away from this surface [22, 23]. Trenching is most prominent towards the base of a masked sample since the ion flux is largest there, due to the constructive interference between the primary incident and reflected ion beams. The effect of trenching is reduced considerably so that it becomes negligible when the angle between the primary incident beam of ions and the normal to the sample surface is greater than 20° [22, 24]. The angle which the primary beam of ions subtends in the present experimental set-up is 68°, so no trenching effects are observed in any of the experimental data. This is in very good agreement with the experimental data of Younger & Haynes [24] who note the same effects at 70°. Accordingly the effect of trenching is dropped, in favour of the more dominant process, namely that of re-deposition.

Computational simulations performed by both Younger & Haynes [24] and Yamauchi *et al.* [25] show that as the ion beam milling process proceeds, the mask side-wall taper angle decreases. Both groups begin with a mask taper angle of 75° which is in very good agreement with the author's experimentally derived values discussed in section 4.2.4. They show a decrease in side-wall taper angle with increasing ion fluence, leading to a reduction in the mask's and thus patterned feature's dimensions. This is in contrast to the author's measured results. However, under closer inspection the simulations of both groups show a gradual emergence of sloped side-walls to the regions from which the material is sputtered. This is attributed to the re-deposition of the sputtered material. If this process is extended over a longer period of time (especially relevant for the self-mask process) it can be seen, from the schematic illustration in Figure 4.24, that re-deposition can lead to the fabrication of features

which not only exhibit rather sloped side-walls but are also considerably larger than those initially defined by the mask.

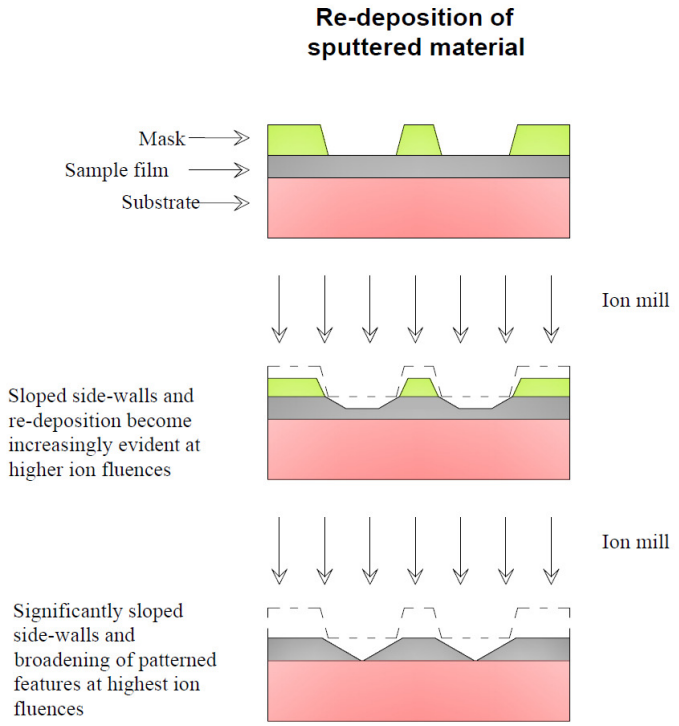

Figure 4.24: Schematic diagram showing the effects of re-deposition during the Ar^+ ion milling pattern transfer process. The side-walls clearly become more sloped as the process continues to higher ion fluences. At the highest fluence, the patterned elements transferred to the sample are significantly larger in lateral dimensions than those originally defined by the mask. The dashed lines represent the outline of the original mask, acting as a guide to the eye.

The re-deposition process provides a good explanation for the patterned elements evidenced in section 4.2.7 and 4.2.8, whereby sloped sidewalls and element sizes larger than those defined in the metallic mask are prevalent. The agreement between the cross-section of the patterned elements at the bottom of Figure 4.24 and the tilted SEM micrograph showing the nominally 1 μm wide lines (lower image in Figure 4.16) is especially obvious. In both instances, the pitch of the patterned features clearly remains constant, while their lateral size increases significantly. This progression in the shape of the patterned elements, under increasing ion fluences, is in good agreement with the recent experimental and theoretical work of Sachan *et al.* [26] and Walter *et al.* [23], who also observe a broadening of features during the ion milling process.

The author is unaware of any reports that discuss the appearance of the higher edges and corners to the patterned elements, as shown in the SEM and AFM micrographs throughout section 4.2.7. The author believes that as the ion milling process continues, the emergence of large, gently sloped side-walls, will lead to

significant re-deposition from these areas too. This is because as the side-wall taper angle becomes shallower, the ion beam is incident on a larger area of the side-wall. Thus sputtering and re-deposition from these areas can no longer be neglected. It is likely, given their gently sloped nature, that some of the material sputtered from the side-walls will be re-deposited on the upper surface of the mask, predominantly at the edges (with the effect exaggerated at the sample corners due to the convergence of perpendicular edges). This is not evident in the simulated models of Youngner & Haynes [24] and Yamauchi *et al.* [25] since these authors consider only re-deposition from the base of the material being removed rather than the side-walls of the mask. In the virgin state this is a good approximation due to the large taper angle to the mask's side-walls, but as the ion milling process continues and the taper angle becomes smaller this approximation must fail. The model of Moreno-Marin *et al.* [27] does consider re-deposition from the mask side-walls but simulations are again only performed with a side-wall taper angle of 90°. Therefore the effects of re-deposition from the side-walls are significantly reduced from those in this work. Clearly these models become less valid as the aspect ratio of the patterned elements becomes greater, and as the separation between the patterned elements is reduced further, leading to increased re-deposition from adjacent side-walls and mask shadowing effects [23].

Yamauchi *et al.* [25] state that their model, which ignores re-deposition for the side-walls of the mask, is valid provided the separation between patterned elements, p satisfies

$$p > 2t \tan \theta_o \tag{4.2}$$

where t is the thickness of mask and θ_o is the angle subtended by the ion beam and the sample surface normal (θ_o = 68° throughout this work). Thus, assuming a nominally 100 nm thick Cr mask is used, this suggests that re-deposition from the side-walls of the mask can be ignored provided there is a critical separation (p_c) between patterned elements. Using the above data and equation (4.2) this is given by $p_c \gtrsim 500$ nm. The three different patterned arrays presented in section 4.2.7 (1 μm wide lines, 600 nm squares and 400 nm squares) are all fabricated in the Cr mask material with a pitch equal to double the patterned element size, hence p is equal to the patterned element size. Therefore for the 1 μm wide lines $p > p_c$, but for both square arrays $p \approx p_c$. Thus it can be assumed that the effects of re-deposition from the side-walls can be neglected for the array of 1 μm wide lines, but not for the square arrays. This is borne out

experimentally by only a small increase in height to the edges of the 1 μm wide lines, but a notable increase in height at the edges and corners of both arrays of squares. The latter is most prevalent when comparison of the AFM micrographs of the respective patterned array is made directly by comparing Figure 4.17 and Figure 4.19.

Finally, it is important to note the consequences of side-wall erosion (see Figure 4.24). It is clear that during the ion milling process the side walls of both the mask and the sample being removed become increasingly sloped. If the fluence is increased beyond that depicted in the lower panel of Figure 4.24 the individual elements will begin to merge together. If the patterned elements are too close and / or the ion milling process is continued for a greatly extended period of time, there will be a significant loss in resolution and aspect ratio of the patterned elements. This is apparent in the AFM micrographs for the array of nominally 400 nm squares (Figure 4.21 and Figure 4.22), recalling that this effect is unlikely to be due solely to the finite dimensions of the AFM probe (section 4.2.7). This reinforces the usefulness of the proof-of-principle experiment conducted with the bi-layer sample which did not exhibit significant re-deposition. It is important to reiterate that the problems ascribed to re-deposition are significantly more prominent in thick films, films which are not the material of choice for use in patterned media *etc*. Thus the successful demonstration of patterning without re-deposition in the thin bi-layer sample is most applicable to ideal materials used in patterned media and other technologies such as MRAM.

4.3.2 Ion implantation

The process of ion milling relies on the use of energetic ions to eject atoms from the target material. Provided enough energy and momentum are transferred in the collision for the target atom to overcome the potential energy barrier associated with the material's surface, the atom will be sputtered away. There does however remain the question of what happens to the incident ion.

When sputtering using energetic ions, there will be inevitable penetration by these ions into the target material. The Ar^+ ions used in the present work to fabricate patterned arrays lose their energy within the sample via predominantly elastic collisions with the target atoms. This causes the target atoms to recoil, displacing them from their original positions within the crystalline lattice. Due to the epitaxial nature of the films studied throughout this thesis, these changes may occur rapidly and throughout the entirety of the material, creating significant changes throughout its structure. Since the

ions remain within the film, depositing the entirety of their energy within the metallic layers, they are said to be "implanted".

The effects of ion milling are therefore twofold: the removal of material via sputtering and induced structural changes within the material's crystalline lattice via ion implantation. As it happens, the latter effect is very significant and can be used to great success to reliably and accurately alter the magnetic properties of these epitaxial $REFe_2$ materials on the atomic scale. This effect is so pronounced that it is explored in depth in a dedicated chapter; the implantation of 3.25 keV Ar^+ ions into YFe_2 and $DyFe_2$ films and a $DyFe_2$ / YFe_2 multilayer are presented in Chapter 5.

4.4 Concluding remarks regarding Ar^+ ion milling as a patterning tool

In this chapter, results demonstrating the first nano-scale pattern fabrication in epitaxial $REFe_2$ films and multilayers have been presented and discussed. Nano-scale fabrication has been achieved using electron beam lithography to define the pattern in a polymer resist, metallic deposition and lift-off to fabricate a hard mask, and Ar^+ ion milling to transfer the pattern into $REFe_2$ films and multilayers. This marks the accomplishment of a process which can attain significantly higher resolution than the previously demonstrated wet etching processes. At the same time it avoids the often complex process of reactive ion etching, for which the author is unaware of any recipes for application to $REFe_2$ materials.

Solutions to the two detrimental effects associated with the Ar^+ ion milling process have been identified: re-deposition of sputtered material may be avoided with further development towards thinner $REFe_2$ multilayer systems, and the implantation of Ar^+ ions may be used to great benefit to accurately engineer the magnetic anisotropies of these materials. The process of re-deposition can be significantly reduced by using a hard metallic mask rather than a polymer mask. When coupled with the use of a technically relevant thin magnetic bi-layer, the metallic mask was shown to be very good at facilitating nano-scale pattern transfer using Ar^+ ion milling. Extension of this process to thicker epitaxial $REFe_2$ multilayers was partly successful. Aspects limiting the usefulness of this process to these thicker materials were identified, but these may be eliminated by the use of mask materials more resilient to Ar^+ ion milling, providing a higher etch selectivity. The effects associated with the implantation of Ar^+ ions into the

substrate material were unavoidable using the ion gun available for this work, but were in fact shown to be very useful in their own right with regard to modification of the material's magnetic properties. This interesting topic is the subject matter of Chapter 5.

To summarise, the process of Ar^+ ion beam milling of $REFe_2$ films and multilayers has been developed from scratch using cost-effective, freely available equipment. The process has been refined to permit nano-scale fabrication, marking an increase in pattern resolution of several orders of magnitude over those defined previously using wet-etching techniques [1, 2, 3, 4]. In addition, the implantation of energetic (keV) Ar^+ ions has been found to induce significant changes at the atomic scale within these samples. The latter forms a process which can, on its own, probe and engineer fundamental magnetic properties, or can be used in conjunction with the lithographically defined procedures described here in a manner akin to that first described by Chappert *et al.* [28].

References

[1] K. Wang, K. N. Martin, C. G. Morrison, R. C. C. Ward, G. J. Bowden & P. A. J. de Groot, *Phys. Stat. Sol.*, vol. **203**, no. 15, pp. 3831 – 3835, 2006.

[2] K. Wang, C. Morrison, K. N. Martin, R. C. C. Ward, G. J. Bowden & P. A. J. de Groot, *J. Alloy. Comp.*, vol **440**, pp. 23 – 25, 2007.

[3] K. Wang, K. N. Martin, C. G. Morrison, R. C. C. Ward, G. J. Bowden & P. A. J. de Groot, *Appl. Phys. A*, vol **86**, pp. 325 – 328, 2007.

[4] K. Wang, K. N. Martin, C. Morrison, R. C. C. Ward, G. J. Bowden & P. A. J. de Groot, *J. Alloy. Comp.*, vol. **455**, pp. 31 – 34, 2007.

[5] J. I. Martín, J. Nogués, K. Liu, J. L. Vicent & I. K. Schuller, *J. Magn. Magn. Mater.*, vol. **256**, pp. 449 – 501, 2003.

[6] A. Mougin, C. Dufour, K. Dumesnil & Ph. Mangin, *Phys. Rev. B*, vol. **62**, no. 14, pp. 9517 – 9531, 2000.

[7] J-. M. L. Beaujour, *Ph. D. Thesis*, University of Southampton, UK, 2003.

[8] A. A. Zhukov, G. J. Bowden, J-. M. L. Beaujour, B. D. Rainford, P. A. J. de Groot, R. C. C. Ward, M. R. Wells & H. Küpfer, *J. Mag. Mag. Mat.*, vol. **270**, pp. 312 – 320, 2003.

[9] D. Wang, *Ph. D. Thesis*, University of Southampton, UK, 2009.

[10] M. Sawicki, G. J. Bowden, P. A. J. de Groot, B. D. Rainford, J-. M. L. Beaujour, R. C. C. Ward & M. R. Wells, *Phys. Rev. B*, vol. **62**, no. 9, pp. 5817 – 5820, 2000.

[11] M. Sawicki, G. J. Bowden, P. A. J. de Groot, B. D. Rainford, R. C. C. Ward & M. R. Wells, *J. Appl. Phys.*, vol. **87**, no. 9, pp. 6839 – 6841, 2000.

[12] J. A. Osborn, *Phys. Rev.*, vol. **67**, nos. 11 & 12, pp. 351 – 357, 1945.

[13] R. L. Comstock, *J. Mater. Sci.: Mater. Elec.*, vol. **13**, pp. 509 – 523, 2002.

[14] R. Skomski & J. M. D. Coey, *Phys. Rev. B*, vol. **48**, no. 21, pp. 15812 – 15816, 1993.

[15] K-. I Aoshima, N. Funabashi, K. Machida, Y. Miyamoto, N. Kawamura, K. Kuga, N. Shimidzu, F. Sato, T. Kimura & Y. Otani, *App. Phys. Lett.*, vol. **91**, p. 052507, 2007.

[16] T. Aoki, Y. Ando, D. Watanabe, M. Oogane & T. Miyazaki, *J. Appl. Phys.*, vol. **103**, p. 103911, 2008.

[17] R. C. C. Ward, M. R. Wells, C. Bryn-Jacobsen, R. A. Cowley, J. P. Goff, D. F. McMorrow & J. A. Simpson, *Thin Sol. Fil.*, vol. **275**, pp. 137 – 139, 1996.

[18] A. Mougin, C. Dufour, K. Dumesnil, N. Maloufi, Ph. Mangin & G. Patrat, Phys. *Rev. B*, vol. **59**, no. 8, pp. 5950 – 5959, 1999.

[19] *Ion Beam Etch Rates and Sputter Yields*, Intlvac, Ontario, data available at http://www.intlvac.com/wp

[20] D. W. Youngner & C. M. Haynes, *J. Vac. Sci. Technol.*, vol. **21**, no. 2, pp. 677 – 680, 1982.

[21] T. C. Tisone & P. D. Cruzan, *J. Vac. Sci. Technol.*, vol. **12**, no. 3, pp. 677 – 688, 1975.

[22] R. E. Lee, *J. Vac. Sci. Technol.*, vol. **16**, no. 2, pp. 164 – 170, 1979.

[23] M. Walter, H. M. Hütten, H. C. Scheer & J. Engemann, *Model. Simul. Mater. Sci. Eng.*, vol. **6**, pp. 251 – 260, 1998.

[24] D. W. Youngner & C. M. Haynes, *J. Vac. Sci. Technol.*, vol. **21**, no. 2, pp. 677 – 680, 1982.

[25] N. Yamauchi, T. Yachi & T. Wada, *J. Vac. Sci. Technol. A*, vol. **2**, no. 4, pp. 1552 – 1557, 1984.

[26] M. Sachan, C. Bonnoit, C. Hogg, E. Evarts, J. A. Bain, S. A. Majetich, J-. H. Park & J-G Zhu, *J. Phys. D: Appl. Phys.*, vol. **41**, p. 134001, 2008.

[27] J. C. Moreno-Marin, J. A. Valles-Abarca & A. Gras-Marti, *J. Vac. Sci. Technol. B*, vol. **4**, no. 1, pp. 322 – 325, 1986.

[28] C. Chappert, H. Bernas, J. Ferré, V. Kottler, J-. P. Jamet, Y. Chen, E. Cambril, T. Devolder, F. Rousseaux, V. Mathet & H. Launois, *Science*, vol. **280**, pp. 1919 – 1922, 1998.

Chapter 5

Ion Implantation in YFe_2, $DyFe_2$ and $DyFe_2$ / YFe_2 Films

When using energetic ions to sputter away material during ion milling, there will inevitably be, to some extent, penetration of the ions into the target material. The extent to which these ions penetrate is determined by its species, the kinetic energy, the angle of incidence subtended by the ions onto the target surface, and the composition and crystalline structure of the target material.

The target materials studied in this work were various $REFe_2$ Laves phase intermetallics. The ion species was fixed as the standard process gas of Ar which is easily available and thus cost effective. As such it is the most commonly used gas for ion milling. The angle which the Ar^+ ions subtend with the sample surface was optimised to promote the highest sputtering yield, thus the only remaining variable was the energy of the ions. A relatively high energy (keV rather than hundreds of eV) was chosen to optimise the ion milling process. At these energies the Ar^+ ions lose all of their kinetic energy within the sample, predominantly via elastic collisions with the target atoms. The subsequent recoil of the target atoms can lead to significant structural changes within the samples. In particular, samples which are initially under a tensile strain (due to their growth conditions) can be relaxed to a configuration more closely resembling that of a bulk, un-strained material. Since the magnetic properties of these materials depend on elastic strains, ion implantation induced relaxation will likely lead to a change in magnetic properties. In addition, whilst the deposition of Ar^+ ion energy is confined to a relatively small region of the sample volume, the effects on the target material's magnetic properties are pronounced and often evident throughout the entire volume.

The reader is referred to section 2.8 to recall details regarding the implantation of energetic ions into various materials. In this chapter, attention is given to the experimental results for Ar^+ ions implanted in YFe_2, $DyFe_2$ and a $DyFe_2$ / YFe_2 multilayer, focussing on the effects which this has on the materials' magnetic and structural properties.

5.1 Ar^+ Ion Implantation in YFe_2 Films

In this section the effects of Ar^+ ions implanted into a YFe_2 sample are discussed. The experimental procedures regarding Ar^+ ion implantation into an YFe_2 sample are described, before results taken using several complimentary techniques are presented and discussed.

5.1.1 Experimental procedure

The YFe_2 laves phase film had a thickness of 100 nm, was grown on a ~ 1 mm thick Al_2O_3 substrate with a 10 nm Nb seed and 2 nm Fe buffer layer and was capped with a 10 nm Y layer to prevent oxidation. The film thicknesses were very accurately controlled during the MBE growth process, and the film quality was determined using XRD (Figure 5.1). This data was used to determine a lattice parameter of 0.7320 nm (in the sample growth direction in the (110) plane). Given that the bulk (un-strained) lattice parameter for YFe_2 is 0.7362 nm [1], these data show a contraction in the lattice parameter of (– 0.6%). This contraction along the growth direction is in reasonable agreement with the results of Mougin *et al.* [1] who report a contraction of –0.4%. Consequently there must therefore be a lattice expansion in the plane of the film along the [001] and [1$\bar{1}$0] directions, in order to conserve volume.

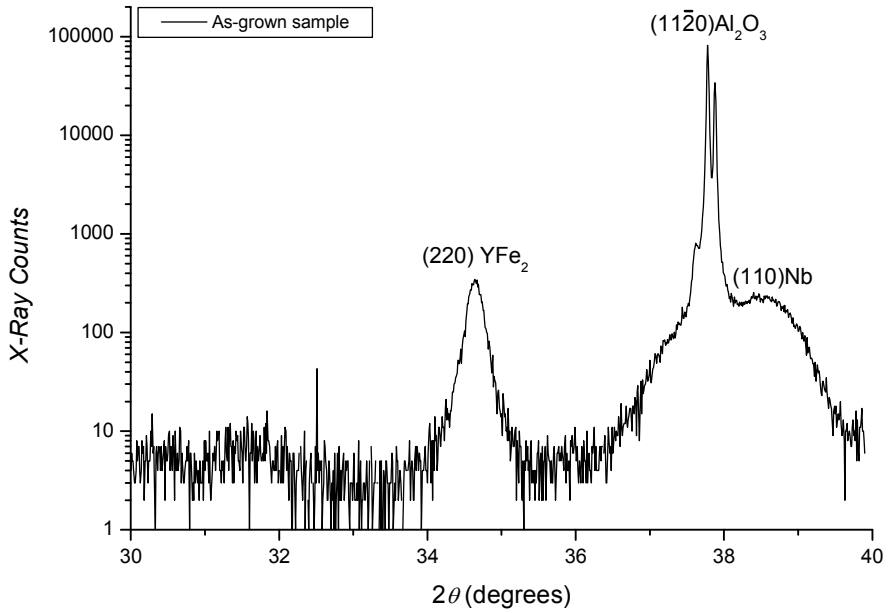

Figure 5.1: XRD data for an as-grown 100 nm YFe_2 sample.

The sample was cut into several pieces, each with lateral dimensions equal to roughly 5 mm, with the different pieces being exposed to increasing Ar^+ ion fluences. The Ar^+ ions made an angle of 68° to the plane of the sample and are accelerated to a voltage of 3.25 keV which is fixed throughout the experiments. The ion-current received at the target surface was approximately 0.5 μAcm^{-2}, corresponding to an Ar^+ ion flux of 3.1×10^{12} ions cm^{-2}s^{-1}.

The magneto optical Kerr effect (MOKE) is used to analyse the as-grown sample and the samples after ion implantation periods of 3, 6, 12 and 15 hours with corresponding fluences of 3.4×10^{16}, 6.8×10^{16}, 1.3×10^{17} and 1.7×10^{17} ions cm^{-2} (section 5.1.2). OOMMF modelling was performed for these samples and is discussed in relation to the MOKE data in section 5.1.3. After this, brief details of vibrating sample magnetometry (VSM) measurements of the samples are presented and discussed in section 5.1.4, with reference to both the MOKE and OOMMF data. X-ray diffraction (XRD) measurements were taken after ion implantation at selected intervals to check for any changes to the crystalline structure of the sample. Such data are presented and discussed in section 5.1.5. Atomic force microscopy (AFM) measurements, taken both before and after ion implantation at selected intervals, are presented and discussed in section 5.1.6 and used to determine if there are any changes present in the sample topography as a result of ion implantation. Discussion of the various experimental results are deferred briefly in favour of presenting SRIM modelling data for the YFe_2 sample (in Table 5.1), since values obtained from this data will be used throughout the forthcoming discussions. As expected, the predominant energy loss mechanism within the sample is via recoiling target atoms, with very few target crystalline lattice vacancies created due to these low energy recoil events.

Incident Ar^+ ion:		**YFe_2**	**Y**
Radial range (± 0.2 nm)		4.5	7.5
Energy loss to: (± 0.1%)	**ionization (ions / recoils)**	13.3 / 18.9	16.8 / 15.4
	vacancies (ions / recoils)	1.1 / 5.5	1.1 / 4.6
	phonons (ions / recoils)	4.2 / 57.0	4.4 / 57.7
Sputtering yield (± 0.1 atoms ion^{-1})		7.0	4.6

Table 5.1: SRIM data calculated for 10,000 3.25 keV Ar^+ ions incident at an angle of 68° on a 100 nm YFe_2 sample with a 10 nm Y cap

Finally, it should be noted that all experimental magnetic characterization techniques were obtained with the magnetic field applied along both the $[\bar{1}10]$ and

$[00\bar{1}]$ directions, to an accuracy of ± 5°. These directions correspond to the "standard" orientations used throughout this work, and make an in-plane angle of ~ 35° to the easy magnetization axis of YFe_2 strained films, which is believed to have its major component along the $[\bar{1}11]$ and $[\bar{1}1\bar{1}]$ directions. Mougin *et al.* [2] suggest that these YFe_2 films also have a small out of plane component of magnetization, making an angle of 15° to the film plane. The resultant easy axis is therefore expected to be along the equivalent ⟨221⟩ directions.

5.1.2 MOKE measurements of ion implanted YFe_2

The skin depth of Y, when probed using a HeNe laser with a wavelength of 633 nm, can be calculated using equation (3.10) to be 18 nm. The thickness of the Y protective cap on the present sample of YFe_2 is 10 nm and therefore provides a significant attenuation of the signal from the magnetic layer below. `SRIM` [117] calculations (Table 5.1) show that the Ar^+ ions are implanted to a distance of approximately 7.5 nm in the Y cap, with a sputtering yield of 4.6 atoms per incident ion. Using this data and the same calculations for the modifications to this rate as were provided in section 3.6.6 (modified downwards to account for the reduced incident Ar^+ ion energy), gives a sputtering rate of 0.3 nm min^{-1}. Thus the entire 10 nm Y cap can be expected to be removed in just over 30 minutes (Ar^+ ion fluence of roughly 6×10^{15} ions cm^{-2}). The removal of the protective Y cap provides a good explanation for the reduced MOKE signal amplitude presented in graphs a) and b) within Figure 5.2 when compared to those taken for increasing Ar^+ ion fluences in images c) through to j). However, it will become apparent throughout the forthcoming sections that the sputtering rate is somewhat lower than that predicted by `SRIM` calculations. These calculations predict that the entire 100 nm YFe_2 film would be removed in approximately 5 to 6 hours (a fluence of between 5×10^{16} and 7×10^{16} Ar^+ ions cm^{-2}), which clearly is not the case otherwise the hysteresis loops in graphs g) – j) would show no data. Calculations providing more accurate values for the sputtering yield will be made from VSM data in 5.1.4 whereby the volume of the material after ion implantation can be calculated and compared to values before ion implantation. This over-estimate in sputtering yields based upon `SRIM` calculations could be due to a number of reasons: i) the software always presuming the implanted material is in its virgin state, ii) the software making no account for the crystalline structure of the material, and iii) errors in the author's

measurements of current density at the sample surface, thus leading to erroneous sputtering rate calculations irrespective of the SRIM data. Note that sputtering rate data for the $DyFe_2$ and $DyFe_2$ / YFe_2 exchange spring sample will also be over-estimated.

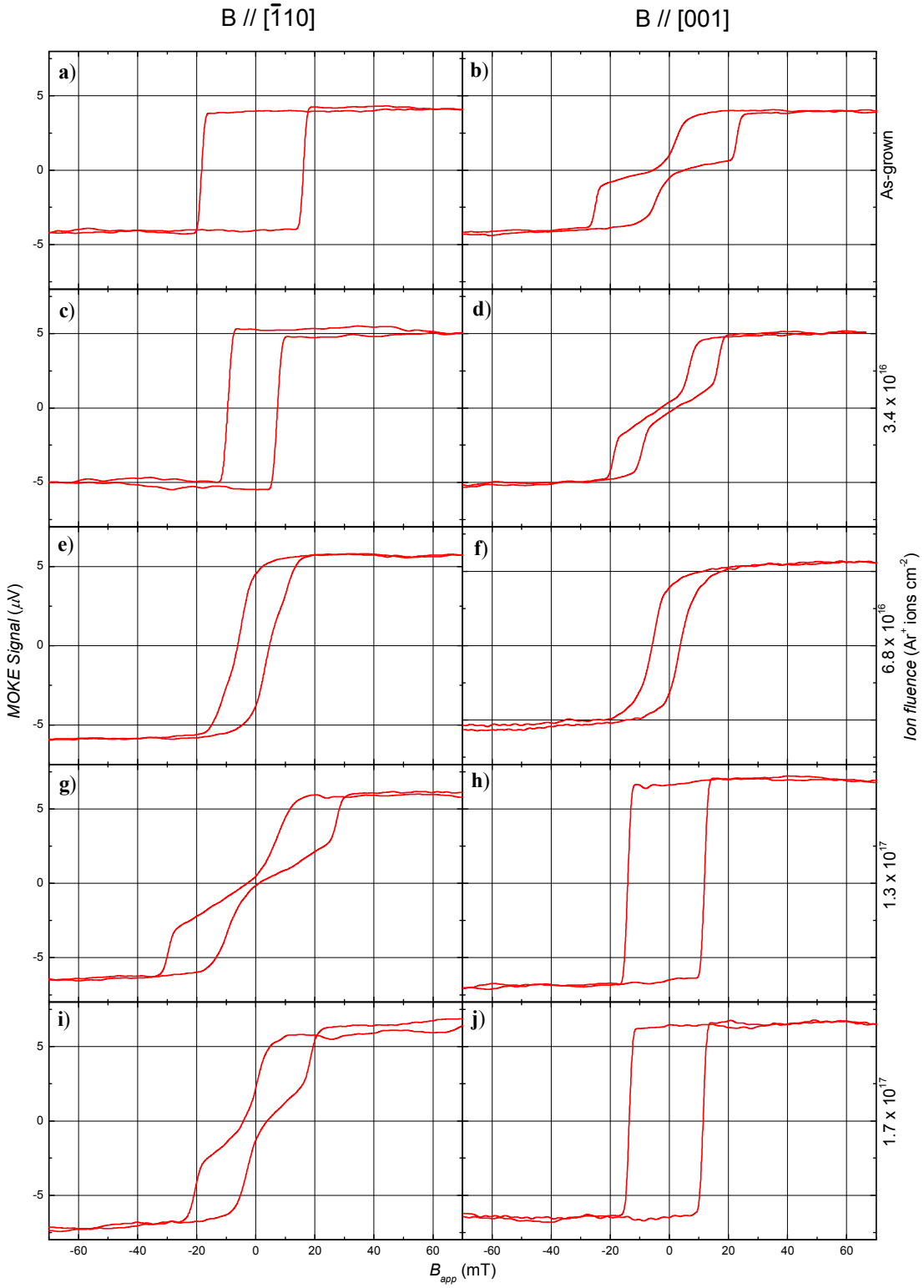

Figure 5.2: MOKE hysteresis loops of a 100 nm YFe_2 sample before and after ion implantations of increasing fluences (see right-hand sub-axis) for the applied magnetic field along the approximate as-grown easy and hard magnetic axes [$\bar{1}$10] and [00$\bar{1}$] respectively.

The MOKE hysteresis loops presented in Figure 5.2 show a clear progression in magnetic behaviour as the Ar^+ ion fluence is increased. The data for the as-grown sample looks very similar to that which would be expected for the field aligned along a direction close to the easy (hard) axes of magnetization $[\bar{1}10]$ ($[00\bar{1}]$).

Along the $[\bar{1}10]$ direction (graph (a)) the magnetization remains pinned under the application of reversed magnetic fields up to a coercive field of H_C = 17.4 mT. At this field the magnetization abruptly and irreversibly switches to align parallel with the applied field. Note that the ratio of the remnant magnetization (M_R) to saturation magnetization (M_S) ("squareness") is $\frac{M_R}{M_S} = 1.00$, corresponding to a very square hysteresis loop. When the field is applied along the $[00\bar{1}]$ direction (graph (b)), the MOKE hysteresis loop exhibits distinctly different properties. The coercivity is reduced to H_C = 5.2 mT and the squareness to $\frac{M_R}{M_S} = 0.2$. An expanded version of this graph can be seen below in Figure 5.3, to permit the discussion of the evolution of the sample magnetization when a field is applied along a hard axis of magnetization.

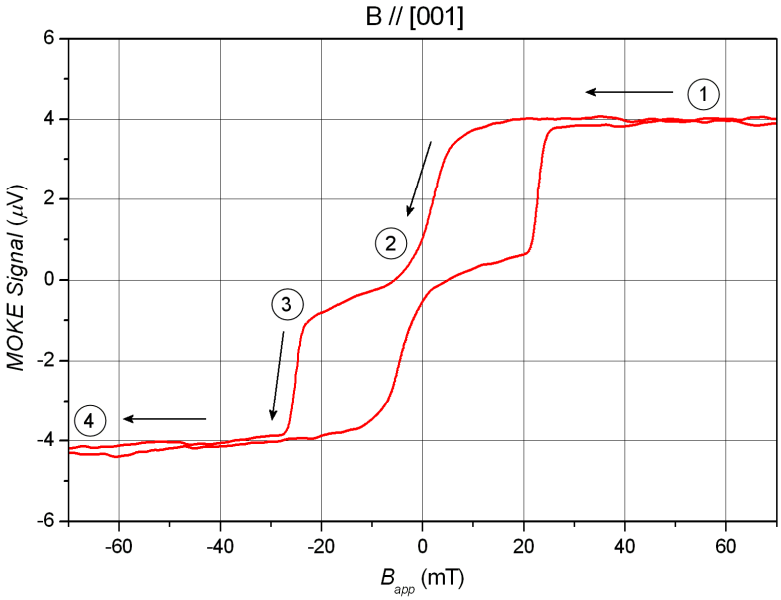

Figure 5.3: MOKE Hysteresis loop of a 100 nm YFe_2 sample magnetized along the $[00\bar{1}]$ direction. The evolution of the magnetization from the [001] to the $[00\bar{1}]$ axis is described in the accompanying text.

Reducing the applied magnetic field from saturation along the $[00\bar{1}]$ direction (point 1), at approximately 18 mT there begins a gradual rotation away from the $[00\bar{1}]$ direction towards a $\langle 111 \rangle$ direction (point 2), corresponding to a gradual decrease in magnetization. As the magnetization is forced to point further and further from the

$[00\bar{1}]$ direction, the rate of rotation increases as a local energy minima along a direction close to $\langle 111 \rangle$ is approached. A $\langle 111 \rangle$ direction is described by Mougin *et al.* [2] and Beaujour [3] as being close to the easy axis of YFe_2 thin film samples. Hence between points 2 and 3 the sample magnetization remains fairly constant as the magnetic moments lie in a close to easy axis direction. This is further confirmed by the sample magnetization being close to zero in this region; the magnetic moments are now lying along a local energy minimum, perpendicular to the direction of the applied field and hence are not sensed in the MOKE apparatus. At an applied field of approximately –22 mT (point 3) the local energy minima along the $\langle 111 \rangle$ direction becomes unstable and the sample magnetization switches abruptly and irreversibly into the [001] direction (point 4). Although measurements to determine the easy (and hard) axis magnetization directions of YFe_2 thin film samples have been reported in the past [2, 3], this is the first detailed report that shows distinct differences in magnetic axes that can be predominantly attributed to the cubic anisotropy of the system.

The MOKE data in Figure 5.2 for the applied magnetic field along the $[\bar{1}10]$ direction for a sample implanted with an Ar^+ ion fluence of 3.4×10^{16} ions cm^{-2} (graph c)), show a coercivity of H_C = 8.5 mT; a reduction of 8.9 mT when compared to the measurement of the as-grown sample (graph a)). At this fluence the squareness of the hysteresis loop remains unchanged. Doubling of this incident Ar^+ ion fluence, as shown in graph e), serves to reduce the coercivity further to H_C = 5.5 mT. At this fluence (6.8×10^{16} Ar^+ ions cm^{-2}), the hysteresis loop still retains a relatively large squareness of $\frac{M_R}{M_S} = 0.79$. A re-doubling of this fluence to 1.3×10^{17} Ar^+ ions cm^{-2} (graph g)), results in a magnetic behaviour which looks almost exactly like that depicted in graph b), completely different from that of graphs a), c) and e). Further ion implantation, up to a fluence of 1.7×10^{17} Ar^+ ions cm^{-2} (graph i)) results in only small changes to the magnetic properties of the sample, with it clearly still displaying a hard axis-like behaviour. Overall, the data measured with the applied magnetic field along the $[\bar{1}10]$ direction changes significantly between the as-grown sample and that implanted with ~ 10^{17} Ar^+ ions cm^{-2}.

When measurements of an ion implanted YFe_2 sample are made with the magnetic field applied along the $[00\bar{1}]$ direction, again no significant changes are noticed for "lightly" ion implanted samples, that is those subjected to an Ar^+ ion fluence less than approximately 5×10^{16} ions cm^{-2}. Under this incident fluence there is a

reduction in H_C from 5.2 to 2.7 mT with a corresponding decrease in squareness from $\frac{M_R}{M_S} = 0.18$ to $\frac{M_R}{M_S} = 0.07$ (Figure 5.2, graphs b) and d) respectively), but the overall shape of the hysteresis loop remains fixed. When measurements are made along this direction for a sample subjected to a greater Ar^+ ion fluence (1.3×10^{17} ions cm^{-2}, graph h)) there are more pronounced changes. The most prominent of these is the emergence of an almost completely square ($\frac{M_R}{M_S} = 0.94$) hysteresis loop with H_C = 13.0 mT. This is very similar to that of the as-grown sample when measured along the perpendicular $[\bar{1}10]$ direction. Further increases of the incident ion fluence to 1.7×10^{17} Ar^+ ions cm^{-2} as depicted in graph j) yields almost no additional changes to the magnetic properties.

In short, the data obtained for the as-grown samples looks virtually identical to that for the samples implanted by a fluence of 10^{17} Ar^+ ions cm^{-2} when characterized with the magnetic field oriented orthogonally, *i.e.* the easy and hard axes of magnetization have been rotated by 90°. Additionally the similarities between graphs e) and f) in Figure 5.2 should be noted. This represents an intermediate transition stage where the sample exhibits either a uniaxial anisotropy or two competing cubic anisotropies, rather than its intrinsic single cubic anisotropy.

5.1.3 OOMMF modelling of YFe_2

Modelling of this 100 nm YFe_2 film using `OOMMF` shows that contrary to previous results [2, 3], the magnetization appears strongly dependent on the presence of magnetoelastic anisotropy. Any weak dependence has previously been attributed to an increase in the exchange anisotropy between the Fe ions due to the induced strain in the Fe sublattice during the MBE growth process [2, 4]. In the present simulations, the contribution of the magnetoelastic anisotropy has been systematically varied by adjusting a "strain pre-factor" which governs the dominance of the magnetoelastic anisotropy energy within the `OOMMF` model. All other parameters have been kept constant. The `OOMMF` data are presented in graphs a) – j) in Figure 5.4, for the magnetic field applied along the $[\bar{1}10]$ and $[00\bar{1}]$ directions (close to the easy and hard axes of magnetization, respectively). These results should be compared with those of Figure 5.2 graphs a) – j). The reader is referred back to section 2.6.5 for further details of the modelling process, recalling that `OOMMF` is essentially a modified zero temperature model and thus there may be some discrepancies between theory and experiment in the values of applied magnetic field at which switching occurs. Note that other modelling

parameters such as the strength of the magnetocrystalline and shape anisotropy have been varied, but only changes in magnetoelastic anisotropy show this effect.

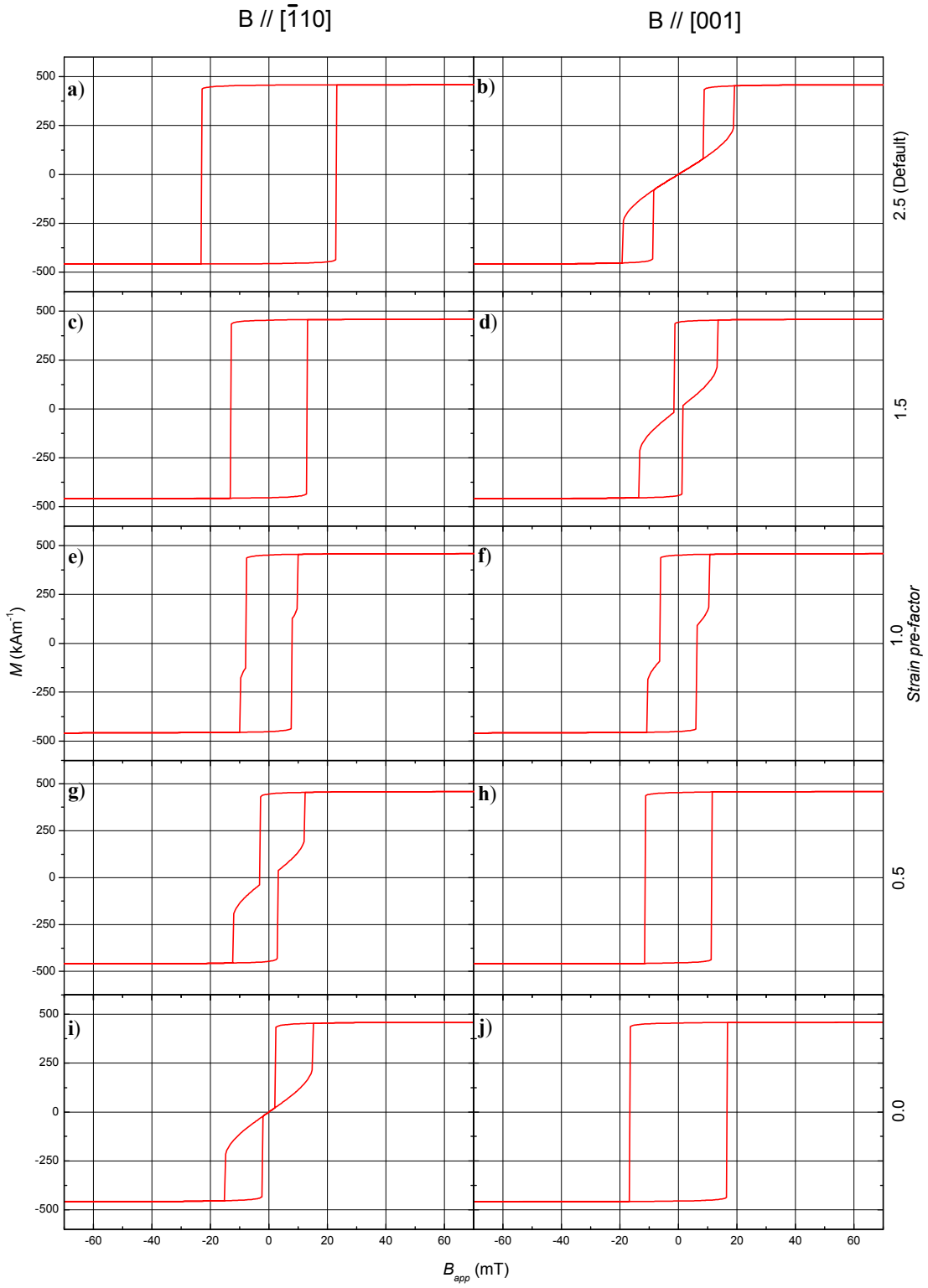

Figure 5.4: Hysteresis loops created from OOMMF data with the applied magnetic field directed along the [$\bar{1}$10] and [00$\bar{1}$] directions for a 100 nm YFe_2 sample. These data are taken whilst systematically reducing the factor multiplying the strain term used to generate the magnetoelastic energy in the model for the calculation of magnetization (M) as a function of applied field ($\mathbf{B}_{app}$) (see right-hand label).

It is clear that the OOMMF results agree very well with the MOKE data. The progression of the hysteresis loop from the strained, magnetoelastic anisotropy dominated configuration (graphs a) & b) in both Figure 5.2 and Figure 5.4) to the completely un-strained, magnetostatic and magnetocrystalline anisotropy dominated configuration (graphs g) – j) in both Figure 5.2 and Figure 5.4) is in good agreement. This is in terms of both general hysteresis loop shape and in relative magnitudes of applied field and sample magnetization. There is also good agreement during the intermediate steps of the hysteresis loops, shown experimentally and modelled in graphs c) – f) in Figure 5.2 and Figure 5.4 respectively. In addition, there is excellent agreement between the coercive fields of the "square" hysteresis loops in the MOKE and OOMMF data (graphs a) & j) in both Figure 5.2 and Figure 5.4 respectively) before and after ion implantation. In the MOKE data the ratio between the coercivity of the as-grown sample magnetized along $[\bar{1}10]$ and the ion implanted sample magnetized along $[00\bar{1}]$ is 1.38, while the OOMMF data gives 1.40. This serves as further proof for the relevance and reliability of the OOMMF modelling package.

The OOMMF data for the $[\bar{1}10]$ direction shows a steady decrease in coercivity, from H_C = 23.2 mT for a strain pre-factor of 2.5 (standard for these models [5]) to H_C = 7.8 mT for a strain factor of 1.0, before finally reducing to H_C = 0 for a complete lack of magnetoelastic anisotropy. For the data obtained with the magnetic field applied along the $[00\bar{1}]$ direction there is a corresponding steady increase in coercivity, up to a maximum of H_C = 16.6 mT for a condition corresponding to a complete lack of magnetoelastic anisotropy. The data for the $[\bar{1}10]$ and $[00\bar{1}]$ directions look identical when the strain pre-factor is set between 0.9 and 0.95 which, when comparison is made with the MOKE data, would correspond to an ion fluence of approximately $8 – 9 \times 10^{16}$ Ar^+ ions cm^{-2}. This fluence is close to the value of 7×10^{16} Ar^+ ions cm^{-2} where uniaxial or competing cubic anisotropies were noted in the MOKE data, *i.e.* where measurements with the magnetic field applied along the $[\bar{1}10]$ and $[00\bar{1}]$ directions looked identical.

Graphs comparing the observed changes in coercivity with respect to increasing Ar^+ ion fluence and decreasing strain pre-factor for MOKE and OOMMF data respectively can be seen in Figure 5.5.

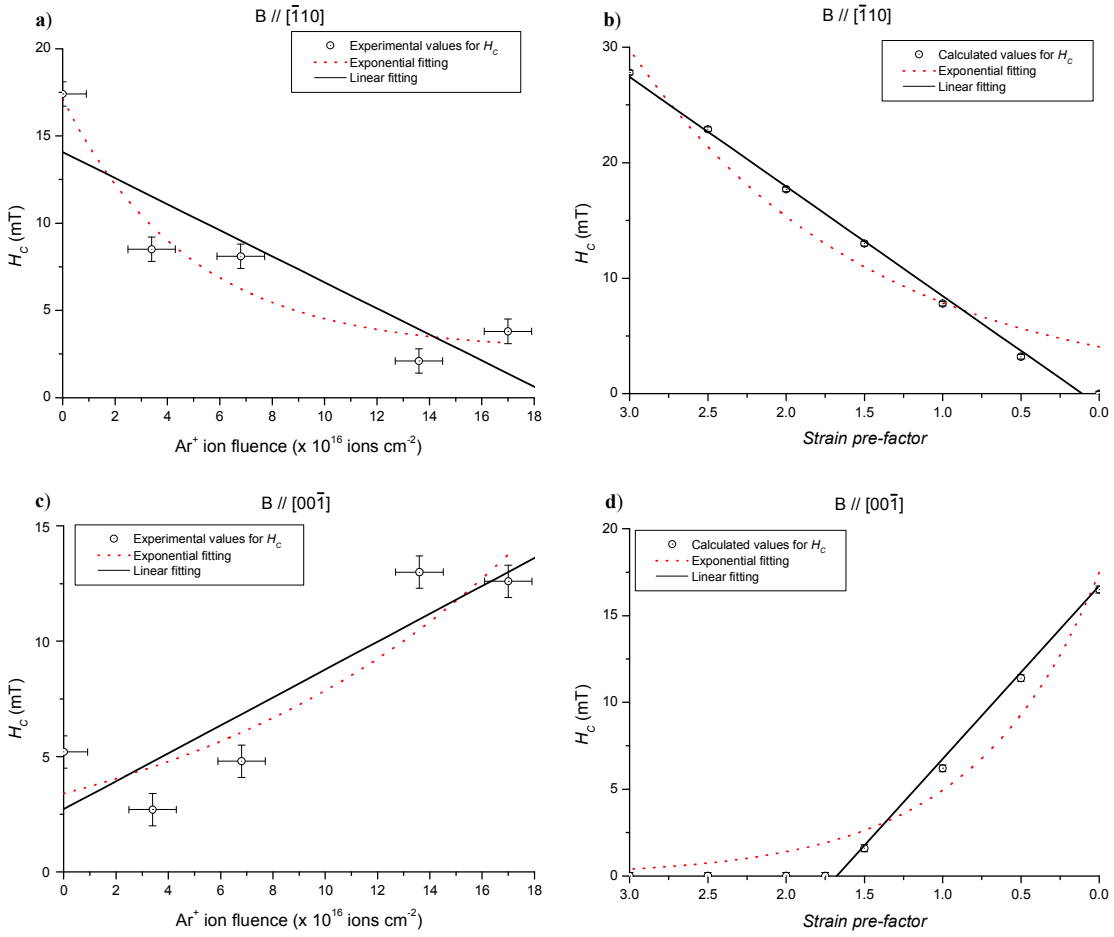

Figure 5.5: Graphs a) and c) show the 100 nm YFe_2 sample coercivity as a function of incident Ar^+ ion fluence from MOKE data. Graphs b) and d) show the coercivity as a function of strain pre-factor from OOMMF modelling data. Magnetic field applied in the direction indicated at the top of the graphs. Linear fits shown in black. Exponential fitting shown in dashed red, to act as a guide for the eye *only* (based upon conclusions drawn in Zhang *et al.* [146]), *not* as a fitting.

Work by Zhang *et al.* [146] on Ni films irradiated with Xe^+ and Ni^+ ions indicate an exponential decay in H_C with increasing ion fluence. Exponential fittings to the present experimental and theoretical data for the nominally 100 nm thick YFe_2 sample are shown as dashed red lines in Figure 5.5. Even considering the rather large error bars in the MOKE data, the experimental data cannot be fitted accurately to an exponential. It is clearly more linear (solid black lines). Similarly the OOMMF data shows a linear behaviour. It should be noted that in the case of Zhang *et al.* [146], they used a film which (in its un-implanted state) exhibited a uniaxial anisotropy and hence it was not possible to observe the systematic evolution between two distinctly different axes of magnetization, as is the case for this epitaxially grown Laves phase YFe_2 film. Florescu *et al.* [6] have implanted 40 keV Ar^+ ions into amorphous Tb_xFe_{1-x} ($0.18 \leq x \leq 0.27$) and find a similar exponential decrease in H_C. As far as the author is aware, this work

provides the first demonstration of a linear and thus more controllable change in H_C with varying fluence of incident ions.

The squareness of the hysteresis loop from the OOMMF data with the magnetic field applied along the $[\bar{1}10]$ direction is $\frac{M_R}{M_S} = 1.00$ for strain pre-factors of 3 and 2.5, reducing very gradually to 0.97 for strain pre-factors down to 0.5, before reducing abruptly to zero for lesser strain pre-factors. By contrast, along the $[00\bar{1}]$ direction $\frac{M_R}{M_S} = 0.00$ for strain pre-factors down to 1.75, before increasing rapidly to 0.95 with a strain pre-factor of 1.5. Subsequently this gradually increases to unity as the magnetoelastic energy is completely eliminated. These calculations are in good qualitative agreement with the MOKE results. This again suggests that for small ion fluences ($\lesssim 5 \times 10^{16}$ Ar^+ ions cm^{-2}) the only significant change in the YFe_2 sample is a gradual reduction in coercivity. A similar fact is evident for high ion fluences ($\gtrsim 10^{17}$ Ar^+ ions cm^{-2}) whereby the hysteresis loops remain essentially constant in shape, exhibiting only a small change in coercivity. Thus it can be concluded that the most significant changes to the strain within the sample occurs at an incident ion fluence in the range $(5 - 10) \times 10^{16}$ Ar^+ ions cm^{-2}. This corresponds to a strain pre-factor in the range 1.2 – 0.6, at the mid-point of which the two orthogonal axes possess approximately equal magnetic responses to an applied field (see graphs e) and f) in both Figure 5.4 and Figure 5.2).

5.1.4 VSM measurements of ion implanted YFe_2

The 100 nm YFe_2 sample was also characterized by room temperature vibrating sample magnetometry (VSM) both before and after ion implantation. These results are presented in Figure 5.6[i].

[i] A 100 nm thick YFe_2 sample, cut into a 5 × 5 mm piece has a volume of magnetic material equal to 2.5×10^{-6} cm^{-3}, equating to a total mass of YFe_2 of just 15 – 20 μg. Thus such a sample requires the room temperature VSM to be operated at the limit of its sensitivity (1 mT field step size and ~ 50 μemu magnetic moment), hence the rather high level of noise present.

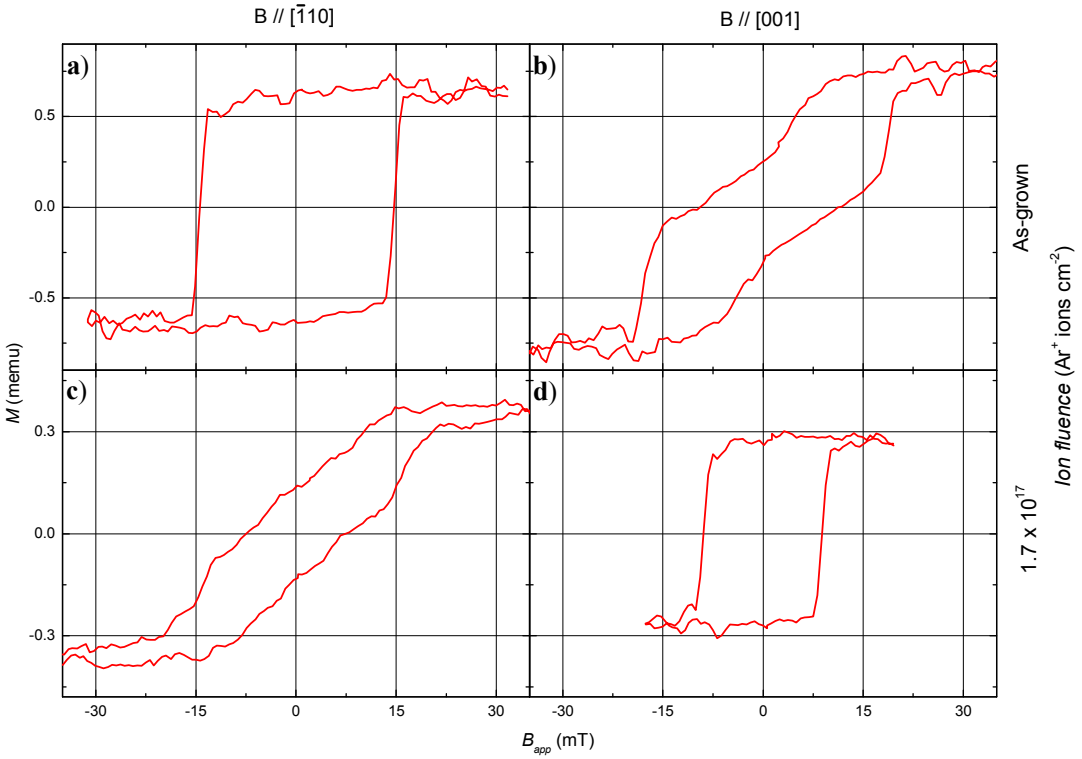

Figure 5.6: VSM hysteresis loops for a 100 nm YFe_2 sample measured with the applied magnetic field along the $[\bar{1}10]$ and $[00\bar{1}]$ directions in the as-grown state and after implantation by 1.7×10^{17} Ar^+ ions cm^{-2}. For graphs a) and d) the maximum applied magnetic field is clear. For graphs b) and c) the maximum applied field was increased to 100 mT to help ensure saturation.

The VSM data of the as-grown sample shown in Figure 5.6 (graphs a) & b)) show good agreement with both the MOKE data (Figure 5.2 graphs a) & b)) and the simulated OOMMF data (Figure 5.4 graphs a) & b)). After implantation by Ar^+ ions with a fluence of 1.7×10^{17} ions cm^{-2} the VSM data (Figure 5.6 graphs c) & d)) show a clear reorientation of the (close to) easy and hard axes of magnetization by approximately 90°, just as evidenced by the MOKE data and the OOMMF simulations. Conducting the same calculation for the ratio between the coercive fields for the two "square" hysteresis loops as that performed for the MOKE and OOMMF data above, gives a ratio of 1.56 from the VSM data (Figure 5.6 graphs a) & d)). Whilst not as exact an agreement as that between the MOKE and OOMMF data (1.38 and 1.40 respectively), it is still sufficient to reinforce the agreement between the two experimental characterization techniques and the computational modelling.

It is also very important to note the simple fact that the VSM data do indeed agree with the MOKE data. Whilst this may seem trivial, it is important to recall that VSM is a bulk sample characterization technique, whilst MOKE is surface sensitive, sampling

only the magnetic material within the skin depth of the sample (~ 21 nm in YFe_2). It has already been shown from SRIM calculations that the mean radial range for 3.25 keV Ar^+ ions is 4.5 nm, therefore with respect to a total film thickness of 100 nm this is very much a modification to the sample surface only. The fact that the VSM data show very good agreement with the MOKE data highlights the fact that the incident Ar^+ ions affect the entirety of this nominally 100 nm thick sample. This is due to the rapid and complete propagation of the defects created at the sample surface throughout the entire sample, due to the epitaxial growth of these films. This will be demonstrated via X-ray diffraction and discussed further in sections 5.1.5 and 5.1.7 respectively. It also further confirms the applicability of the OOMMF modelling, which used a 100 nm thick model sample, yielding results which are in good agreement with both the bulk technique of VSM and the surface sensitive technique of MOKE. OOMMF modelling with samples varying in thickness from 30 – 100 nm have been investigated and show no appreciable change in general shape, coercivity or magnetization.

After implantation by 1.7×10^{17} Ar^+ ions cm^{-2} (15 hours), some of the YFe_2 is sputtered away, but this is by no means the entire 100 nm film as may be expected using the ion milling rate calculations described in section 3.6.6 (and noted again in section 5.1.1). The rate of removal was shown to be approximately 0.26 nm min^{-1} for YFe_2 at 5 keV. At 3.25 keV this rate is reduced slightly; from SRIM calculations, the sputtering yield is reduced from 9.37 atoms ion^{-1} to 7.66 atoms ion^{-1} respectively. Accordingly the sputtering rate is reduced to 0.23 nm min^{-1}. 15 hours Ar^+ ion milling should therefore remove in excess of 200 nm of material, but this is not the case since clearly magnetic material remains. This is evidenced further by the fact that there is no apparent reduction in the MOKE signal amplitude between ion implantations of 10^{16} – 10^{17} Ar^+ ions cm^{-2} (Figure 5.2 graphs c) – j)). Thus, a film thickness at least equal to the skin depth must still exist, *i.e.* > 21 nm. However, the VSM data does show a reduction in signal amplitude, from $M_S \approx 0.78$ memu to $M_S \approx 0.33$ memu. This may be used to provide an estimate on the thickness of the magnetic material remaining, providing details of the actual sputtering rate of YFe_2. This is achieved using the method in the Appendix to derive

$$t = \frac{M_S a^3}{8 N \mu_B d_1 d_2} \tag{5.1}$$

M_S = 0.33 memu = 3.3×10^{-7} JT^{-1} from graph c) in Figure 5.6, and there are approximately $1.5\mu_B$ $f.u.^{-1}$ ($N\mu_B$) in YFe_2 [3] (f.u. = formula unit, see section 2.4.1).

Furthermore, a = 0.7362 nm [1] and $d_1 = d_2 = d$ = 5 mm. Hence $t_{ion\text{-}milled}$ = 47 nm[ii]. The thickness of the as-grown sample may be verified by taking $M_S = 7.5 \times 10^{-7}$ JT^{-1} from graph b) within Figure 5.6. This gives $t_{as\text{-}grown}$ = 108 nm, which is in good agreement with the known 100 nm sample thickness. Hence the incident 3.25 keV Ar^+ ions have removed approximately 50 nm of material, suggesting that the actual rate of removal is as little as ¼ of that expected. This will have implications in the Ar^+ ion fluences required to pattern these samples, as will become apparent in Chapter 6.

From these VSM data it is also possible to estimate the volume magnetization of the sample. In the as-grown state the sample volume is approximately 2.5×10^{-6} cm^3 and its saturation magnetization 0.8 memu. This gives a volume magnetization of 300 emu cm^{-3}. This is a good order of magnitude agreement with the OOMMF data in Figure 5.4 which shows a volume magnetization of 450 kAm^{-1} (1 emu cm^{-3} = 1 kAm^{-1}), considering OOMMF is essentially a zero-temperature model and thus only approximates quantitative values as highlighted earlier.

5.1.5 XRD analysis of an ion implanted YFe_2 film

The X-ray diffraction (XRD) data for a 100 nm YFe_2 sample is presented in Figure 5.7. The XRD data is for the as-grown sample (black), a sample implanted with 6.8×10^{16} Ar^+ ions cm^{-2} (red), 1.0×10^{17} Ar^+ ions cm^{-2} (green) and 1.7×10^{17} Ar^+ ions cm^{-2} (blue).

[ii] This is in agreement with the MOKE data which suggests that this sample is still thicker than its skin depth of 21 nm after being subjected to an incident Ar^+ ion fluence of 1.7×10^{17} ions cm^{-2}.

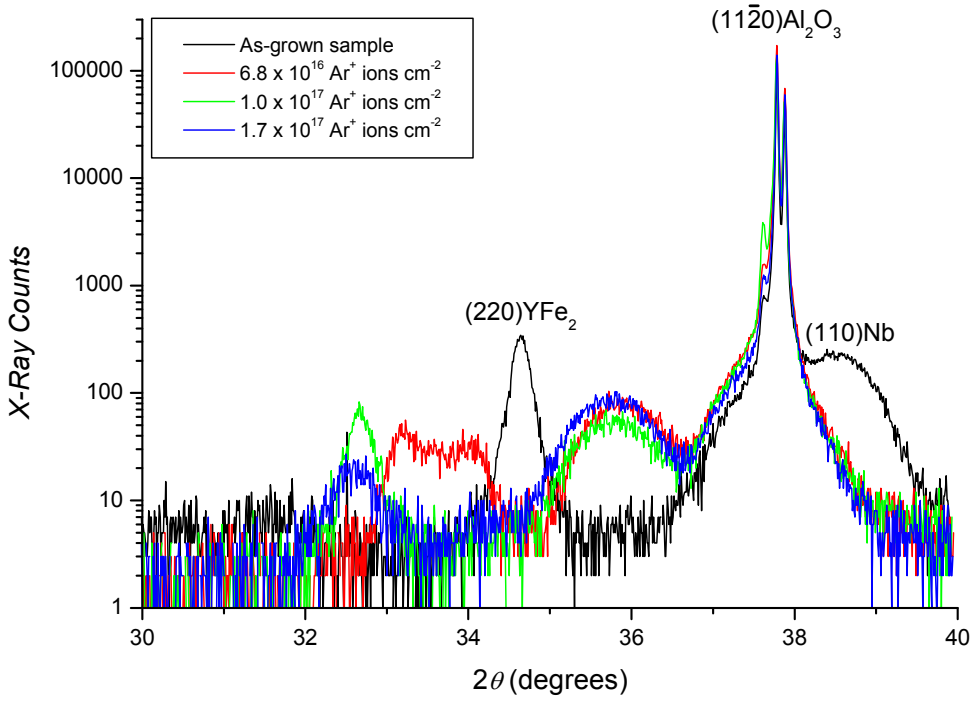

Figure 5.7: XRD data for a 100 nm YFe_2 sample showing the (220) reflection of the as-grown sample and other peaks after implantation by increasing Ar^+ ion fluences (see key).

In Figure 5.7 the data for the as-grown sample show a peak at 2θ = 34.64° corresponding to a lattice parameter of 0.7320 nm as detailed in section 5.1.1. The ion implanted data lack the broad peak centred around 38.5° corresponding to the Nb buffer layer. The reasoning behind this remains unknown, but it could be explained in one of two ways.

1. The incident Ar^+ ions have caused the Nb layer to become inter-mixed with the YFe_2 film, forming a different, very disrupted or irregular crystalline structure which corresponds to the broad peak in all of the ion implanted data centred around 35.8°.
2. The Nb lattice has expanded preferentially along the growth direction, resulting in the shift of the peak from 38.5° to 35.8°. This could be due to the absorption of H into the sample ("hydridging") [7, 8, 9]. Hydridging may be caused by the presence of a small amount of H_2O vapour during the Ar^+ ion implantation process, although it is more likely that the RE absorbs this due to its higher reactivity.

Clearly further work is required to provide a full understanding of the processes occurring here. This could take the form of more detailed XRD and transmission

electron microscopy studies of the sample. This would also probably help explain the new peak formed around 32.6° in the samples subjected to high Ar^+ ion fluences. The emergence of these peaks only at higher ion fluences is confirmed by the data for sample subjected to 6.8×10^{16} Ar^+ ions cm^{-2}, which exhibits a double-peak structure, part way between that corresponding to the YFe_2 in the as-grown XRD data and the peak at 32.6° in the heavily ion implanted data. The lattice parameter attributed to the right-most peak in this double-peak is 0.745 nm. It is possible that this corresponds to the emergence of a compressive stress in the film, *i.e.* the strain has been completely relaxed and the tensile forces begin to act in the opposite direction. Given that the thermal strain has been shown to be relaxed almost completely for incident Ar^+ ion fluences of order $5 \times 10^{16} - 1 \times 10^{17}$ Ar^+ ions cm^{-2}, it is reasonable to assume that this compressive stress is due to a different source. Once a critical incident Ar^+ ion fluence is reached there can be no further relaxation of the thermal strain. There is some evidence which suggests that the strain term can change sign after reaching this critical ion fluence. In the work by Zhang *et al.* [146] and Gupta *et al.* [10], this is evidenced by the formation of a compressive stress after further ion implantation in films that have already had their tensile stress relaxed to zero. This has been attributed to the accumulation of non-soluble noble gas atoms and radiation damage induced by the very high energy incident ions (~ 100 keV), plus the subsequent recoil collisions. Due to the large number of incident ions there should have been the formation of a significant number of Xe atoms but the authors do not detect this directly. Some of the Ar^+ ion implanted films studied in this thesis have been investigated by energy dispersive X-ray analysis (EDX, see section 3.3.7), but revealed no Ar content. At this point the reader is referred back to Figure 3.12 and the accompanying data of Table 3.2. From here it may be seen that the characteristic X-rays come from a depth of at least 200 nm into the sample. Therefore the detection of any Ar atoms which form in the sample due to ionization (roughly 13 % of the Ar^+ ions, see Table 5.1) is not expected to be possible using EDX, since the Ar^+ ions have an average range of just 4.5 nm. Therefore it is unsurprising that both this author, Zhang *et al.* [146] and Gupta *et al.* [10] note no atoms of the process gas in the EDX data[iii]. On a further note, both contraction and expansion

[iii] This author has calculated the range of 100 keV Xe^+ ions in, *e.g.* Ni in the case of Zhang *et al.* [146], to be less than 10 nm on average using `SRIM` modelling.

of the substrate have also previously been observed in the work by Terris *et al.* [140, 141], attributed to elastic collisions between the incident ions and the target material. It therefore remains reasonable to assume that the high Ar^+ ion fluences used in this work could be responsible for a further contraction of the crystalline lattice once the thermal strain has been fully relaxed.

Finally it should be noted that the amplitude of the Al_2O_3 peak is somewhat increased for the ion implanted sample. This is due simply to the removal of the Y and YFe_2 through sputtering (ion milling) of the sample, giving rise to a larger signal from the substrate. Also, given that the YFe_2 peak disappears, or is at least significantly shifted from its original position, confirms that the effects of Ar^+ ion implantation extend over ranges significantly greater than their implantation depth within these films (recall Table 5.1). If these effects were only present at the surface then the YFe_2 peak would remain present in the ion implanted sample's data at the original position

5.1.6 AFM characterization of an ion implanted YFe_2 film

Example AFM data for the 100 nm YFe_2 sample, in the as-grown state and after ion implantation with a fluence of 6.8×10^{16} Ar^+ ions cm^{-2} can be seen in Figure 5.8.

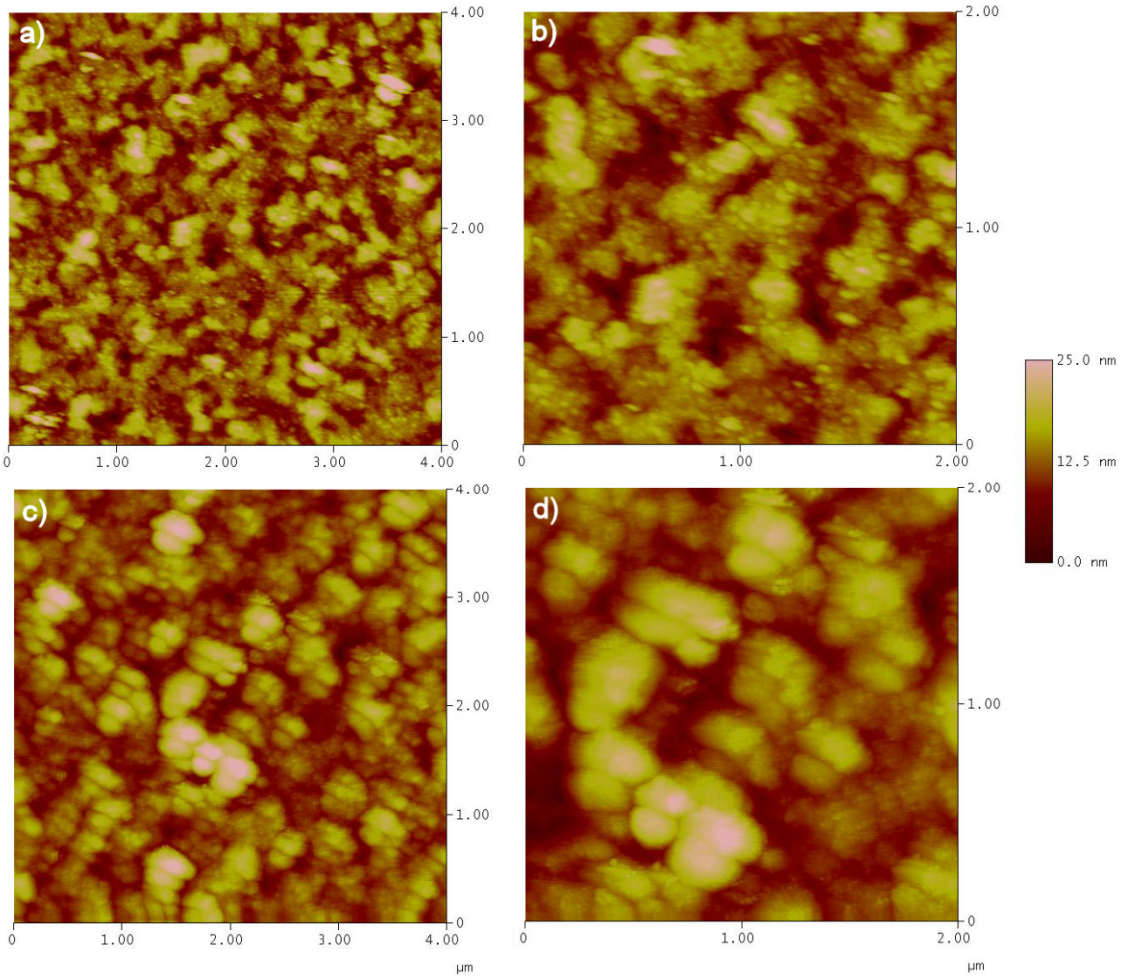

Figure 5.8: AFM micrographs of the 100 nm YFe_2 sample. The as-grown sample is represented in images a) and b) (increasing magnification, respectively) whilst that subjected to 1.0×10^{17} Ar^+ ions cm^{-2} is shown in images c) and d). The vertical (contrast) scales are maintained constant to act as a guide to the eye.

From simple comparison by eye, two salient features can be identified from Figure 5.8. One, the as-grown and ion implanted samples exhibit an approximately equal level of surface roughness, and two, the ion implanted sample shows a reduction in the number of islands. Numerical analysis of these data using the software provided with the *Veeco Multimode* SPM confirms that the film roughness remains approximately constant throughout the ion implantation process[iv], with a mean value of 3.1 ± 0.2 nm. The average grain height is slightly reduced from 5.8 to 5.1 nm, while the average grain size is increased significantly from 4,200 ± 200 nm^2 to 10,700 ± 200 nm^2. This general smoothing of the sample surface is due to ion milling. It is safe to assume that there

[iv] AFM topography data have been acquired for each step / break in the ion implantation process for the 100 nm YFe_2 sample, example data are presented here.

will be a loss of the smaller surface features in favour of fewer, larger grains. This occurs because the smaller features are affected by ion milling to a greater extent due to their larger surface area to volume ratio. It is however important to note that ion milling has removed a significant proportion of the YFe_2 sample (see section 5.1.4), possibly exposing a region of the surface which was partially dominated by the island growth mechanism. Of course, this would be more apparent at reduced sample thicknesses (recall section 3.2). The thickness of the remaining material was estimated from the VSM measurements of 5.1.4 to be just under 50 nm which is indeed approaching the regime whereby island growth is dominant [11]. There is, however, no clear evidence that in the present YFe_2 sample that ion milling causes smoothing of the sample surface, rather if only favours the formation of larger islands. This is in contrast with work reported elsewhere [12, 13] which suggests ion milling causes smoothing of the sample surface.

5.1.7 Discussion of and conclusions for an ion implanted YFe_2 sample

It is well known that the MBE grown $REFe_2$ Laves phase thin film samples experience an in-plane stress due to differential thermal contraction during sample cool-down after growth. This was described in section 3.2 to be a shear, described by $\varepsilon_{xy} = -0.5\%$. This structural change has been experimentally confirmed using both XRD and neutron diffraction [1]. For the YFe_2 sample, a –0.4% lattice contraction in the film growth direction and a 0.6% lattice expansion perpendicular to this (in the plane of the film) is expected to conserve volume. The author's measurements of the 100 nm YFe_2 sample were obtained using a standard XRD arrangement, which permits measurement of the lattice parameter in the growth direction ($a_\perp$) only. From the data of Figure 5.1, a lattice parameter of $a_\perp$ = 0.7320 nm is found, which is *smaller* than the bulk value of $a_{\perp b}$ = 0.7362 nm, *i.e.* there is a contraction in the film growth direction of –0.6%. This is in reasonable agreement with previous reports [1]. The observed increase in $a_\perp$ after ion implantation towards and beyond that of the bulk film, corresponds to a significant reduction in the strain of the film. This strain gives rise to ε_{xy} (the shear present in the film), which the reader will recall as the dominant term responsible for the magnetoelastic anisotropy energy (E_{ME}) in equation (2.35), so clearly any alterations to this strain will have important consequences for the magnetic properties of the sample.

In thin film $REFe_2$ Laves phase epitaxial samples the contribution from E_{ME} to the total magnetic energy always dominates over that of the magnetocrystalline anisotropy

energy term (E_{MC}) at room temperature [2]. Accordingly, the easy axis of magnetization is determined primarily by the direction that minimizes E_{ME}. For YFe_2 samples this is expected to be in the equivalent ⟨221⟩ directions [2], all of which lie approximately 15° out of the plane of the sample. During the reversal of the sample magnetization this out of plane component tends to be pushed into the plane of the sample before the entire sample magnetization direction is reversed. This is characterized by a curvature to the hysteresis loops which are measured with the magnetic field applied in a direction close to this. Whilst this is experimentally verified for $DyFe_2$ samples (see ref. [14] and section 5.2), this is not the case for the present YFe_2 samples which show a perfectly square hysteresis loop when characterized by MOKE, VSM and OOMMF, suggesting that the magnetization tends to lie in a direction very close to the plane of the sample.

SRIM modelling has been used to confirm that the Ar^+ ions incident on a 100 nm YFe_2 sample with a 10 nm Y protective cap are stopped fully within the metallic structure, never reaching the buffer or seed layers or the Al_2O_3 substrate. Therefore the majority of the Ar^+ ions energy is lost via elastic collisions within the YFe_2 layer (once the Y cap is sputtered away). As discussed in section 2.8.3 the large amount of energy deposited results in many collisions between the incident energetic Ar^+ ion and atoms within the crystalline target material, causing the target atoms to recoil. It is therefore logical to assume that the incident Ar^+ ions cause the atoms in the Laves phase sample (predominantly the Y atoms as these form the "corners" of the unit cell (see Figure 2.7)) to experience a recoil and subsequently relax back into their un-strained lattice sites. Due to the epitaxial structure of these samples this effect is expected to rapidly propagate throughout distances within the sample far greater than the Ar^+ ions penetrate since many layers of the crystalline structure are intimately linked by the same recurring structure. Further work is required to confirm this mechanism of relaxation propagation.

In summary, from the four independent sets of data (MOKE, VSM, OOMMF and XRD) it is clear that implantation by a critical ion fluence of between approximately 5×10^{16} and 1×10^{17} Ar^+ ions cm^{-2} causes a rotation by 90° of the easy and hard axes of magnetization in a strained, epitaxially grown 100 nm thick YFe_2 film. This is a bulk effect as evidenced by the OOMMF, VSM and XRD data which is attributed to the epitaxial structure of these films. The rotation of the easy and hard axes is attributed to

implanted Ar^+ ions causing dislocations and recoils within the crystalline lattice, relaxing the shear strain within the sample. This is the first report that shows, contrary to previous investigations [2], that there is a significant contribution from the magnetoelastic anisotropy energy within an epitaxially grown YFe_2 thin film sample. It is worthwhile noting that the magnetoelastic anisotropy usually originates from second-order crystal field terms associated with the RE ion (technically, Y ≠ RE), induced by the most prominent strain term, ε_{xy}. These results tentatively suggest that there could be a significant magnetoelastic anisotropy energy associated with the 4d electrons in the Y atoms, but clearly this warrants more specialised experimental procedures for full clarification. The magnetoelastic anisotropy, whatever its origin, has been shown to be reliably and accurately controlled by the implantation of Ar^+ ions, which themselves have been shown by AFM to effect little change on the sample morphology.

5.2 Ar^+ Ion Implantation in $DyFe_2$ Films

In this section the effects of implanting Ar^+ ions into an epitaxially grown $DyFe_2$ Laves phase film are discussed. The section is arranged in the same general order as that for the YFe_2 sample. To avoid repetition, the work discussed here is not as exhaustive as that for the YFe_2 sample in section 5.1.

5.2.1 Experimental procedure

The sample investigated here is an MBE grown $DyFe_2$ laves phase film with a thickness of 400 nm. Since the growth procedure of this sample is identical to that of the YFe_2 sample in section 5.1, it is also subject to shear-strain. The lattice parameter of the 400 nm $DyFe_2$ film in the growth direction (along (110)) determined from XRD (Figure 5.9) is found to be 0.7284 nm. This is 0.5% smaller than the bulk value of 0.7324 nm [1]. Thus there is a – 0.5% contraction in the direction perpendicular to the plane of the film, very similar to that found for the YFe_2 sample.

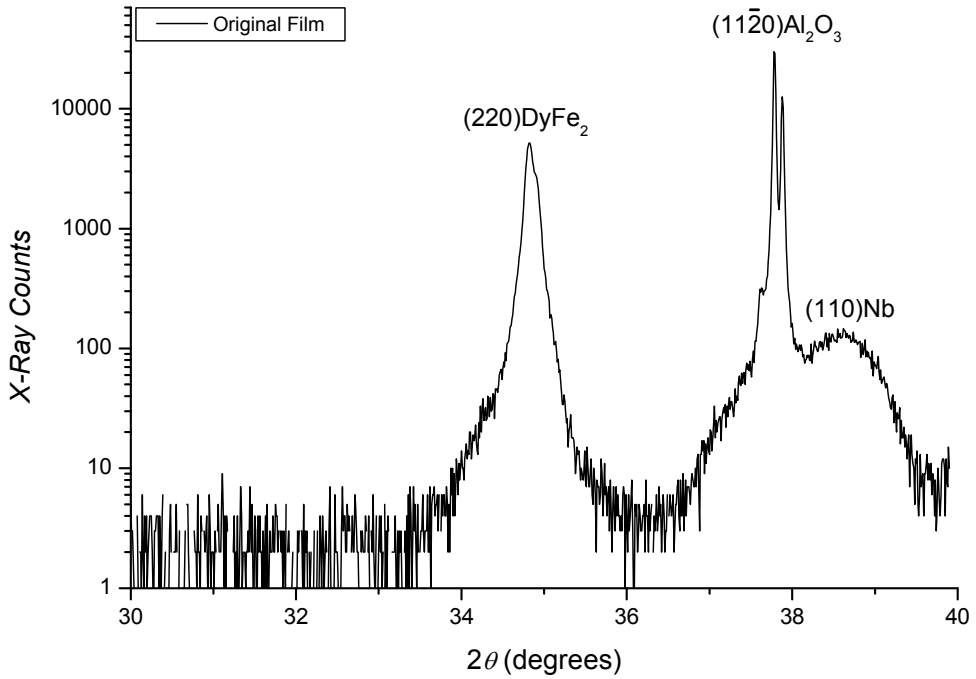

Figure 5.9: XRD data for the as-grown 400 nm $DyFe_2$ sample. Note that the $DyFe_2$ peak is greater in magnitude than the YFe_2 peak in Figure 5.1. This is due to the increased thickness of the $DyFe_2$ film.

The $DyFe_2$ sample was cut into roughly 5 × 5 mm pieces, with each piece exposed to increasing Ar^+ ion fluences. MOKE was used to analyse the magnetic behaviour of the sample both before and after ion implantation. The Ar^+ ion fluences used were 3.4×10^{16}, 6.8×10^{16}, 1.0×10^{17}, 1.3×10^{17} and 1.7×10^{17} ions cm^{-2}. The MOKE results are presented in section 5.2.2, which, along with sections 5.2.3 to 5.2.7 (OOMMF modelling, VSM measurements, XRD characterization and both AFM and He^+ ion microscopy visualization of the sample), provide a complete picture for these ion implanted samples. Finally, further discussion and conclusions are presented in section 5.2.8.

First, SRIM modelling data can be seen in Table 5.2 for the 400 nm $DyFe_2$ sample and its protective Y capping layer. Once again, the predominant energy loss mechanism of Ar^+ ions within the sample is via low energy recoiling target atoms. Correspondingly, there are an associated small number of crystalline lattice vacancies formed. The radial range of Ar^+ ions within the $DyFe_2$ is slightly less than that in YFe_2 (Table 5.1) due its greater density.

Incident Ar^+ ion:		$DyFe_2$	Y
Radial range (± 0.2 nm)		4.1	7.5
Energy loss to: (± 0.1%)	ionization (ions / recoils)	13.1 / 22.1	16.8 / 15.4
	vacancies (ions / recoils)	1.1 / 5.2	1.1 / 4.6
	phonons (ions / recoils)	4.5 / 54.0	4.4 / 57.7
Sputtering yield (± 0.1 atoms ion^{-1})		7.6	4.6

Table 5.2: SRIM data calculated for 10,000 3.25 keV Ar^+ ions incident at an angle of 68° on a 400 nm $DyFe_2$ sample with a 10 nm Y cap

As before, the data acquired throughout this section was achieved with the magnetic field applied along the $[\bar{1}10]$ and $[00\bar{1}]$ directions, corresponding to the (in-plane) easy and hard axes of magnetization for the $DyFe_2$ sample. As mentioned in section 4.1, the strained film exhibits an out of plane component of magnetization due to the contribution from the magnetoelastic anisotropy energy. This causes the easy axis of magnetization to make an angle of approximately 15° out of the plane, close to the $[\bar{3}50]$ or $[\bar{5}30]$ directions [14].

5.2.2 MOKE measurements of ion implanted $DyFe_2$

As noted in section 5.1.2, the protective Y cap will be sputtered away after a relatively low incident Ar^+ ion fluence of 6×10^{15} ions cm^{-2}. Thus the amplitude of the MOKE signal increases when comparison is made between the Ar^+ ion implanted samples and the as-grown sample. The data in Figure 5.10 is for incident ion fluences up to 1.3×10^{17} Ar^+ ions cm^{-2}.

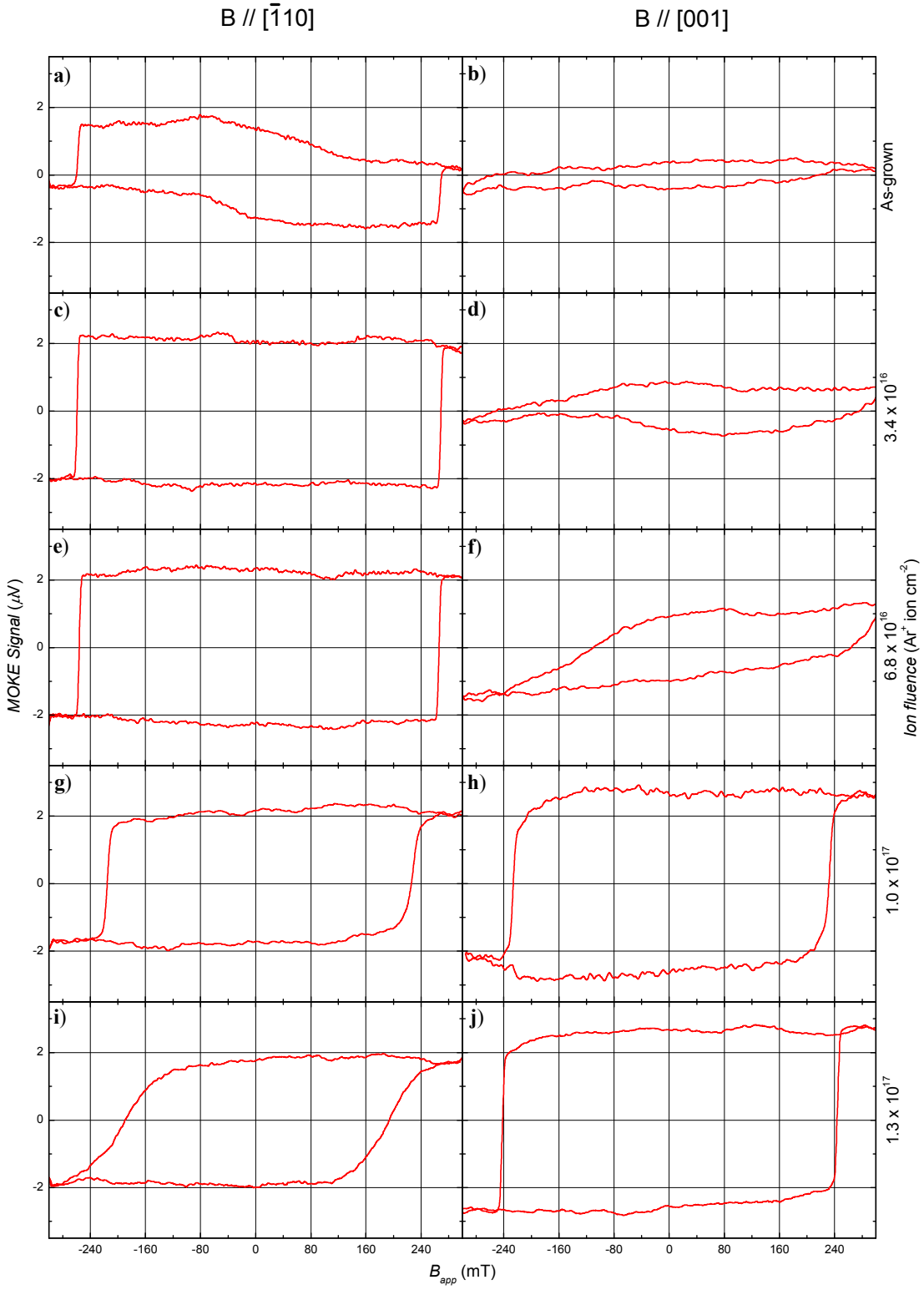

Figure 5.10: MOKE hysteresis loops of a 400 nm $DyFe_2$ sample before and after ion implantations of increasing fluences (see right-hand axis) for the applied magnetic field along the $[\bar{1}10]$ and $[00\bar{1}]$ directions. Note that the $[00\bar{1}]$ data is essentially meaningless for graphs b), d) & f) since the maximum applied field ($\mathbf{B}_{app}$) from the MOKE apparatus is insufficient to reverse the magnetization of this sample. Once a sufficiently high ion fluence of ~ 10^{17} Ar^+ ions cm^{-2} is reached is it possible to reverse the magnetization of the sample with $\mathbf{B}_{app}$ along the $[00\bar{1}]$ direction.

These MOKE hysteresis loops for the 400 nm $DyFe_2$ sample show a pronounced transformation in magnetic behaviour, dependent on the incident Ar^+ ion fluence. The data for the as-grown sample, magnetized along the in-plane easy axis direction of $[\bar{1}10]$ (graph a) in Figure 5.10) shows two distinctly different regions of magnetization reversal, warranting further discussion. An enlarged, annotated diagram showing the direction of the magnetization reversal process is presented in Figure 5.11.

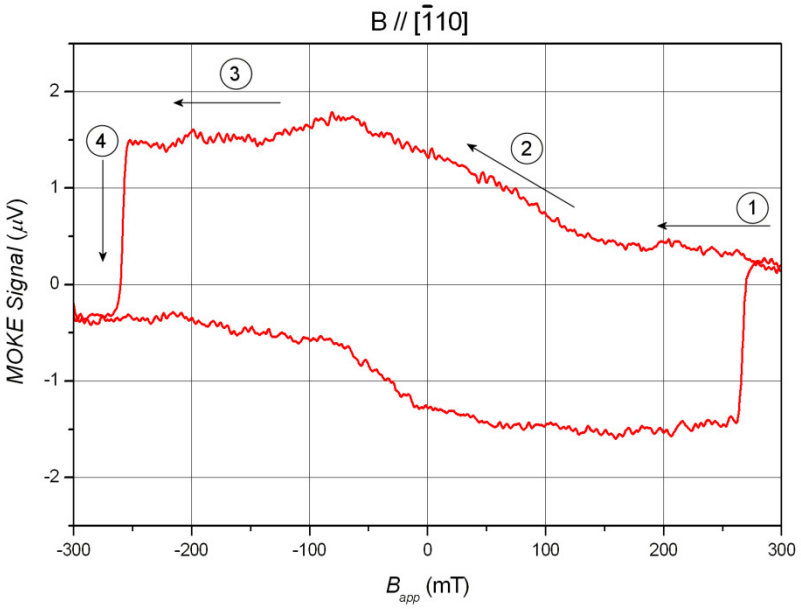

Figure 5.11: MOKE Hysteresis loop of a 400 nm $DyFe_2$ sample magnetized along the $[\bar{1}10]$ direction.

As the sample magnetization is reduced from positive saturation (point 1, Figure 5.11), the magnetization remains relatively constant until $\mathbf{B}_{app} \approx 150$ mT is reached. Here, and through to $\mathbf{B}_{app} \approx -100$ mT, the rate of change of magnetization remains relatively constant (through point 2). In this region, the rate of change of magnetization is *greatest* and has a non-zero magnitude as $\mathbf{B}_{app}$ is swept through zero, thus is *not* indicative of the underlying cubic anisotropy of the system present in the YFe_2 sample (Figure 5.3). A detailed explanation for this phenomenon is not forthcoming, but it could be due an admix of both longitudinal and polar MOKE components (see experimental arrangement in section 3.10, noting how Figure 3.27 has both longitudinal and polar components from Figure 3.26). As the out of plane component of the sample magnetization begins to point into the sample plane, this increases the amplitude of the MOKE signal since polar MOKE is generally a more sensitive technique. In the region of $-265 \lesssim \mathbf{B}_{app} \lesssim -100$ mT (point 3) the magnetization again remains relatively

constant, until, at point 4, an abrupt switch at $\mathbf{B}_{app} \approx -265$ mT occurs. This rotation of the sample magnetization is irreversible and the magnitude at which it occurs is in good quantitative agreement with VSM measurements [14].

When the as-grown sample is subject to a magnetic field applied along a hard $[00\bar{1}]$ direction (graph b), Figure 5.10), the maximum attainable field from the electromagnets in the MOKE apparatus (~ 350 mT) is insufficient to cause the complete reversal of the sample's magnetization. This is characterized by relatively flat hysteresis "loops" as presented in graphs b), d) and e) within Figure 5.10, where no reversal of the sample magnetization is apparent. With reference to Figure 2.11, the same sample has been characterized by VSM under an applied magnetic field of 12 T. The value of the saturation magnetization when $\mathbf{B}_{app}$ is along the $[00\bar{1}]$ direction was found to be ~1 T at room temperature; clearly well above that attainable in the MOKE set-up.

The coercive field of the 400 nm $DyFe_2$ sample magnetized along the $[\bar{1}10]$ direction remains almost constant at $H_C = 265 \pm 2$ mT for incident Ar^+ ion fluences up to 1.0×10^{17} ions cm^{-2} (graphs a), c) and e) in Figure 5.10), but the gradual change in sample magnetization as the applied field is swept through zero is lacking from all graphs except a). This strongly suggests that the out of plane component of the magnetization in the $DyFe_2$ sample is quickly removed by ion implantation with a fluence of just 3.4×10^{16} Ar^+ ions cm^{-2}. Further to this, above an Ar^+ ion fluence of 1.0×10^{17} ions cm^{-2}, the coercive field of the sample (when measured along the easy axis ($[\bar{1}10]$ direction)) begins to steadily decrease and the magnetization reversal becomes less abrupt (Figure 5.10, graph g)). As the incident Ar^+ ion fluence is increased further (graph i)), the field required to saturate the sample magnetization begins to gradually increase. Clearly the magnetic anisotropic properties of the Ar^+ ion implanted sample have been altered to become more like a hard axis response; a significant departure from its as-grown easy axis behaviour. This change is most likely due to a reduction in the magnetoelastic anisotropy, in a rather similar way to that experienced in the YFe_2 sample.

When the magnetic field is applied along the as-grown sample's hard axis of magnetization ($[00\bar{1}]$ direction) the magnetic properties are once again dependent on the fluence of incident Ar^+ ions. When the Ar^+ ion fluence reaches a value of 1.0×10^{17} ions cm^{-2}, the applied magnetic field is sufficient to completely reverse the sample's

magnetization. This is depicted clearly by the stark contrast between graphs b), d) and f) to graph h) within Figure 5.10. This behaviour becomes more pronounced when the Ar^+ ion fluence is increased still further to 1.3×10^{17} ions cm^{-2} (graph j)). Here the hysteresis loop is very square, showing characteristics associated with an easy axis of magnetization in a $DyFe_2$ film.

Above a critical fluence of approximately 1×10^{17} Ar^+ ions cm^{-2} (the same value as noted in section 5.1.7 for the YFe_2 sample), the directional response, *i.e.* the easy and hard magnetic axes, begin to rotate away from their directions associated with the as-grown sample, towards directions more commonly associated with those in a bulk, un-strained $DyFe_2$ sample. The physical reasoning behind this is much the same as for the YFe_2 sample studied in section 5.1 that is a reduction in strain within the crystalline structure. This serves to reduce the magnetoelastic anisotropy and is due to the implantation of Ar^+ ions and the subsequent formation of dislocations and recoil atoms. This conclusion will be corroborated in the following sections.

5.2.3 OOMMF modelling of $DyFe_2$

When modelling a 400 nm $DyFe_2$ sample using `OOMMF`, various "strain pre-factors" (scaling factors which determine the dominance of the magnetoelastic energy) are used to model the response of the $DyFe_2$ film to Ar^+ ion implantation. Significant changes in the sample's simulated behaviour are apparent. For the $DyFe_2$ strained film the dependence of the easy axis direction on magnetoelastic anisotropy has been well documented [2, 14, 15]. The calculated magnetization curves can be seen in Figure 5.12 graphs a) – j) for the magnetic field applied along the $[\bar{1}10]$ (as-grown easy axis) and $[00\bar{1}]$ (as-grown hard axis) directions. Recall that the `OOMMF` modelling employed here is essentially an adaptation to a zero temperature model. It should be noted that `OOMMF` also does not consider the small out of plane component of magnetization already observed experimentally in $DyFe_2$. Thus, considering these two factors, it is unlikely that `OOMMF` modelling will give exactly quantitative agreement with experimental data.

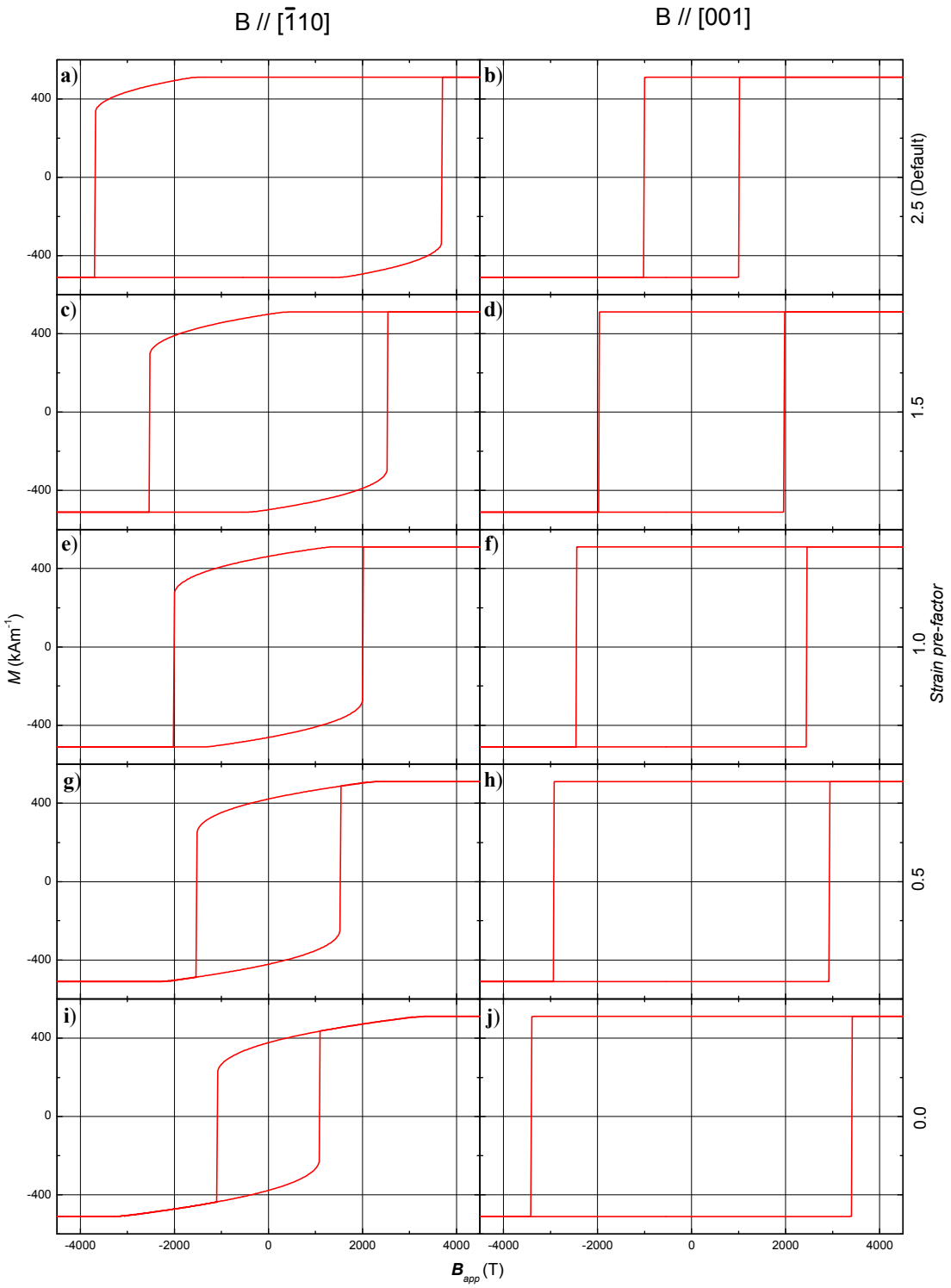

Figure 5.12: Hysteresis loops created from OOMMF data with the applied magnetic field directed along the $[\bar{1}10]$ and $[00\bar{1}]$ directions for a 400 nm $DyFe_2$ sample. These data are taken whilst systematically reducing the factor multiplying the strain term used to generate the magnetoelastic energy in the model for the calculation of magnetization (M) as a function of applied field ($\mathbf{B}_{app}$) (detailed on the right-hand axis).

The data in Figure 5.12 show a clear progression of the magnetic behaviour of the $DyFe_2$ sample as the magnetoelastic anisotropy contribution to the total energy of the system is gradually reduced, from the default strain pre-factor value of 2.5 (graphs a) and b)) down to a system corresponding to magnetostatic and magnetocrystalline anisotropies only (graphs g) & h)). On comparing the $[\bar{1}10]$ data from this figure and the experimental results from MOKE (Figure 5.10) there is moderate agreement between theory and experiment. Both sets of data clearly show a reduction in coercivity and a progressive increase in the curvature to the hysteresis loop before the sample magnetization is reversed. This can be attributed to an evolution from an easy axis of magnetization (graphs a) in both Figure 5.10 and Figure 5.12) towards that of a hard axis. This is illustrated more predominantly in the OOMMF simulation data than the MOKE hysteresis loop (compare graphs i) in both Figure 5.10 and Figure 5.12). So it is logical to assume that a total elimination of the sample's magnetoelastic anisotropy by ion implantation has yet to be reached after an incident Ar^+ ion fluence of 1.3×10^{17} ions cm^{-2}. Thus it is more useful to compare this MOKE data with OOMMF simulated data corresponding to diminished, rather than totally eliminated magnetoelastic anisotropy, *e.g.* Figure 5.12 graph e). This is probably due to the utilisation of a much thicker sample, thus the effect of ion implantation, whilst strong and relatively long-range due to the epitaxial growth to the sample, is not dominant throughout the entire volume. In parallel with the steady decrease in H_C present for the simulated data with the magnetic field applied along the $[\bar{1}10]$ direction, there is a steady increase in H_C with the field perpendicular to this. This is the same behaviour to that evidenced in the case of OOMMF modelling of the YFe_2 sample, which was also attributed to a reduction in the dominance of magnetoelastic anisotropy within the sample.

The simulations for the magnetic field applied along the $[\bar{1}10]$ and $[00\bar{1}]$ axis possess the same value of coercive field when the strain pre-factor is set to a value between 1.20 and 1.25. Assuming a roughly linear relationship between the OOMMF model's strain pre-factor and incident ion fluence (and assuming that the standard strain pre-factor of 2.5 corresponds to the as-grown, strained sample), a strain pre-factor of between 1.20 and 1.25 corresponds to an incident Ar^+ ion fluence of $1.0 - 1.1 \times 10^{17}$ ions cm^{-2}. Whilst this is only a rough assumption, it is in good agreement with the experimental MOKE results shown in graphs g) and h) within Figure 5.10, whereby an incident Ar^+ ion fluence of 1.0×10^{17} ions cm^{-2} gives rise to a sample which appears to

have very similar magnetization curves irrespective of the direction of applied magnetic field. This is close to the value of incident Ar^+ ion fluence that was responsible for creating either a uniaxial anisotropy or competing cubic anisotropies within the YFe_2 sample.

In section 5.1.3, excellent agreement was found between the ratio of the coercive fields for the as-grown YFe_2 sample magnetized along the $[\bar{1}10]$ direction, to the Ar^+ ion implanted YFe_2 sample magnetized along the $[00\bar{1}]$ direction, between the MOKE and OOMMF data. The same comparison, when conducted on the present $DyFe_2$ sample subject to a similar Ar^+ ion fluence, gives a ratio of 1.09 for the MOKE data and 1.08 for the OOMMF data (graphs a) and j) within both Figure 5.10 and Figure 5.12). This excellent agreement further reinforces the reliability of the OOMMF modelling, reiterating the notion that implanted Ar^+ ions are significantly altering the sample's magnetoelastic anisotropy.

5.2.4 VSM measurements of ion implanted $DyFe_2$

The 400 nm $DyFe_2$ sample was characterized by room temperature vibrating sample magnetometry, both before and after ion implantation (see Figure 5.13). Note that these VSM data, taken after ion implantation, are for a slightly increased fluence than the MOKE results presented in section 5.2.2. However, the benefit of this is that these data are thus directly comparable to the previous VSM data for the 100 nm YFe_2 sample in section 5.1.4.

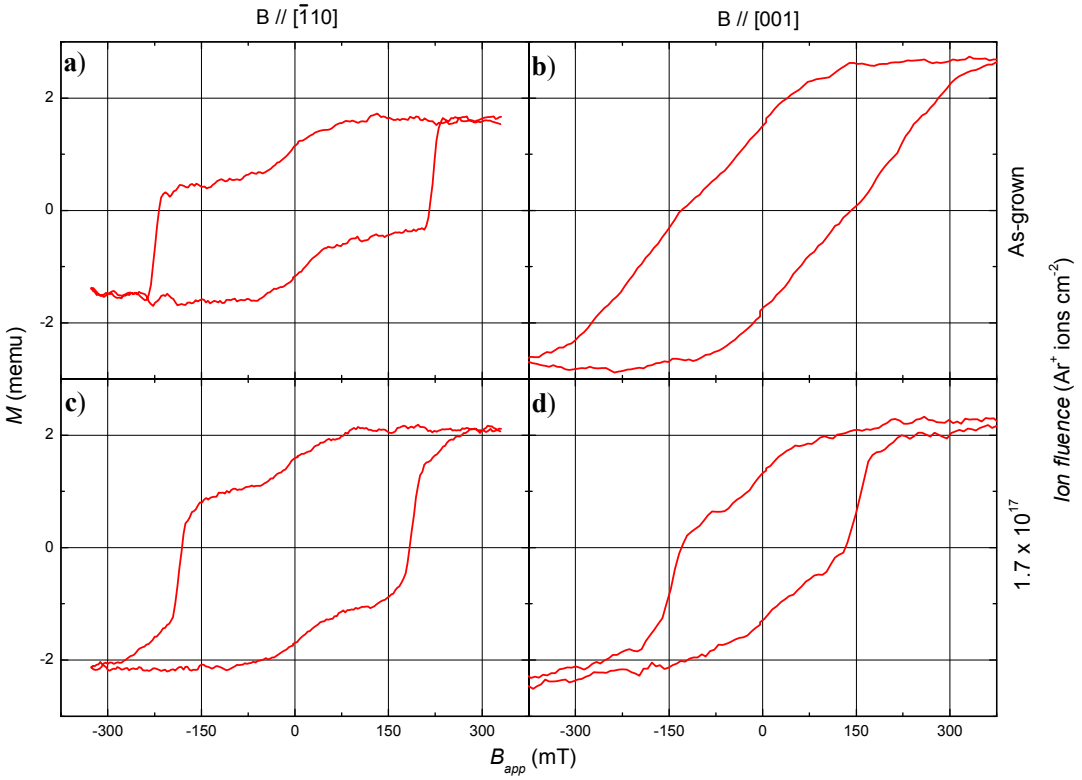

Figure 5.13: VSM hysteresis loops for a 400 nm $DyFe_2$ sample, measured with the applied magnetic field along the [$\bar{1}$10] and [00$\bar{1}$] directions in the as-grown state and after implantation by 1.7 × 10^{17} Ar^+ ions cm^{-2} (see right-hand axis). The maximum applied fields are shown for the [$\bar{1}$10] direction and were 1.0 T for the [00$\bar{1}$] direction.

When characterized by VSM, the 400 nm $DyFe_2$ sample, in its as-grown state, shows the hysteretic behaviour expected[v]. The general shape of graph a), taken with the applied magnetic field along the easy [$\bar{1}$10] direction, is qualitatively in good agreement with the same measurement obtained using MOKE (graph a) in Figure 5.10). However, the measurement made with the magnetic field applied along the hard axis ([00$\bar{1}$] direction), reinforces the inability of the electromagnet in the MOKE apparatus to fully reverse the magnetization of this sample, since it can clearly be seen from graph b) that the saturation magnetization is $\gtrsim$ 350 mT; the maximum field that can be reached in the MOKE apparatus.

[v] When compared to the measurement made using a 12 T superconducting magnet VSM (Figure 2.12) the out of plane component along the sample's easy axis is more evident in Figure 5.13. This is attributed to the data above not reaching full saturation of the sample magnetization whereas that in Figure 2.12 was taken with an applied magnetic field of ± 12 T thereby guaranteeing saturation.

The VSM measurements made for the sample implanted with 1.7×10^{17} Ar^{+} ions cm^{-2} (graphs c) & d)) again show a clear difference when compared to the as-grown sample. However, the reorientation of the two respective axes by 90°, corresponding to the complete removal of the strain within the sample due to ion implantation is not evident, reinforcing the assumptions made in section 5.1.3 when relating the OOMMF strain pre-factor to incident Ar^{+} ion fluence. There is, however, clear evidence of a partial reorientation of the magnetic axes, corresponding to a notable reduction in magnetoelastic anisotropy. This causes the easy and hard axes of magnetization to rotate partially towards the directions expected in a bulk, rather than epitaxially strained sample. These partial reorientations are highlighted when two sets of data, for an as-grown and ion implanted sample, with the applied magnetic field rotated by 90° with respect to each other are superimposed, *i.e.* direct comparison is made between graphs a) & d) and b) & c) from Figure 5.13. These comparisons can be seen in Figure 5.14. Note that the data have been normalized to permit simpler comparison.

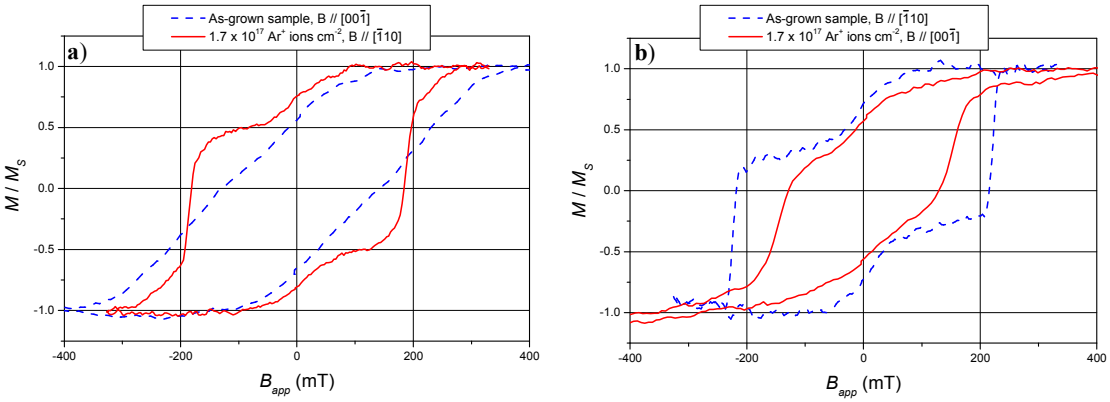

Figure 5.14: Normalized VSM data, whereby the red data represents the sample implanted with 1.7×10^{17} Ar^{+} ions cm^{-2}, whilst the dashed blue represents the as-grown sample. In graph a), direct comparison between the as-grown sample measured with the applied magnetic field along the $[00\bar{1}]$ direction and the Ar^{+} ion implanted sample with the field applied along the $[\bar{1}10]$ direction is made. The reverse arrangement is presented in Graph b) (see keys). These data illustrate the *partial* reorientation of easy and hard axes of magnetization in the ion implanted $DyFe_2$ sample.

From Figure 5.14 the *partial* reorientation of the easy and hard axes of magnetization is clear. Unlike in Figure 5.6 for the much thinner and magnetically softer YFe_2 sample, the ion implanted $DyFe_2$ sample data (red hysteresis loops) shows unambiguously the components of both easy *and* hard axis magnetization. When the ion implanted $DyFe_2$ sample is subject to a magnetic field applied along the $[\bar{1}10]$ direction (red data, graph a)) it exhibits a further characteristic over the as-grown sample subject to the same field (dashed blue data, graph b)). There is a clear emergence of an additional component to

the magnetization reversal behaviour between field ranges of ±195 to ±300 mT, corresponding very closely to the data for the as-grown sample with the field applied in the perpendicular direction (dashed blue data, graph a)). Similar conclusions can be drawn from graph b). The ion implanted sample (red data), instead of showing a completely slanted hysteresis loop as would be expected, exhibits "kinks" at roughly ± 50 mT, corresponding closely to the hysteresis loop for the as-grown sample in a magnetic field oriented perpendicular to this (dashed blue data). This further confirms the notion that there is only a *partial* relaxation of the strain within the $DyFe_2$ film for this incident ion fluence. In both sets of data there is clear evidence for a competition between the magnetoelastic *and* magnetocrystalline anisotropies as the dominant energy form. This is unmistakably shown by the ion implanted hysteresis loops (red data) showing components of both hard and easy axes of magnetization. Rather than a complete reorientation of the magnetic axes by 90° as evidenced in the thinner YFe_2 sample (section 5.1), the effect present in the thicker $DyFe_2$ sample can be analogously thought of as a rotation by approximately 45°.

Once again it is important not to overlook the significance of the simple fact that the VSM results show considerable differences between the as-grown and the ion implanted sample. From Table 5.2 the average radial range of an Ar^+ ion within the $DyFe_2$ sample can be seen to be just 4.1 nm. This fact, combined with the lack of recoil events (see section 2.8.3) confirms that the ion implantation is indeed very localized. Given that only the top 1% of the 400 nm sample is actually implanted with Ar^+ ions, the significant differences in the VSM data between the as-grown and ion implanted samples serves as further strong evidence for the propagation of ion-induced dislocations throughout a large fraction of the epitaxial sample's crystalline structure. It is also necessary to note that since the $DyFe_2$ sample possesses a much larger intrinsic anisotropy than the YFe_2 sample [2], the effects of ion implantation by a fixed fluence in the $DyFe_2$ sample will be less pronounced than those in the YFe_2 sample.

Finally, it is again possible to use the VSM data to make an estimate towards the ion-implanted sample's thickness, providing an estimate on the rate at which the material is sputtered away. This may be conducted using equation (5.1), based upon methods derived in the Appendix. For the as-grown sample, the value for M_S is determined from graph b) in Figure 5.13 to be 2.7 memu (2.7×10^{-6} JT^{-1}). $a = 0.7324$ nm for $DyFe_2$ [1]. In $DyFe_2$ the magnetic moment is $4.22\mu_B$ $f.u.^{-1}$ ($N = 4.22$) [3]. Due to inaccuracies during cutting of the sample, chipping away of the $DyFe_2$ during

handling, and regions with no $DyFe_2$ due to the clamping / mounting procedure during the MBE growth process, the present sample in fact had a surface area of approximately 9 mm^2. Hence the thickness of the as grown sample is calculated to be $t_{as\text{-}grown}$ = 390 nm which is in good agreement with the known 400 nm thickness. For the sample subject to implantation and sputtering by Ar^+ ions, the thickness may be calculated using M_S = 2.3 memu (2.3×10^{-6} JT^{-1}) from graph d) in Figure 5.13. This gives $t_{ion\text{-}milled}$ = 320 nm. Hence the incident 3.25 keV Ar^+ ions have removed approximately 70 nm of material. This further confirms that the actual rate at which material is sputtered away is significantly less than predicted from `SRIM` simulations. Thus proportionally, only a small fraction of the $DyFe_2$ has been removed ($\lesssim$ 20%) compared to the YFe_2 ($\approx$ 50%) which helps further explain the emergence of both magnetocrystalline and magnetoelastic anisotropy dominance within the $DyFe_2$ sample. Towards the top of the sample, the strain within the film has been relaxed and hence the anisotropic characteristics are dominated by magnetocrystalline effects. Towards the bottom of the sample where, given the initially large intrinsic anisotropy of the $DyFe_2$ sample and its very thick nature, the effects of the implanted Ar^+ ions have not yet been felt; the sample remains dominated by magnetoelastic effects. VSM, as a bulk measurement technique, senses both regions, giving rise to the observed hysteresis loops. The VSM data can also be used to calculate a volume magnetization. The volume of the as-grown sample is approximately 3.6×10^{-6} cm^3 and the saturation magnetization 2.5 memu. This gives a volume magnetization of 700 emu cm^{-3} which is again a good order of magnitude agreement with the `OOMMF` data (550 kAm^{-1} = 550 emu cm^{-3}).

5.2.5 XRD characterization of an ion implanted $DyFe_2$ film

XRD data for the 400 nm $DyFe_2$ sample implanted with 1.7×10^{17} and 3.4×10^{17} Ar^+ ions cm^{-2} can be seen in Figure 5.15. These data are shown in conjunction with that of the as-grown sample.

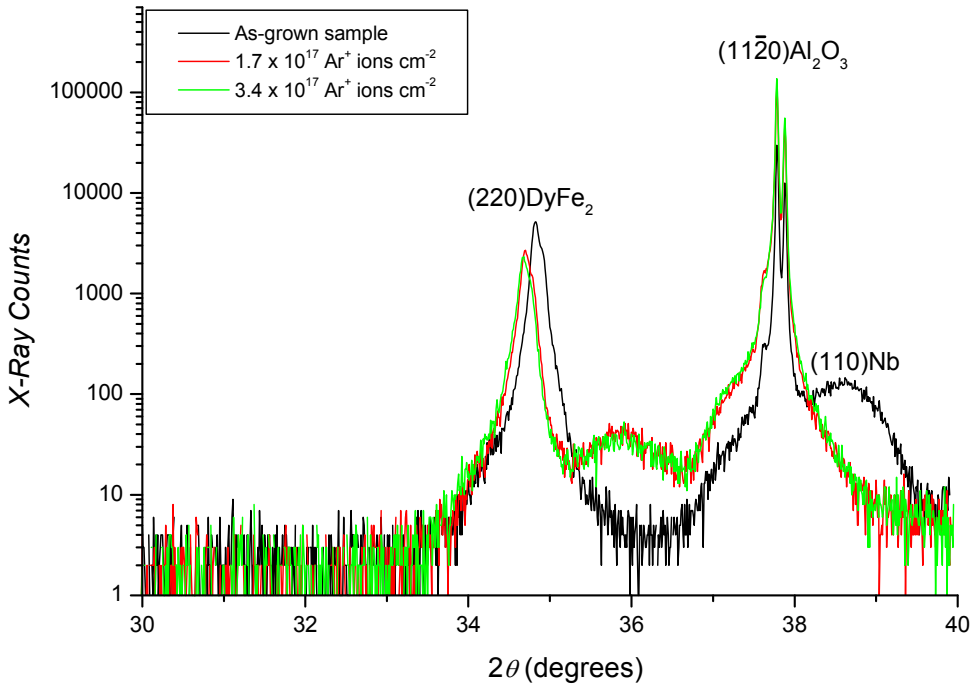

Figure 5.15: XRD data for the 400 nm $DyFe_2$ sample showing the (220) reflection in the as-grown state and the shift in peak position after implantation by a fluence of 1.7×10^{17} and 3.4×10^{17} Ar^+ ions cm^{-2} (see key).

The XRD data in Figure 5.15 show, with increasing Ar^+ ion fluence, a pronounced shift in the $DyFe_2$ peak towards a smaller angle. The $DyFe_2$ peak before ion-implantation (shown in black) corresponds to a lattice parameter of 0.7284 nm, which, as already noted, corresponds to a –0.5% contraction in the growth direction of the sample. Shifts in the position of this $DyFe_2$ peak are made clearer in Figure 5.16 where only the region of $2\theta = 33.5 - 35.5°$ is plotted.

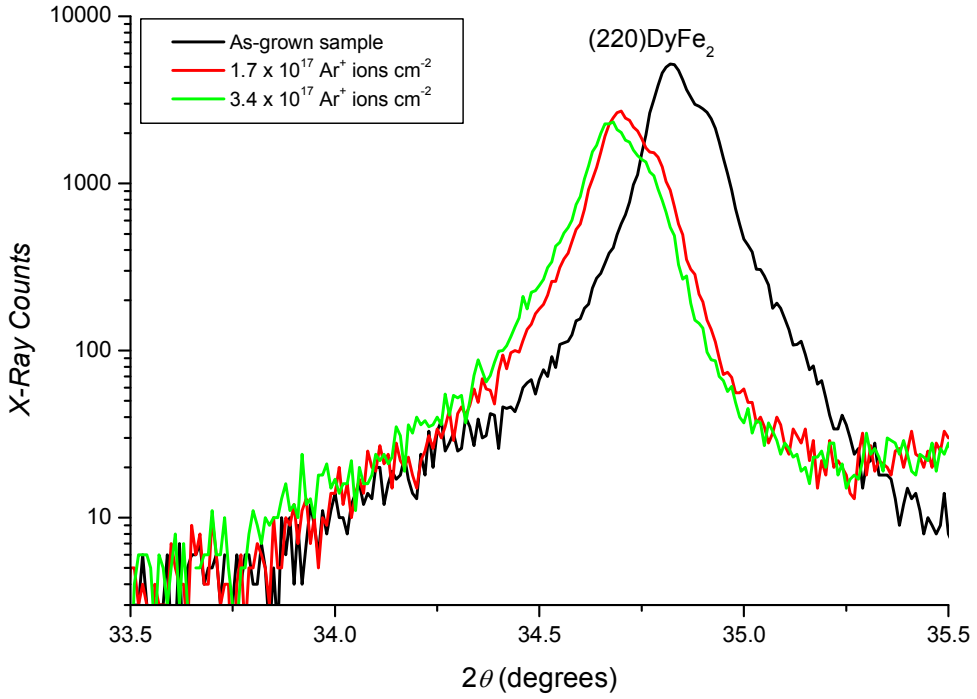

Figure 5.16: The XRD data of Figure 5.15 plotted between $2\theta = 33.75 - 35.25°$ only.

After implantation by a fluence of 1.7×10^{17} Ar^+ ions cm^{-2} (red data in Figure 5.16) the $DyFe_2$ peak has shifted to a much smaller value of 2θ, corresponding to an increased lattice parameter of 0.7308 nm, significantly closer to that of the bulk, un-strained sample (0.7324 nm [1]). This increase in lattice parameter represents a reduction of the strain (in the growth direction) to just –0.2 %. This forms unquestionable evidence that the implanted Ar^+ ions have caused the epitaxially grown, strained $DyFe_2$ sample to relax to a state more closely corresponding to that of the bulk film. After the sample has been subjected to twice the incident Ar^+ ion fluence (green data in Figure 5.16), the lattice parameter is increased further still, to 0.7312 nm. This is even closer to that of the un-strained film. It is interesting to note that an initial ion fluence of 1.7×10^{17} Ar^+ ions cm^{-2} caused the lattice parameter to change by 2.4 pm, whilst implantation by this same fluence of Ar^+ ions for a second time caused only a change of 0.4 pm. This helps confirm that Ar^+ ion implantation induced relaxation of the strain within the sample is rapid, with again the most prominent changes in sample behaviour being noted for a critical ion fluence of order 1×10^{17} Ar^+ ions cm^{-2}.

The diffraction between the incident X-rays and the material being probed renders standard skin depth calculations irrelevant for X-rays, with a detailed calculation of their propagation within the crystalline material being far more complex. However the

direct calculation is not necessary in the present study, since the appearance of a peak for the substrate material provides direct evidence that the X-rays penetrate through the entirety of the nominally 400 nm thick $DyFe_2$ film. In the XRD data for the ion implanted samples there is the clear emergence of a single $DyFe_2$ peak shifted to smaller 2θ values as well as the appearance of a new peak at 35.8°. Other than the important interpretation of an increased lattice parameter, three further factors can be identified from these data.

1. A single peak, shifted to lower values, is representative of the increase in $DyFe_2$ lattice parameter throughout the *entire* sample. If the lattice parameter was altered within a reduced volume only, two distinct peaks would be present. It can therefore be concluded that the strain has been relaxed throughout a large proportion of the entire sample. The propagation of effects throughout the crystalline lattice is attributed to the regular, epitaxial structure of the Laves phase system. The work by Florescu *et al.* [6] should be recalled where a similar material was irradiated with Ar^+ ions; here the authors noted no long range Ar^+ ion induced effects, simply the creation of a modified surface layer. This is due to the amorphous nature of this film preventing the propagation of dislocations, in sharp contrast with the results observed here.
2. The full width half maximum (FWHM) value of both the as-grown and ion implanted $DyFe_2$ peaks is 0.15° ± 0.01°. This illustrates that the high quality epitaxial nature to the film remains after ion implantation, providing further proof that the overall crystalline structure is not significantly disrupted despite the propagation of defects throughout its entire structure. This remanence of the FWHM also confirms the first point, that is, the change in lattice parameter is prominent throughout the entire sample.
3. The emergence of a new peak at 35.8° could be due to H absorption into the Nb. A peak at the same value of 2θ is also present in the Ar^+ ion implanted YFe_2 sample (section 5.1.5). This peak is therefore unlikely to be due to an inter-mixed $REFe_2$ and Nb layer since this would occur at different values for RE = Dy and Y. This also agrees with point 2 since it is believed that hydridged samples remain epitaxial. However, the more reactive $REFe_2$ is expected to be effected more by any H present during the ion implantation process than the Nb, thus the reasoning behind this process still remains unclear.

To summarise, if the XRD data before and after Ar^+ ion implantation had shown no differences, the sample would still exhibit magnetic properties dominated by the intrinsic magnetoelastic anisotropy. If, however, the XRD data showed complete agreement between the ion implanted sample and the bulk, un-strained sample, then the ion-implanted sample should show magnetic characteristics consistent with a system governed by magnetocrystalline anisotropy effects only. However, the lattice parameters of the samples implanted by Ar^+ ions, 0.7308 nm and 0.7312 nm, are approximately mid-way between that of the epitaxially strained sample (0.7286 nm) and that of the bulk (0.7324 nm). So it is logical to assume that the sample will be dominated by neither of these anisotropies, but rather exhibit characteristics common to both. This is indeed the case when the entirety of the sample volume is characterized by VSM measurements.

5.2.6 AFM characterization of an ion implanted $DyFe_2$ film

AFM micrographs for the 400 nm $DyFe_2$ sample, in the as-grown state and after ion implantation with a fluence of 1.7×10^{17} Ar^+ ions cm^{-2}, can be seen in Figure 5.17. It is clear from images a) and b) that the as-grown sample is characterized by a non-uniform appearance of rough and smooth regions. The small white (high) specks are attributed to oxidation of the sample surface, causing an increase in roughness. The protective Y cap helps prevent oxidation but there are still small regions towards the sample edge which are not as well protected from oxidation. So over time O_2 may still penetrate the Y cap. Images c) and d), corresponding to the ion implanted sample, are generally more free from such high contrast white specks. This can be explained in the same way as that for the YFe_2 sample; Ar^+ ion milling causing sputtering of the target material, which favours the more rapid removal of small, high aspect ratio structures, due to the larger surface area to volume ratio exposed to the incident ions.

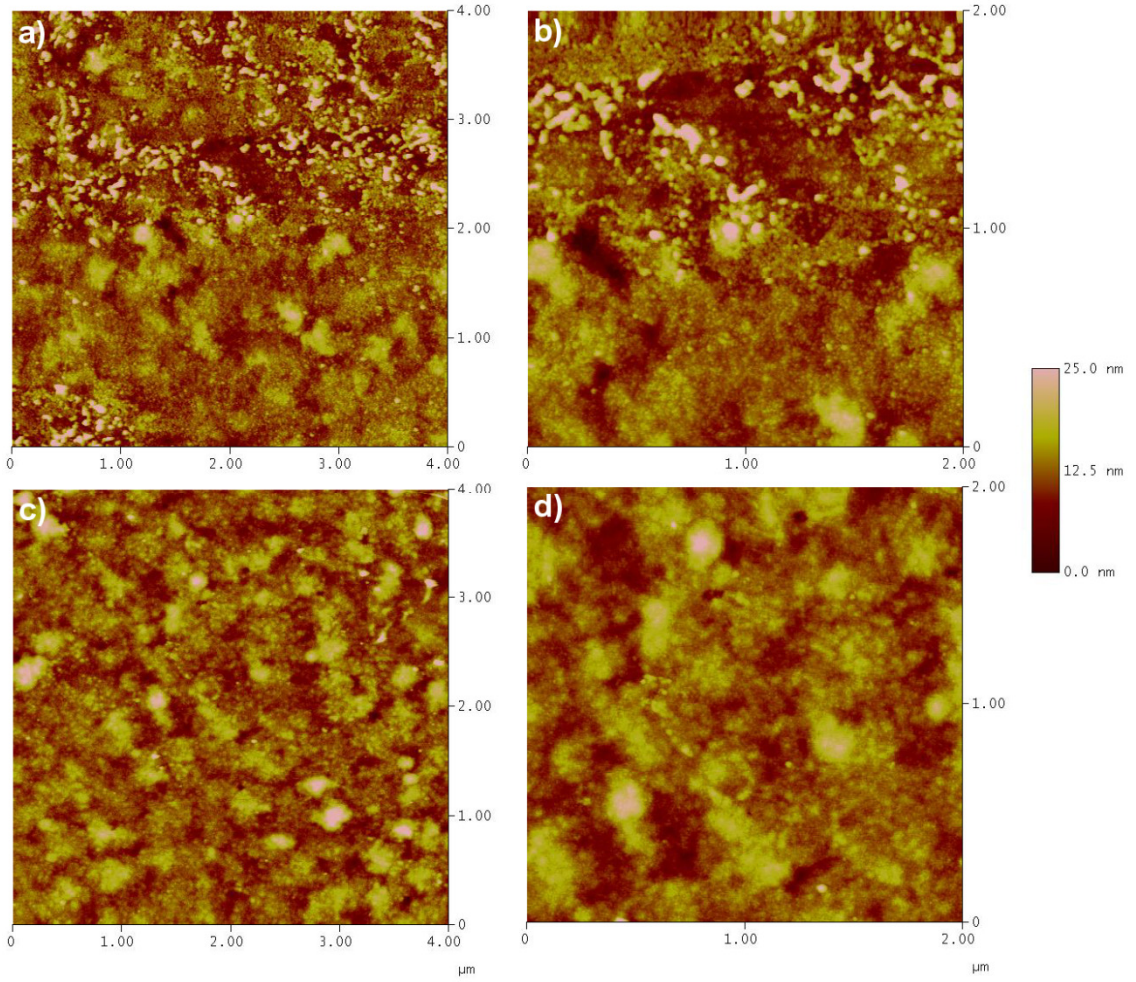

Figure 5.17: AFM micrographs of a 400 nm $DyFe_2$ sample in the as-grown state (images a) and b)) and after ion implantation with 1.7×10^{17} Ar^+ ions cm^{-2} (images c) and d)). Images b) and d) provide an increased level of magnification of the areas shown in images a) and b) respectively. The vertical (contrast) scales are maintained constant to act as a guide to the eye.

Using the same software based numerical analysis methods discussed earlier (section 5.1.6), the roughness of the ion implanted $DyFe_2$ sample was found to be 2.2 ± 0.2 nm, *c.f.* the as-grown sample where the roughness was found to be 2.8 ± 0.2 nm. Also the Ar^+ ion implanted sample shows a slightly reduced average surface feature height of 4.8 nm compared to 6.1 nm in the as-grown sample, while the average feature size increases from 750 ± 200 nm^2 to 1,100 ± 200 nm^2. This change in surface feature dimensions is evidence of the same trend found in the YFe_2 sample; the overall smoothness of the sample is not changed significantly, but there is a general trend toward larger surface features in the ion milled sample.

5.2.7 He^+ ion microscopy characterization of $DyFe_2$ samples

He^+ ion microscopy, described in see section 3.8, has been used to characterize the sample topography of as-grown and ion implanted $DyFe_2$ samples. Example He^+ ion micrographs for the 400 nm $DyFe_2$ sample, in both the as-grown and Ar^+ ion implanted states, can be seen in Figure 5.18.

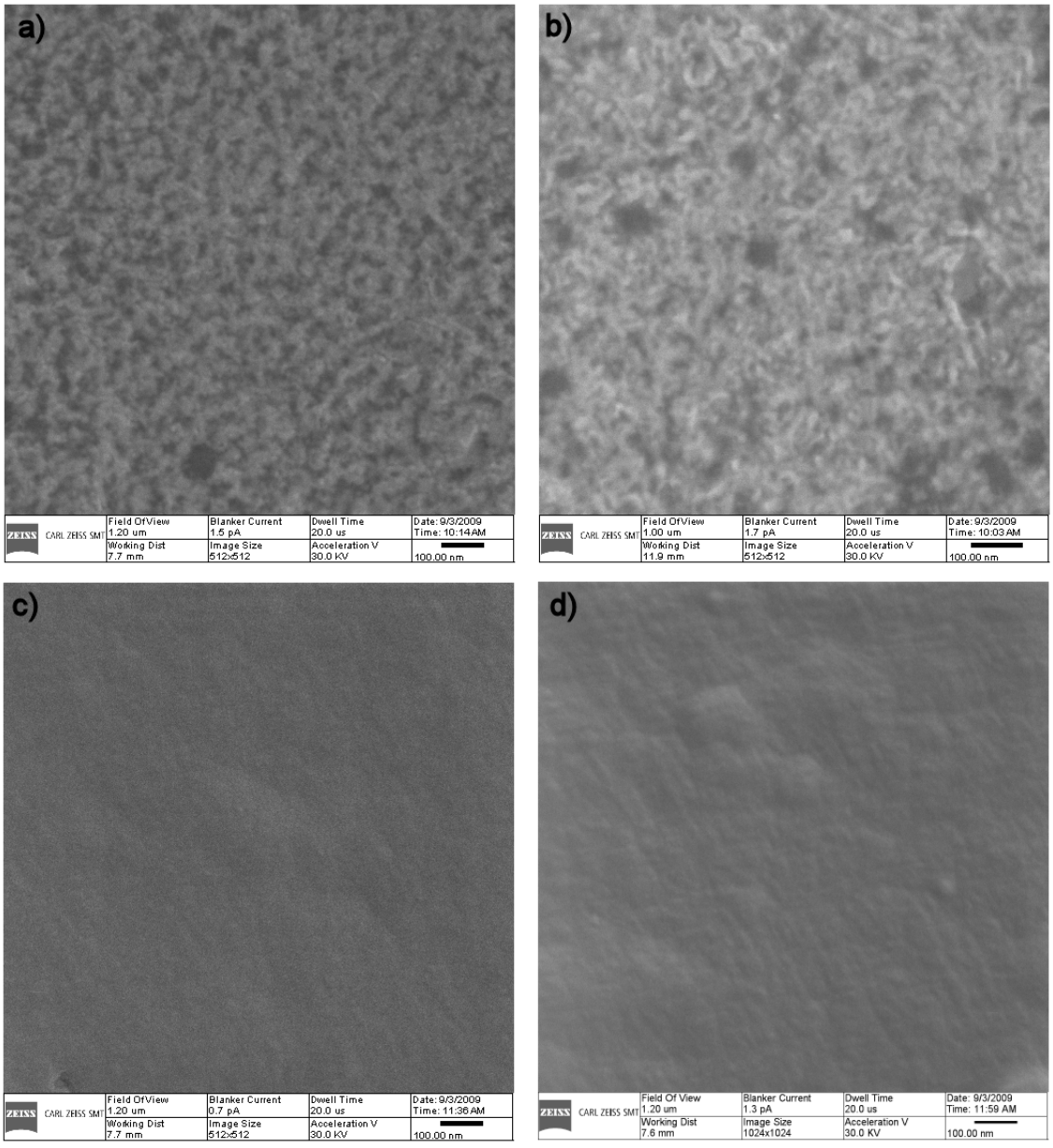

Figure 5.18: He^+ ion micrographs of the as-grown $DyFe_2$ sample (images a) and b)) and of the $DyFe_2$ sample implanted with 1.3×10^{17} Ar^+ ions cm^{-2} (images c) and d)). Clearly the sample surface is much smoother in images c) and d) due to the effects of sputtering material during the ion implantation process.

The He^+ ion micrographs show the appearance of a considerably smoother sample surface after the ion milling. Images a) and b) within show, in great detail, the small defects on the sample surface presumed to be caused by oxidation of the $DyFe_2$ film.

The dimensions of the defects have not been analysed in detail, but visual inspection suggests that the average surface feature has lateral dimensions of order 30 – 50 nm and thus occupies an area very similar to that derived from the AFM data in section 5.2.6. In images c) and d) where the sample subjected to a fluence of 1.3×10^{17} Ar^+ ions cm^{-2} is depicted, it is apparent that the ions have had a smoothing effect on the sample surface. These images show that the sample surface is almost completely smooth, with very few, relatively large islands of material. At present it remains unclear why there are these discrepancies between the AFM and He^+ ion micrographs since both are surface-sensitive techniques.

5.2.8 Discussion of and conclusions for an ion implanted $DyFe_2$ sample

The deviation from the bulk lattice parameter for $REFe_2$ films grown epitaxially on Al_2O_3 substrates is well known and documented [16, 17]. This is due primarily to strains induced within the metallic films as a result of the differential thermal contraction between the metallic films and the Al_2O_3 substrate after sample growth [1, 2]. It has been shown from XRD measurements of the lattice parameter that this is indeed evidenced for the $DyFe_2$ sample studied in this section (see Figure 5.9). The change in lattice parameter, as measured from the (220) XRD peaks, is due to a contraction in the growth direction. The contraction is assumed to be accompanied by an increase in lattice parameter in the plane of the sample, as the Laves phase structure alters to maintain a constant volume [1]. The implantation of Ar^+ ions with a fluence greater than approximately 1.0×10^{17} ions cm^{-2} has been shown to partially relax this strain, as monitored by an increasing lattice parameter in the direction of the growth of the sample, returning it to a value much closer to that of the bulk material (see Figure 5.15 and Figure 5.16).

The aforementioned strain is responsible for the magnetoelastic anisotropy energy term (E_{ME}). At room temperature, this term is of greater dominance than the magnetocrystalline anisotropy energy (E_{MC}) within these samples [18]. Therefore the easy axis of magnetization is principally governed by the vector sum of directions which serves to minimize E_{ME} rather than E_{MC}. The former is dependent on the sign of the magnetoelastic constant (b_2) which appears in the magnetoelastic energy term (equation (2.35)). If $b_2 < 0$, the easy axis of magnetization is along $[\bar{1}10]$, whilst if $b_2 > 0$ it is along $[001]$. The $[\bar{1}10]$ direction is in the film plane, whilst the $[001]$

direction is perpendicular to the film plane. In $DyFe_2$ at room temperature, $b_2 < 0$ hence the easy axis of magnetization in the thin film samples lies in the plane of the sample. Consequently, any significant variation to the lattice parameter of the sample due to "damage" induced by incident Ar^+ ions will affect the strain of the system and thus have a profound effect on the dominance of the magnetoelastic anisotropy, possibly altering the sign of b_2. Clearly this will alter the easy and hard axes of magnetization within the samples.

SRIM modelling for a $DyFe_2$ film confirms that the incident Ar^+ ions are stopped fully within the metallic Laves phase structure, rather than within the sample substrate. Some of the Ar^+ ion energy is lost to recoils, *i.e.* elastic collisions between the ion and the target atoms (see Table 5.2). It is important to note that the formation of recoil cascades, that is the displacement of target atoms by more than one lattice site, is extremely rare due to the large mass difference between the incident ion and target atom. Thus it would appear that the overall structure of the cubic Laves phase crystalline lattice should be maintained, resulting in only slight variations in dimensions. This results in a steady change to the anisotropy axes within the sample since its epitaxial nature will remain, rather than the formation of an amorphous or polycrystalline sample with poorly defined magnetic anisotropy. Woods *et al.* [149] used 200 keV Ar^+ ions to probe the effect of ion implantation on angular dispersion in anisotropy. They found that the dispersion in anisotropy direction increases when the sample is irradiated by Ar^+ ions. This was attributed to increased disorder within the crystalline lattice, as a result of significantly more energetic collisions between ions and atoms, resulting in large dislocations within the crystalline lattice and ultimately its partial destruction. The expansion, rather than destruction, of the present strained $DyFe_2$ Laves phase structure is attributed to the use of comparatively low energy Ar^+ ions. The recoiled Dy atoms, which form the "corners" of the cubic Laves phase unit cell, are displaced from their initial position due to the energy imparted from the Ar^+ ions, and subsequently relax back to their original, un-strained position, thus relieving strain throughout the epitaxially grown system. The atoms are not displaced so far that the order of the system is totally disrupted. This is similar to the work of Chang *et al.* [19], who argued that the quenching of recoiling atoms at room temperature in a Co / Pt system is over a very short timescale. This causes the recoiled atoms to be frozen in at a

metastable state since the timescale is too short for recrystallization at the equilibrium state, and instead an expansion of the crystalline lattice parameter is apparent.

The reduction of the strain in the epitaxially grown samples is clearly responsible for a significant decline in the dominance of the magnetoelastic anisotropy of the system. Of course, a reduction in magnetoelastic anisotropy results in an increase in the relative importance of the intrinsic magnetocrystalline anisotropy. If the 400 nm $DyFe_2$ sample were totally relaxed by the implantation of Ar^+ ions with a fluence of 1.7×10^{17} ions cm^{-2}, then the hysteresis loops would show a complete exchange of characteristics between the as-grown and ion implanted samples as witnessed in the YFe_2 system (section 5.1). However, for the thick $DyFe_2$ sample, Figure 5.14 shows that this is clearly not the case; only a partial reorientation of the easy and hard axes of magnetization is achieved. The hysteresis loops for the ion implanted sample show aspects of both the easy and hard axis response when a magnetic field is applied along the $[\bar{1}10]$ and $[00\bar{1}]$ directions. This provides evidence for a roughly equal success in the competition between magnetoelastic and magnetocrystalline anisotropy. There is clear evidence for the beginnings of the rotation of the easy and hard axes of magnetization away from the magnetoelastic anisotropy dominated directions, towards equivalent directions corresponding to a magnetocrystalline anisotropy dominated system.

The emergence of a behaviour which is reminiscent of a system where magnetoelastic and magnetocrystalline anisotropies are approximately equal serves once again to prove that Ar^+ ion implantation is responsible for reducing the strain in these thin-film samples. The fact that this relaxation is only partial is confirmed by the XRD data, but this data also shows that this relaxation is throughout the entire film. When comparison is made to `SRIM` modelling data, whereby the average radial range of low keV Ar^+ ions within $DyFe_2$ is just 4.1 nm (Table 5.2), it is clear that the effects of Ar^+ ion implantation must propagate *throughout* the sample by some means. It is suspected that this is due to the well ordered, epitaxial structure to the samples. A small defect induced towards the sample surface (*e.g.* the relaxation of a strained Laves phase unit cell due to an atomic recoil induced by an incident energetic Ar^+ ion) may affect the overall sample structure a much greater distance away due to the very rigid and regular ordering between the individual Laves phase unit cells. These relatively long range effects were shown to extend throughout the YFe_2 film (section 5.1), but given the

$DyFe_2$ film's much greater thickness it is plausible that their propagation be attenuated. Further, a critical Ar^+ ion fluence which changes to the dominant anisotropy energy term from magnetoelastic to magnetocrystalline has been identified to lie in the range of $5 \times 10^{16} - 1 \times 10^{17}$ Ar^+ ions cm^{-2}, similar to that in the YFe_2 sample. Also similar to the results obtained in the YFe2 sample, the ion milling induced during this process does not significantly effect the sample morphology; this was shown by both AFM and He^+ ion microscopy.

In conjunction with the author's work on YFe_2 samples (section 5.1), this work provides the first demonstration of ion implantation induced changes to the magnetic properties of epitaxial $REFe_2$ materials. A uniaxial anisotropy has been induced in polycrystalline Ni and Fe films via implantation with Xe^+ ions before [20, 21], but this work is the first that demonstrates ion implantation as a tool to induce a *progressive* change in the dominant anisotropy energy of a well ordered (epitaxial) system. The author has demonstrated that it is possible to reliably and readily engineer which anisotropy energy is dominant, simply by varying the incident Ar^+ ion fluence. Such a controllable way of tailoring magnetic properties could be useful for the fabrication of patterned magnetic media if combined with the use of a mask. Furthermore, the use of higher energy and / or lighter ions, at normal incidence to the sample surface, would significantly attenuate the sputtering yield. This would permit the fabrication of flat patterned media, in a vein very similar to that used by Chappert *et al.* [124]. If so, the production of very high resolution and dense media should be possible, since the read / write head fly height can be significantly reduced. This nano-fabrication process also offers significant cost savings, since complex sample planarization processes may be eliminated. Similarly, the use of very high energy ions to pattern media through a mask might be used to increase this resolution yet further, since, within the sample volume of interest, the collisions are inelastic (and thus ballistic). As a result therefore the patterned region would not be unduly affected by the proximity effect [22].

5.3 Ar^+ Ion Implantation of a $DyFe_2$ / YFe_2 Multilayer Exchange Spring

The effects of implanted Ar^+ ions on a sample comprised of 27 repeats of [3 nm $DyFe_2$ / 12 nm YFe_2] have been investigated. The primary role of this sample was to investigate the effects of patterning nano-scale structures in an epitaxially grown multilayer

exchange spring system, with the aim of inducing a shape anisotropy more dominant than both the intrinsic magnetocrystalline and magnetoelastic anisotropies. For reasons already described, the process of Ar^+ ion milling with high energy ions (~ keV regime) involves their implantation. Where a thick mask material is used during the pattern transfer process the epitaxial material below it will be protected from these implanted ions. However, as the mask material grows thinner, the Ar^+ ions will be implanted into the epitaxial magnetic material itself. In such samples it is therefore necessary to consider the effects of *both* the lithographically defined structures *and* the implanted Ar^+ ions, the latter forming the content of this brief section.

The present multilayer system of $DyFe_2$ / YFe_2 within which the effects of patterning are studied, are comprised entirely from two materials which have been shown under the implantation of Ar^+ ions to experience strain relaxation. Therefore it is logical to assume that similar effects in multilayer structures comprised of the same materials will be present. Consequently it is important to characterize the magnetic behaviour of an un-patterned multilayer sample of $DyFe_2$ YFe_2 both before and after Ar^+ ion implantation in order to identify any change in anisotropic magnetic response. The reader should note that this study of the effects of Ar^+ ion implantation in such a complex epitaxial exchange spring system is not intended to be as exhaustive as those for the simpler epitaxial films of YFe_2 and $DyFe_2$ (sections 5.1 and 5.2 respectively).

5.3.1 Experimental procedure

The exchange spring sample investigated, [3 nm $DyFe_2$ / 12 nm YFe_2] × 27, has a thickness very close to 400 nm, ensuring epitaxial growth and excellent anisotropic magnetic properties. The sample was cut into multiple pieces, each approximately 5 × 5 mm. These pieces were exposed to 3.25 keV Ar^+ ions with fluences ranging from 1.7 to 3.4×10^{17} ions cm^{-2}. As would be expected from the data previously provided with regard to Ar^+ ion energy loss mechanisms in YFe_2 and $DyFe_2$, the primary route for ion energy dissipation in this sample was through recoiling target atoms. Accordingly it is intuitive to predict the relaxation of the strain throughout the system and the associated reorientation of the magnetic axes.

5.3.2 MOKE measurements of an ion implanted $DyFe_2$ / YFe_2 multilayer

The multilayer exchange spring sample was characterized by MOKE in the as-grown state and at two different incident Ar^+ ion fluences; 1.7×10^{17} ions cm^{-2} and 3.4×10^{17} ions cm^{-2}. These data, taken with the magnetic field applied along the orthogonal $[\bar{1}10]$ and $[001]$ directions (easy and hard axis of magnetization in the strained, as-grown sample) are presented in Figure 5.19. Note that this sample was fabricated without a protective Y cap, resulting in oxidation to the upper layers of the multilayer film. Therefore the hysteresis loops associated with MOKE, a surface sensitive technique, look somewhat different to those obtained by bulk magnetometry measurements. The corresponding two hysteresis loops are presented in graphs a) and b). These data are in very good agreement with the experimental results in Wang *et al.* [23] for almost identical samples where "surface exchange springs" are identified to be responsible for these very well pronounced shapes to the hysteresis loops.

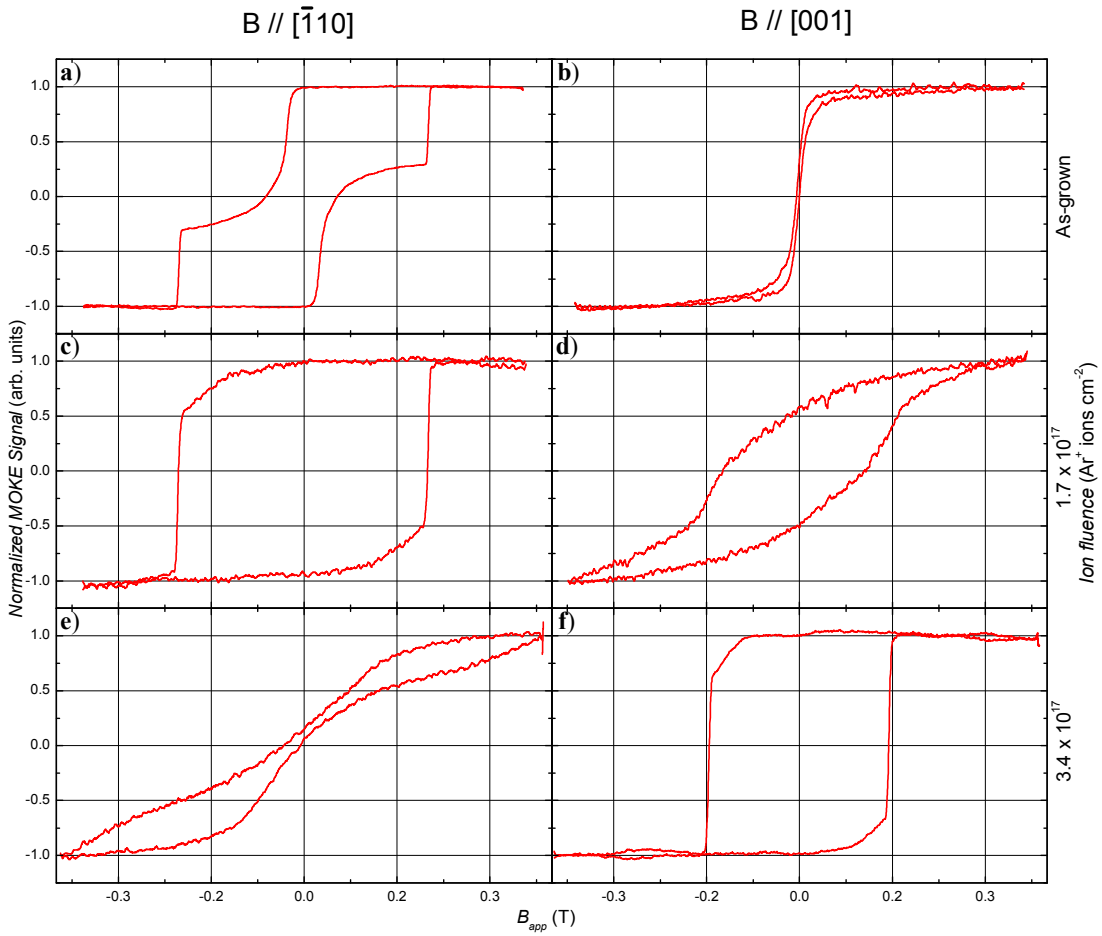

Figure 5.19: MOKE hysteresis loops of a [3 nm $DyFe_2$ / 12 nm YFe_2] × 27 multilayer exchange spring sample before and after ion implantations of increasing fluences (see right-hand axis) for the applied magnetic field along the [$\bar{1}$10] and [00$\bar{1}$] directions.

After implantation of Ar^+ ions with a fluence of 1.7×10^{17} ions cm^{-2} the hysteresis loops displayed in graphs c) and d) are obtained, corresponding to samples which have had this upper oxide layer removed[vi]. The data from graph c) is in very good agreement with that modelled for exchange spring-like behaviour detected by MOKE for these samples [23]. Thus it is possible to conclude that the oxide layer on top of the sample, specifically the upper-most YFe_2 layer, is most likely to be de-coupled from the bulk of the exchange spring system. Accordingly this explains the data obtained in graph b) which looks very similar to that of pure YFe_2 (*c.f.* Figure 5.2, but note the different ranges of applied field), which also appears to be responsible for the surface exchange

[vi] A simple visual check also confirms this; before Ar^+ ion milling (and implantation) these samples appear a dull golden-brown colour, whilst after the ion milling process they appear silver with a mirror-like finish. The latter is the same as new, un-oxidised samples and those with a protective Y cap.

spring-like behaviour observed in graph a)[vii]. This can account for the differences between the experimental and theoretical results of Wang *et al.* [23].

Graphs c) and d) clearly correspond to easy and hard axis magnetic behaviour when a magnetic field is applied along the $[\bar{1}10]$ and [001] directions respectively. This is due to the magnetic anisotropy being dominated by the hard $DyFe_2$ layers [17, 24] which have easy and hard axes of magnetization parallel to these crystallographic directions [2, 18]. This is confirmed in measurements of $DyFe_2$ / YFe_2 multilayer samples which show a room temperature hard axis response along the [001] direction [25]. It is assumed therefore, that the easy axis will be orthogonal to this, along an equivalent $\langle 110 \rangle$ direction. Some doubt about this orientation was raised in Dumesnil *et al.* [26], although these samples have indeed been confirmed by K. Wang *et al.* [27], D. Wang *et al.* [23] and the author to have an easy axis of magnetization along the $[\bar{1}10]$ direction at room temperature. Since the $[\bar{1}10]$ and [001] directions are maintained as easy and hard axes of magnetization respectively, it can be concluded that an incident Ar^+ ion fluence of 1.7×10^{17} ions cm^{-2} is insufficient to cause any notable relaxation of the strain. Doubling the incident Ar^+ ion fluence to 3.4×10^{17} ions cm^{-2} gives rise to the hysteresis loops presented in graphs e) and f). These data appear to roughly mirror the magnetic response of the data in graphs c) and d) but rotated by 90°. The easy axis response with $\mathbf{B}_{app}$ parallel to the $[\bar{1}10]$ direction in graph c) has now become a hard axis dominated response shown in graph e), whilst similarly the hard axis response in graph d) with $\mathbf{B}_{app}$ parallel to the [001] direction has become an easy axis of magnetization in graph f).

5.3.3 Concluding remarks on Ar^+ ion implantation in a $DyFe_2$ / YFe_2 multilayer

It has been well documented that the easy and hard axes of magnetization in epitaxially grown multilayer samples of $DyFe_2$ / YFe_2 are dependent on temperature [3, 25]. At temperatures below approximately 200 K, the [001] direction is an easy axis of magnetization, whilst above this temperature it is a hard axis of magnetization. This is due to the magnetic anisotropy being dominated by the hard $DyFe_2$ layers [17, 24]. The effects of temperature on the reorientation of easy and hard axes of magnetization in

[vii] Before normalization of the MOKE data the amplitude of the MOKE signal (photodetector volts) in Figure 5.19 graph b) was identical within experimental accuracy to that for the curved regions of graph a).

$DyFe_2$ were discussed in section 5.2.8, but in summary, at low temperatures magnetocrystalline effects are dominant, whereas at high temperatures magnetoelastic effects become the overriding effect. The result of this is a rotation of the easy and hard axis of magnetization from the [001] and [$\bar{1}$10] directions to the [$\bar{1}$10] and [001] directions respectively.

In section 5.2 it was shown that the implantation of Ar^+ ions causes the relaxation of strain within epitaxial $DyFe_2$ films thereby returning the easy and hard axis of magnetization to those present in the un-strained bulk samples. The data in Figure 5.19 show clearly that Ar^+ ion implantation in these multilayer films of $DyFe_2$ / YFe_2 also causes the rotation of the magnetic easy and hard axis by approximately 90°, such that the easy axis of magnetization lies along the [001] direction whilst the hard axis lies along the [$\bar{1}$10] direction. This is to be expected since the magnetic anisotropy in both samples is dominated by the hard $DyFe_2$. The response of the multilayer sample to implantation by ~ keV Ar^+ ions is near identical to that of the constituent materials, in both of which this reorientation of the magnetic anisotropy axes was shown to be due to the relaxation of the strain induced during growth.

Therefore it may be concluded that ~keV Ar^+ ion implantation in multilayer exchange spring systems is responsible for the creation of long-range dislocations within the crystalline structure. This causes an expansion of the lattice parameter in the growth direction towards that of the bulk, un-strained material. The reduction in strain significantly reduces the magnetoelastic energy. Consequently the intrinsic magnetocrystalline energy becomes the driving force behind the sample's magnetic anisotropy, causing the easy and hard axes of magnetization to reorient by 90°. It is also interesting to note this effect at a fundamental but practical level. The benefits of composite exchange spring media as data storage elements were discussed in section 2.7 whilst the potential of patterning media via the direct modification by energetic ions was highlighted in section 5.2.8. For example, using the ion implantation process on selected regions within an exchange spring sample could create soft magnetic inclusions (regions which may be easily written to) in a hard magnetic background (for thermal stability), leading to perfectly flat, patterned composite media. This is a subject which clearly warrants future investigation.

References

[1] A. Mougin, C. Dufour, K. Dumesnil, N. Maloufi, Ph. Mangin & G. Patrat, *Phys. Rev. B*, vol. **59**, no. 8, pp. 5950 – 5959, 1999.

[2] A. Mougin, C. Dufour, K. Dumesnil & Ph. Mangin, *Phys. Rev. B*, vol. **62**, no. 14, pp. 9517 – 9531, 2000.

[3] J-. M. L. Beaujour, *Ph. D. Thesis*, University of Southampton, UK, 2003.

[4] G. J. Bowden, *J. Phys. F, Metal Phys.*, vol. **3**, pp. 2206 – 2217, 1973.

[5] J. P. Zimmermann, *Ph. D. Thesis*, University of Southampton, UK, 2007.

[6] V. Florescu, M. D. Serbanescu, R. Manaila & W. A. Grant, *J. Mag. Mag. Mater.*, vol. **92**, pp. 137 – 142, 1990.

[7] H. Malettaa, Ch. Rehma, F. Kloseb, M. Fieber-Erdmanna & E. Holub-Krappe, *J. Mag. Mag. Mater.*, vol. **240**, pp. 475 – 477, 2002.

[8] G. Song, A. Remhof, D. Labergerie, C. Sutter & H. Zabel, *J. Alloys. Comp.*, vol. **293 – 295**, pp. 476 – 479, 1999.

[9] K. E. Chang & G. W. Warren, *IEEE Trans. Mag.*, vol. **31**, no. 6, pp. 3671 – 3673, 1995.

[10] R. Gupta, K-. H. Han, K. P. Lieb, G. A. Müller, P. Schaaf & K. Zhang, *J. Appl. Phys.*, vol. **97**, p. 073911, 2005.

[11] A. R. Wildes, R. A. Cowley, R. C. C. Ward, M. R. Wells, C. Jansen, L. Wireen & J. P. Hill, *J. Phys. Condens. Matt.*, vol. **10**, pp. L631 – L637, 1998.

[12] G. Carter, *J. Phys. D: Appl. Phys.*, vol. **34**, pp. R1 – R22, 2001.

[13] U. Valbusa, C. Boragno & F. Buatier de Mongeot, *J. Phys. C, Condens. Matt.*, vol. **14**, pp. 8153 – 8175, 2002.

[14] A. A. Zhukov, G. J. Bowden, J.-M. L. Beaujour, B. D. Rainford, P. A. J. de Groot, R. C. C. Ward, M. R. Wells & H. Küpfer, *J. Mag. Mag. Mat.*, vol. **270**, pp. 312 – 320, 2003.

[15] A. Mougin, C. Dufour, K. Dumesnil, N. Maloufi & Ph. Mangin, *Appl. Phys. Lett.*, vol. **76**, no. 11, pp. 1449 – 1451, 2000.

[16] A. R. Wildes, R. A. Cowley, R. C. C. Ward, M. R. Wells, C. Jansen, L. Wireen & J. P. Hill, , *J. Phys.: Condens. Matt.*, vol. **10**, pp. L631 – L637, 1998.

[17] M. J. Bentall, R. C. C. Ward, E. J. Grier & M. R. Wells, *J. Phys.: Condens. Matt.*, vol. **15**, pp. 6493 – 6512, 2003.

[18] V. Oderno, C. Dufour, K. Dumesnil, Ph. Bauer, Ph. Mangin & G. Marchal, *Phys. Rev. B*, vol. **54**, no. 24, p. R17375 – R17378, 1996.

[19] G. S. Chang, Y. P. Lee, J. Y. Rhee, J. Lee, K. Jeong & C. N. Whang, *Phys. Rev. Lett.*, vol. **87**, no. 6, p. 067208, 2001.

[20] K. Zhang, K. P. Lieb, P. Schaaf, M. Uhrmacher, W. Felsch & M. Münzenberg, *Nuc. Instrum. Meth. Phys. Res. B*, vol. **161**, pp. 1016 – 1021, 2000.

[21] M. Neubauer, N. Reinecke, M. Uhrmacher, K. P. Lieb, M. Münzenberg & W. Felsch, *Nuc. Instrum. Meth. Phys. Res. B*, vol. **139**, pp. 332 – 337, 1998.

[22] T. Mewes, R. Lopusnik, J. Fassbender, B. Hillebrands, M. Jung, D. Engel, A. Ehresmann & H. Schmoranzer, *Appl. Phys. Lett.*, vol. **76**, no. 8, pp. 1057 – 1059, 2000.

[23] D. Wang, C. G. Morrison, A. R. Buckingham, G. J. Bowden, R. C. C. Ward & P.

A. J. de Groot, *J. Mag. Mag. Mater.*, vol. **321**, pp. 586 – 589, 2009.

[24] M. J. Bentall, R. A. Cowley, W. J. L. Buyers, Z. Tun, W. Lohstroh, R. C. C. Ward & M. R. Wells, *J. Phys. Condens. Matt.*, vol. **15**, pp. 4301 – 4330, 2003.

[25] M. Sawicki, G. J. Bowden, P. A. J. de Groot, B. D. Rainford & J-. M. L. Beaujour, *Phys. Rev. B*, vol. **62**, no. 9, pp. 5817 – 5820, 2000.

[26] K. Dumesnil, C. Dufour, Ph. Mangin, A. Rogalev & F. Wilhelm, *J. Phys.: Condens. Matt.*, vol. **17**, pp. L215 – L222, 2005.

[27] K. Wang, K. N. Martin, C. G. Morrison, R. C. C. Ward, G. J. Bowden & P. A. J. de Groot, *Appl. Phys. A*, vol **86**, pp. 325 – 328, 2007.

Chapter 6

Patterned Elements in $REFe_2$ Laves Phase Intermetallics

In this chapter results regarding the magnetic characterization of patterned elements within $REFe_2$ thin films and multilayer structures are presented. Here, the discussion is limited to patterned elements created using electron beam lithography and Ar^+ ion milling. In particular, this chapter aims to quantify the effects associated with the creation of artificially defined nano- and micro-scale geometric structures within $REFe_2$ materials. This has been accomplished using results from two distinctly different experimental techniques; magnetic force microscopy (MFM) and the magneto optical Kerr effect (MOKE).

This chapter begins by detailing the affects of micro- and nano-scale patterned elements within a thin bi-layer sample of $DyFe_2$ / YFe_2. These results will be seen to provide an illustration of the length-scales needed to create single-domain elements within such $REFe_2$ materials. Attention is then turned to the effects of patterning arrays of both lines and squares in thicker multilayer samples of $DyFe_2$ / YFe_2. Both the success of the patterning process and its drawbacks are discussed in some detail. MFM and MOKE measurements are used together to provide a picture of the effects of competing anisotropies in these thicker samples. Finally, conclusions are given, highlighting the achievements of this patterning process within these novel materials. This will illustrate their suitability as devices to provide corner-stone research into the wider use of antiferromagnetically coupled exchange spring media, where modifications to the magnetic properties may be obtained by tuning length scales in the micro- and nano-metre regimes.

6.1 Patterned Elements in a $DyFe_2$ / YFe_2 bi-layer

The successful fabrication of nano-scale patterned elements in a thin, bi-layer film of 7.5 nm $DyFe_2$ / 30 nm YFe_2 was described in section 4.2.6. This sample acted as a

proof of principle regarding nano-scale pattern definition within epitaxially grown $REFe_2$ films using electron beam lithography and Ar^+ ion milling, reinforcing the versatility of this process. Nevertheless there were issues regarding the island-like growth of such thin $REFe_2$ films. These were discussed in conjunction with the choice of metallic mask materials used. With further developments, it is hoped that either the island-like growth can be avoided [1, 2, 3, 4] or new mask materials, more resilient to Ar^+ ion milling, can be employed. Either way, such new methods would permit fabrication of nano-scale elements in high quality, thin epitaxial films, or high aspect ratio structures spanning the entire depth of a thick (~ 400 nm) multilayer sample. Given the likely development of such techniques, it is therefore useful to characterize the magnetic response of a nano-scale patterned bi-layer sample. It will be shown that the effect of patterned elements does indeed alter the sample's response to an applied magnetic field.

6.1.1 Characterization by magnetic force microscopy

Magnetic force microscopy presents itself as a very attractive tool for characterizing the 7.5 nm $DyFe_2$ / 30 nm YFe_2 bi-layer sample since it is a very sensitive technique that is readily able to detect the very small, stray magnetic field components from this sample. This is in contrast to MOKE which requires a high quality sample in order to achieve an appreciable signal with a good SNR. The island-like growth of this sample, responsible for the poor SNR when characterized by MOKE, is further compounded by the removal of material during the patterning process, reducing the SNR so much that MOKE characterization becomes impossible. This patterning induces changes in the stray magnetic field which are easily detected by MFM. In practice these are most likely to appear as alternating light and dark regions if the sample is comprised of multiple domains, or single bright or dark regions if the sample is comprised of just one domain. It is expected from equation (2.43) that, depending on the field history (*i.e.* the state in which the sample has been prepared), for patterned elements on the scale of approximately 1 μm there will be multiple domains. Single domain elements may occur when the feature size is reduced to ~ 100 nm or less.

AFM and MFM micrographs of nominally 1 μm and 500 nm squares defined in the 7.5 nm $DyFe_2$ / 30 nm YFe_2 sample can be seen in Figure 6.1. These are the same square arrays as depicted in the SEM and AFM micrographs in Figure 4.14 and Figure 4.15 respectively. AFM measurements of the samples show that the patterned elements

are slightly larger than intended. The square elements in fact have dimensions of 1.05 μm (pitch 2 μm) and 550 nm (pitch 1 μm) respectively. This slight increase in patterned element size may be attributed to small but constant errors in the lithography process (slight deviation of the dose factor from the optimal value) or to the sloped nature of the Cr mask side-walls and subsequent etching and re-deposition (see section 4.3). The sample has been subjected to an incident ion fluence of 5.7×10^{16} Ar^{+} ions cm^{-2}.

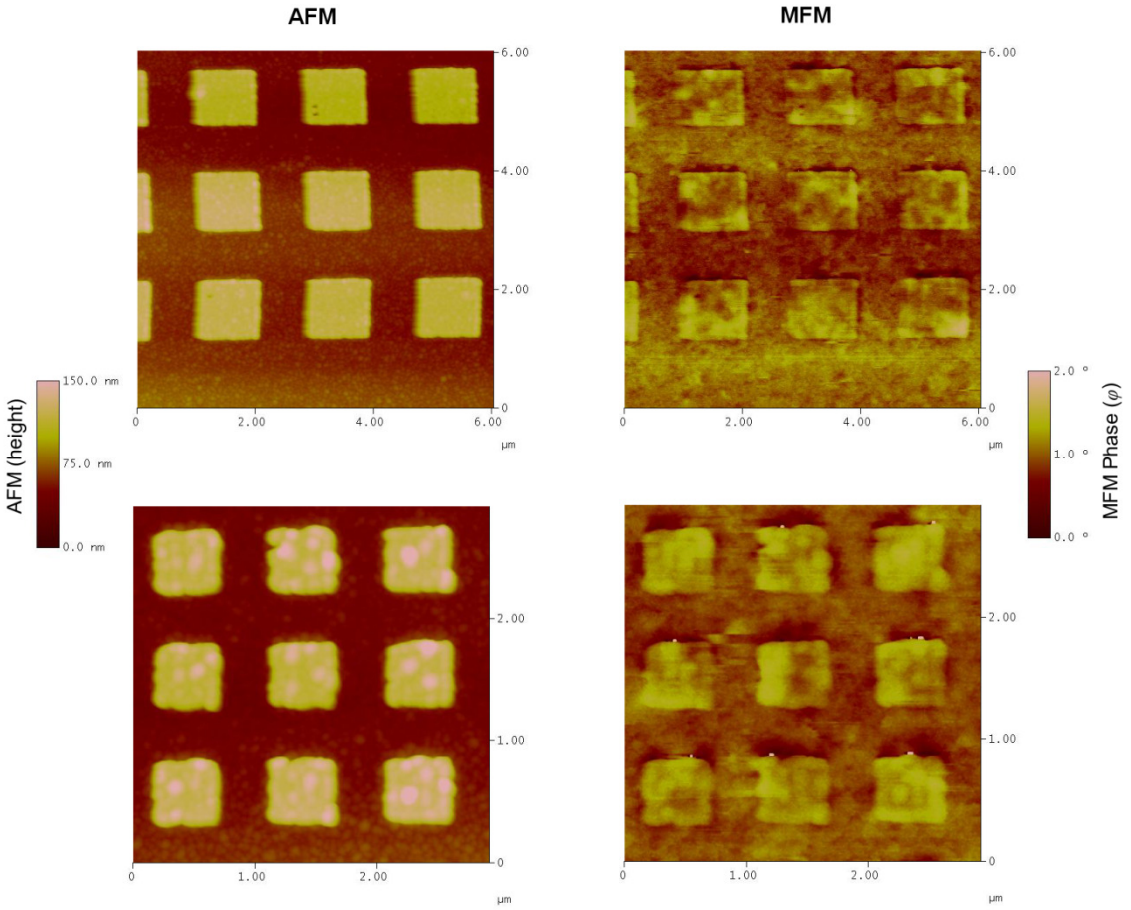

Figure 6.1: AFM (left) and MFM (right) micrographs of 1.1 μm (top) and 550 nm (bottom) squares defined in a 7.5 nm $DyFe_2$ / 30 nm YFe_2 bi-layer sample. The patterned array has been subjected to a fluence of 5.7×10^{16} Ar^{+} ions cm^{-2}. The AFM data show that the squares have an edge roughness of ~ 50 nm and radius of curvature to the corners of ~ 50 nm. The MFM data is taken in the remnant state and shows magnetic elements superimposed on a magnetic background.

The AFM micrographs (left) show that both the 1.1 μm and the 550 nm squares remain as well defined as they were in the Cr mask material. They exhibit an edge roughness of approximately 50 nm with a similar radius of curvature to the corners. The MFM micrographs (right) provide a clear representation of the square magnetic elements, yet these are superimposed on a rather similar looking background. The presence of this

background indicates that the incident fluence of Ar^+ ions was not great enough to remove the entirety of the un-masked bi-layer. In this regard, MFM provides a useful tool for checking the progression of the Ar^+ ion milling process.

The incident ion fluence was subsequently doubled to 1.1×10^{17} Ar^+ ions cm^{-2} in order to ensure the removal of the entirety of the un-masked material. The corresponding AFM and MFM micrographs can be seen in Figure 6.2.

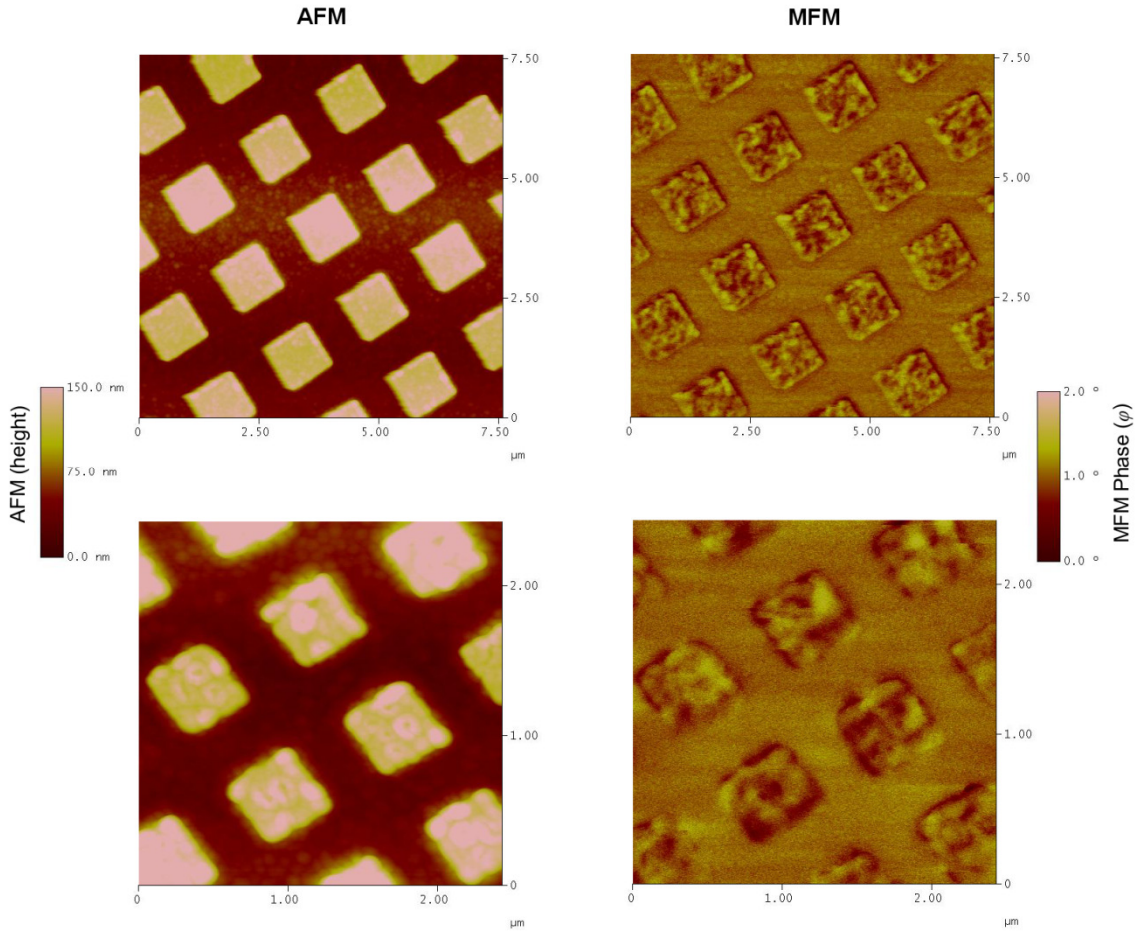

Figure 6.2: AFM (left) and MFM (right) micrographs of 1 μm (top) and 500 nm (bottom) squares. The patterned array has been subjected to a fluence of 1.1×10^{17} Ar^+ ions cm^{-2}. The AFM data show the same degree of resolution as those subjected to half this Ar^+ ion fluence in Figure 6.1. The MFM data is taken in the remnant state and show magnetic contrast in the patterned elements only.

From the AFM micrographs (left) it is immediately clear that doubling the incident Ar^+ ion fluence has not resulted in a loss of pattern resolution. The patterned element sizes remaining as 1.1 μm and 550 nm suggest that the fabrication of slightly larger features than intended was in fact an error in the lithography process and was *not* due to sloped-side walls and re-deposition in this *thin* sample. The MFM micrographs (right) show that both the 1.1 μm and 550 nm squares are composed of multiple magnetic domains. This is to be expected since the sample was measured in the remnant state, and had been

subjected to a demagnetization process before fabrication of the patterned arrays. The only magnetic field which the patterned elements have experienced is the very small stray field from the MFM cantilever. This is too weak to cause anything other than a very small, local perturbation in the magnetization. The alignment of the domains is completely random, confined only by the geometry of the patterned elements, so as to minimize the demagnetizing energy of the sample. Closer inspection of these MFM data show the domains to have, on average, lateral dimensions between 50 and 100 nm, as anticipated earlier. It would also appear that one patterned region does not affect another, in that there is no long-range ordering between adjacent elements.

The bi-layer sample has been characterized in its remnant state and no magnetic field has been applied prior to this, therefore the reader should not expect to see the alternating bright and dark lines such as those depicted in Figure 3.25 at the edges of the patterned elements. Such features are indicative of a sample characterized at remanence after it has been exposed to an applied magnetic field. What is made clear from the random variations in MFM contrast in this sample is that it comprises a random array of components pointing both into and out of the plane, which are confined by the lithographically defined patterns.

6.2 Patterned Elements in a $DyFe_2$ / YFe_2 Exchange Spring Superlattice

The epitaxially grown [3 nm $DyFe_2$ / 12 nm YFe_2] × 27 multilayer exchange spring sample that was successfully patterned in section 4.2.7 exhibits a high degree of magnetic anisotropy due to both magnetocrystalline and magnetoelastic effects. Accordingly this makes the sample a prime candidate for studying the effects of artificially induced shape anisotropies, providing a means to investigate the potential uses of nano-scale patterned epitaxial exchange spring systems. It is believed that the patterning of these samples may find applications in ultra-high density magnetic data storage [5], magnetoresistive random access memory (MRAM) [6] or as hard nano-magnets in microelectromechanical systems (MEMS) [7]. At this point, the reader should be aware that given the thickness of this multilayer sample (~ 400 nm), the patterning process employed herein does not transfer the patterned elements throughout the entire sample. The self-mask process has been used to help alleviate this, but for reasons regarding the preservation of well defined, isolated patterned elements as

discussed in section 4.2.8, has been terminated prior to completion. The result is the first demonstration of nano-scale patterned elements in a $DyFe_2$ / YFe_2 multilayer exchange spring sample, superimposed on a thin background of magnetic material.

The sample was prepared with various patterned elements, ranging from small arrays of squares with lateral dimensions on the scale of hundreds of nm (ideal for MFM studies) to arrays of 1 μm lines covering an area of 500 × 500 μm (especially suited to MOKE characterization). In an attempt to minimize the effects of re-deposition (see section 4.3), the author has ensured that the pitch of the patterned elements is suitably large so that the ensuing sloped side-walls (due to Ar^+ ion milling) can be accommodated. First, an MFM study of the sample is presented and discussed, providing an insight into the sample's nano-scale magnetic properties. This data is then complimented by a larger scale MOKE characterization of the magnetic properties and a discussion of competing magnetic anisotropies.

6.2.1 Arrays of lines characterized by magnetic force microscopy

Magnetic force microscopy has been used to probe and characterize the local magnetization states of arrays of lines patterned in the [3 nm $DyFe_2$ / 12 nm YFe_2] × 27 exchange spring sample. The reader should recall from Chapter 5 that due to the ions implanted during the patterning process, there should be a departure of the sample's easy and hard axes of magnetization from that of the as-grown, un-patterned sample. This is caused by a relaxation of the strain and accordingly there is a significant reduction in the magnetoelastic anisotropy. In the as-grown sample, the easy and hard axes of magnetization lie along the $[\bar{1}10]$ and $[001]$ directions respectively [8, 9] (with a small out of plane component [10]). This is reversed in the Ar^+ ion implanted sample (specifically, see section 5.3. All of the MFM data are taken at remanence after the sample has been prepared using an external magnetic field of 1.0 T provided by an electromagnet in a VSM. The corresponding hysteresis loops (obtained by VSM) are also shown to illustrate the magnetic properties of the bulk of the sample (both patterned and un-patterned regions) at remanence.

In Figure 6.3, AFM and MFM micrographs for the [3 nm $DyFe_2$ / 12 nm YFe_2] × 27 sample patterned with 1.9 μm wide (2.0 μm pitch) lines can be seen. The lines were patterned with their major axis parallel to the $[\bar{1}10]$ direction, which is close to the easy axis of magnetization in the as-grown sample. However, due to the Ar^+ ion implantation and subsequent relaxation of the strain, the $[\bar{1}10]$ direction is now a hard

axis of magnetization. The magnetic field ($\mathbf{B}_{app}$) was applied perpendicular to the major axis of the lines, along the [001] direction. A hysteresis loop, showing the sample prepared with the magnetic field applied along the [001] direction can be seen in Figure 6.4, confirming that this is indeed now an easy axis of magnetization.

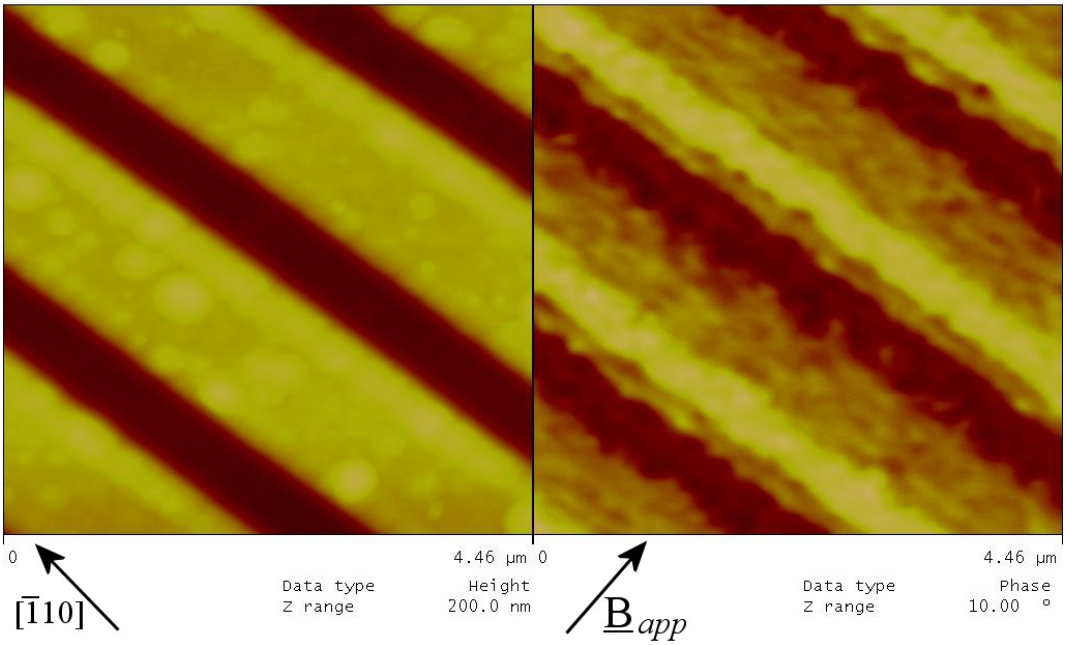

Figure 6.3: AFM (left) and MFM (right) micrographs of 1.9 μm wide (2.0 μm pitch) lines patterned in the [3 nm $DyFe_2$ / 12 nm YFe_2] × 27 sample. The major axis of the lines is parallel to the [$\bar{1}$10] direction, now a hard axis of magnetization. $\mathbf{B}_{app}$ is along an easy axis. The MFM tip to sample separation is 50 nm. The MFM data show the increased stray field ($\mathbf{B}_S$) at the edges of the patterned elements. Yellow represents a significant $\mathbf{B}_S$ out of the plane of the sample, whilst brown represents a $\mathbf{B}_S$ into the sample plane. Regions where $\mathbf{B}_S$ is small are represented by orange. Note that the AFM data show patterned elements that appear narrower than 1.9 μm. A cross-sectional AFM scan (*e.g.* Figure 6.5) confirms these dimensions to be correct; the discrepancy in the *image* is purely due to a lack of available contrast.

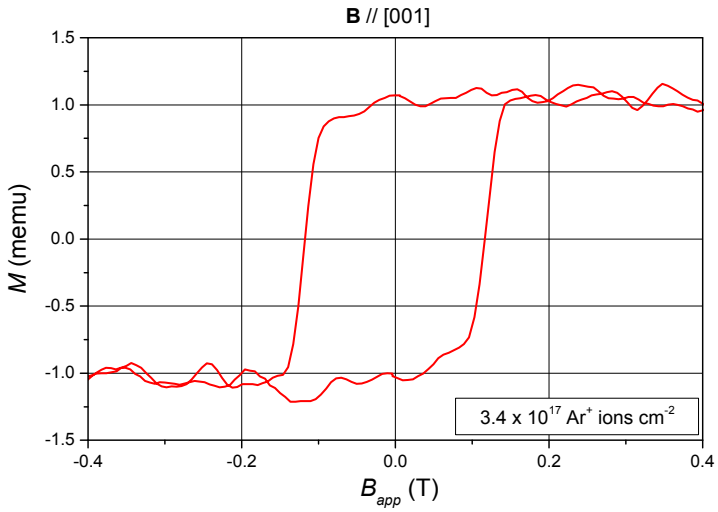

Figure 6.4: VSM hysteresis loop of the [3 nm $DyFe_2$ / 12 nm YFe_2] × 27 sample prepared with the magnetic field aligned along the [001] direction (easy axis of magnetization after Ar^+ ion implantation). The hysteresis loop has a high squareness, *i.e.* $\frac{M_R}{M_S} \approx 1.0$.

In the MFM data of Figure 6.3 (right-hand image) there are three general colour regimes: brown (corresponding to a maximum cantilever phase change angle $\Delta\varphi \gtrsim -5°$), orange ($\Delta\varphi \approx 0°$) and yellow ($\Delta\varphi \lesssim +5°$). $\Delta\varphi \gtrsim -5°$ represents the stray magnetic field ($\mathbf{B}_S$) pointing into the sample plane, whilst $\Delta\varphi \lesssim +5°$ represents $\mathbf{B}_S$ pointing out of the plane. This is analogous with the "–" and "+" signs in Figure 3.24. Clearly, $\Delta\varphi \approx 0°$ is indicative of very few surface poles and hence a small $\mathbf{B}_S$, as would be expected for a sample in which the magnetization lays predominantly in the plane. The fact that there are extensive regions of continuous contrast illustrate that the sample magnetization is directed predominantly in one direction, as would be expected from the high squareness of the accompanying hysteresis loop (Figure 6.4)

In the MFM data of Figure 6.3, between the brown and yellow regions there are two orange regions, one with a width of ~ 850 nm, the other ~ 150 nm. The wider region is representative of the minimal $\mathbf{B}_S$ atop the patterned regions as would be expected. The narrower region corresponds to a small $\mathbf{B}_S$ present in the "substrate" between the patterned elements. As already pointed out, the substrate is in fact part of the continuous under-layer of magnetic material, from which a small $\mathbf{B}_S$ should also be expected. Presented in Figure 6.5 are the AFM and MFM micrographs of Figure 6.3 in conjunction with cross-sections through these data. From the cross-sections it is clear that the regions where $\mathbf{B}_S$ points predominantly into or out of the sample plane extend over significantly larger areas than those corresponding to the side-walls of the patterned region. The distance between the green markers (MFM data) is ~ 460 nm whilst that between the red markers (AFM data) is ~ 275 nm.

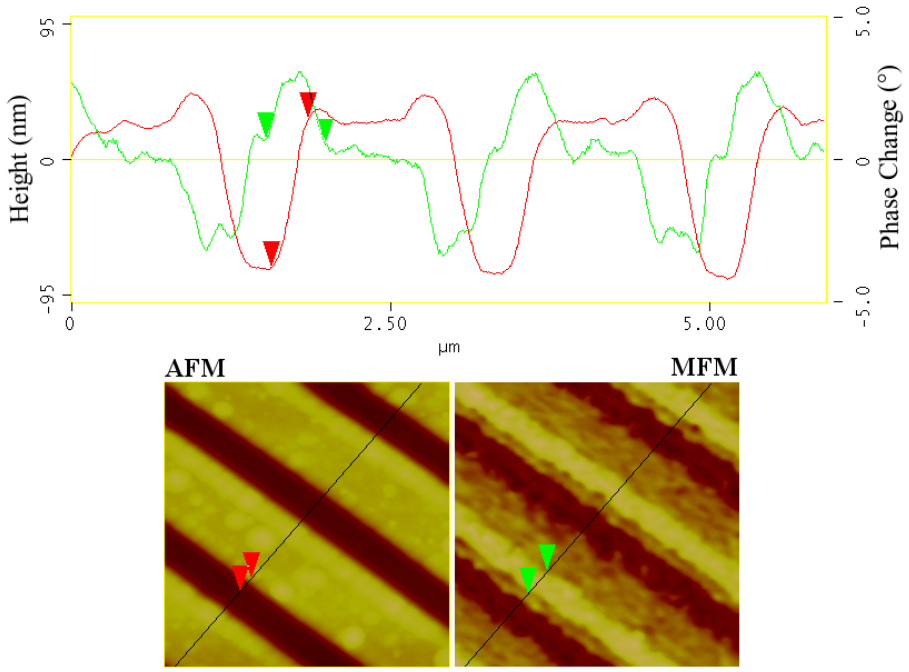

Figure 6.5: In the top image cross-sections of AFM (red) and MFM (green) can be seen, derived from the accompanying AFM and MFM micrographs in the lower images. The change in MFM phase, proportional to $\mathbf{B}_S$, extends laterally over ~ 460 nm, encroaching on the flat surfaces of both the patterned and un-patterned regions. In contrast, the lateral size of the sloped side-walls is just ~ 275 nm. Note that the "peaks" in the AFM data are due to re-deposition, as discussed in section 4.3.

The lateral area which $\mathbf{B}_S$ extends over provides a useful visualisation of the distribution of magnetic surface poles. Their presence has been induced by patterning the sample. From these data it is clear that the underlying magnetocrystalline anisotropy is more dominant than the induced shape anisotropy since the stray magnetic field remains predominantly confined to the sample plane. This is illustrated by the abundant orange regions in the MFM data, corresponding to a small $\mathbf{B}_S$ and hence in-plane sample magnetization. However, at the *edges* of the patterned regions, the in-plane magnetization gives rise to large $\mathbf{B}_S$, as depicted schematically in Figure 3.24. The fact that the yellow and brown regions (large out-of plane components of $\mathbf{B}_S$) in the MFM data extend over lateral dimensions greater than the width of the side-walls provides further confirmation that the sample magnetization lays slightly out of the plane of the material. This gives rise to a large number of magnetic surface poles towards the edges of the flat regions atop the patterned elements (again, see Figure 3.24). Thus the combination of sloped side-walls *and* an out of plane component to the sample magnetization is responsible for the extent of the lateral areas in which there is a large $\mathbf{B}_S$. Therefore the patterning process may be readily used to act as a useful tool to visualise the magnetization of the sample using MFM. In this example it is clear that

the magnetization of the sample lies in the plane and is relatively unaffected by the patterning process. The patterning process simply provides a "window" which can be used to visualize the magnetization of the sample. This process could be used as a "tag" to identify samples.

In Figure 6.6, further AFM and MFM micrographs of the same [3 nm $DyFe_2$ / 12 nm YFe_2] × 27 sample can be seen. Again the lines are 1.9 μm wide (2.0 μm pitch), however the major axis of these lines is parallel to the [001] direction. Due to the strain relaxation induced by the implantation of Ar^+ ions this is now the easy axis of magnetization. $\mathbf{B}_{app}$ remains in the same direction as that of Figure 6.3. Note that the AFM *z*-axis (colour contrast) data scales are constant between Figure 6.3 and Figure 6.6 as would be expected, but the MFM phase angle (φ) is different in amplitude by a factor in excess of two. Since almost all variables are kept constant between successive AFM / MFM data acquisitions (see section 3.9.5), it is possible to conclude that $\mathbf{B}_S$ from the sample with lines patterned along the [001] direction is significantly less than that of the sample with lines patterned along the $[\bar{1}10]$ direction.

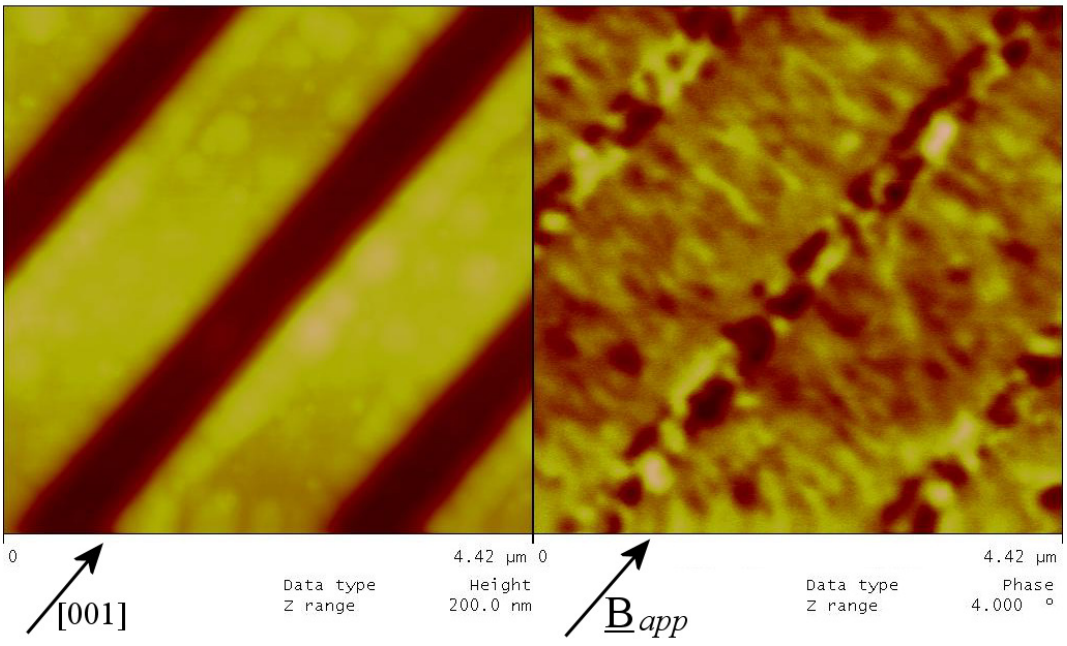

Figure 6.6: AFM (left) and MFM (right) micrographs of 1.9 μm wide (2.0 μm pitch) lines patterned in the [3 nm $DyFe_2$ / 12 nm YFe_2] × 27 sample with the major axis parallel to the [001] direction. This is an easy axis of magnetization, thus $\mathbf{B}_{app}$ is along an easy axis. The MFM tip to sample separation is 50 nm. The highest contrast MFM data occurs in the trenches between adjacent patterned elements, thus $\mathbf{B}_S$ is greatest in this region.

From Figure 6.6 it is clear that when $\mathbf{B}_{app}$ lies along the major axis of the patterned array of lines, the sample magnetization tends to remain predominantly confined in the plane.

This is indicated by the small values of $\Delta\varphi$ detected; less than half that of the sample with lines with a major axis orthogonal to these. This is to be expected since these patterned elements are exactly the same as those in the previous paragraph, thus have an associated shape anisotropy notably less dominant than the intrinsic magnetocrystalline anisotropy. Since the edges of these patterned elements are parallel to the direction in which $\mathbf{B}_{app}$ was applied, there are relatively few magnetic surface poles, giving rise to the observed lack of MFM contrast. This is indicative of a small $\mathbf{B}_S$ from the sample.

A further striking result from Figure 6.6 is the appearance of regularly arranged elements, concentrated in the trenches between the patterned regions. This is presented in more detail in a cross-sectional arrangement in Figure 6.7.

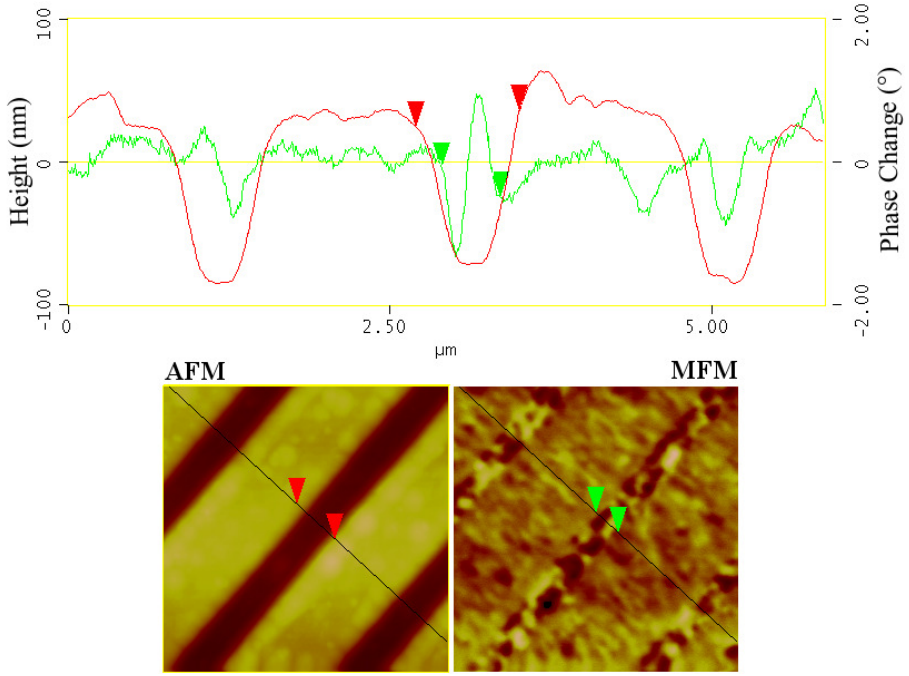

Figure 6.7: In the top image, cross-sections of AFM (red) and MFM (green) data are presented. These are derived from the accompanying AFM and MFM micrographs. The change in MFM phase, proportional to $\mathbf{B}_S$, is confined almost entirely in the trenches between patterned regions. Note that the "peaks" in the AFM data are due to re-deposition, as discussed in section 4.3.

Each individual bright and dark region has a size equal to approximately 400 × 200 nm, elongated along the [001] (easy axis) direction. From the cross-sectional image in Figure 6.7 it is clear that these elements are confined to be almost completely in the trenches between the patterned regions, extending little or no distance up the side-walls. The exact nature of the $\mathbf{B}_S$ responsible for these bright and dark regions is currently unclear. It is possible that they are domains, occurring since the patterned lines provide a physical barrier that stops the magnetization from pointing in the sample plane,

forcing it to point out of the plane in order to minimize energy. This could lead to an abundance of magnetic surface poles with a comparatively large $\mathbf{B}_S$ confined to a small region such as that presented in these MFM data. Clearly further work is required to investigate this interesting phenomenon further.

The key effects described in the preceding paragraphs may be summarised thus. After application of a magnetic field parallel to the easy axis of magnetization (the [001] direction), the sample remained magnetized in this direction once the field was removed and the MFM data obtained (recall the high squareness of the hysteresis loop in Figure 6.4). Hence for lines patterned along both the $[\bar{1}10]$ and [001] directions the sample magnetization remained parallel to the applied magnetic field, irrespective of the orientation of the lines, since the shape anisotropy induced by the lines was small compared to that of the intrinsic magnetocrystalline anisotropy. Thus the magnetization of the sample encounters many more "edges" in the case of the lines parallel to the $[\bar{1}10]$ direction than for the [001] direction. These edges give rise to surface poles and the associated stray magnetic fields. This is summarised elegantly in the illustrations provided in Figure 6.8.

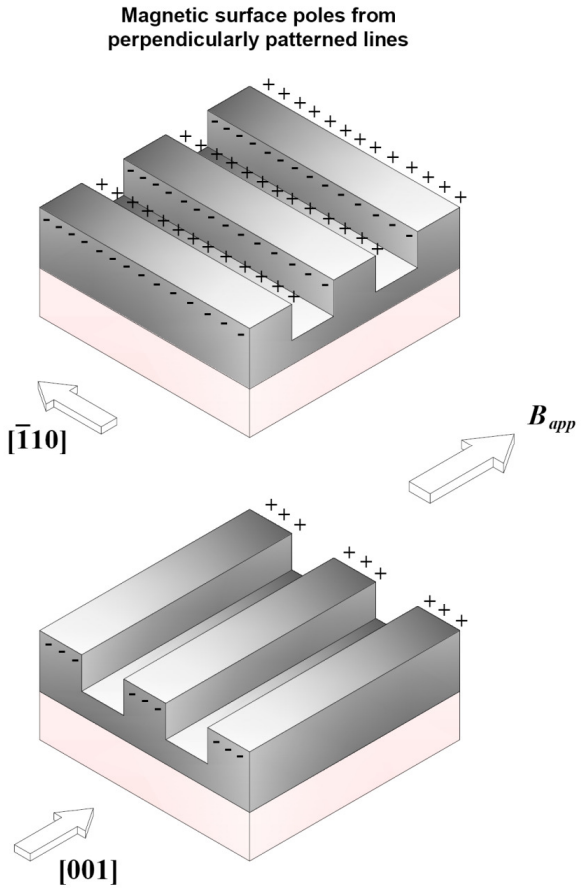

Figure 6.8: Schematic illustration (not to scale) of the magnetic surface poles induced by patterning lines along different crystallographic directions. "+" and "–" indicate $\mathbf{B}_S$ into and out of the plane of the sample respectively. When $\mathbf{B}_{app}$ is perpendicular to the major axis of the patterned lines (top image) there are many surface poles (*c.f.* MFM data of Figure 6.3), whereas there are very few present when the applied magnetic field is parallel to the lines' major axis (lower image) (*c.f.* MFM data of Figure 6.6 (taken away from the ends of the lines)).

Figure 6.8 suggests that at the ends of the lines patterned with the major axis along the [001] direction (lower image), there should exist regions where there are many magnetic surface poles and hence a large $\mathbf{B}_S$. When analyzed by MFM this should give rise to large shifts in the cantilever phase, comparable in magnitude to those experienced when the lines are oriented orthogonal to this (upper image of Figure 6.8 and Figure 6.3). Indeed this is observed experimentally. MFM micrographs, taken at adjacent ends of the entire 500 μm array of lines with the major axis along the [001] direction, prepared with the magnetic field parallel to this, can be seen in Figure 6.9 and Figure 6.10.

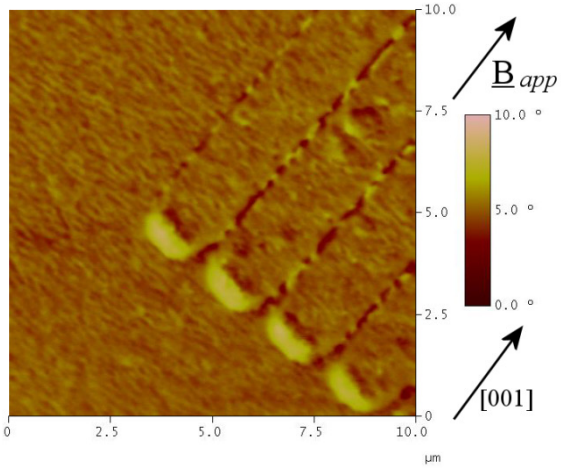

Figure 6.9: MFM micrograph taken at the end of an array of lines patterned with major axis parallel to the [001] direction. The MFM tip to sample separation is 50 nm. The phase change experienced by the MFM cantilever is $\Delta\varphi \approx +3.3 \pm 0.2°$.

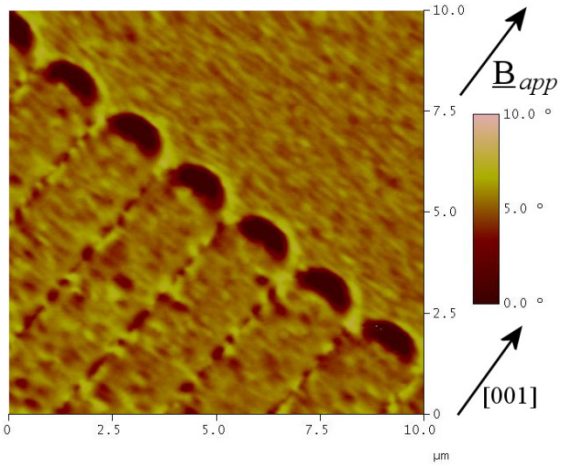

Figure 6.10: MFM micrograph taken at the opposite end of the array of lines presented in Figure 6.9. The MFM tip to sample separation remained as 50 nm. The phase change experienced by the MFM cantilever is $\Delta\varphi \approx -3.5 \pm 0.2°$.

The average phase change angle in the MFM measurements in Figure 6.9 and Figure 6.10 is $|\Delta\varphi| = 3.4°$. This is close to that for the lines patterned orthogonal to this (see Figure 6.3, where $|\Delta\varphi| \lesssim 5°$). Thus it is reasonable to assume that $\mathbf{B}_S$ present in both samples is roughly the same at the edges of the patterned elements which are parallel to the $[\bar{1}10]$ direction. This confirms the schematic representation of the surface poles model presented in Figure 6.8.

The same sample of [3 nm $DyFe_2$ / 12 nm YFe_2] × 27 has also been characterized after preparation with the magnetic field oriented along the $[\bar{1}10]$ direction (a hard axis of magnetization after Ar^+ ion implantation). The corresponding hysteresis loop taken during this preparation can be seen in Figure 6.11.

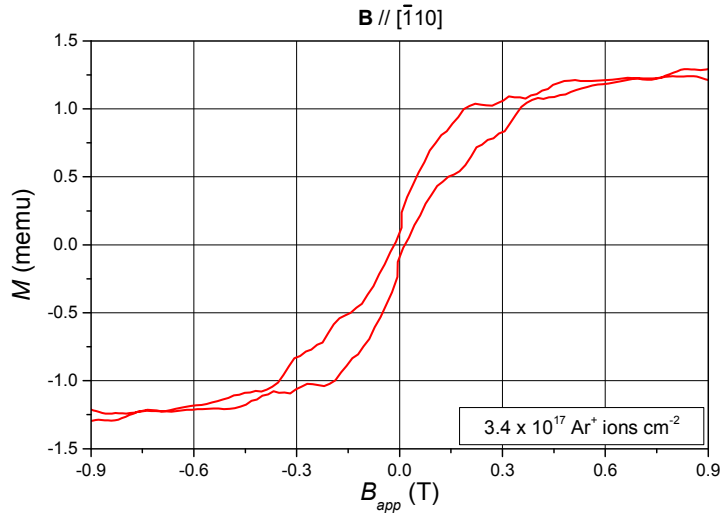

Figure 6.11: VSM hysteresis loop of the [3 nm $DyFe_2$ / 12 nm YFe_2] × 27 sample prepared with the magnetic field aligned along the [$\bar{1}$10] direction (hard axis of magnetization). At $\mathbf{B}_{app}$ = 0, $\mathbf{M}_R$ < 0.1 memu.

The hysteresis loop confirms that the [$\bar{1}$10] direction is indeed now a hard axis of magnetization. The magnetization at remanence ($\mathbf{M}_R$) is ≤ 0.1 memu and the coercive field is ≤ 10 mT[i]. These data would therefore suggest that, at remanence, in the un-patterned material at least, the individual magnetic domains are arranged randomly throughout the entire sample with no long range order.

In Figure 6.12 AFM and MFM micrographs of lines with the major axis parallel to the [$\bar{1}$10] direction in the [3 nm $DyFe_2$ / 12 nm YFe_2] × 27 sample can be seen. These data were taken at remanence, after the sample had been subjected to a magnetic field parallel to this direction.

[i] This magnetization is equal to approximately the sensitivity of the VSM, and step size of 10 mT was to obtain the data for this measurement.

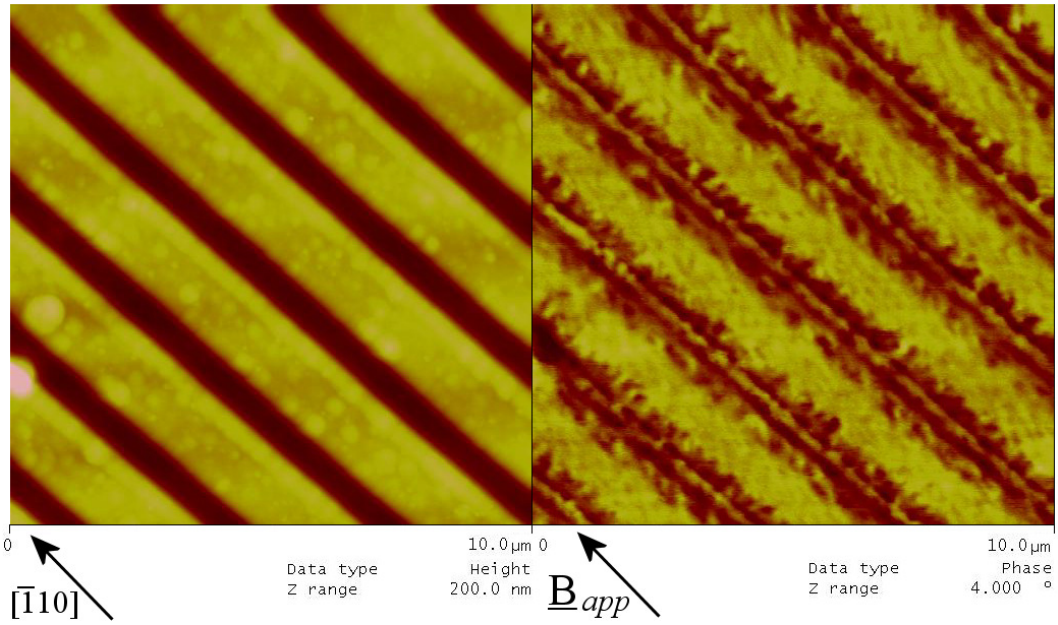

Figure 6.12: AFM (left) and MFM (right) micrographs of 1.9 μm wide (2.0 μm pitch) lines patterned in the [3 nm $DyFe_2$ / 12 nm YFe_2] × 27 sample with their major axis parallel to the [$\bar{1}$10] direction (hard axis of magnetization) and $\mathbf{B}_{app}$ parallel to this. The MFM tip to sample separation is 50 nm.

The MFM data suggests that the local shape anisotropy induced by the patterned array of lines does induce a change in the sample magnetization at remanence. The VSM data in Figure 6.11 show that there is only a negligible component of magnetization along the [$\bar{1}$10] direction at remanence (as expected since this is a hard axis). Accordingly the sample should be broken down into multiple domains with no long-range magnetic ordering. The MFM data in Figure 6.12 does show these domains, but also some ordering of $\mathbf{B}_S$. Whilst the magnetization is generally confined to the sample plane (note the much smaller phase change scale on the MFM data in Figure 6.12 *c.f.* data with the magnetic field applied along the [001] direction, *e.g.* Figure 6.3), at the top of (sides of) the patterned regions, B_S points slightly out of (into) the plane of the sample, illustrated by the predominantly yellow (brown) colour. $\mathbf{B}_S$ is now of opposite signs in well defined regions. This is in contrast to the un-patterned sample, where $\mathbf{B}_S$ varies randomly across the entire sample surface.

Analysis of samples prepared with the magnetization forced to lie along a hard axis is often more complex than those samples with magnetization aligned along the easy axis, due to the random distribution in the magnetization of the domains in order to minimize energy. Clearly in order to fully interpret the above MFM measurements further work is needed, but it is safe to conclude that the induced shape anisotropy has provided a constraint on the occurrence of surface magnetic poles. On top of the

patterned regions a small component of $\mathbf{B}_S$ points out of the plane of the sample, whilst at the sloped side-walls to these regions a small component points into the sample plane.

6.2.2 Arrays of squares characterized by magnetic force microscopy

This section provides MFM characterization of the patterned arrays of square elements, defined in the [3 nm $DyFe_2$ / 12 nm YFe_2] × 27 exchange spring sample. The lateral dimensions of these squares range from 1 μm down to 100 nm. However, due to reasons associated with re-deposition of sputtered material (described in detail in section 4.3), the squares with lateral dimensions less than nominally 400 nm merged together. The nominally 400 nm elements (800 nm pitch) have actual lateral dimensions of 700 nm (with the same pitch) as shown in the SEM and AFM micrographs of Figure 4.20 and Figure 4.21. Nevertheless, these are the smallest square elements to be defined in a thick, epitaxial multilayer sample of $REFe_2$ to date. MFM characterization was performed at remanence after the sample was prepared by saturation of the magnetization with a 1.0 T electromagnet which was subsequently removed.

In Figure 6.13 an MFM micrograph of an array of 700 nm squares patterned in a [3 nm $DyFe_2$ / 12 nm YFe_2] × 27 multilayer sample can be seen. The square elements are patterned with their edges parallel to the $[\bar{1}10]$ and [001] axes. The magnetic field ($\mathbf{B}_{app}$) was applied parallel to the [001] direction (an easy axis of magnetization in this Ar^+ ion implanted sample).

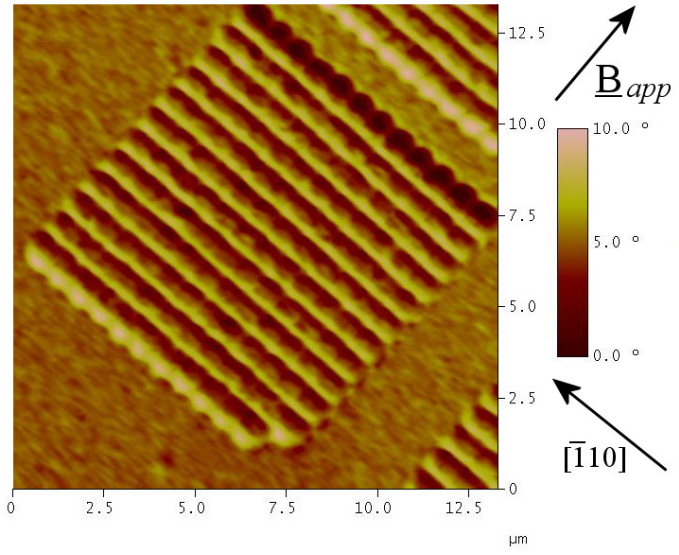

Figure 6.13: MFM micrograph of an array of 143 squares with 700 nm lateral dimensions in the [3 nm $DyFe_2$ / 12 nm YFe_2] × 27 multilayer sample. The sample was prepared with $\mathbf{B}_{app}$ along the [001] direction (easy axis of magnetization). The data clearly show the existence of significant $\mathbf{B}_S$, which is greatest at the edges of the patterned array. Missing square to assist in sample orientation only.

When prepared with a magnetic field along the [001] direction it is to be expected that these arrays of squares will behave as a combination of the lines with major axis parallel to the $[\bar{1}10]$ direction (Figure 6.3) and those with major axis perpendicular to this (Figure 6.6). Accordingly the MFM micrograph would show bright and dark edges to the square elements running parallel to the $[\bar{1}10]$ direction, with smaller, lower contrast regions corresponding to domains running along to the [001] direction. The MFM data in Figure 6.13 clearly shows the former effect but not the latter. Indeed the possible domains so prominent in Figure 6.6 are not apparent even at increased magnification (not shown). The individual square elements remain equally well defined along each axis (recall Figure 4.20 and Figure 4.21), thus the loss of the small $\boldsymbol{B}_S$ parallel to the [001] direction is not due to an A^{r+} ion milling induced loss of resolution. It is suggested that domains are not trapped along the [001] direction since there are many more patterning induced defects in this sample leading to more favourable lower energy states.

As noted in section 4.2.7, specifically Figure 4.21 and Figure 4.22, the "individual" magnetic nano-elements have begun to merge together in this sample. Since the physical surface area of the side-walls is reduced in this configuration, there are less magnetic surface poles present in the regions between adjacent elements. This leads to a reduction in $\mathbf{B}_S$. This reduction should lead to a concomitant reduction in the change of phase ($\Delta\varphi$) experienced by the MFM cantilever. Thus the magnitude of $\Delta\varphi$ should be greatest at the *edges* of the array, with a reduced value *between* adjacent elements. This is exactly what is observed in the MFM data in Figure 6.13 where brighter stripes are clearly present at the extremes of the patterned region.

As a final remark, it is interesting to note effects induced by rotating the applied magnetic field through 180°. At remanence, standard magnetization measurement techniques such as VSM and MOKE provide equivalent data at two points on the hysteresis loop; one originating from positive saturation of sample magnetization (+ $\mathbf{M}_S$) and one from negative saturation (– $\mathbf{M}_S$). MFM can be used to probe these two states and provide a clear picture of any different orientation to $\mathbf{B}_S$, depending on whether remanence was approached from + $\mathbf{B}_{app}$ or – $\mathbf{B}_{app}$. The data presented thus far has been taken after the sample was prepared in the + $\mathbf{M}_S$ state. This results in an MFM micrograph for the [3 nm $DyFe_2$ / 12 nm YFe_2] × 27 multilayer sample such as that in

Figure 6.14. When the same sample is prepared in the opposite state (– $\mathbf{M}_S$), the MFM micrograph in Figure 6.15 is obtained.

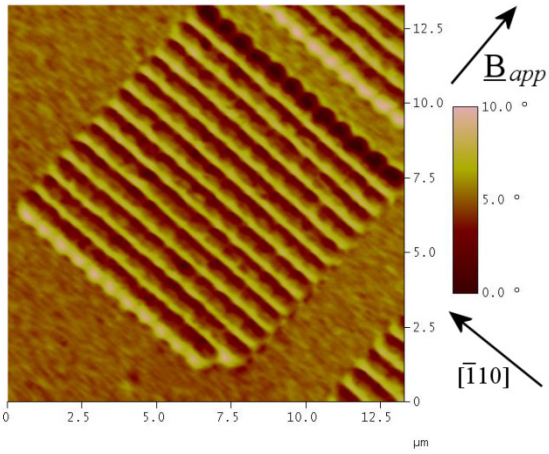

Figure 6.14: MFM micrograph taken from Figure 6.13. The sample was prepared with $\mathbf{B}_{app}$ along the [001] direction, corresponding to $\mathbf{M}_R$ approached from + $\mathbf{B}_{app}$.

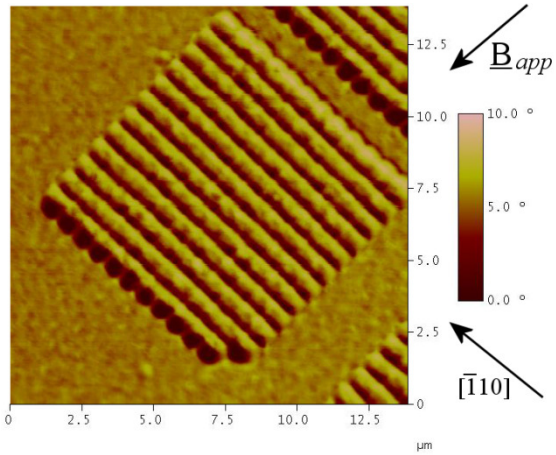

Figure 6.15: MFM micrograph prepared with $\mathbf{B}_{app}$ in the opposite direction to that of Figure 6.14, along the [00$\bar{1}$] direction. This corresponds to $\mathbf{M}_R$ approached from – $\mathbf{B}_{app}$.

Side-by-side comparison of these data immediately shows that all of the light and dark regions have exchanged positions. This corresponds to the entire rotation of $\mathbf{B}_S$ by 180° through the plane of the sample, as expected. This is equivalent to exchanging the position of all the "+" and "–" symbols in the schematic representation in Figure 3.24, resulting in all of the $\mathbf{B}_S$ vectors changing sign. Note that the overall background contrast and texture remains constant since this corresponds to a *random* arrangement of small $\mathbf{B}_S$.

Repeated measurements of this region taken at different times (over a period of weeks) after preparation in either the + $\mathbf{M}_S$ or – $\mathbf{M}_S$ state reveal identical MFM micrographs to those of Figure 6.14 and Figure 6.15. This confirms that the sample is thermally stable, even in the 700 nm square elements over relatively long lifetimes. Such analysis cannot readily be performed using techniques such as MOKE or VSM since these require the application of a comparatively large external magnetic field to acquire data. This process will destroy any small changes in sample magnetization due to thermally induced events *etc*. Thus MFM is a very useful tool for the rapid characterization of the magnetization of a sample in its remnant state, with the stray fields from the cantilever producing only a negligible perturbation in the sample magnetization and local sample $\mathbf{B}_S$.

6.2.3 Magneto optical Kerr effect characterization of arrays of lines

Arrays of lines 1.9 μm wide, separated from adjacent elements by 100 nm (2.0 μm pitch) patterned in the [3 nm $DyFe_2$ / 12 nm YFe_2] × 27 multilayer exchange spring sample have been characterized by MOKE. A benefit of MOKE over MFM is that it provides hysteresis loops from which some quantitative data can be drawn. As identified in section 6.2.1, the arrays of patterned lines in the sample remain superimposed on a magnetic background. This has the net effect of reducing any apparent changes in the characteristics of the hysteresis loops obtained for the patterned regions, since here both the magnetic background *and* the patterned elements are sampled at the same time. Nevertheless, if a hysteresis loop of a patterned region is different in nature to that of an un-patterned region, then this change, although attenuated by the presence of the background signal, must be due to artificially induced shape anisotropy.

The data presented here were acquired after implantation by 3.4×10^{17} Ar^+ ions cm^{-2}, thus it will again be apparent that the easy and hard axes of magnetization within this sample have been rotated by 90° from that of the as-grown epitaxial sample (see sections 5.3 and 6.2.1). Accordingly, the $[\bar{1}10]$ direction is a hard axis of magnetization whilst the $[001]$ direction is an easy axis.

Hysteresis loops obtained by MOKE can be seen in Figure 6.16. Graphs a) and b) pertain to the un-patterned (Ar^+ ion implanted) sample and as such are identical to graphs f) and e) in Figure 5.19. Note that graph b) in Figure 6.16, taken with the magnetic field ($\mathbf{B}_{app}$) applied along the $[\bar{1}10]$ direction, is neither exactly symmetric nor centred about the origin. These features are characteristic of a partial loop and confirm that along the hard axis, magnetic saturation is not attainable in the MOKE apparatus. Graphs c) and d) correspond to data taken from a region where lines were patterned with major axis parallel to the hard axis of magnetization ($[\bar{1}10]$ direction) whilst graphs e) and f) were acquired from a region with lines patterned with major axis parallel to the easy axis ($[001]$ direction).

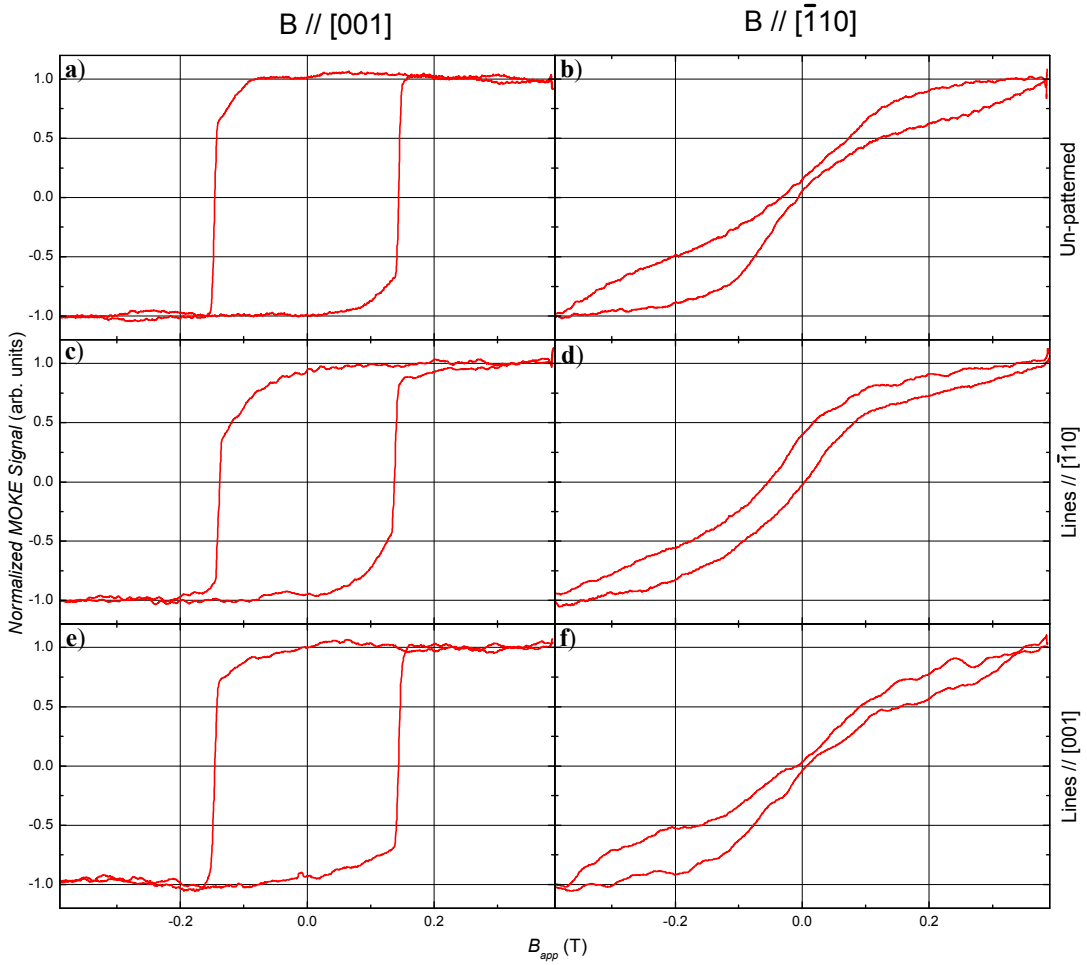

Figure 6.16: MOKE hysteresis loops of the [3 nm $DyFe_2$ / 12 nm YFe_2] × 27 multilayer exchange spring sample. Un-patterned regions (graphs a) and b)), regions with lines patterned with major axis parallel to the [$\bar{1}$10] direction (graphs c) and d)), and parallel to the [001] direction (graphs e) and f)).

It is clear from Figure 6.16 that the effect of creating patterned lines on this length scale does not induce any significant changes to the magnetization reversal properties of this sample. Hysteresis loops taken with $\mathbf{B}_{app}$ along the easy axis of magnetization (*i.e.* graphs a), c) & e)) remain relatively square. When $\mathbf{B}_{app}$ is orthogonal to this (*i.e.* graphs b), d) & f)), hysteresis loops remain characteristic of a hard axis of magnetization; the saturation magnetization of the sample is never reached nor are the hysteresis loops symmetric about the origin.

Lines patterned with major axis parallel to the easy axis of magnetization ([001] direction) show hysteresis loops which are almost identical to those measured for the un-patterned sample (Figure 6.16; graphs e) & f) *c.f.* graphs a) & b)). When characterized with $\mathbf{B}_{app}$ along the [001] direction, the un-patterned sample has $\frac{M_R}{M_S} = 1.00$ and a coercivity $H_C = 146 \pm 2$ mT. The patterned sample has $\frac{M_R}{M_S} = 0.95$ and

$H_C = 146 \pm 2$ mT, clearly very similar. Note that both samples exhibit the same amount of gradual rotation of magnetization (curved regions of the hysteresis loops), with the remaining 65 ± 5 % being attributed to the rapid motion of domain walls. It is not possible to quantify the hysteresis loops for $\mathbf{B}_{app}$ along the $[\bar{1}10]$ direction since these are partial loops, but all data appear relatively similar, *i.e.* a very similar partial loop is obtained, whether it be measured in patterned or un-patterned regions. Since graphs a), b), e) & f) are essentially identical, it is possible to conclude that patterning lines on this scale with their major axis parallel to the easy axis of magnetization has no notable effect on the magnetization reversal properties of the sample.

The array of lines fabricated with major axis parallel to the hard axis of magnetization ($[\bar{1}10]$ direction, Figure 6.16, graphs c) & d)) exhibit hysteretic behaviour which is slightly different to that of the un-patterned sample. When $\mathbf{B}_{app}$ is along the $[001]$ direction (graph c), *i.e.* perpendicular to the major axis of the lines), the sample has $\frac{M_R}{M_S} = 0.90$ and $H_C = 140 \pm 2$ mT. These values are smaller than those for the un-patterned sample (graph a)). There is now evidence for a larger proportion of the sample magnetization reversal to be gradual rather than via rapid domain wall motion, illustrated by the greater curvature to the hysteresis loop. For the data obtained when $\mathbf{B}_{app}$ is parallel to the major axis of the lines (graph d)), there is increased evidence for a partial loop. The two halves of the hysteresis loop are of very similar shape, only shifted from each other by a small amount. It would appear therefore, that the patterning process has in this instance increased the saturation magnetization of the sample by a small, but noticeable amount. This is in rough qualitative agreement with the MFM data of the same region (see Figure 6.12 and the accompanying text in section 6.2.1), where this configuration showed slight modifications to the remnant state of magnetization.

6.2.4 Comparison of induced shape and intrinsic magnetocrystalline anisotropies

It is possible to approximate the additional shape anisotropy induced in the system by the presence of the patterned arrays of lines. Comparison can then be made between the shape anisotropy and that associated with the intrinsic anisotropy of the epitaxial system, *i.e.* the magnetocrystalline and magnetoelastic anisotropies. The induced shape anisotropy, K_s, may be determined from equation (2.27).

In determining the value attributed to the saturation magnetization, M_S, it is necessary to exercise caution. The author has measured the saturation magnetization of the [3 nm $DyFe_2$ / 12 nm YFe_2] × 27 multilayer sample using a VSM both before (not shown) and after the ion milling process (Figure 6.4 & Figure 6.11). The values are 2.1 ± 0.1 memu and 1.1 ± 0.1 memu, respectively. Previously it was shown that ion implantation does *not* affect the saturation magnetization of these samples. Any change in the saturation magnetization is simply due to the removal of material during the ion milling process (see sections 5.1.4 and 5.2.4). Thus the value for M_S for the ion implanted sample may be used to determine the sample volume. This is performed using equation (5.1) and the method discussed in the Appendix. The ion implanted sample has a saturation magnetization of M_S = 1.1 memu and lateral dimensions of d_1 = d_2 = d = 5 mm. Using data from Mougin *et al.* [11], the lattice parameters for YFe_2 and $DyFe_2$ are 0.7362 nm and 0.7324 nm respectively, giving an average parameter of a = 0.734 nm for the $DyFe_2$ / YFe_2 multilayer system. From Wang *et al.* [12] there are known to be 1.4 μ_B f .u.$^{-1}$ in such a multilayer exchange spring sample. From these data the thickness of the ion milled sample may be calculated to be $t_{ion\text{-}milled}$ = 170 nm. This is clearly a reasonable value when compared to results for YFe_2 and $DyFe_2$ in sections 5.1.4 and 5.2.4 respectively, especially considering this sample has been subject to a much greater fluence of 3.25 keV Ar^+ ions (3.4×10^{17} ions cm^{-2}). Thus the physical sample volume (V) may be calculated as $V = td^2 = 4.25 \times 10^{-12}$ m^3, hence the volume magnetization is 260 emu cm^{-3} (260 kAm^{-1}).

The demagnetizing factor, ΔN, in equation (2.27), can be found using the approximation of Osborn [13], where the patterned lines are considered as infinitely long elliptical cylinders. If the geometry of the lines is considered such that they are patterned in the x-y plane of the sample, *i.e.* an infinite length along the x-axis, a width w along the y-axis and a thickness t given by the z-dimension, the demagnetizing factors are given by:

$$\begin{aligned} N_x &= 0 \\ N_y &= \frac{t}{w+t} \\ N_z &= \frac{w}{w+t} \end{aligned} \qquad (6.1)$$

Thus $N_x + N_y + N_z = 1$, as expected. The longitudinal MOKE experiments conducted throughout this work probe primarily the in-plane components of magnetization, thus

only the demagnetizing factors N_x and N_y will be considered in the forthcoming analysis.

Using the values for $t \approx 110$ nm and $w \approx 1.90$ μm derived earlier, the in-plane induced shape anisotropy is given by $N_y = 0.054 = \Delta N$ (since $N_x = 0$). Combining this difference in demagnetizing factors with the value for M_S above gives, from equation (2.27), $K_s = 2.2 \times 10^3$ Jm^{-3}. This value of K_s can now be used to determine the magnetostatic energy (E_{MS}) of the system according to equation (2.28). However, given that the anisotropy of the present system is cubic rather than uniaxial, values for the direction cosines must first be defined. This is briefly described below and is based upon the work of Dr J. Zimmermann [14] who implemented this model into the `OOMMF` simulation package based upon work by Martin *et al.* [15] and Bowden *et al.* [16].

It has been clear throughout this work, that the easy and hard axes of magnetization of the present epitaxial Laves phase systems ("crystallographic directions") are not orthogonal with the reference *x*-, *y*- and *z*-directions ([100], [010] and [001] base vectors respectively), required for the use of direction cosines (α_i). Therefore it is necessary to perform a coordinate transformation to relate the crystallographic directions onto the base vectors of the system. This is achieved by two successive Euler rotations as described in [14]. The resulting transformation is given by the following matrix

$$\begin{pmatrix} x \\ y \\ z \end{pmatrix} = \begin{pmatrix} 0 & -\frac{1}{\sqrt{2}} & \frac{1}{\sqrt{2}} \\ 0 & \frac{1}{\sqrt{2}} & \frac{1}{\sqrt{2}} \\ -1 & 0 & 0 \end{pmatrix} \begin{pmatrix} x'' \\ y'' \\ z'' \end{pmatrix} \tag{6.2}$$

where the double-prime indicates the coordinates in the rotated system, *i.e.* the crystallographic directions. The direction cosines α_x α_y and α_z may now be defined as, for example $\alpha_x = -\frac{1}{\sqrt{2}} y'' + \frac{1}{\sqrt{2}} z''$, hence $\alpha_x{}^2 = \frac{1}{2}(y'' - z'')^2$.

It is now possible to define E_{MS} by substituting the transformations of equation (6.2) into equation (2.28) to give

$$E_{MS} = K_s \left(\tfrac{1}{2}(y'' - z'')^2 + \tfrac{1}{2}(y'' + z'')^2 \right) \tag{6.3}$$

When considering the patterned elements described in sections 6.2.1 and 6.2.3, interpretation of the data for the easy axis of magnetization was more readily performed than that for the hard axis. Accordingly, the shape anisotropy effects will be calculated for this axis only, with comparison made to the accompanying intrinsic anisotropy

energies of the system. The easy axis of magnetization within the present system, due to the effects of Ar^+ ion implantation during the patterning process is the [001] direction. Accordingly E_{MS} may be given from equation (6.3) as $E_{MS_{[001]}} = K_{S_{[001]}}\left(\frac{1}{2}(0-1)^2+\frac{1}{2}(0+1)^2\right) = K_{S_{[001]}}$. The in-plane demagnetizing factor has already been defined as $\Delta N = 0.054$ to give $K_S = 2.2 \times 10^3$ Jm^{-3}. Inserting this value gives an induced shape anisotropy energy of $E_{MS_{[001]}} = 2.2 \times 10^3$ Jm^{-3}. This induced anisotropy may be compared to the intrinsic anisotropy of the system, which the reader will recall is governed by both magnetocrystalline and magnetoelastic anisotropies. However, due to the Ar^+ ion implantation process, the magnetoelastic anisotropy of these epitaxial films has been shown to be eliminated (see Chapter 5). Thus, the remaining intrinsic anisotropy of the system is entirely magnetocrystalline in nature. The magnetocrystalline anisotropy energy (E_{MC}) may be calculated from equation (2.31) which must be used in conjunction with the coordinate transformations of equation (6.2) to give

$$E_{MC} = K_1\left(\frac{1}{4}\left(y''^2-z''^2\right)^2+x''^2\left(y''^2+z''^2\right)\right)+K_2\left(\frac{1}{4}x''^2\left(y''^2-z''^2\right)^2\right)+K_3\left(\frac{1}{16}\left(y''^2-z''^2\right)^4+\frac{1}{2}x''^2\left(y''^4+z''^4+6y''^2z''^2\right)\right) \quad (6.4)$$

The values K_1, K_2 and K_3 are derived from equation (2.32) using data from Zimmermann [14] for the temperature dependent multipolar coefficients ($\tilde{A}_j$). At room temperature these values are: $\tilde{A}_4 = -0.746752$ K f.u.$^{-1}$, $\tilde{A}_6 = -0.002870$ K f.u.$^{-1}$ and $\tilde{A}_8 = 0.0$ K f.u.$^{-1}$. This gives the following values for $\widetilde{K}_j$: $\widetilde{K}_4 = -2.086 \times 10^5$ Jm^{-3}, $\widetilde{K}_6 = -8 \times 10^2$ Jm^{-3} and $\widetilde{K}_8 = 0$. The values of K_1, K_2 and K_3 may now be defined as the following (using equation (2.33)): $K_1 = 8.91 \times 10^5$ Jm^{-3}, $K_2 = -9.4 \times 10^4$ Jm^{-3} and $K_3 = 0$. Since K_3 = 0 at room temperature, equation (6.4) is made significantly simpler. For the [001] direction it is given as $E_{MC_{[001]}} = K_1\left(\frac{1}{4}(0-1^2)^2+0\right)+K_2\left(\frac{1}{4}(0)\right) = \frac{K_1}{4} = 2.23 \times 10^5$ Jm^{-3}. $E_{MC_{[\bar{1}10]}} = \frac{5}{4}K_1+\frac{1}{4}K_2 = 1.09 \times 10^6$ Jm^{-3}, which is significantly larger than $E_{MC_{[001]}}$ as expected for a hard axis of magnetization. It is clear that $E_{MC_{[001]}} \gg E_{MS_{[001]}}$, hence the affects of patterning features with these lateral

dimensions will only have a very small, most likely negligible effect on the overall anisotropy of the system. Thus magnetic characterization of the patterned regions would be dominated by the underlying magnetocrystalline anisotropy. This is indeed what is evidenced by the MOKE characterization of the patterned regions in Figure 6.16. To achieve a shape anisotropy equal in magnitude to the intrinsic magnetocrystalline anisotropy (and assuming a patterning depth of 110 nm as before), lines with a width of approximately 90 nm would be required. Patterning on this scale is perfectly possible with small improvements to the pattern definition process and equipment.

The similarity between patterned and un-patterned media is most obvious when comparison is made between graphs a) and e) in Figure 6.16, data which for all intents and purposes is identical to within the noise and thermal drift of the system; lines patterned with their major axis parallel to the [001] direction (graph e)) appear to provide no constraining effects on the magnetization reversal properties of the system. This is confirmed by the very small shape anisotropy that is induced in the system, and can be considered physically as the lines having a width that is much larger than the lateral dimensions of a single magnetic domain. Therefore they provide only a very weak pinning effect. The vast majority of individual domains within each patterned element are not constrained by its extremities, thus are likely to be unaffected by this patterning process. This is further confirmed by the magnetization reversal process remaining very similar as highlighted in section 6.2.3; predominantly via rapid domain wall motion. A small reduction in coercivity and increase to the curvature of the hysteresis loop is noticed in graph c) (lines patterned with their major axis parallel to the $[\bar{1}10]$ direction). Whilst comparisons in anisotropy energies for lines patterned parallel to this axis are not as readily calculated as for those above, these data do suggest that the patterning process induces irregularities into the material's structure. It would appear that these irregularities favour gradual rotation of the magnetization over domain wall motion, illustrated by the greater curvature in the hysteresis loops. This could be due to the sample magnetization remaining less rigidly confined to the [001] direction, because there are now additional axes perpendicular to this in which the magnetization may preferentially wish to lie. Instead of the sample magnetization being confined by one of two easy axes, the magnetization may now gradually rotate into the $[\bar{1}10]$ direction during the reversal process (due to the presence of the patterned lines). Since

the magnetization reversal is now more gradual, this results in an increase to the curvature of the hysteresis loops when compared to the un-patterned media. However, since the induced shape anisotropy effects are so small, the magnetization does not remain pinned along this intermediate axis, thus the coercivity is not increased.

6.3 Concluding remarks on patterned elements in $REFe_2$ materials

For the first time, nano-scale patterns defined in bi- and multilayers of $DyFe_2$ / YFe_2 have been fabricated and characterized by both MFM and MOKE.

In section 6.1, a thin bi-layer sample of $DyFe_2$ / YFe_2 was successfully patterned into square elements with dimensions ranging between 1 μm and 500 nm. MFM was used to show that even on a scale as small as this the individual magnetic square elements contained multiple domains. These domains had lateral dimensions equal to between 50 and 100 nm. Moreover, each patterned element appeared to act completely independently to its neighbours, with no long-range order present throughout the entire array. Due to the relatively high anisotropy of these magnetic materials, the patterning process would have to be extended further into the nano-scale regime in order to define single-domain elements. However, thin films such as this bi-layer are very technologically relevant, especially in terms of magnetic data storage, thus the work represents important first steps towards the fabrication of prototype devices, which could be used for further investigations towards the use of antiferromagnetically coupled $REFe_2$ exchange spring media in magnetic data storage. This could also lead to applications in nano-scale sensors and actuators for MEMS, and spin transfer torque devices.

The fabrication and characterization of patterned elements in a thick (~ 400 nm) multilayer sample of epitaxial $DyFe_2$ / YFe_2 was shown to be successful. This included analysis of micron-sized elements separated by approximately 100 nm, the first time such high resolution patterning has been demonstrated in these materials. Due to the very hard, well-defined magnetic properties of the $DyFe_2$ / YFe_2 multilayer, it was found that the patterning process would need to be conducted on significantly smaller scales in order to induce an anisotropy more dominant than those intrinsic to the material. On the other hand, it is very important to note that hard magnetic media, unaffected by nano-scale patterning, is of great technological significance. For

example, intrinsically hard magnetic media which remains unaffected by nano-scale pattern definition could find application in the data storage industry. The need for media that remains magnetically very hard, even when patterned on the nm length scale is important in order to avoid superparamagnetic effects. So whilst patterning did not induce any prominent effects, this may in fact be beneficial in illustrating a candidate media ideally suited to structuring on the nano-scale. The higher magnetic fields required to write to this patterned media could be achieved by improvements to write-head design or via the inclusion of heat or microwave-assisted magnetic recording (HAMR [17] and MAMR [18] respectively, see section 2.7.4). In softer magnetic materials, where it is true the patterning processes have enjoyed more success due to its relative maturity in this field, induced shape anisotropy effects on media structured on similar length scales have been demonstrated (for example, see [19, 20, 21, 22, 23, 24]). Typically the patterned media may change its magnetization at very low applied magnetic fields, making it increasingly susceptible to erroneous reading and writing due to stray magnetic fields, as well as being very susceptible to superparamagnetic effects. Thus the hard $REFe_2$ media investigated in this work provides a useful route towards avoiding some of these shortcomings. It is also worthwhile noting that many of these soft materials were prepared using the arguably simpler fabrication process of lift-off. This work exclusively uses ion milling, a fabrication process which permits the use of much higher quality media and is already well established in the magnetic data storage industry for magnetic write head fabrication.

Finally, a useful spin-off from the patterning process was identified. Since the $REFe_2$ media is unaffected by patterning on the 100 nm length scale, the stray magnetic fields associated with such patterned elements can provide useful information on the remnant magnetization of the media. This provides a useful "lithographic imprinting" system where different regions of the media prepared in different magnetic states may be identified by simple MFM characterization. This could, for example, provide cornerstone research into lab-on-chip experiments, whereby the effects of the magnetic media on many external factors such as chemicals may be readily identified, or the media itself used for bio-analysis of organic materials [25, 26], all within a small and cost-effective local environment.

References

[1] Z.Q. Ma, W. Li, D.M. Wang, Z.X. Zhao, Y. Wang, W.J. Yang & W.G. Zhao, Sol. State Com., vol. 137, pp. 413 – 416, 2006.

[2] M. A. Herman & H. Sitter, *Microelec. J.*, vol. **27**, pp. 257 – 296, 1996.

[3] O. Biham, I. Furman, M. Karimi, G. Vidali, R. Kennett & H. Zeng, *Sur. Sci.*, vol. **400**, pp. 29 – 43, 1998.

[4] V. A. Shchukin & D. Bimberg, *Rev. Mod. Phys.*, vol. **71**, no. 4, pp. 1125 – 1171, 1999.

[5] D. Suess, *Appl. Phys. Lett.*, vol. **89**, p. 113105, 2006.

[6] R. L. Comstock, *J. Mater. Sci.: Mater. Elec.*, vol. **13**, pp. 509 – 523, 2002.

[7] R. Skomski & J. M. D. Coey, *Phys. Rev. B*, vol. **48**, no. 21, pp. 15812 – 15816, 1993.

[8] A. Mougin, C. Dufour, K. Dumesnil & Ph. Mangin, *Phys. Rev. B*, vol. **62**, no. 14, pp. 9517 – 9531, 2000.

[9] D. Wang, C. G. Morrison, A. R. Buckingham, G. J. Bowden, R. C. C. Ward & P. A. J. de Groot, *J. Mag. Mag. Mater.*, vol. **321**, pp. 586 – 589, 2009.

[10] M. J. Bentall, R. A. Cowley, W. J. L. Buyers, Z. Tun, W. Lohstroh, R. C. C. Ward & M. R. Wells, *J. Phys.: Condens. Matt.*, vol. **15**, pp. 4301 – 4330, 2003.

[11] A. Mougin, C. Dufour, K. Dumesnil, N. Maloufi, Ph. Mangin & G. Patrat, *Phys. Rev. B*, vol. **59**, no. 8, pp. 5950 – 5959, 1999.

[12] K. Wang, K. N. Martin, C. G. Morrison, R. C. C. Ward, G. J. Bowden & P. A. J. de Groot, *Appl. Phys. A*, vol. **86**, pp. 325 – 328, 2007.

[13] J. A. Osborn, *Phys. Rev.*, vol. **67**, nos. 11 & 12, pp. 351 – 357, 1945.

[14] J. P. Zimmermann, *Ph. D. Thesis*, University of Southampton, UK, 2007.

[15] K. N. Martin, P. A. J. de Groot, B. D. Rainford, K. Wang, G. J. Bowden, J. P. Zimmermann & H. Fangohr, *J. Phys.: Condens. Matt.*, vol. **18**, pp. 459 – 478, 2006.

[16] G. J. Bowden, P. A. J. de Groot, B. D. Rainford, K. Wang, K. N. Martin, J. P. Zimmermann & H. Fangohr, *J. Phys.: Condens. Matt.*, vol. **18**, pp. 5861 – 5871, 2006.

[17] T. W. McDaniel, W. A. Challener & K. Sendur, *IEEE Trans. Mag.*, vol. **39**, no. 4, pp. 1972 – 1979, 2003.

[18] J-. G. Zhu, X. Zhu & Y. Tang, *IEEE Trans. Mag.*, vol. **44**, no. 1, pp. 125 – 131, 2008.

[19] A. Aziz, S. J. Bending, H. Roberts, S. Crampin, P. J. Heard & C. H. Marrows, *J. Appl. Phys.*, vol. **98**, p. 124102, 2005.

[20] Q. F. Xiao, J. Rudge, B. C. Choi, Y. K. Hong & G. Donohoe, *Appl. Phys. Lett.*, vol. **89**, p. 262507, 2006.

[21] S-. K. Kim, Y-. S. Choi, K-. S. Lee, K. Y. Guslienko & D-. E. Jeong, *Appl. Phys. Lett.*, vol. **91**, p. 082506, 2007.

[22] M. Huber, J. Zweck & D. Weiss, *Phys Rev. B*, vol. **77**, p. 054407, 2008.

[23] C. Dietrich, R. Hertel, M. Huber, D. Weiss, R. Schäfer & J. Zweck, *Phys. Rev. B*, vol. **77**, p. 174427, 2008.

[24] M. Tanase, A. K. Petford-Long, O. Heinonen, K. S. Buchanan, J. Sort & J. Nogués, *Phys. Rev. B*, vol. **79**, p. 014436, 2009.

[25] U. Lehmann, S. Hadjidj, V. K. Parashar, C. Vandevyver, A. Rida & M. A. M. Gijs, *Sens. Act. B*, vol. **117**, pp. 457 – 463, 2006.
[26] C. Yi, C-. W. Li, S. Ji & M. Yang, *Anal. Chim. Acta*, vol. **560**, pp. 1 – 23, 2006.

Chapter 7

Summary and Outlook

The famous talk by Feynman entitled "There's Plenty of Room at the Bottom" made some 50 years ago, introduced the world to the concept of nano-technology [1]. Feynman envisaged new types of microscopy, permitting imaging of atomic scale structures, and the construction of smaller electronic circuitry, allowing for the fabrication of denser and higher performance computer components. Today these are no longer postulations, but are reality. The transmission electron microscope [2], atomic force microscope [3] and He^+ ion microscope [4] all offer the potential to visualise the atomic-scale world, a vast improvement to the microscopy techniques available half a decade ago. Modern computer chips are now based upon true nano-scale technology with typical circuitry dimensions of 65 and 45 nm, and more recently, 32 nm [5]. In contrast to nano-technology, the subject of magnetism has existed for millennia. It has found a wide range of technological applications over the centuries ranging from magnetic needles in compasses through to electric motors and data storage. The concept of teaming up nano-technology with magnetism opens up a vast number of opportunities [6, 7]. These range from microelectromechanical systems and actuators [8, 9] to magnetoresistive random access memory (MRAM) [10, 11, 12, 13], and from improvements in magnetic data storage media [14, 15] to developments in hard disk drive read / write heads [16, 17].

In this thesis, attention has been focussed on the fundamental properties of nano-structuring epitaxially grown rare earth – transition metal magnetic films and "exchange spring" systems. The use of alternating layers of soft and hard magnetic films to form an exchange spring system was initially proposed by Goto *et al.* [18] some 45 years ago. Due to advances in thin-film deposition techniques, the idea was revived nearly 20 years ago by Kneller & Hawig [19] and Skomski & Coey [20, 21, 22] in an attempt to increase the maximum energy product of permanent magnets. Not long after, it was realised that these materials could provide a solution to the superparamagnetic limit in magnetic data storage [23]. Exchange spring systems can be used to provide a high thermal stability against magnetization reversal, but with a reduced coercivity which

will aid in writing information to the media [24]. The work contained in this thesis provides a cornerstone in the research into the use of novel exchange spring media throughout a range of fields. The epitaxial nature of these media makes them ideally suited as model systems for investigating fundamental physical effects. Here, nano-structuring has been used to accurately engineer the dimensions of the media, and so investigate their potential in a range of fields, with particular focus being given to magnetic data storage. The nano-structuring was achieved using two distinctly different methods, i) Electron beam lithography and ion milling was used to artificially structure the media at the nano-scale, and ii) energetic ion implantation was used to accurately control the internal crystalline structure of the media at the atomic-scale.

The key results obtained in this thesis are summarised in section 7.1, followed by a brief overview in section 7.2 aimed at suggesting new experiments which are likely to lead to fruitful developments.

7.1 Summary of results

In this thesis, several new nano-fabrication techniques for Rare earth – iron ($REFe_2$) media have been introduced. Nano-structured $REFe_2$ media has been achieved by following two distinctly different routes; one lithographically based, and one centred on energetic ion implantation. For clarity, this summary is broken into three sections. Firstly, the fabrication techniques developed and employed in order to permit nano-scale patterning in $REFe_2$ media are summarised. Secondly, the most striking and important results regarding the direct and accurate modification of the dominant source of magnetic anisotropy using Ar^+ ion implantation are described. Finally, a summary of the results regarding the study of the magnetic properties of nano-scale patterned $REFe_2$ media is given.

7.1.1 Nano-scale fabrication techniques

To define nano-scale patterned elements in epitaxially grown $REFe_2$ films and multilayers it was necessary to devise and implement some new experimental procedures. This originates from the lack of compatibility between the processes of MBE growth and lift-off. Accordingly, it is necessary to use an etch-back process to define patterns in MBE grown $REFe_2$ media. This in itself is non-trivial since the media is etched so readily by wet chemical methods it is impossible to reliably achieve nano-

scale resolution. Similarly, the media does not lend itself to reactive ion etching due to its complex composition. Therefore the process of Ar^+ ion milling was developed and employed to enable nano-scale pattern definition in this media for the first time.

To facilitate pattern definition on the nano-scale, the in-house electron beam (eBeam) lithography equipment required significant modification. This focussed on the installation of a lanthanum hexaboride (LaB_6) crystal electron source to replace the standard W filament, and the implementation of proximity effect correction software (PECS). The LaB_6 crystal increased the brightness by nearly two orders of magnitude. This in turn made it possible to use a beam of electrons with a diameter ($Ø_b$) much smaller than that used previously; $Ø_{b_{LaB_6}} \approx 10$ nm, *c.f.* $Ø_{b_W} \approx 30$ nm. The smaller $Ø_b$ permitted the definition of patterns in the eBeam resist with a resolution of less than 100 nm, leading to an increase of more than an order of magnitude over previous work. When coupled with PECS, this allowed sub-micron sized square elements to be defined with near right-angled corners and very smooth, regular edges.

Substantial development was undertaken in order to define a metallic mask suited to the ion milling process. This stemmed from original work using a polymer mask which was shown to afford good resolution, but at the expense of resilience to energetic Ar^+ ions during the etching process. Research into designing a suitable metallic mask began with the development of a bi-layer eBeam resist process. Here, two eBeam resists, each having a different response to the incident beam of electrons are separately applied to the sample. The bottom resist layer has weaker bonds between the polymer chains, thus more chains are broken ("scissoned") per unit of incident electron energy. The result is the formation of an under-cut in the lithographically defined pattern, introducing the possibility of defining a thick metallic mask using the lift-off process. Subsequently, nano-scale Cr metallic masks were successfully deposited using thermal evaporation and lift-off.

To transfer the lithographically defined patterns into the epitaxially grown $REFe_2$ films and multilayers an Ar^+ ion milling process was designed and implemented. Ar^+ ion milling was chosen since it offers far superior resolution to wet etching of $REFe_2$ materials using HNO_3, while avoiding the serious complexities associated with reactive ion etching. Design and implementation of a suitable, low-cost Ar^+ ion source took considerable effort. Demonstrations of the first nano-scale patterns defined in various $REFe_2$ media by Ar^+ ion milling were presented, marking significant improvements in

terms of both ultimate scale and pattern resolution over previous work in similar media [25, 26, 27, 28]. This confirms the success of the electron beam lithography and metallic mask based Ar^+ ion milling process as a suitable technique to define micro- and nano-scale elements in multilayer $REFe_2$ exchange spring media.

7.1.2 Ar^+ ion induced modification to crystalline structures and magnetic properties

The $REFe_2$ Laves phase films and multilayers investigated in this work were grown on an Al_2O_3 substrate at elevated temperatures to promote epitaxial growth [29, 30]. During the post-growth cool-down process, there is a differential thermal contraction between the substrate and the metallic film [31]. This gives rise to a change in the crystalline lattice of the metallic film, resulting in a shear-strain of ε_{xy}= –0.5% [32]. The corresponding changes in lattice parameter were found to be a reduction in the growth direction by –0.4%, accompanied by an expansion in the plane of the film by 0.6% in order to conserve volume. The X-ray diffraction (XRD) measurements repeated in this work agree well with this value, identifying a contraction in the growth direction of –0.6% for the 100 nm thick YFe_2 film, and a –0.5% contraction for the 400 nm $DyFe_2$ film.

The XRD data for the YFe_2 sample show that once subject to a critical fluence of order 7×10^{16} Ar^+ ions cm^{-2}, the strain in the growth direction of the film is completely relaxed. The XRD data for the $DyFe_2$ sample show very similar results. After implantation by a critical fluence of order 10^{17} Ar^+ ions cm^{-2}, the lattice parameter in the film growth direction is notably increased to just –0.2% less than that in the bulk material, corresponding to a large reduction in strain. Changes in strain gives rise to significant changes to the magnetic behaviour since the strain term, ε_{xy}, is the dominant factor in determining the magnetoelastic anisotropy energy. This is borne out in MOKE and VSM experimental results, which both show significant changes in the magnetization reversal mechanisms between as-grown samples and those implanted with Ar^+ ions. In the case of the YFe_2 sample, implantation by a fluence of $\sim 7 \times 10^{16}$ Ar^+ ions cm^{-2} causes orthogonal axes of the sample to exhibit equal magnetic behaviour, corresponding to an equivalent dominance of magnetoelastic and magnetocrystalline anisotropies. Further increases to the fluence result in an increased dominance of the magnetocrystalline anisotropy, corresponding to a sample which is increasingly approaching that of a bulk, un-strained film. For the $DyFe_2$ sample, the strain is only

partially eliminated, with experimental results showing a combination of both magnetoelastic and magnetocrystalline behaviour. These key results are well reproduced in the accompanying micromagnetic simulations when the strength of the magnetoelastic anisotropy is reduced.

At room temperature in the epitaxially grown $REFe_2$ Laves phase materials studied in this work, the magnetoelastic anisotropy energy is always dominant over the magnetocrystalline anisotropy energy [33]. Thus, the easy axis of magnetization is governed primarily by the direction which serves to minimise the magnetoelastic anisotropy energy. Implantation of Ar^+ ions, which cause the strain in the film to be relaxed, in turn result in a reduction to the magnetoelastic anisotropy. Once a critical fluence of Ar^+ ions is reached ($\sim 7 \times 10^{16}$ and $\sim 1 \times 10^{17}$ ions cm^{-2} in the YFe_2 film and $DyFe_2$ film respectively), the magnetocrystalline anisotropy will begin to dominate. This is evidenced by a change in lattice parameter towards that of the bulk film, and a corresponding change in easy and hard axes of magnetization, again characteristic of that in the bulk film. This is exactly what is observed experimentally and confirmed by computational modelling. Similarly, the effects of Ar^+ ion implantation are equally well reproduced in a $DyFe_2$ / YFe_2 multilayer exchange spring sample. This is to be expected since in such a sample the magnetic anisotropy is dominated by the $DyFe_2$ layers.

SRIM modelling of the interactions between energetic Ar^+ ions and $REFe_2$ films show that the ions are stopped fully within the film, penetrating less than 10 nm into the material. But XRD measurements, which analyse the entire sample thickness, clearly show that the strain is altered throughout the *entire* sample. This is quite possibly due to the epitaxial nature of the film. The energetic Ar^+ ions incident on the target material impart energy to the constituent atoms, causing them to recoil by small distances. The recoiled atoms subsequently relax into their energetically favourable unstrained lattice positions, thereby causing the crystalline structure to revert to that of the un-strained material, while retaining its epitaxial structure. This effect then propagates rapidly throughout the entire sample volume due to the epitaxial structure and brittle nature of $REFe_2$ films. The effect of implanted ions could also be amplified due to the "channelling" effects present when ordered crystalline structures are subject to ion implantation. Ions that are approximately parallel to crystalline planes experience additional interatomic forces [34], reducing the number of collisions between the ions and atoms thus increasing the implantation depth [35]. However, during this work the

samples are continuously rotated, thereby significantly reducing the chances of incident ions aligning parallel to crystalline planes.

This work provides the first demonstration of energetic Ar^+ ion induced modification to the magnetic and crystalline structure of epitaxially grown $REFe_2$ films and multilayers. Not only are the effects pronounced, but they can be accurately and reproducibly controlled by varying just one factor; the incident Ar^+ ion fluence. Thus when combined with a mask, broad-beam Ar^+ ion implantation could provide a useful tool by means of which nano-scale patterned magnetic media may be rapidly fabricated without the need for complex media planarization processes. In addition to the practical benefits, Ar^+ ion implantation has also provided the first conclusive evidence that there is in fact a significant magnetoelastic anisotropy in epitaxial YFe_2 films, contrary to previous predictions [33]. Magnetoelastic anisotropy is usually associated with second order crystal field terms originating from the RE atoms. Clearly in the case of YFe_2 this is not the case, thus the magnetoelastic anisotropy is tentatively ascribed to the 4d electrons of the Y atoms.

7.1.3 Patterned elements in $REFe_2$ multilayers

The fabrication techniques summarised in section 7.1.1 have been used to define nano-scale elements in epitaxial $REFe_2$ exchange spring media. Not only is this the first demonstration of nano-scale structuring in these media, it also provides the first experimental verification of the use of eBeam lithography and Ar^+ ion milling to pattern such media.

Whilst nano-scale pattern definition in these media was clearly successful, it was found that, due to the very large intrinsic magnetocrystalline and magnetoelastic anisotropies, the effects of induced shape anisotropies on the scale of hundreds of nm were minimal. Whist the specific materials studied throughout this work are not of direct relevance to magnetic data storage media due to their predominantly in plane magnetization, it does confirm that similar high anisotropy media with perpendicular magnetization (*e.g.* Laves phase $ErFe_2$ / YFe_2 exchange spring systems) could be excellent candidates for magnetic data storage media. The fact that the nano-structured $REFe_2$ exchange spring multilayers remain magnetically hard shows that they can be implemented as a good candidate to avoid superparamagnetic effects. In addition to investigating the effects of artificially nano-structuring hard magnetic exchange spring media, the patterning process was also implemented on arguably more technologically

relevant thin film bi-layers of $REFe_2$ media. Whilst there are problems with the media's magnetic properties due to the nature of the MBE growth process, the patterning process was shown to be more successful, permitting the definition of smaller structures as well as avoiding any drawbacks which may deteriorate the minimum attainable size of the lithographically defined features.

Thus the work as a whole, combining the excellent magnetic anisotropy and exchange spring characteristics of thicker media, and the improved pattern definition and resolution in bi-layer media, represents important first steps towards future research. Transfer of the fabrication processes demonstrated in this work to other transition metal based exchange spring media such as FePt / NiFe, will likely see applications in magnetic data storage, nano-scale sensors and actuators for MEMS, MRAM and spin transfer torque devices. Furthermore, the patterning process also provides the potential for "lithographically imprinting" magnetic media. In such a process, the remnant magnetic properties of the media may be readily identified by simple MFM characterization. This also offers the potential for pin-pointing any changes in local magnetic properties which may be induced by the presence of organic materials in lab-on-chip type arrangements [36, 37].

7.2 Outlook to Future Work

Given the successes enjoyed in terms of both improvements to nano-scale patterning in $REFe_2$ media and the interesting emergence of the new phenomenon caused by ion implantation, there is ample scope for further work.

There exists the possibility for significant further investigation of the crystalline structure of Ar^+ ion implanted samples. This could take the form of performing more detailed XRD measurements, where the crystalline structure is investigated not only in the growth direction of the media, but also in the film plane. This would provide a more complete understanding of the dynamic changes in $REFe_2$ Laves phase volume induced by the Ar^+ ion implantation process. Combination of detailed XRD analysis with transmission electron microscopy (TEM) should also provide a clearer picture with regard to any disruptions induced in the Nb and Fe seed and buffer layers.

The effects of Ar^+ ion implantation in multilayer exchange spring systems have only been touched upon in this work. Thus there exists considerable scope for detailed investigations regarding the effects of ion implantation in these structures, whereby it

may be possible to identify and isolate effects in the different magnetic layers. XRD and TEM analysis of such samples should make it possible to build a more detailed picture of the Ar^+ ion induced intermixing at the interfaces between the hard and soft magnetic layers. Similarly, in all of the films and multilayers, detailed measurements of the electrical resistance, both before and after Ar^+ ion implantation, would provide further insight into changes in the crystalline structure.

A topic which definitely warrants further investigation concerns the effects of *selective* Ar^+ ion implantation. That is, the process of Ar^+ ion implantation in $REFe_2$ media through a lithographically defined mask, in a manner similar to the pioneering work of Chappert *et al.* [38]. In this thesis, the effects of broad-beam Ar^+ ion implantation have been shown to significantly alter magnetic properties of $REFe_2$ films and multilayers. Isolating these effects to lithographically defined nano-scale regions opens the real potential for completely flat, nano-scale patterned magnetic media. This may serve to simplify bit-patterned media fabrication *significantly*. Of course there also exists the possibility to investigate the potential use of nano-fabricated $REFe_2$ media in MRAM and MEMS devices, microwave structures for ferromagnetic resonance studies and domain-wall racetrack memories such as those proposed by Parkin *et al.* [39, 40]

On a more immediate time-scale, there exists the potential of investigating artificially induced shape anisotropies in epitaxial $REFe_2$ thin film media, structured on the scale of tens of nm, or even on the single nm scale, with the use of new and superior fabrication equipment. In fact this is available on a very realistic time scale; during the writing of this thesis, the new nano-fabrication centre at the University of Southampton has been opened [41]. The author believes that the future researcher would not have to wait long to demonstrate pronounced shape anisotropy effects in sub-100 nm scale patterned $REFe_2$ media.

References

[1] R. P. Feynman, *Eng. Sci.*, vol. **23**, no. 5, pp. 22 – 26, 30, 34 & 36, 1960.

[2] A. V. Crewe, J. Wall & J. Langmore, *Science*, vol. **12**, no. 3937, pp. 1338 – 1340, 1970.

[3] G. Binning, C. F. Quate, Ch. Gerber, *Phys. Rev. Lett.*, vol. **56**, no. 9, pp. 930 – 933, 1986.

[4] Carl Zeiss Press Release, *Carl Zeiss SMT Ships World's First ORION™ Helium Ion Microscope to U.S. National Institute of Standards and Technology*, PI no. 125/07, p. 4, 2007.

[5] J. Casazza, *First the Tick, Now the Tock: Intel® Microarchitecture (Nehalem)*, White Paper, Intel® Xeon® Processor 3500 and 5500 series, Intel® Microarchitecture, 2009.

[6] S. D. Bader, *Rev. Mod. Phys.*, vol. **78**, pp. 1 – 15, 2006.

[7] G. Srajer, L. H. Lewis, S. D. Bader, A. J. Epstein, C. S. Fadley, E. E. Fullerton, A. Hoffmann, J. B. Kortright, K. M. Krishnan, S. A. Majetich, T. S. Rahman, C. A. Ross, M. B. Salamon, I. K. Schuller, T. C. Schulthess & J. Z. Sun, *J. Mag. Mag. Mater.*, vol. **307**, pp. 1 – 31, 2006.

[8] R. Bogue, *Assem. Autom.*, vol. **29**, no. 4, pp. 313 – 320, 2009.

[9] D. P. Arnold & N. Wang, *J. Microelectromech. Sys.*, vol. **18**, no. 6, pp. 1255 – 1266, 2009.

[10] J-. G. Zhu, Y. Zheng & G. A. Prinz, *J. Appl. Phys.*, vol. **87**, no. 9, pp. 6668 – 6673, 2000.

[11] S. Tehrani, J. M. Slaughter, M. Deherrera, B. N. Engel, N. D. Rizzo, J. Salter, M. Durlam, R. W. Dave, J. Janesky, B. Butcher, K. Smith & G. Grynkewich, *Proc. IEEE*, vol. **91**, no. 5, pp. 703 – 714, 2003.

[12] J-. G. Zhu, *Proc. IEEE*, vol. **96**, no. 11, pp. 1786 – 1798, 2008.

[13] J. M. Slaughter, *Annu. Rev. Mater. Res.*, vol. **39**, pp. 277 – 296, 2009.

[14] H. J. Richter, *J. Phys. D: Appl. Phys.*, vol. **40**, pp. R149 – R177, 2007.

[15] S. N. Piramanayagam, *J. Appl Phys.*, vol. **102**, p. 011301, 2007.

[16] A. Moser, K. Takano, D. T. Margulies, M. Albrecht, Y. Sonobe, Y. Ikeda, S. Sun & E. E. Fullerton, *J. Phys. D: Appl. Phys.*, vol. **35**, pp. R157 – R167, 2002.

[17] N. X. Sun & S. X. Wang, *IEEE Trans. Mag.*, vol. **36**, no. 5, pp. 2506 – 2508, 2000.

[18] E. Goto, N. Hayashi, T. Miyashita & K. Nakagawa, *J. Appl. Phys.*, vol. **36**, no. 9, pp. 2951 – 2958, 1965.

[19] E. F. Kneller & R. Hawig, *IEEE Trans. Mag.*, vol. **27**, no. 4, pp. 3588 – 3600, 1991.

[20] R. Skomski & J. M. D. Coey, *Phys. Rev. B*, vol. **48**, no. 21, pp. 15812 – 15816, 1993.

[21] J. M. D. Coey, *Sol. Stat. Com.*, vol. **102**, no. 2 – 3, pp. 101 – 105, 1997.

[22] R. Skomski, *J. Appl. Phys.*, vol. **76**, no. 10, pp. 7059 – 7064, 1994.

[23] I. A. Al-Omari & D. J. Sellmyer, *Phys. Rev. B.*, vol. **52**, no. 5, pp. 3441 – 3447, 1995.

[24] E. Girt & H. J. Richter, *IEEE Trans. Mag.*, vol. **39**, no. 5, pp. 2306 – 2310, 2003.

[25] K. Wang, K. N. Martin, C. G. Morrison, R. C. C. Ward, G. J. Bowden & P. A. J. de Groot, *Phys. Stat. Sol.*, vol. **203**, no. 15, pp. 3831 – 3835, 2006.

[26] K. Wang, C. Morrison, K. N. Martin, R. C. C. Ward, G. J. Bowden & P. A. J. de Groot, *J. Alloy. Comp.*, vol **440**, pp. 23 – 25, 2007.

[27] K. Wang, K. N. Martin, C. G. Morrison, R. C. C. Ward, G. J. Bowden & P. A. J. de Groot, *Appl. Phys. A*, vol **86**, pp. 325 – 328, 2007.

[28] K. Wang, K. N. Martin, C. Morrison, R. C. C. Ward, G. J. Bowden & P. A. J. de Groot, *J. Alloy. Comp.*, vol. **455**, pp. 31 – 34, 2007.

[29] M. J. Bentall, R. A. Cowley, W. J. L. Buyers, Z. Tun, W. Lohstroh, R. C. C. Ward & M. R. Wells, *J. Phys.: Condens. Matt.*, vol. **15**, pp. 4301 – 4330, 2003.

[30] M. J. Bentall, R. C. C. Ward, E. J. Grier & M. R. Wells, *J. Phys.: Condens. Matt.*, vol. **15**, pp. 6493 – 6512, 2003.

[31] A. R. Wildes, R. A. Cowley, R. C. C. Ward, M. R. Wells, C. Jansen, L. Wireen & J. P. Hill, , *J. Phys.: Condens. Matt.*, vol. **10**, pp. L631 – L637, 1998.

[32] A. Mougin, C. Dufour, K. Dumesnil, N. Maloufi, Ph. Mangin & G. Patrat, *Phys. Rev. B*, vol. **59**, no. 8, pp. 5950 – 5959, 1999.

[33] A. Mougin, C. Dufour, K. Dumesnil & Ph. Mangin, *Phys. Rev. B*, vol. **62**, no. 14, pp. 9517 – 9531, 2000.

[34] G. Carter, *J. Phys. D: Appl. Phys.*, vol. **34**, pp. R1 – R22, 2001.

[35] M. T. Robinson & O. S. Oen, *Appl. Phys. Lett.*, vol. **2**., no. 2, pp. 30 – 32, 1963.

[36] U. Lehmann, S. Hadjidj, V. K. Parashar, C. Vandevyver, A. Rida & M. A. M. Gijs, *Sens. Act. B*, vol. 117, pp. 457 – 463, 2006.

[37] C. Yi, C.- W. Li, S. Ji & M. Yang, *Anal. Chim. Acta*, vol. **560**, pp. 1 – 23, 2006.

[38] C. Chappert, H. Bernas, J. Ferré, V. Kottler, J-. P. Jamet, Y. Chen, E. Cambril, T. Devolder, F. Rousseaux, V. Mathet & H. Launois, *Science*, vol. **280**, pp. 1919 – 1922, 1998.

[39] M. Hayashi, L. Thomas, R. Moriya, C. Rettner & S. S. P. Parkin, *Science*, vol. **320**, pp. 209 – 211, 2008.

[40] S. S. P. Parkin, M. Hayashi & L. Thomas, *Science*, vol. **320**, pp. 190 – 194, 2008.

[41] *The Southampton Nano-fabrication centre*, more details available on-line at http://www.southampton-nanofab.com/

Appendix

Electron beam resist application recipe

The sample must first be thoroughly cleaned to ensure no foreign bodies (dust *etc.*) appear in the patterns and also to ensure good resist adhesion. A 10 minute isopropanol (IPA) ultra-sonic bath at 100% standard power at room temperature, followed by a further 10 minute ultra-sonic bath using methanol provides adequate cleaning. For samples that have more stubborn debris *etc.*, for example those which have been coated with ebeam- or photo-resist in the past, the above process can be preceeded by a 10 minute acetone ultra-sonic bath (heated to 50°C if required). After each ultra-sonic bath step the sample should be blown dry with N_2 or filtered compressed air. The author's eBeam resist application process takes the following form:

1. Set a digital hot plate to 180°C.
2. Place the sample onto a spin coater and check the vacuum functionality (if applicable).
3. Dispense a set amount (~ 10 – 100 μl depending on the sample size) of MMA-MAA using an *Eppendorf* pipette. The resist should form a "mound" approximately 1 mm high on the sample surface.
4. Spin coat at 500 rpm for 5 seconds to spread across the sample surface, then accelerate to 4,000 rpm for 40 seconds to form a layer 100 – 200 nm thick.
5. Immediately pre-bake on the digital hot-plate (at 180°C) for 1 minute to remove the solvent. Remove and allow to cool for 2 minutes.
6. Repeat steps 2 – 5 for PMMA.

Electron beam resist development

The patterns are developed by using a developer that preferentially removes regions with a lower molecular weight, *i.e.* in a positive resist those regions which have been exposed to electron radiation, and *vice-versa* for a negative resist. It is important to note that this is a differential process, so it is not possible to develop for an arbitrarily long period of time as eventually (typically after ~ 5 minutes) the developer will begin to remove the un-irradiated resist as well. The author has used the developer MIBK combined with IPA (100%) at a ratio of 1:3 to reduce the development rate with the intention of improving its accuracy, reliability and reproducibility. The development process is as follows:

1. Dispense MIBK:IPA (1:3) and IPA (100%) into two separate Petri dishes.
2. Submerge and agitate the sample in the MIBK:IPA developer solution for 30 seconds. Remove the sample and shake to remove any liquid on the surface.
3. Immediately submerge and agitate the sample in IPA for 15 seconds to halt development. Remove the sample.
4. Blow dry with N_2 / compressed air.
5. Check the development in an optical microscope.
6. If the sample is fully developed the process is complete, if not repeat steps 2 – 5 until fully developed.

Incomplete development of a sample often appears as streaks or changes in contrast when viewed with an optical microscope. Over development is characterized by the remaining resist appearing “speckled” in nature.

Calculation of sample thickness by vibrating sample magnetometry

As alluded to in the experimental methods description of VSM (section 3.11), it is possible to determine the physical dimensions of a sample from a hysteresis loop obtained by VSM measurements.

The saturation magnetization, M_S, may be derived from the VSM hysteresis loop. For the samples studied in this work, the number of Bohr magnetons ($N\mu_B$) per formula unit (f.u.) of the Laves phase unit cell is known. The number of f.u. within the sample ($n_{f.u.}$) is given by $n_{f.u.} = \frac{M_S}{N\mu_B}$. The number of Laves phase unit cells (l) is $l = \frac{n_{f.u.}}{8}$, so the total volume (v) of the sample is given by $v = la^3$ (where a is the lattice parameter of the Laves phase unit cell). Accordingly, the thickness (t) of the sample is given by $t = \frac{v}{d_1 d_2}$, where d_n is a (measured) lateral dimension of the sample. These equations may be combined to give $t = \frac{M_S a^3}{8N\mu_B d_1 d_2}$.

Thus the thickness t of the sample may be derived from knowledge of M_S (derived from the hysteresis loop), a (derived from X-ray diffraction measurements), N (available in the literature) and d_n (physically measured).